Computational Modelling of Spinal Control of Larval Zebrafish Swimming Speeds

Emine Topcu

A thesis submitted in partial fulfillment of the requirements for the Master's degree in Biology

Department of Biology
Faculty of Science
University of Ottawa

I dedicate this work to my late great-aunt, Emine Coşkun.

You were a remarkable educator, a role model for many, and touched countless lives.

Carrying your name gives me honour and responsibility.

Abstract

The zebrafish (*Danio rerio*) is a commonly used animal model for biological study due to its available transgenic lines, fast life cycle, transparency, and relative simplicity. Zebrafish are also a great candidate to study locomotion, as most of the neuronal populations responsible for locomotion in zebrafish are evolutionarily conserved, including in mammals. From very early stages, embryonic and larval zebrafish display a wide range of swim-like behaviour following the neuronal development of their spinal cord. During the larval stages, they display a beat and glide swimming pattern consisting of frequent tail beats at various tail beat frequencies (TBFs) followed by a quiescent period. The literature strongly supports the idea that there are spinal cord speed microcircuits behind these different TBFs. However, the structure and mechanism of operation of these microcircuits are not well understood.

Computational models are excellent tools for studying model animals as they enable tests which are not possible with the current experimental techniques. Previously, our lab has created computational models of various forms of swim-like behaviours of embryonic and larval zebrafish, displaying how different cellular populations interact to create the behavioural repository of the early stages of zebrafish development. This study aims to simulate the activation of speed microcircuits that can generate different speeds of the beat and glide swimming of larval stages.

Based on the information presented in the literature, I hypothesize that there are speed microcircuits in the larval zebrafish spinal cord that are differentially recruited by the supraspinal regions and generate different tail beat frequencies. Different intrinsic properties, spatial distributions, projection lengths, patterns, and synaptic strengths are the building blocks of these microcircuits.

There are currently close to twenty cell subgroups known to be differentially recruited at different swimming speeds. To be able to generate a model handling such complexity, a software tool, *Sili*Fish, was implemented to create and test computational models of spinal control of swimming behaviour easily and quickly. Using *Sili*Fish, a network of 440 cells and more than 8K synapses were created that can generate different ranges of tail beat frequencies, recruiting different cellular groups. The model is able to generate tail beats at different TBFs and replicates several features of spinal circuits observed experimentally, as reported in the literature.

Résumé

Le poisson zèbre (*Danio rerio*) est un animal modèle couramment utilisé pour la recherche en biologie en raison de ses lignées transgéniques disponibles, de son cycle de vie rapide, de sa transparence et de sa relative simplicité. Le poisson zèbre est également un excellent candidat pour étudier la locomotion, car la plupart des populations neuronales responsables de la locomotion chez le poisson zèbre sont conservées au cours de l'évolution, y compris chez les mammifères. Dès les premiers stades, les poissons zèbres embryonnaires et larvaires présentent un large éventail de comportements de nage en fonction du développement neuronal de leur moelle épinière. Au cours des stades larvaires, ils présentent un modèle de nage en battement et en glissement composé de battements de queue fréquents à diverses fréquences de battement de queue (FBQ) suivis d'une période de repos. La littérature soutient fortement l'idée selon laquelle il existe des microcircuits de vitesse de la moelle épinière derrière ces différents TBF. Cependant, la structure et les mécanismes d'opération de ces microcircuits ne sont pas bien compris.

Les modèles informatiques sont d'excellents moyens d'étudier des animaux modèles car ils permettent des tests impossibles avec les techniques expérimentales actuelles. Auparavant, notre laboratoire a créé des modèles informatiques de diverses formes de comportements de nage du poisson zèbre embryonnaire et larvaire, montrant comment différentes populations cellulaires interagissent pour créer le référentiel comportemental des premiers stades du développement du poisson zèbre. Cette étude vise à simuler l'activation de de microcircuits de vitesse capables de générer différentes vitesses de battement et de nage planée des stades larvaires.

Sur la base des informations présentées dans la littérature, j'émets l'hypothèse qu'il existe des microcircuits de vitesse dans la moelle épinière des larves de poisson zèbre qui sont recrutés de manière différentielle par les régions supraspinales et génèrent différentes fréquences de battement de queue. Différentes propriétés intrinsèques, distributions spatiales, longueurs de projection, modèles et forces synaptiques sont les éléments constitutifs de ces microcircuits.

Il existe actuellement près de vingt sous-groupes de cellules connus pour être recrutés de manière différentielle à différentes vitesses de nage. Pour pouvoir générer un modèle gérant une telle complexité, un outil logiciel, SiliFish, a été mis en œuvre pour créer et tester facilement et rapidement des modèles informatiques de contrôle spinal du comportement de nage. Grâce à *Sili*Fish, un réseau de 440 cellules et plus de 8 000 synapses ont été créés, capables de générer

différentes plages de fréquences de battement de queue, recrutant différents groupes cellulaires. Le modèle est capable de générer différentes FBQ et recréer plusieurs données expérimentales publiées.

Acknowledgment

This research is funded by the Natural Sciences and Engineering Research Council of Canada (NSERC), [NSERC Discovery Grant (RGPIN-2015-06403), NSERC Canadian Graduate Scholarship M award (NSERC 566014-2021)], and the Ontario Graduate Scholarship (OGS).

Being a graduate student is much easier if you have the intellectual and mental support. Many people helped me along my journey in various ways that I am indebted to.

I want to extend my gratitude to all my Thesis Advisory Committee members, Dr. Tuan Bui, Dr. John Lewis and Dr. Jeff Dawson, for their guidance, insightful feedback, and support.

My supervisor, Dr. Tuan Bui: You deserve special thanks for your mentorship, availability for help, saving me when I got stuck, asking the right questions, and your generosity allowed me to share my research at many conferences and meetings. What you had in mind for my project when I first joined your lab is very different than the end product. You have been very flexible in accommodating my ideas to incorporate and gave me vital directions. You are the ideal supervisor a graduate student can wish for.

Dr. John Lewis: You helped me tremendously by catching my mistakes in one shot during our meetings. Your attention to detail far surpasses mine and saved me from tight spots multiple times. I also learned a lot by being a teaching assistant to your classes in terms of how to reach out to students. I will carry this experience when I have a class to teach of my own.

Dr. Jeff Dawson: Thank you for your continuous support and encouragement. I did not listen to you when you asked for the “simplest model” initially, which I ended up switching to eventually. I should have known better. You gave me a very strong foundation in my undergrad that I did my best to incorporate during my research. Thank you.

I want to thank the current and past members of the Bui Lab, particularly Stephanie Gaudreau, Dr. Sara Goltash, Dr. Alex Laliberte, and Sarah Chiasson, for their insightful feedback throughout the last couple of years. Dr. Yann Roussel: even though our times in the lab did not coincide, your code and model I inherited gave me a big head-start.

Thank you, Dr. Emily Standen, for showing me how cool biomechanics is and giving me ideas on how to model swimming behaviour.

I want to send a heartful thanks to Stephanie Gaudreau, Maddison Reed, and Mary Patricia Upshall for organizing the Neurophysiology Journal Club. The deep discussions we had during the club meetings were priceless and taught me so much in terms of understanding other researchers' studies. I always had this knowledge with me when I was reading the literature for my research.

Thank you, my partners in crime in assisting the same courses, Jeffrey Hainer and Sarah Chiasson, for being flexible in sharing our TA duties when my research requested a specific time.

My family has been my biggest support throughout this journey. My sister, Prof. Sibel Aydin warned me about the hardship the academia requires and has been showing her full support since I started this journey anyway. I submitted my university application with her by my side; I picked her brains doing the statistical analysis for this thesis—it was literally continuous support.

My husband, Feti Can: I would not survive if it were not for you. I don't think I can give justice to how much you helped me during my research. You fed me, literally and intellectually. You know my research in and out, you were never tired of listening to how my fish or neurons behave. You deserve a special thank you for recommending genetic algorithms for me, which became an important component of *Sili*Fish. This is only one example. Allowing my research to be part of our lives, you always had something to suggest.

I am appreciative of my parents' support, both intellectually and emotionally. You believed in me from the very start, even when I did not. The first time I learned how neurons worked was from my mother. Furthermore, we will continue our talks on the damped pendulum of the tail modelling after my dissertation because you know I will want to continue expanding the tool. I will always continue to learn from you.

I thank my friend and Bio Coders Club partner, Andre Telfer, for listening to my research for countless hours and our brainstorming chats.

Dr. Annemarie Dedek: Every paragraph in my thesis is written with the knowledge you gave me on how to write. I was one of the luckiest undergrad students to have a mentor like you.

I thank my old band members for patiently waiting for me until I realized I could not continue being part of a band with academia and had to retire. It was not an easy decision, but two passions were hard to have at this age. I am glad our paths crossed, even though not long enough to finish our next EP. I do miss you all.

Part of my research constitutes software development. The generous community of software developers deserves a very special thank you. They do not know my existence, but Vasco Asturiano's graphing libraries, Diego Giacomelli's genetic algorithms, Dan Vanderkam's charting libraries, and AmCharts (by Antanas, Martynas, Gediminas, Ty, Paul, Anthony, and Alan) brought my software to a totally different level. Lastly, a very special thanks to the community members who contributed to Obsidian development: Without Obsidian, I would be lost.

Using the right tools makes a huge difference in the success of a project. I was fortunate to have access to many great, open source, and free tools to use. I am hoping the tool I developed will be beneficial to other researchers as well.

Statement of Contributions

The work described in this thesis is my own. However, the core components of the *Sili*Fish algorithm were translated from Python and expanded upon from Dr. Roussel's and Dr. Bui's code (Roussel et al., 2021), which is available at https://github.com/Bui-lab/Code: the choice of mathematical formulizations of cells and synapses, the main logic of calculating membrane potential changes throughout the simulation time, the main logic of the simulation, and the uncoupled damped pendulum modelling of the tail behaviour.

Disclaimer

The software implemented as part of my research, *Sili*Fish, is made available without any warranties. The source code is available on https://github.com/Bui-lab/SiliFish for anyone interested in using or expanding upon it. If the user finds any problems with the software, they can create an issue on GitHub, and every reasonable effort will be made to overcome the issue.

Table of Contents

List of Tables

List of Figures

Abbreviations

C: Capacitance
CaP: Caudal primary
CiA: Circumferential ascending
CoBL: Commissural bifurcating longitudinal
CoPr: Commissural premotor neurons
CPG: Central pattern generators
dpf: Days post fertilization
dRoP: Dorsal rostral primary
E_{rev}: Reversal potential
G: Conductance
GA: Genetic algorithms
HB: Hindbrain
IBI: Inter-burst interval
IN: Interneuron
IQR; Inter quartile range
McoD: Multipolar commissural descending
MiP: Middle primary
MLF: Medial longitudinal fasciculus
MN: Motoneuron
mV: MiliVolt
NMJ: Neuromuscular junction
OOD: Object-oriented design
pA: PicoAmpere
pF: PicoFarad
pMN: Primary motoneuron
R: Resistance
sMN: Secondary motoneuron
T: Tension
TBF: Tail beat frequencies
UI: User interface
V: Membrane Potential
VaP: Variable primary
V_{max}: Maximum membrane potential
V_r: Reset membrane potential after a spike
V_{rest}: Resting membrane potential
vRoP: Ventral dorsal primary
V_t: Threshold membrane potential for spiking

Chapter 1. Introduction

In 1979, the British statistician George E.P. Box had a section titled "All models are wrong, but some are useful" in his technical summary report (Box, 1979). Despite this valid realization that models do not reflect reality with perfect precision or accuracy, they are the scientists' lifeline, allowing them to work with simplified versions of complex systems. From animal to computational models, these simple models can help us better understand nature.

My project is the computational modelling of larval zebrafish swimming speeds to understand how spinal cord central pattern generators dictate different speeds in locomotion. The thesis below explains the rationale behind the model, the software tool developed to create the model, the software and biological design, and the scientific benefits of using the tool and the model.

1.1 Locomotion

From escape behaviour to predation, migration to exploration, animals move by crawling, flying, walking, or swimming. Whatever its form, locomotion is a behaviour executed by every animal in different forms and is crucial for survival. Yet, we do not fully understand how it is generated and modulated. The diversity of locomotor maneuvers, the differences in size and complexity of the ambulatory animals, and the role of the different mediums on which animals move impose possible variety in how locomotor activity is produced.

Various neural regions are involved in the initiation, maintenance, and completion of vertebrate locomotion (Arber and Costa, 2018; Grillner and El Manira, 2020). Supraspinal regions determine the goal of motor actions and can adjust ongoing movements at different stages of locomotion (Berg et al., 2023; Carbo-Tano et al., 2023; Dal Maschio et al., 2017; Hsu et al., 2023; Huang et al., 2013; Juvin et al., 2016; Kimura et al., 2013; Kinkhabwalaa et al., 2011). In vertebrates, downstream from supraspinal regions are central pattern generators (CPG) of the spinal cord that have been known to be responsible for the rhythmic, alternating behaviour of the body or the limbs for over a century (Brown, 1911; Getting et al., 1980; Grillner et al., 1981; Wilson, 1961). Proprioception, mechanoception, and other sensory feedback are also important in modulating ongoing locomotion (Brown, 1911; Fidelin et al., 2015; Picton et al., 2021; Wu et al., 2021).

Supraspinal input has multiple roles like initiation or cessation of movement, steering, turning, or speed control (Bouvier et al., 2015; Capelli et al., 2017; Dubuc et al., 2008; Juvin et al., 2016; Thiele et al., 2014). In lampreys and cats, the increased electrical stimulation of the same mesencephalic locomotor region in the midbrain can generate different locomotor patterns (Cabelguen et al., 2003; Grillner and El Manira, 2020; Leiras et al., 2022; Whelan, 1996). Furthermore, unilateral stimulation of the MLR region was sufficient enough to generate a bilateral movement (Leiras et al., 2022). While these experiments suggest that these supraspinal regions play a key role in commanding locomotor activity, spinal CPGs may play the role of translating supraspinal commands into actual locomotor activity. The capacity to evoke swimming in spinalized zebrafish through chemical or optogenetic stimulations (Eklöf Ljunggren et al., 2014; McDearmid and Drapeau, 2006; Montgomery et al., 2021; Wahlstrom-Helgren et al., 2019; Wiggin et al., 2014, 2012) strongly suggests the presence of CPGs in the zebrafish spinal cord.

CPGs are the building blocks of rhythmic behaviour. They can be activated by the afferent commands from the higher brain regions as well as inputs from sensory neurons (Bui et al., 2016; Kinkhabwalaa et al., 2011; Nakanishi and Whelan, 2012; Rossignol and Frigon, 2011; Severi et al., 2014; Thiele et al., 2014; Whelan, 1996). CPGs gain special attention as they can generate rhythmic motion without the need for rhythmic input from the higher brain regions (Brown, 1911; Downes and Granato, 2006; Eklöf Ljunggren et al., 2014; Masino and Fetcho, 2005; McDearmid and Drapeau, 2006; Wahlstrom-Helgren et al., 2019; Wiggin et al., 2014, 2012). The CPGs consist of inhibitory and excitatory interneurons that create a reciprocal network to generate different activity patterns for different locomotory behaviours (Buchanan and Sten, 1987; Roberts et al., 2008a, 2008b). Over a century ago, Graham Brown introduced the idea of half-centers on the two sides of the spinal cord that allow the stepping behaviour of four-limbed animals (Brown, 1911). The synchronous activity of the left and right CPGs generates flying in birds or galloping in four-limbed animals (Grillner and El Manira, 2020). On the other hand, the alternation of the left and right CPGs generates walking or swimming-like behaviour.

1.2 Zebrafish

Zebrafish is a commonly used model animal due to its available transgenic lines, fast life cycle, transparency, and relative simplicity. A homology of 70% is observed between zebrafish and the human genome (Howe et al., 2013). From biomedical to fertility, from cardiac to mental

health research, there are many studies using zebrafish as a model (Choi et al., 2021; Demin et al., 2019; Hirata and Iida, 2018; Hoo et al., 2016; Lieschke and Currie, 2007).

Zebrafish are also a great candidate to study locomotion, as most of the neuronal populations responsible for locomotion in zebrafish are evolutionarily conserved, including in mammals (Fetcho et al., 2008; Grillner et al., 2008; Kiehn, 2016; Wilson and Sweeney, 2023). There are many similarities between the CPG architectures and second and last-order neuronal populations that drive the locomotion of mammals and zebrafish (Berg et al., 2018; Sagner and Briscoe, 2019; Wilson and Sweeney, 2023). The rapid maturation of zebrafish locomotor control coupled with easy access to spinal circuits in the developing zebrafish have enabled researchers to gain great insight into how neuronal and muscular developments generate different locomotory behaviours (for a review, please refer to Berg et al., 2018; Roussel et al., 2021). The similarities between zebrafish to more complex animals and the technical and experimental advantages of studying zebrafish create a very valuable stepping stone for researchers to learn more about locomotor control by the nervous system.

1.2.1 Different swimming behaviour of embryonic, larval, and adult zebrafish

Despite the relative simplicity of the zebrafish spinal cord versus more complex animals, zebrafish display various forms of swimming-like behaviours from the early stages of development (Knogler et al., 2014; Naganawa and Hirata, 2011; Saint-Amant, 2010; Saint-Amant and Drapeau, 1998). During embryonic stages, the single coiling behaviour that consists of a single tail bend to one side, followed by double coil bends with successive bends to opposite sides, is mostly generated by electrical junctions and neurons with intrinsic firing behaviours (Knogler et al., 2014; Roussel et al., 2021). Following the developmental changes of the musculature, the brain, and spinal cord regions, the zebrafish add more swim-like locomotion to its portfolio, starting from burst swimming composed of sudden bursts of tail beat at 2-3 days post fertilization (dpf) to beat and glide swimming at 4-5 dpf (Budick and O'Malley, 2000; Buss and Drapeau, 2001; Roussel et al., 2020). The beat and glide swimming behaviour consists of frequent tail beats that continue for a couple hundred milliseconds, followed by a no-tail-beat gliding period that lasts close to half a second (Buss and Drapeau, 2001; Drapeau et al., 2002).

Both larval and adult zebrafish display different speeds of beat and glide swimming measured as tail beat frequencies (TBF) (Ampatzis et al., 2014; Berg et al., 2023; Björnfors et al.,

2019; Callahan et al., 2019; Kimura and Higashijima, 2019; McLean and Fetcho, 2009; Song et al., 2020) (Table 1). Following the conventions of the literature, in the rest of the document, swimming speed stands for the tail beat frequency rather than the actual speed of the fish.

Table 1. Different swimming speeds of zebrafish as measured as tail beat frequencies.

	Slow (Hz)	**Intermediate (Hz)**	**Fast (Hz)**
Larval zebrafish*	20 – 40	40 – 60	60 – 80
Adult zebrafish †	< 3	3 – 8	> 8

* (Berg et al., 2023; Björnfors et al., 2019; Callahan et al., 2019; Kimura and Higashijima, 2019; McLean and Fetcho, 2009)

† (Ampatzis et al., 2014; Song et al., 2020)

The literature strongly supports that these different speeds are generated by different speed microcircuits in the spinal cord (Ampatzis et al., 2014; Ausborn et al., 2012; McLean et al., 2008). These microcircuits are thought to act as individual units that interact with each other. The core of these microcircuits is slow, intermediate, and fast motoneurons (MNs) and slow, intermediate, and fast pre-motor excitatory interneurons (INs) that drive to the corresponding MN populations. The presence of these microcircuits is shown to exist during both larval and adult stages; however, they show differentiation in their connectivities (Pallucchi et al., 2022). Some researchers consider the presence of three separate microcircuits (Ampatzis et al., 2014); however, the organization of speed microcircuits as a continuum rather than a discrete set is also accepted by some (Ausborn et al., 2012). Despite MNs having three types for three speeds of swimming, they are recruited incrementally, starting from slow MNs to fast MNs (Ampatzis et al., 2014; Fetcho and Mclean, 2010; Gabriel et al., 2011). The same incremental recruitment pattern is considered to be present for the INs (Ampatzis et al., 2014), however, a speed-dependent order of inhibition of slow INs is also observed (McLean et al., 2008). These findings begin to reveal highly organized spinal circuits for generating different tail beat frequencies. The complete architecture of these speed microcircuits and how they interact with each other remain to be fully detailed.

Speed-dependent spinal circuits are also evolutionarily conserved and seen in mammals, including humans (Talpalar et al., 2013; Yokoyama et al., 2016). This evolutionary conservation makes it more crucial to understand how different speed microcircuits work in simpler animals.

1.2.2 Spinal Cell Populations

The vertebrate spinal cord comprises multiple cell populations arising from different progenitor cell populations (Goulding, 2009). The dorsal and ventral progenitors develop into sensory and motor behaviour related neurons, respectively (Figure 1). These neuronal populations have specific molecular markers, facilitating the use of genetic or molecular techniques to investigate each population to determine whether each population is responsible for different aspects of zebrafish swimming (Table 2). The motoneuron (MN) populations directly project onto the muscle cells. The interneuron (IN) populations play a role in coordinating motoneurons as well as integrating information from the supra-spinal or sensory regions. In zebrafish, the ventrally located neuronal populations are particularly involved in swimming and are important in determining the swimming speeds.

A list of infographics visually summarizing the cell populations explained below is included in the supplementary documents.

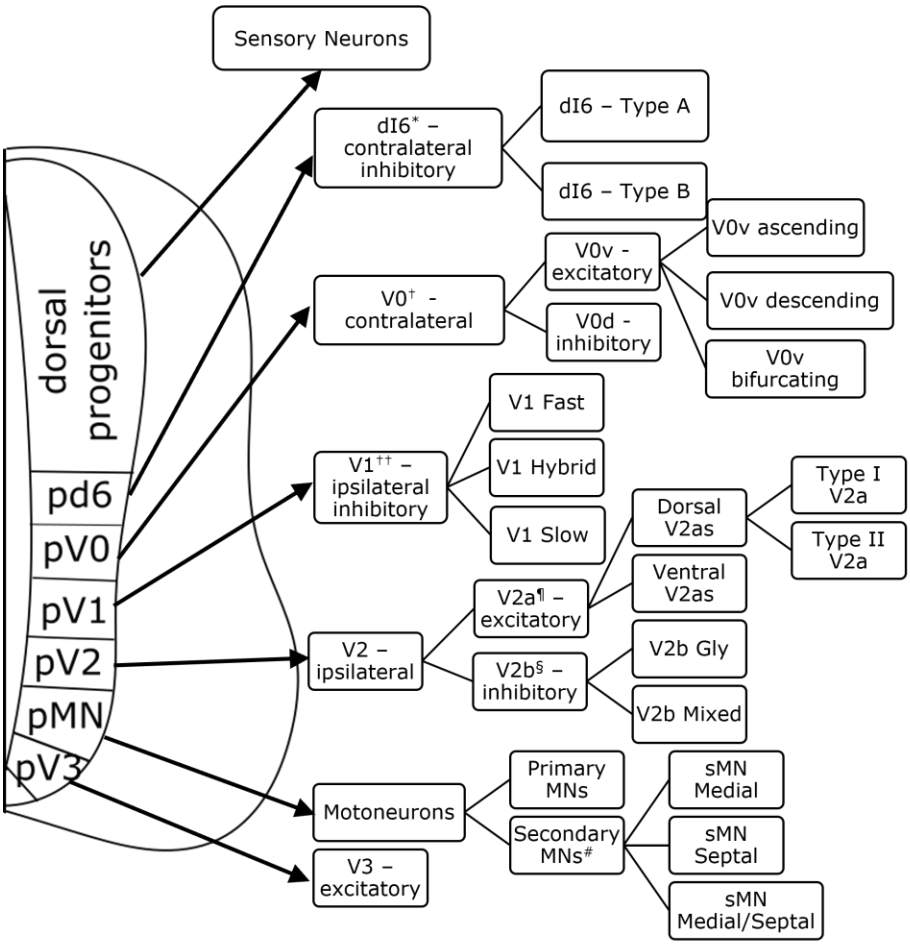

Figure 1. The progenitor domains of the zebrafish spinal cord and the neuronal populations generated.

The spinal cord hosts several progenitor domains that differentiate into different neuronal populations. The figure was modified and expanded from an article by Goulding (2009). *: (Satou et al., 2020); †: (Satou et al., 2012); ††: (Kimura and Higashijima, 2019); ¶: (Menelaou and McLean, 2019); §: (Callahan et al., 2019); #: (Bello-Rojas et al., 2019)

1.2.2.1 Muscle Cells

The vertebrates have fast-acting white skeletal muscles that tire easily and more endurant, slow-acting red skeletal muscles. In zebrafish, these fast and slow skeletal muscle cells are shown to be differentiated from different progenitor cells of different layers of the spinal cord (Devoto et al., 1996; Stellabotte and Devoto, 2007). This difference of origin allows these muscle cells to have different characteristics.

In adult zebrafish, intermediate (pink) muscle cells are observed, as well as the fast and slow (Ampatzis et al., 2013). The differentiation of three types of muscle cells is not fully complete during larval stages; however, both fast and slow muscle fibres are known to be present (Ampatzis et al., 2013; Dou et al., 2008). Fast muscle cells are activated during fast swimming and escape behaviours and are not activated during slow swimming. Slow muscle cells are activated at all speeds but show reduced activity at the highest speeds (Buss and Drapeau, 2002).

1.2.2.2 Motoneurons

The last-order motoneurons with direct projections to muscle cells are divided into two basic groups based on their differentiation time. Early-born, more dorsally located primary motoneurons (pMN) are involved in ballistic movements like escape behaviour and fast swimming (Asakawa et al., 2013; Bello-Rojas et al., 2019; Menelaou and McLean, 2012; Roussel et al., 2020). Later-born secondary motoneurons (sMN) are involved in slow swimming and show a wider distribution in the dorsal-ventral axis (McLean et al., 2008).

Secondary MNs are also more populated in caudal regions than in rostral regions (Roussel et al., 2020). Even within sMNs, there is a speed preference amongst dorsal versus ventrally located neurons. In larval zebrafish, dorsally located lower resistance sMNs are active during fast swimming. Ventrally located secondary sMNs are smaller, have higher input resistance, and are active at slower swimming. (Kimura et al., 2006; Menelaou and McLean, 2012). In adult zebrafish, three subgroups of MNs are recruited for slow, intermediate, and fast swimming (Ampatzis et al., 2014).

1.2.2.3 Interneurons

The second-order neurons that do not directly connect to muscle cells are important components of CPGs. They are differentiated from different progenitor domains and are classified by different molecular markers.

V0

V0 interneurons express the homeoprotein *Dbx1* and make contralateral projections to MNs (Brownstone and Bui, 2010; Lanuza et al., 2004). They form 30% of all commissural interneurons in the cat and mouse spinal cord (Brownstone and Bui, 2010). About 70% of V0s are inhibitory, while the rest are excitatory. The inhibitory V0s can be glycinergic, GABAergic, or both (Lanuza et al., 2004). Based on their ventral/dorsal locations, V0s are further classified into V0vs and V0ds, which are excitatory and inhibitory, respectively (Arber, 2012).

In larval zebrafish, dorsally located V0ds are inhibitory and recruited at faster swimming speeds through the activation of fast V2a neurons (Menelaou and McLean, 2019). V0ds are part of commissural bifurcating longitudinal (CoBL), similar to dI6 (Fidelin and Wyart, 2014; Satou et al., 2020). Speed-dependent slow, intermediate, and fast V0ds exist during the adult stages of zebrafish but not during the larval stages (Picton et al., 2022).

Ventrally located V0v commissural INs are excitatory and consist of rhythmic and non-rhythmic V0vs (Björnfors and El Manira, 2016). In the adult stages, rhythmic V0vs can be divided into slow, intermediate, and fast (Björnfors and El Manira, 2016). They show different dynamics and are recruited at different swimming speeds. Slow and intermediate V0vs have descending and bifurcating projections, while fast V0v shows only ascending projections (Björnfors and El Manira, 2016; Kishore et al., 2014; McLean et al., 2008; Satou et al., 2012). However, V0vs act differently in larval zebrafish, like the speed ranges of their recruitment, but little is known (Björnfors et al., 2019). One hypothesis is that V0vs and V2as fire at different swimming speeds, that V0vs are active during slow speeds and silenced during faster speeds, and that dorsal V2as take over (McLean et al., 2008).

dI6

A group of INs are derived from dorsal progenitors pd6 (Goulding, 2009), whose role in swimming has been studied. V0ds and dI6s together constitute the CoBL neurons: the inhibitory INs that project contralaterally (Roussel et al., 2021). The dI6s express *wt1* and *dmrt3* (Laliberte et al., 2019). The subpopulation that expresses the transcription factor *Dmrt3* has been shown to be an important contributor to the acceleration of zebrafish swimming (Del Pozo et al., 2020). dI6s make contralateral projections to MNs and work synergistically with V0ds to coordinate left-right movements in zebrafish swimming (Satou et al., 2020).

V1

V1s, also called circumferential ascending (CiA) INs, are observed in zebrafish and other vertebrates like mice and express the transcription factor *Engrailed-1* (Higashijima et al., 2004a). They are inhibitory, ipsilateral, and mostly ascending neurons (Higashijima et al., 2004b; Kimura and Higashijima, 2019). Despite the name, V1s can also have descending projections, which are shorter and weaker than their ascending projections (Higashijima et al., 2004b).

There are three types of V1s: fast, slow, and hybrid (Kimura and Higashijima, 2019). The late-born slow V1s are active during slow swimming, inhibiting slow swimming circuits to regulate swimming frequency. The early-born fast V1s are active during fast swimming and turn off the slow swimming circuits. The hybrid V1s are active for all swimming speeds. In addition, V1s shape V2a recruitment, which also influences the swimming speed in zebrafish, as explained below (Kimura and Higashijima, 2019).

V1s are mostly glycinergic, and some are also GABAergic (Higashijima et al., 2004a; Kimura and Higashijima, 2019). V1s show in-phase activity with MN during swimming, and their numbers and location in the lateral-medial plane change across development (Higashijima et al., 2004a). V1s project ipsilaterally to ventral MNs and probably other inhibitory INs (Higashijima et al., 2004a).

In zebrafish, the ablation of V1 neurons prolongs the swimming duration, which is more prominent in fast swimming (Kimura and Higashijima, 2019). Furthermore, V1s are shown to be involved in the inhibition of slow INs and slow MNs during fast swimming (Kimura and Higashijima, 2019). The involvement of V1s in fast walking in the mouse (Gosgnach et al., 2006) shows that the functionality of V1s is conserved across vertebrates.

V2

V2s are differentiated from the p2 progenitor domain and divided into V2as and V2bs based on their relative Lhx3 and GATA2/3 expression (Batista et al., 2008). Their notch signaling-based differentiation of V2as and V2bs are conserved across vertebrates (Batista et al., 2008; Peng et al., 2007).

V2a

V2as are excitatory neurons that receive supraspinal input as MNs (Pujala and Koyama, 2019). V2as are sufficient for the left-right coordination and rostrocaudal wave propagation

observed during swimming (Eklöf-Ljunggren et al., 2012; Eklöf Ljunggren et al., 2014). V2as drive the excitatory input to dorsal and ventral musculature through MNs (Bagnall and McLean, 2014).

There are two types of V2a neurons in zebrafish based on their birth time and what type of swimming they are involved in (Kimura et al., 2006). Earlier-born V2as that are more dorsally located are recruited during fast swimming (Eklöf-Ljunggren et al., 2012; Menelaou and McLean, 2019). They make ipsilateral excitatory descending connections to MNs. Similarly, late-born and ventrally located V2as are involved in slow swimming (Kimura et al., 2006). The connections between V2as and MNs are both electrical and chemical (Kimura et al., 2006).

Dorsal V2a can be divided into Type I and Type II based on their dynamics (Menelaou and McLean, 2019). Type I V2as have strong connections to other excitatory V2as and inhibitory V0ds (Menelaou and McLean, 2019). They are mostly involved in the timing of the swimming. Type II V2as project to MNs and are involved in the amplitude of swimming (Menelaou and McLean, 2019). Type II V2as also project to V0ds but with different dynamics than type I V2as (Menelaou and McLean, 2019). Type I and Type II V2as have stronger connections within and weaker connections between different V2a subgroups. Both Type I and Type II V2as are preferentially recruited at fast swimming speeds (Menelaou and McLean, 2019)

In larval zebrafish, V2as are shown to be necessary and sufficient for swimming (Eklöf-Ljunggren et al., 2012; Eklöf Ljunggren et al., 2014). The excitatory V2a neurons have ipsilateral monosynaptic inputs to MNs (Callahan et al., 2019; Zhang et al., 2008). The ablation of V2as causes an increase in the delay between the segments in the rostrocaudal axis, a decrease in the bursting pattern, and a higher stimulation threshold required to trigger the swimming activity (Eklöf-Ljunggren et al., 2012; Eklöf Ljunggren et al., 2014).

In adult zebrafish, three types of V2as are observed: slow, intermediate, and fast (Ampatzis et al., 2014; Song et al., 2018). These V2as project to slow, intermediate, and fast MNs with stronger connections to the MNs in the same group and weaker connections to the MNs in the neighbouring group (Ampatzis et al., 2014). There are no connections between the slow V2as and fast MNs, and vice versa. There are dynamic differences between different subpopulations of V2a in adult zebrafish as well, like their firing thresholds (Ampatzis et al., 2014). The slow V2as have the lowest threshold; the fast V2as have the highest.

Another classification of larval zebrafish V2as is based on their projections, which divides them into ones with only descending projections (V2a-D) and ones with both descending and supraspinal projections (V2a-B) (Menelaou et al., 2014). V2as can also be divided into bursting and non-bursting types based on their firing patterns (Song et al., 2018). Bursting V2as have descending projections to the dendrites of slow MNs, while non-bursting V2a have weak connections to the somas of fast MNs (Song et al., 2018).

V2b

V2bs are generated from the same progenitor domain as V2a (Fetcho and Mclean, 2010). They are inhibitory with descending projections (Andrzejczuk et al., 2018). In zebrafish embryos, V2b neurons are GABAergic (Callahan et al., 2019). In larval stages, they are all glycinergic (V2b-Gly), but half also release GABA (V2b-Mixed) (Callahan et al., 2019). V2b-Glys and V2b-Mixeds also differ in their projections. V2b-Mixeds inhibit slow motor neurons ventrally located, while V2b-Glys inhibit dorsally located fast MNs (Callahan et al., 2019).

V2b neurons that express transcription factor *Gata3* are involved in alternating extensor and flexor muscles in mammals (Callahan et al., 2019). In larval zebrafish, they have direct connections to MNs, and different subgroups project to different MNs based on the speed circuit they belong to (Callahan et al., 2019). V2b activation lowers the swimming frequency, and its suppression causes faster swimming (Callahan et al., 2019). V2b is involved in speed control by ipsilateral inhibition (Callahan et al., 2019).

V3

Ventrally located V3 neurons are glutamatergic and have descending and bifurcating projections to sMNs (Böhm et al., 2022). They have both ipsilateral and commissural projections (Böhm et al., 2022; Fetcho and Mclean, 2010). They are thought to be involved in tail beat amplitude rather than the tail beat frequency, impacting the number of MNs involved (Wiggin et al., 2022).

Table 2. A summary table of INs and MNs that are part of zebrafish spinal cord CPGs.

Neuronal group	Subpopulations	Molecular Identity	Projection	Neurotransmitter phenotypes	Putative Functional Roles	Main References
V0	V0v-A V0v-B V0v-D	Homeoprotein *Dbx1*, *Pax7*.	Contralaterally to MNs and V2as	Glutamate	Contralateral activation	(Kiehn, 2016; McLean et al., 2008; Satou et al., 2012)
	V0d	Homeoprotein *Dbx1*, *Evx1*		Glycine, GABA	Contralateral inhibition	(Kiehn, 2016; Satou et al., 2020, 2012; Svara et al., 2018)
V1	V1-Slow V1-Hybrid V1-Fast	Transcription factor *Engrailed-1*	Ipsilaterally to MNs and other INs	Glycine, GABA	local inhibition of MN, V2a, V2b, and commissural premotor neurons	(Higashijima et al., 2004a; Kimura and Higashijima, 2019; Sengupta et al., 2021; Wilson and Sweeney, 2023)
V2	V2a Type I V2a Type II V2a-VB	*chx10*	Ipsilaterally to MNs, to excitatory V2as, and inhibitory V0ds.	Glutamate	Timing and amplitude of swimming, Rostrocaudal propagation Regulating tail beat frequency	(Menelaou and McLean, 2019)
	V2b-Gly V2b-Mixed	*Lhx3, gata2/3*	Ipsilaterally to MNs and other inhibitory INs	Glycine, GABA	MN inhibition	(Callahan et al., 2019; Sengupta and Bagnall, 2023)
V3		*sim1a*	Ipsilaterally and contralaterally to MNs		Tail beat amplitude	(Böhm et al., 2022; Wiggin et al., 2022)
dI6	dI6 A dI6 B	*dmrt3*	Contralaterally to MNs	Glycine, GABA	Acceleration, left/right alternation, contralateral inhibition	(Del Pozo et al., 2020; Kishore et al., 2020; Satou et al., 2020)
MN	pMN			Cholinergic	Fast muscle activation	(Bello-Rojas et al., 2019)
	sMN-m-type sMN-s-type sMN-ms-type			Cholinergic	Fast and slow muscle activation	(Bello-Rojas et al., 2019; Kishore et al., 2020; Satou et al., 2020)

Table 3. The proposed recruitment patterns of different cell populations in the larval zebrafish spinal cord at different swimming speeds.

Cell Group	Slow (20-40 Hz TBF)	Intermediate (40-60 Hz TBF)	Fast (60-80 Hz TBF)	Source
dI6-A	Activated		Inhibited	(Satou et al., 2020)
dI6-B	Activated		Inhibited	
Muscle Fast AP	None	None	Activated	(Buss and Drapeau, 2002)
Muscle Slow	Activated	Activated	Reduced activity (fastest)	
pMN	None	None	Fastest	(Ampatzis et al., 2013; Liu and Westerfield, 1988; McLean et al., 2007; Wen et al., 2020)
sMN-m-type	None	None	Activated	(Bello-Rojas et al., 2019; Fetcho and Mclean, 2010; Kishore et al., 2014; Knafo et al., 2017; McLean et al., 2007; Svara et al., 2018)
sMN-ms-type	None	Activated	Activated	
sMN-s-type	Activated	Activated	Activated	
V0d	None		Activated	(Satou et al., 2020)
V0v-A	None	None	Activated	(Satou et al., 2012)
V0v-B	Activated	Activated		(Satou et al., 2012)
V0v-D	Activated	Activated	Silenced	(Kimura et al., 2006; McLean et al., 2008; Satou et al., 2012)
V1-Fast	None		Activated (initial phases)	(Kimura and Higashijima, 2019; Wilson and Sweeney, 2023)
V1-Hybrid	Activated			
V1-Slow	Activated (late phases)			
V2a Type I	None		Activated	(Menelaou and McLean, 2019)
V2a Type II	None		Activated	
V2a-VB	Activated		Inhibited	(Kimura and Higashijima, 2019; Wilson and Sweeney, 2023)
V2b-Gly			Activated	(Callahan et al., 2019)
V2b-Mixed	Activated			

1.3 Hypothesis and Objectives

My hypothesis follows what is suggested in the literature on the swimming speeds of larval zebrafish with a tweak:

I hypothesize that there are speed microcircuits in the larval zebrafish spinal cord that are differentially recruited by the supraspinal regions and generate different tail beat frequencies. Different intrinsic properties, spatial distributions, projection lengths, patterns, and synaptic strengths are the building blocks of these microcircuits. These microcircuits are not mutually exclusive but have common neuronal pools that may have different roles in each microcircuit. Rather than three layers of circuits with little connections in between, they are more entangled with each other.

My objective is to determine the composition of larval zebrafish speed microcircuits, the connectivity patterns within and between these microcircuits and to create a computational model that will generate the expected behaviour using the simulations of the resulting architecture. Understanding how neurons interact in zebrafish can shed light on understanding more complex animals, even humans.

Chapter 2. Methods – Software Implementation

To date, the current literature shows that over twenty larval zebrafish spinal cord cell populations are differentially recruited at different TBFs (Figure 1). The combination of projections between these populations increases the complexity of the model even further and exponentially. It was apparent from the very start of my project that it is crucial to have a tool with high performance to create, modify, and test models.

Previously, our lab has generated computational models of different swim-like behaviours observed in embryonic and larval zebrafish (Roussel et al., 2021). The models were implemented using the Python Programming Language (RRID:SCR_008394). Python is commonly used among scientists and is a great language to access many available libraries; however, it is not an efficient language for CPU-intensive workloads such as loops, which are used extensively in a computational model simulation. A simple comparison of how long it takes to run a nested loop in different programming languages is listed in Table 4. C# and C++ languages display a huge difference in performance compared to Python.

Table 4. The run time comparison of four programming languages.

Number of calculations	**C#**	**C++**	**R**	**Python**
$\mathbf{10^9}$	1.8 sec	1.9 sec	42 sec	4 min 25 sec
$\mathbf{10^{10}}$	18.5 sec	19 sec	8 min 57 sec	48 min 26 sec

Given the apparent advantage of C-family languages, *Sili*Fish was developed using the C# language in the Microsoft Visual Studio 2022 environment (Hejlsberg et al., 2003; Microsoft, 2022). The development environment is free for open-source software developers and students.

The name of the tool is derived from "*in **Silico*** **Fish**." The source code and the executable file have been made available to the public since August 13, 2022, at https://github.com/Bui-lab/SiliFish. A step-by-step guide on how to use the first public version, version 1.0, was previously published as a STAR Protocol (Topcu et al., 2023). The current version is 2.7.

2.1 Architecture

*Sili*Fish is a Windows desktop software tool and has two components: (1) the main engine and (2) the user interface (UI) that allows a graphical user interface for easy data entry,

manipulation, and inspection. The main engine is cross-platform and is responsible for keeping the data, running the simulation, and creating the result files as text or HTML files. The UI is platform-dependent and runs only on machines with Windows 10+ operating systems (Bott and Stinson, 2019). The separation of these components was done to allow quick UI implementation and still have the option of converting the core to a library accessible for environments and operating systems other than Windows.

Another main constraint considered was the segregation of data and code. *Sili*Fish is itself a standalone application with no information on the model created. The model files, however, have only information on the generated models and no programmatic details.

2.2 Software Design

*Sili*Fish uses the object-oriented design (OOD) paradigm, which is based on defining objects with different functionalities and associations with other objects. The main advantage of OOD is the ability to create reusable, expandable, and modular code. *Sili*Fish is open source, and the full source code is available for anyone to use and expand upon.

2.2.1 Generic Concepts

2.2.1.1 Common Components

To increase code reusability, some generic features are used across the software to give flexibility.

Distribution

Many properties throughout the program can be defined as a distribution rather than a single number, which represents the biological values better. The distributions included in the program are Gaussian, Bimodal, and Uniform distribution. There is also a "Constant" distribution, which represents a number with noise. It can be used as a single number if no noise is defined. An additional "Equally Spaced" distribution is also defined to handle the cases where the user wants to space out a parameter value equally.

Timeline

Every structure in the software can be assigned a timeline, defining when it is active. It can be a single period across the simulation or multiple periods with variable breaks in between. The

timeline is defined to allow testing the impact of various structures (like a neuronal population, a junction, etc.) by turning it on or off at different simulation times.

2.2.1.2 Activation/Deactivation

*Sili*Fish offers the ability to deactivate cell groups, cells, synapses, and stimuli. Deactivation is like removing a component of the model, e.g., a cell group, from the model without actually removing it. This ability was implemented to reduce the need to delete and redefine cell populations while testing different scenarios.

2.2.1.3 Export/Import

At every level of the model creation and after the simulation, the software allows exporting and importing the data in JSON, CSV, or Excel formats for backup and easy bulk data update.

2.2.2 Model Components

2.2.2.1 Model Template and Running Model

The model template is the blueprint of the fish's architecture, representing the definitions of its cellular populations, external stimulations applied, body dimensions, and various parameters used to run and analyze the swimming behaviour. The running model represents the actual fish, with all the cells distributed spatially across its body, with individual projections and information about its dynamics: the membrane potential across time.

After the model template definition, a running model is generated using this model template as the blueprint. As the next step, a simulation is run to observe the behaviour of each cell, eventually the fish, across time. Figure 2 is a class diagram that explains how the model template and running model are represented in *Sili*Fish.

2.2.2.2 Fish body

The fish body is designed to be the container of multiple cells that interact with each other to generate swimming behaviour.

The fish model has two cylindrical structures with an extension. The cylindrical structures represent the spinal cord, the musculoskeletal area surrounding the spinal cord, and the extension represents the supraspinal region on the dorsal end of the spinal cord. The fish body is composed of multiple somites with equal dimensions.

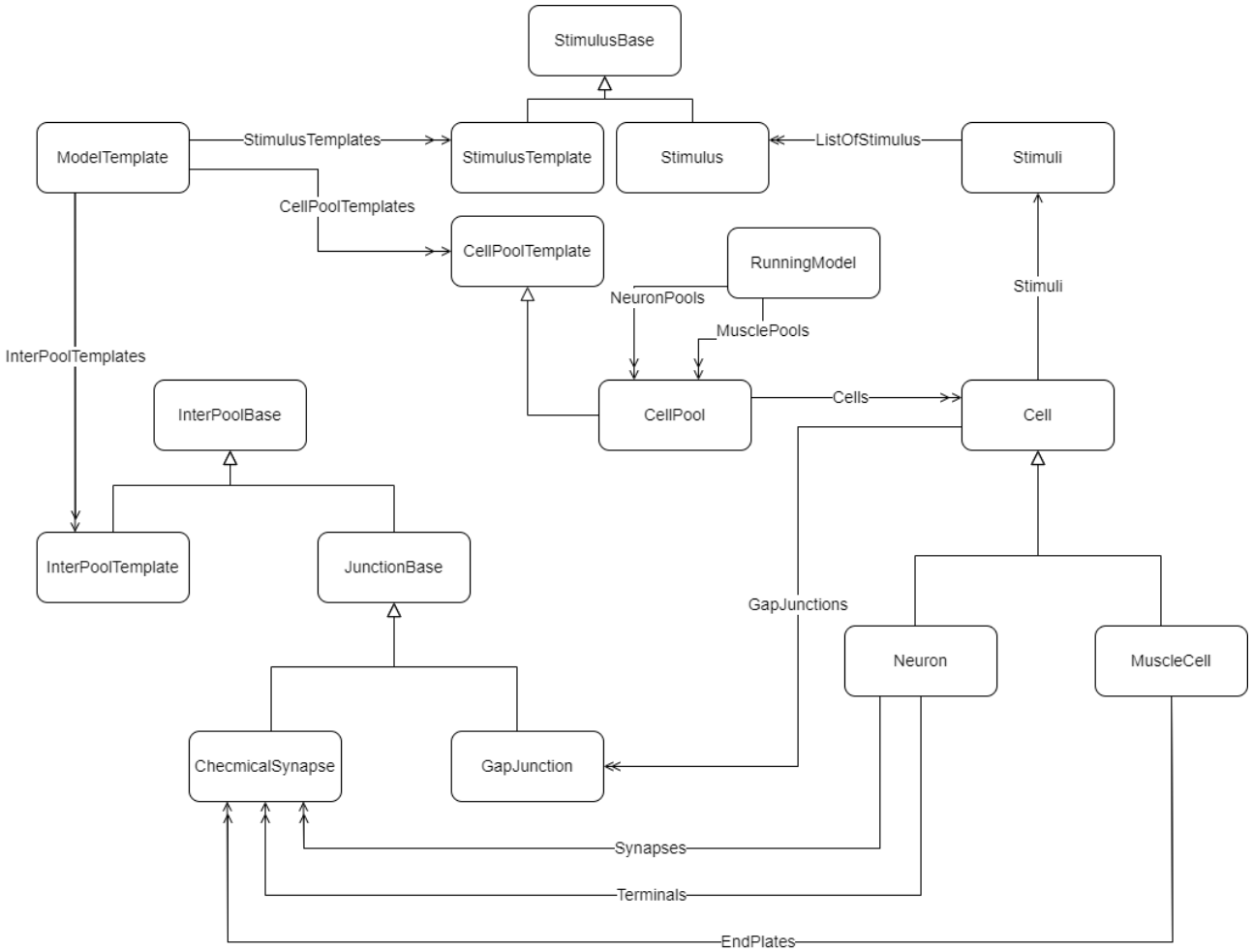

Figure 2. The class diagram of the Model Template, Running Model, and related classes.

The boxes correspond to a class, the formal definition of an object in OOD, e.g., the 'Cell' class. The open-headed arrow (⇾) stands for inheritance, where a class inherits another class and carries the properties and functionalities of the base class. For example, a "Muscle Cell" class is inherited from the "Cell" class. It has all the properties of the Cell class, like the membrane potential, but also some additional properties, like a list of "End Plates." The line arrow (→) stands for association or a link. For example, a "Cell" has a link to a "Stimuli" class that encapsulates all the stimuli applied to the cell. The two-headed arrow (↠) represents a collection association. For example, a "Muscle Cell" has EndPlates, a list of its NMJs.

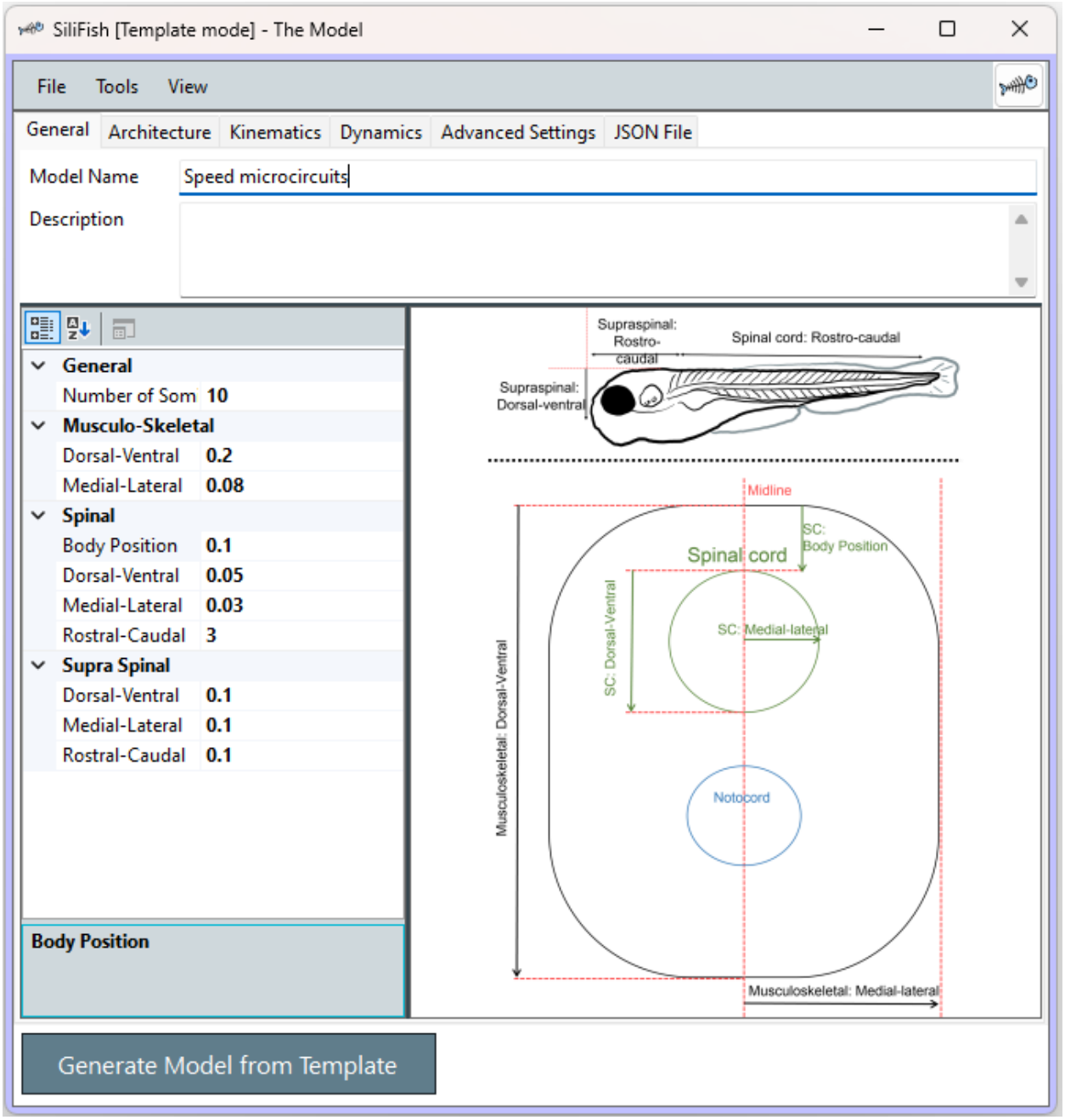

Figure 3. The general properties of the model represent the dimensions of the fish body.

The fish body is considered to be composed of multiple somites. The size of the spinal cord, the musculoskeletal structure surrounding the spinal cord, and the supraspinal region can be defined.

2.2.2.3 Cells

Cells are modelled as point cells, with no size information and a single coordinate specifying the soma location, with projections representing the axons. Dendrites are not implemented.

To facilitate the use of all these properties with minimal user input, there are three levels of class structures: Cell Pool Template, Cell Pool, and Cell. In this document, “cell group” and “cell pool” are used interchangeably.

Cell Pool Template

A cell pool template represents the definition of a certain cellular group with a common molecular marker and other distinguishing properties. It contains information on the cell type, the number of cells, how they are distributed across the various axes, their intrinsic properties, their ascending and descending axon lengths, and the timeline—between which time points the cells in this group will be active (Figure 4).

A cell pool template can represent a specific type of cell. The options are currently "Neuron" and "Muscle Cell". Neurons can have synapses (incoming chemical junctions), terminals (outgoing chemical junctions), and gap junctions. Muscle cells, on the other hand, can have neuromuscular junctions (NMJs; endplates) and gap junctions only. The neurotransmitter properties (such as GABAergic and cholinergic) can also be set for the neuron cell pool template.

A new cell type (e.g., glial cells) can be defined by adding a single C# file with its implementation and a single line at the beginning of the "Cell.cs" file. As for my project's requirements, neurons and muscle cells suffice—therefore, no other cell types were defined in the software.

The rostrocaudal distribution can be defined as per somite or for the full body. The mediolateral and dorsoventral distribution can be defined separately or together as an angular distribution. All these values can be a single value or a distribution (see above).

Although cells are modelled as point cells with no size information and no compartmentalization, axons are implicitly defined as projection lengths in the cell pool template definition. The ascending and descending axon lengths can be defined as a distribution.

The most important aspect of computational cell modelling is mathematically representing them. A “Cell Pool Template” has a “Core Type” property that defines the mathematical unit representing the cells within. In the current model, the Izhikevich 9P, leaky integrator, leaky integrate and fire mathematical models were used to model the neurons, non-spiking muscle cells, and spiking muscle cells, respectively. To increase the accessibility of the software, Izhikevich 5P, Hodgkin and Huxley, Quadratic Integrate and Fire models were also implemented in *Sili*Fish. Every mathematical model contains specific parameters, some of which are user-defined. In the cell pool template, these parameters can be defined as a distribution or a specific number. The ability to define parameters as distributions allows variability of intrinsic properties of cells in a cell pool, which is a more accurate representation of a biological system (Marder and Taylor, 2011).

A new core type (mathematical model) can be defined by adding a single C# file with its implementation and a single line at the beginning of the "CellCoreUnit.cs" file.

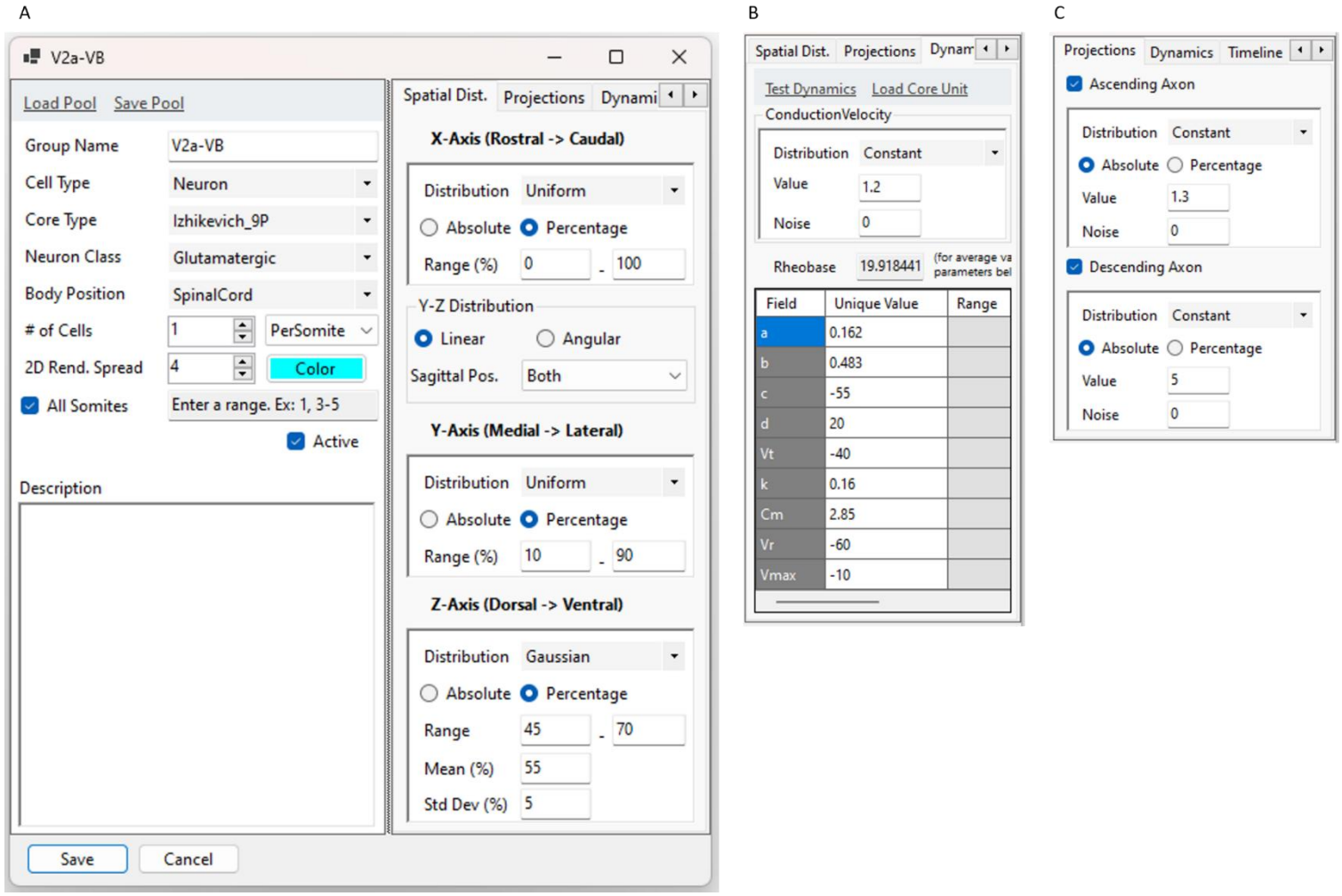

Figure 4. The user interface of the cell pool template definition.

(A) General information about the cell group and its spatial distribution, which can be defined as a distribution. (B) Parameters defining the dynamical properties of the cell group, like conduction velocity and the parameters of the mathematical model it relies on. All of these parameters can be defined as a single value or a distribution. (C) The ascending and descending lengths of the axons.

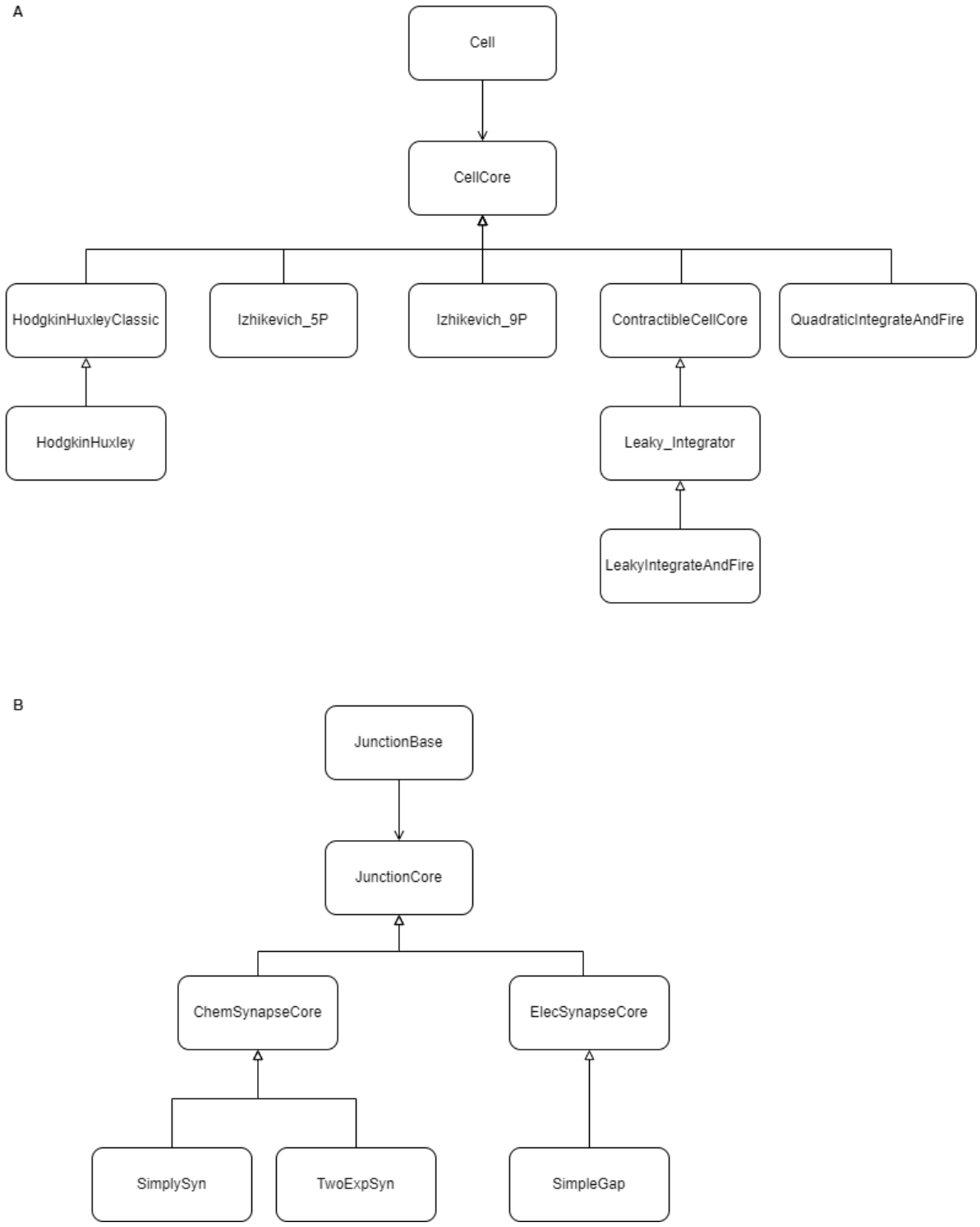

Figure 5. The class diagram of the mathematical models of cells and junctions.

(A) The “Cell” class has a link to a “CellCore” class, which is the base class from which all mathematical cell models are derived. This hierarchy allows the implementation of different mathematical models without making any changes in the “Cell” class. (B) “Cell” also has links to the “Junction Base” class (Figure 2), which allows new junction type implementation without any hierarchical changes in the software.

Cell Pool

A “Cell Pool” is a container structure that keeps the Cells created per the “Cell Pool Template” definition.

Cell

Cells are the main components of the model. The definitions in the cell pool template become unique values of the cells. For example, the rostrocaudal distribution defined in the cell pool template is used to populate the X coordinates of the individual cells in a cell pool.

As my research is about the spinal cord control of the swimming behaviour in larval zebrafish, the main players are interneurons, motoneurons, and muscle cells. “Cell” is defined as a base class with basic cellular properties, and “Neuron” and “Muscle Cell” classes are inherited from the base class. There is no specific classification of interneurons and motoneurons by the user. Motoneurons are determined by the presence of projections to muscle cells, and interneurons are the rest of the neurons. Sensory neurons are not yet implemented.

2.2.2.4 Connections

To facilitate the use of all these properties with minimal user input, there are two levels of class structures: “Inter Pool Template,” and the classes are generated as a result: “Gap Junction” and “Chemical Synapse.”

Inter Pool Template

Like “Cell Pool Template,” the inter pool template class defines how one cell population is projecting to another cell population, without actually creating the individual connections. It contains information on the source cell pool, target cell pool, how the distance between the two and the duration of the signal transduction will be calculated, and the conductance, or the weight, of the junction.

Gap Junctions

Gap junctions are the electrical junctions between two cells. The involved cells can be any type of cell: a neuron, a muscle cell, or any cell type that can be implemented in the future.

Chemical Synapse

Chemical synapses can be NMJs between a neuron and a muscle cell or a synapse between two neurons. The neuron class has terminals and synapses to represent the terminal buttons and the synapses, whereas the muscle cell has end plates to represent the NMJs (Figure 2).

The synapse classes have a link to the "junction core" to make the mathematical modelling of the synapse apart from the cell. This allows the implementation of new synapse types without changing the cell class (Figure 5B).

2.2.2.5 Mathematical Models

Computational modelling requires mathematical modelling of each cell or junction. Different mathematical models can be appropriate to represent different cell types and firing patterns. The mathematical model information is kept separate from the cell to allow flexibility to adapt new mathematical models in the future. This mathematical model is called "Core". The cores currently defined are Hodgkin and Huxley, Izhikevich 5 and 9 parameter models, Leaky Integrator, Leaky Integrate and Fire, and Quadratic Integrate and Fire (Izhikevich, 2007).

Izhikevich 9-Parameter

There are multiple mathematical models implemented in *Sili*Fish. The Izhikevich 9-parameter, or Izhikevich 9P, formalization is used to model all neuronal populations in the speed circuits modelled.

$$C\frac{dV}{dt} = k * (V - V_r) * (V - V_t) - u + I$$

$$\frac{du}{dt} = a * (b * (V - V_r) - u)$$

$$if\ V > V_{max} \rightarrow V = c; u = u + d$$

V_r, V_t, and V_{max} are the neurons' resting, threshold, and maximum membrane potentials. I represents the stimulus, either the external stimulus or incoming and outgoing currents, due to the gap junctions and chemical synapses the neuron is receiving. C is the membrane capacitance, and

c is the reset potential after a spike. The two values that are changing across time are *V*, the membrane potential, and *u*, the recovery current. The constants *k* and *b* are the time constant and sensitivity of *V*, respectively. *a* is the time constant of *u*, and *d* is its reset value. This formalism enables the modelling of subthreshold membrane dynamics as well as most firing behaviours without requiring the modelling of individual active conductances.

Leaky Integrator

The leaky integrator model is a model that uses the passive electrical properties of a cell membrane, where it is considered to be a resistor and a capacitor in parallel (Gerstner et al., 2014). *R* and *C* are the cell membrane's resistance and capacitance, respectively. V_r is the resting membrane potential of the cell.

$$\frac{dV}{dt} = \frac{-(V - V_r)}{R * C} + \frac{I}{C}$$

Leaky Integrate and Fire

This mathematical model is an extension of the leaky integrator, except for the ability to fire. V_{reset}, V_{max}, and V_{thres} are the reset (after a spike), maximum, and threshold membrane potentials, respectively.

$$if\ V \geq V_{max} \rightarrow V = V_{reset}$$

$$if\ V > V_{thres} \rightarrow V = V_{max}$$

Implementing a new Mathematical Model

Many other models can be used to represent neurons, like Bonhoeffer-van der Pol, FitzHugh-Nagumo, Golomb, Morris-Lecar, and Wang-Buzsaki, to count a few (Izhikevich, 2007; Stefanescu et al., 2013). To facilitate future expansions and easy addition of mathematical models, the software was designed to make implementing a mathematical model easy, which consists of adding the implementation file and a single line to the base class file.

Synapse Modelling

Chemical Synapses

There are two models of chemical synapses implemented in *Sili*Fish.

The "Simple Synapse" is the single exponential synapse model with a tau rise (τ_r) and a single tau decay (τ_d), reversal potential (E_{rev}), and synaptic weight ($W_{pre,post}$). V_{post} is the membrane potential of the postsynaptic neuron at time t-Δt. The calculated $I_{pre,post}$ represents the current imposed on the postsynaptic neuron.

$$I_{pre,post} = \left(V_{post} - E_{rev}\right) * \left(e^{-\frac{t-t_0}{\tau_r}} - e^{-\frac{t-t_0}{\tau_d}}\right) * W_{pre,post}$$

This formulation does not generate any current in the case of $\tau_r = \tau_d$ and generates a negative current in the case of $\tau_r > \tau_d$. Therefore, this synapse model covers only a limited range of synapses, and the check $\tau_r < \tau_d$ is introduced in *Sili*Fish.

The two-exponential synapse with slow and fast decay components is implemented as the following, where τ_s and τ_f are the slow and fast decay time constants, respectively, and s is the weight of the slow component (Gerstner et al., 2014):

$$I_{pre,post} = \left(V_{post} - E_{rev}\right) * \left((1 - e^{-\frac{t-t_0}{\tau_r}}) * ((1-s) * e^{-\frac{t-t_0}{\tau_f}} + s * e^{-\frac{t-t_0}{\tau_s}}\right) * W_{pre,post}$$

The generated model used simple synapses to represent chemical synapses for simplicity.

Gap Junctions

Electrical gap junctions implemented in *Sili*Fish are bidirectional. The amount of current that will flow through a gap junction at time t is calculated as below: The duration of time it would take for each cell to impact the other is calculated by using the conduction velocity and the distance between the two cells: let us say Δt_{12} and Δt_{21}. These Δt's can be different when the cells have different conduction velocities. The difference between the membrane potential of the first at $t - \Delta t_{12}$ and the second cell at t-1 will dictate the current that will flow from the first cell to the second. Similarly, the difference between the membrane potentials of the second cell at $t - \Delta t_{21}$ and the first cell and t-1 will dictate the current that will flow from the second cell to the first. The net current is the difference between these two calculated currents.

Differential Equation Calculations

The Forward Euler method is used to solve differential equations to calculate:

$$y_{i+1} = y_i + \Delta t * y'$$

The Δt used throughout the modelling is 0.1 ms. However, biological systems do not have discrete time units. It is important to pick a unit of time that would be smaller than the time scales of all the components of the current model.

2.2.3 Outputs

The downside of creating a user interface for easy model creation is that the user has limited access to the data. Various features were implemented to give the user the ability to troubleshoot.

The testing of the model is two-fold: testing whether the definition of the model is done properly and whether the model is representative of the speed microcircuits of larval zebrafish.

2.2.3.1 2D and 3D Rendering

A third-party library was used to generate 2D and 3D renderings of the model: Force-Graph and 3D Force-Directed Graph, respectively (Asturiano, 2022a, 2022b) (Figure 11-Figure 12). Both libraries are JavaScript libraries that are accessed by an HTML file. HTML code is populated programmatically using the cell pool and cell classes. 2D-Rendering creates an HTML file where it is possible to see visually how each cell pool is connected to each other. In the 3D rendering, a more detailed representation of the model is generated, showing each cell at its actual coordinates, how they are connected, and the weights of those connections. As the complexity of the model increases, the 3D rendering can become crowded and hard to read. Various features were implemented to make the complex renderings easier to study, like turning on or off gap or synaptic junctions, generating views from different camera angles (e.g., dorsal/ventral/caudal), limiting the view to a selection of somites rather than the full body, selecting a single cell or cell pool. These renderings can be used to visually check for the accuracy of where the cells are located and how they are projecting to each other.

2.2.3.2 Plots

Swimming behaviour is caused by the contraction of the muscles, which is caused by the excitation they are getting from the motoneurons. Seeing how the membrane potential of each neuron and muscle cell changes across time is crucial in understanding the driving force behind the behaviour observed. To examine how the model behaves in detail, a third-party JavaScript library was used to create plots to display how membrane potentials and other variables change: DyGraph (Vanderkam, 2022) (Figure 17). DyGraph generates user interactive plots synchronized in time, which allows detailed data inspection.

Various plots were implemented to display imperative variables in understanding the model's behaviour: membrane potentials, synaptic currents, gap currents, stimuli, muscle tension, episodes, and full dynamics. The full dynamics plot combines multiple graphs showing the incoming currents to a cell, the stimuli applied, how the membrane potential changes against these inputs, and the output to other cells. The episode plots display information like the tail beat frequency, number of beats per episode, and length of episode necessary for analyzing the swimming speeds.

Additional features were added to the UI to make it easier to plot a specific model unit: cell pool, cell, or junction. Specifically, plotting a junction allows very detailed analysis. For example, for a chemical synapse, a junction-based plot displays the membrane potential of the presynaptic and postsynaptic neurons and the current that the postsynaptic neuron is exposed to due to the potential difference between the two neurons and the synaptic weight of the junction.

2.2.3.3 Animation

Another third-party library, amCharts 5, was used to display the swimming behaviour as an animation (Antanas et al., 2022). The fish's tail is modelled as an uncoupled pendulum, with a node representing each somite (Roussel et al., 2021). The force that causes the pendulum oscillation is the difference in relative force generated by the muscle contractions on both sides.

$$\theta_i'' + 2\zeta\,\omega_0\theta_i' + \omega_0^2\theta_i = \delta\,(\sum F_{right\ muscle} - \sum F_{left\ muscle})$$

- F: the force generated by the tension.
- ζ: damping coefficient
- ω_0: the natural oscillation frequency
- δ: the conversion coefficient is the coefficient that transforms the membrane potential or tension to the force applied.

The deflection angle θ_i is used to calculate the coordinate of the somite i based on the position of the next rostral somite *i-1* (Roussel et al., 2021)—the rostrocaudal axis of the fish is represented from top to bottom.

$$x_i = x_{i-1} + l * \sin(\theta_i)$$

$$y_i = y_{i-1} - l * \cos(\theta_i)$$

To calculate the force the muscle tension applies, the torque the muscle cell generates (tension x distance of the muscle cell) was divided by half of the body width to be able to incorporate the muscle location information.

2.2.3.4 Spike and Episode Statistics

The determination of when a spike happens is embedded in the mathematical models of the cells. For the Izhikevich 9P model used, a spike was considered to happen when the membrane potential reached the V_{max} value. A user interface was created to list and export all the spikes of a single cell, all cells in a somite, or a cell group. The feature was expanded to list the episodes to determine the beat and glide sections of the swimming behaviour.

The majority of the literature reports motor output as the ventral root output rather than muscle behaviour (Kawano et al., 2022; Kimura et al., 2013; Menelaou et al., 2014; Satou et al., 2020, 2009; Talpalar et al., 2013; Wilson et al., 2010; Zhang et al., 2011). Therefore, the episode determination by either the motoneurons on a specific somite or the movement of the tail tip was implemented.

For the MN-based episode calculation, the spikes of all MNs on the left and right sides of the somite are merged and sorted separately. The left and right spikes that coincide are removed from the lists. The result lists are traced sequentially to determine the left tail beat (where there is a spike on the left MNs) or the right tail beat (where there is a spike on the right MNs). Multiple spikes can be part of a single beat if no spikes are on the opposite side. An episode break is considered to happen if the time between two spikes exceeds a used defined value (called Episode Break – defined in ms).

For muscle-based episode calculation, the tip of the tail indicates whether there is a left or right beat (Roussel et al., 2021). If the distance between the tail tip and the centerline is greater than a threshold defined by the user, it is considered to be part of a beat.

2.2.4 Parameter Fitting

One of the major tasks of this project is to generate the cell populations that will properly represent the cells in the larval zebrafish spinal cord. The Izhikevich model used has nine parameters to be tweaked. Cell models whose firing behaviour resembles experimentally observed

patterns can be generated by properly setting those parameters. Several firing properties of the neurons can be used to constrain or set those parameters.

2.2.4.1 Rheobase current

One of the basic properties of a neuron is its rheobase, the minimum amount of current necessary to fire an action potential if applied for an infinite duration. The rheobase is specifically important for this project as the difference in the rheobase of cells receiving the same input can determine the response to particular inputs. The "infinite duration" is limited to a user-set value of 500 ms by default. The software calculates the rheobase by starting a high current (set to 1000 pA by default). If there are no spikes, the rheobase is defined as N/A. If there is a spike, the current is adjusted in a binary search: if *x* amount of current causes a spike, a current of *x/2* is tried. If *x/2* causes a spike, a current of *x/4* is tried, and so forth. If the halved current does not cause a spike at any point, the middle point between the last current causing a spike and the current not causing a spike is tested. This loop is continued until the minimum amount of current is reached to create at least one spike.

2.2.4.2 Firing Pattern

The temporal pattern of neuron firing varies: firing patterns can be phasic or tonic, spiking or bursting, or somewhere in between. Firing patterns may depend on input current or duration. To decide whether a specific firing pattern matches the observed activity in experimental studies, first, it is necessary to analyze and quantify the membrane potential changes of a neuron.

The first step is determining the spikes. The spike definition is embedded within the mathematical models. For the Izhikevich 9P model, a spike is the time point where the membrane potential value reaches V_{max}. The number of spikes before, during, or after a stimulus can be directly deducted from generating the spike list.

The next step is analyzing the firing pattern for the possible presence of bursting or adaptation. For this, the times between the spikes are grouped into two categories: the smaller and larger durations are considered to be intra-burst and inter-burst durations, respectively. If the inter-burst duration is larger than the intra-burst duration multiplied by a parameter defined by the user (set to 2 by default), then the spikes are grouped into bursts for the next analysis step. Otherwise, every spike is considered individually.

From here, a few decisions can be made: whether the cell is firing rhythmically or randomly, whether the spiking is phasic or tonic, the bursting or spiking frequency, the number of spikes per burst (if bursting), whether the time between spikes decreases or increases with time (which shows sensitization or adaptation). The irregularity between the intervals is also calculated. If the intervals are equal, or there is a continuous increase or decrease trend, the irregularity is zero. Otherwise, irregularity is calculated as the standard deviation divided by the average of intervals. The genetic algorithm can use all these statistics for parameter fitting. The pseudo-code of how the firing pattern is determined is below:

```
If there is a single spike → phasic spiking
else if there is a single burst
    with no quiescent period at the end → tonic spiking
    with a quiescent period at the end → phasic bursting
else if there are only bursts with no individual spikes → tonic bursting
else if there are only individual spikes
    with regular intervals (equal or increasing or decreasing) → tonic spiking
    with irregular intervals
    with no quiescent period at the end → tonic chattering
    with a quiescent period at the end → phasic chattering
```

2.2.4.3 Genetic Algorithms

Genetic algorithms (GA) are algorithms that can be employed to determine a parameter set that would give a desired solution. GA works similarly to how genetics works in evolution (Figure 6A). Sets of parameter values are considered as individuals. Individuals are tested to see if they produce the desired output. The algorithm makes directed changes in the individuals to attempt to improve the output if it is not close to the desired output. Periodically, random mutations change the fitness of individuals, increase their chance of survival, and pass those "traits" (i.e., parameter values) to the next generations.

Rather than implementing the genetic algorithms from scratch, an open-source library developed in C# was used: Genetic Sharp (Giacomelli, 2022). The library offers many settings that define how the selection, crossover, mutation, reinsertion, and termination steps will take place. All the relevant setting options are offered to the user to select from (Figure 6B).

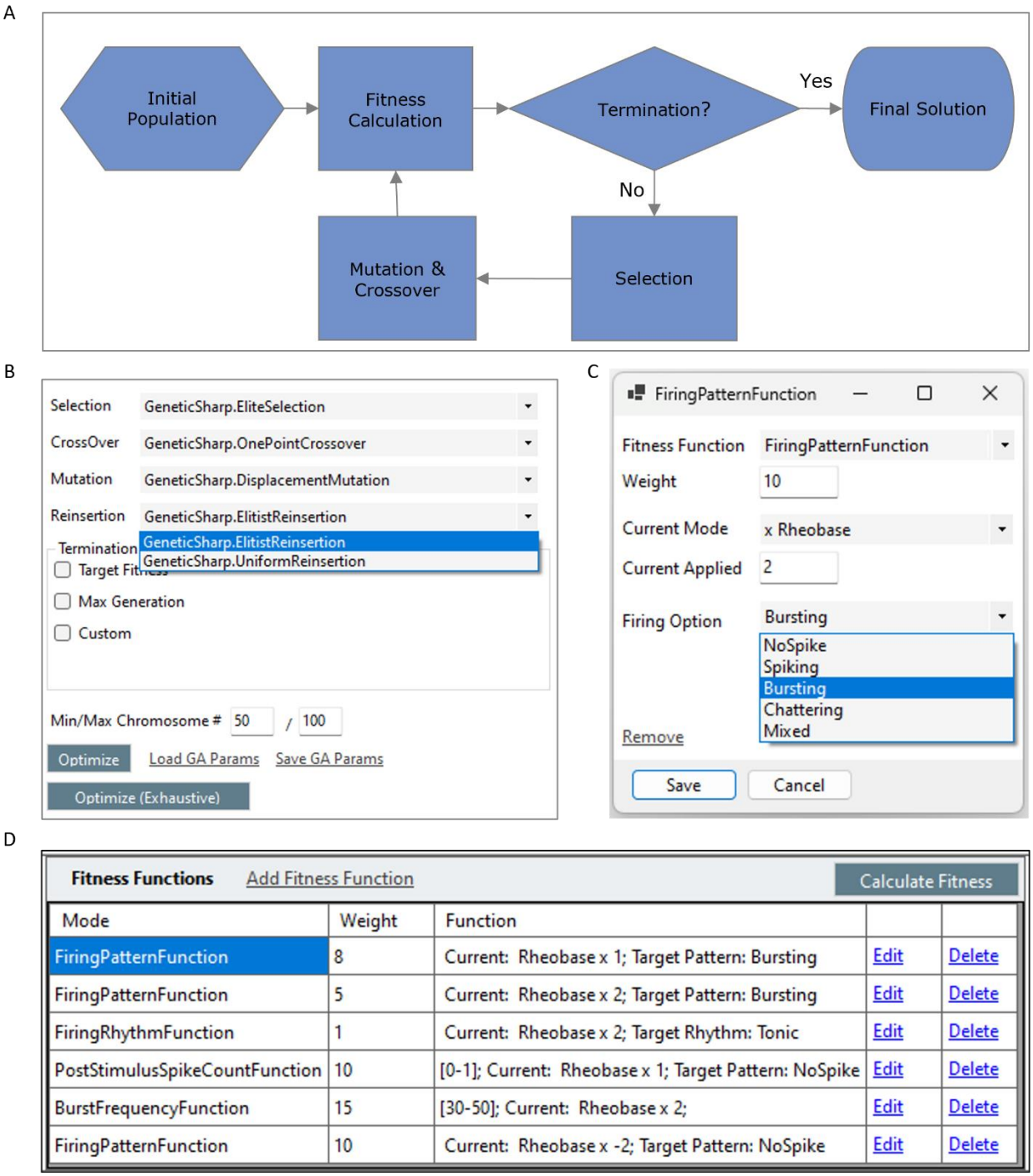

Figure 6. Genetic algorithms offer many options to do parameter fitting efficiently.

(A) Flow chart of genetic algorithms. (B) *Sili*Fish offers a UI to tweak the options Genetic Sharp offers (Giacomelli, 2022). (C) Users can define fitness functions easily using the UI provided. (D) One or more fitness functions can be defined to find the parameter set of a specific firing pattern.

The genetic algorithm iterates many parameter combinations and finds the combination(s) with the best fitness values. The most important part of genetic algorithms is the fitness calculation: What is the system's fitness for a set of parameter values? The system is considered to be a list of fitness functions with different weights (Figure 6C-D). Each function is calculated using the parameter combination tested, and the values of all functions are summed up. The genetic algorithm aims to find the maximum value these fitness functions can sum up. Various fitness functions that were crucial for this project were implemented, as described below. For all functions that have a target value as a number or a range, unless otherwise stated, the conditions below were used to calculate the fitness, where v_c is the calculated value, and v_{tmin} and v_{tmax} are the minimum and maximum target values:

$$if\ v_{tmin} \leq v_c \leq v_{tmax} \rightarrow fitness = Weight$$

$$if\ v_c < v_{tmin} \rightarrow fitness = Weight/(v_{tmin} - v_c)$$

$$if\ v_c > v_{tmax} \rightarrow fitness = Weight/(v_c - v_{tmax})$$

Fitness function for target rheobase

The literature reports the rheobase of certain zebrafish spinal neurons, which indicates their firing potential (Fidelin et al., 2015; Menelaou and McLean, 2019, 2012). The target rheobase fitness function calculates the rheobase of a neuron with a specific parameter set and the fitness based on how far the rheobase is to the target value or range.

Weight is the weight of the fitness function: how much it would impact the total fitness. If the target rheobase is a unique number r_t, the fitness value is calculated as:

$$if\ r_c = r_t \rightarrow fitness = Weight$$

$$if\ \frac{r_t}{2} \leq r_c \leq r_t \rightarrow fitness = Weight * \frac{2 * |r_c - r_t/2|}{r_t}$$

$$if\ r_t \leq r_c \leq 3\frac{r_t}{2} \rightarrow fitness = Weight * \frac{2 * \left|{}^3/_2\, r_t - r_c\right|}{r_t}$$

$$otherwise \rightarrow fitness = 0$$

If the target rheobase is a range of [r_{min}, r_{max}]:

$$r_{range} = r_{max} - r_{min}$$

$$if\ r_{min} \leq r_c \leq r_{max} \rightarrow fitness = Weight$$

$$if\ r_{min} - r_{range} \leq r_c \leq r_{min} \rightarrow fitness = Weight * \frac{(r_{min} - r_c)}{r_t}$$

$$if\ r_{max} \leq r_c \leq r_{max} + r_{range} \rightarrow fitness = Weight * \frac{(r_c - r_{max})}{r_t}$$

$$otherwise \rightarrow fitness = 0$$

Fitness function for firing pattern

The firing pattern is determined as explained in the Firing Pattern section. If the target firing pattern is the same as the resulting pattern, the fitness is equal to the full weight. If the target is no spiking and there is spiking, or vice versa, the fitness is zero. The fitness is zero if the target is spiking and the current spiking is bursting. In all other cases, fitness is a function of the irregularity of the intervals. Below is a pseudocode that summarizes how firing pattern fitness is calculated.

```
Target = Spiking → Fitness = Weight * Max(0, (1 – irregularity))
Target = Bursting → Fitness = Weight * Min(1, irregularity)
Target = Chattering → Fitness = Weight * Min(1, irregularity)
Target = Mixed → Fitness = Weight * Min(1, irregularity)
```

Fitness function for firing rhythm

The firing rhythm value can be phasic or tonic. If spiking continues till the end of the stimulus minus a certain range (called tonic padding, which is set to 1 ms by default but can be modified by the user), it is considered tonic firing. Otherwise, it is considered phasic firing. The fitness value is the full weight if the firing rhythm fits the target firing; otherwise, it is zero.

Fitness function for firing delay

The firing delay is the distance between the first spike and the onset of the stimulus, measured in ms.

Fitness function for burst frequency

Burst frequency is the number of bursts divided by the stimulus duration, reported in Hz.

Fitness function for spike per burst

Spike per bust is the average number of spikes in all the bursts. In the case of spikes and bursts existing together, individual spikes are considered as bursts with a single spike.

Fitness function for spike frequency

Spike frequency is the number of spikes divided by the stimulus duration, reported in Hz.

Fitness function for pre- and post-stimulus spike counts

Some intrinsic properties may allow a cell to fire after a stimulus ends or even without a stimulus. To be able to catch those cases, the number of spikes before an applied stimulus and after the stimulus ends is reported.

2.2.4.4 Parameters

Each mathematical model contains a set of parameters. The genetic algorithm requires a start value, minimum and maximum values, and the sensitivity in terms of the decimal digits need to be defined for each parameter. The mathematical models in *Sili*Fish all have default values for the parameters they use and suggested min and max values. Users can change these minimum and maximum values before running the GA.

To facilitate determining the parameter range and making the most of the GA by minimizing the parameter space, two extra tools were implemented: Sensitivity analysis and firing pattern detection.

Rheobase Sensitivity Analysis

The sensitivity analysis takes one parameter at a time, tries various values between a minimum and maximum, and displays how it will impact the rheobase of the cell (Figure 7). This tool helps determine some parameters' minimum and maximum values.

Firing Pattern Detection

The firing pattern detection tool takes one parameter at a time, tries various values between a minimum and maximum, and displays the firing pattern when a specific current is applied (Figure 8). This tool helps determine some parameters' minimum and maximum values as well.

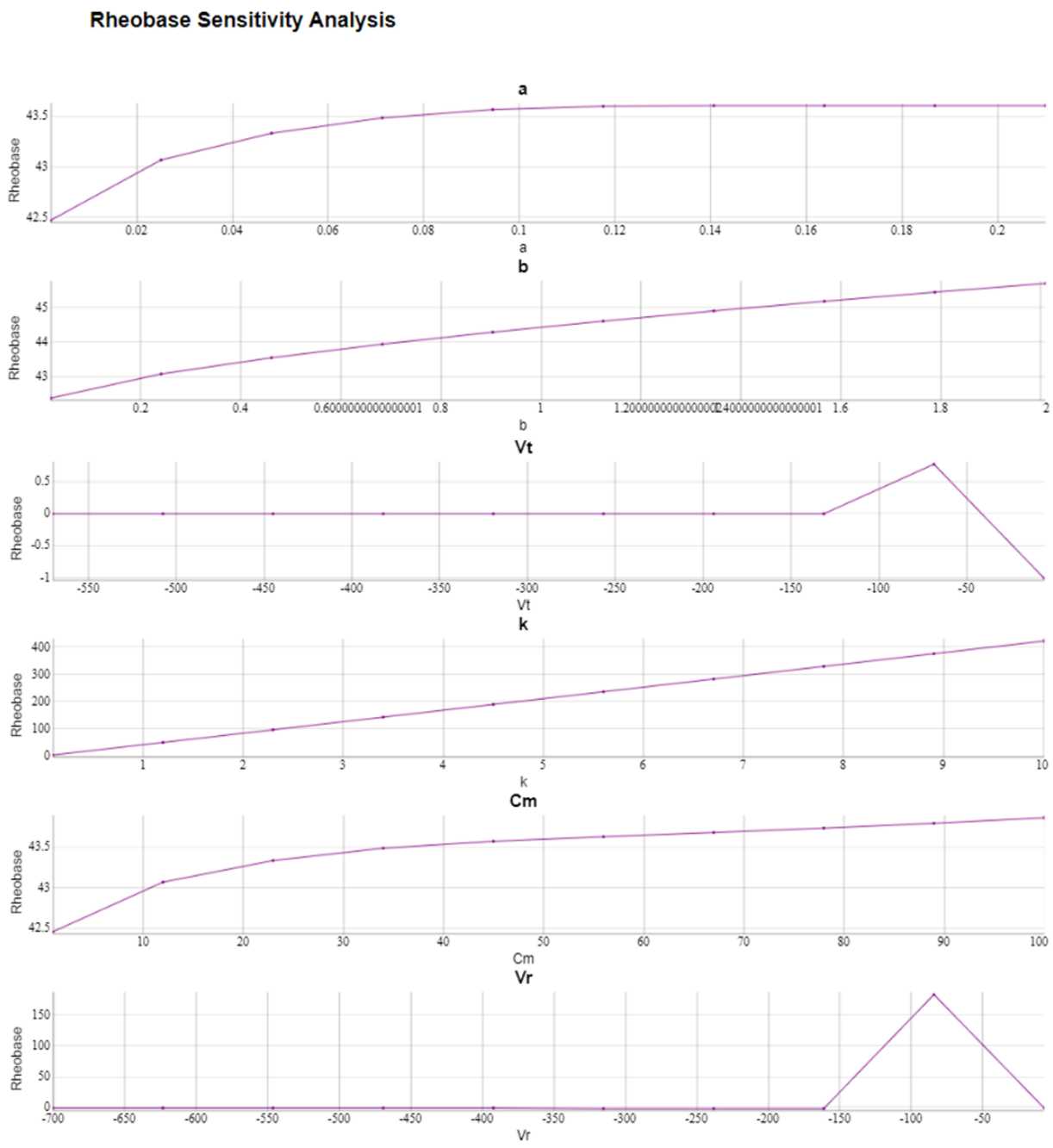

Figure 7. Rheobase Sensitivity Analysis

Rheobase sensitivity analysis can help determine the valid range of a specific parameter by fixing all other parameters and calculating the rheobase for a wide range of values of the target parameter.

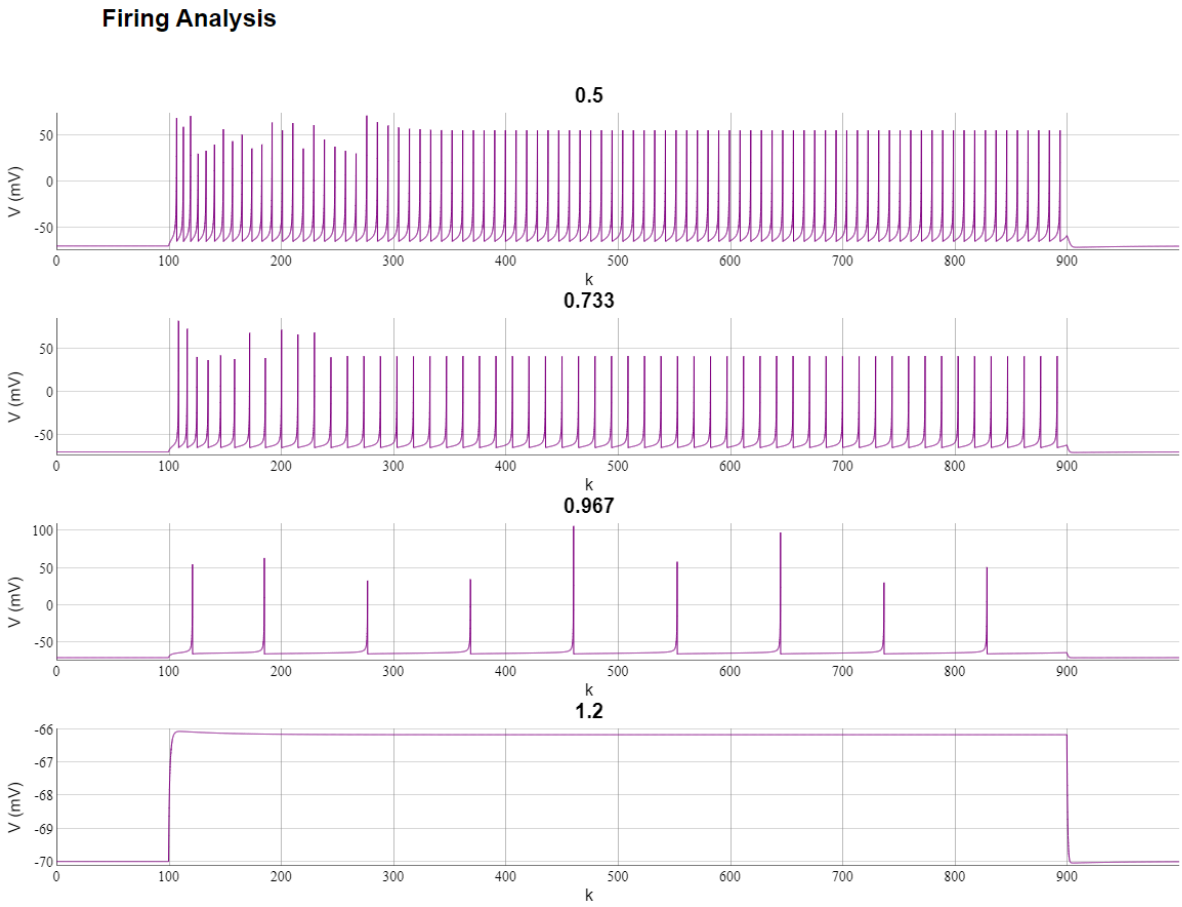

Figure 8. Firing Pattern Analysis

Firing pattern analysis can help determine the valid range of a specific parameter by fixing all other parameters and displaying the firing pattern for a wide range of values of the target parameter.

2.2.4.5 Exhaustive search

Genetic Sharp has various setting options, as explained above (Figure 6B). The stochastic component of genetic algorithms and the non-linear interactions of each setting affect the algorithm's outcome; thus, different combinations of settings can work better for different required outcomes. To remove the need to update these settings manually and to streamline the parameter fitting process, an exhaustive search option was implemented to try all 350 combinations of all the settings and get the ten (a number the user can set) best parameter sets with the best fitness values.

2.2.5 Memory Requirement

The memory requirement increases as the complexity of the model and the simulation time increases. Memory usage has two main contributors: the membrane potentials of the cells across time and the currents that pass through the junctions at each time point. The memory usage of the final model was tested with a simulation time of 5000 ms, which would take less than 1GB of memory space. However, this requirement increases more than 20-fold with the synaptic current information. Therefore, memory optimization was done so that the current information was not kept during the simulation but recreated when the user requested any plots related to the current. The user is warned that there will be an increased memory requirement so that they can continue by selecting the relevant subset they absolutely want to see and not overload the resources.

Chapter 3. Methods – Generating Swim Circuits

This section explains how the *Sili*Fish features listed above, and the information in the literature was used to create and test the model.

3.1 Creating Model Template

A model template is the definition of the actual model. The cell pool templates are generated to represent each cell group relevant to swimming speeds. The unit of time used is ms, and the unit of length is mm.

3.1.1 General Properties

The length of the larval zebrafish spinal cord was set to 3mm using the numbers reported in the literature for 4-5 dpf larva (Dou et al., 2008; Fuiman and Webb, 1988). Considering the largest width of the larva is about 150 µm, the medial-lateral length of the musculoskeletal region was set to 0.08 mm. The number of somites was set as 30, later reduced to 10 to lower the complexity.

Defining the size of the zebrafish in actual dimensions allows for using some neuron properties reported in the literature directly, like axon length and conduction velocity.

3.1.2 Cell Groups

The parameters extracted from the literature fell into these categories: molecular markers, number, position, distribution, size, projection lengths (for neurons), and firing patterns (for spiking cells). Molecular markers are implicitly implemented as different cell pools. Size information is not explicitly implemented but is used to derive various values lacking in the literature.

Twenty different spinal cell groups plus two types of muscle cells were created to represent the larval zebrafish spinal cord speed circuits (Table 2). The full model representing the true number of somites and cells per somites was generated. Due to the complexity of the resulting model and challenges that arise to troubleshoot, after a point, a reduced model was created with ten somites and one cell representing each cell group per somite instead.

3.1.2.1 Determining parameters for the mathematical model

The neurons' firing behaviour and membrane potential dynamics were modelled using the Izhikevich 9P formalism. As there are nine parameters to set for each cell type, the parameter fitting was automated using genetic algorithms as described earlier. The literature offers some of the Izhikevich properties, like resting or maximum membrane potential (Table 5). Some of these values were reported as a range, and they were used directly; some of them were inferred from published outputs like figures or plots. Where available in the literature, these ranges were fed for each of the nine parameters of the Izhikevich model (Table 6). Some ranges were tweaked (e.g., increased, decreased, sensitivity changed by changing the decimal point) based on how well the output of the genetic algorithm parameter fitting worked. These decisions were mainly made using sensitivity analysis and firing pattern detection tools.

Additional Range Checks for the Parameter Fitting

To make the GA more efficient and ensure that the estimated parameter combinations are biologically meaningful, additional criteria were checked when setting the minimum and maximum values of each parameter of the Izhikevich model.

After some testing, it became obvious that the *k* parameter of the Izhikevich model has a high impact on the firing behaviour, as it is directly multiplied by $(V - V_r) * (V - V_t)$ to calculate the change in membrane potential. An example of how the same parameter set reacts when *k* = 0.24 and *k* = 1.24 is displayed in Figure 9. Therefore, *k* was set to be between 0.01 and 1 for all cell populations.

Before the 9-parameter model that is used in the current model, Izhikevich had come up with a 5-parameter model with some four parameters replaced as constant values to represent the majority of Hodgkin-Huxley model cells that he modelled (Izhikevich, 2003):

$$C\frac{dV}{dt} = 0.04 * V^2 + 5\mathrm{V} + 140 - u + I$$

$$\frac{du}{dt} = a * (\mathrm{bV} - u)$$

$$if\ V > V_{max} \rightarrow V = c; u = u + d$$

Obviously, it is not expected for this 5-parameter model to be as comprehensive as the 9-parameter model. Regardless, after some basic algebra, a few approximations were made to come up with a few checks: $k/C_m = 0.04$, $-k/C_m\,(V_{rest} + V_{thres}) = 5$, $k/C_m * V_{rest} * V_{thres} = 140$. Izhikevich also states that b approximates to $1000/R + k(V_r - V_t)$ (Izhikevich, 2007). These equations were not used for hard checks but rather for selecting the parameter combinations among the multiple choices GA generated.

Table 5. Firing-related properties of the cell groups derived from literature.

Cell Group	Rheobase (pA)	Firing Pattern	Membrane Potential (mV)	Main Resources
dI6-A		Bursting	$V_t = V_r + 20$ $V_{max}=V_r + 40$ $V_{reset} = V_r + 10$	(Satou et al., 2020)
dI6-B		Chattering	$V_t = V_r + 10$ $V_{max}=V_r + 60$ $V_{reset} = V_r + 5$	(Satou et al., 2020)
Muscle Fast AP		Phasic firing, with twitches, action potential	$V_r = -71 \pm 3$	(Luna et al., 2015) (Buss and Drapeau, 2000)
Muscle Slow		Tonic firing, no action potential	$V_r = -56 \pm 1$	
pMN	300	Tonic firing	$V_r = -74 \pm 0.4$ [-63, -79]	(Menelaou and McLean, 2012) (Buss et al., 2003)
sMN-m-type	150	Chattering	$V_{th} = -23 – -48$ $V_r = -55.5 – -75.7$	(Menelaou and McLean, 2012)
sMN-ms-type	65			
sMN-s-type	35	Bursting		
V0d		Chattering	$V_{th} = V_r + 10$ $V_{max} = V_r + 55$; $V_r = -54$ mV $V_{th} = \sim -40$ $V_{max} = -10$ mV $V_{reset} = -30$ mV	(Kishore et al., 2020) (Menelaou and McLean, 2019) (Satou et al., 2020)(Picton et al., 2022)
V0v-A	15.4 ± 8.3		$V_r = -50 – -40$, $V_{th} = -35 – -30$; $V_{max} = 0$-30	(Fidelin et al., 2015) (McLean et al., 2008)
V0v-B				
V0v-D				
V1-Fast			$V_r = -76.5 \pm 5.6$ $V_{max} = V_r + 50$ $V_{reset} = V_r + 20$ $V_{th} = V_r + 28$	(Sengupta et al., 2021)
V1-Hybrid				
V1-Slow				
V2a-Type-I-DH-Displaced	40-200	Tonic firing	$V_r = -53$ V_{th}: -36--25; V_{max}: -21 – +40	(Menelaou and McLean, 2019)
V2a-Type-I-DL	~10			
V2a-Type-I-DM	15-40			
V2a-Type-II-D	60-600	Chattering	$V_r = -70$ $V_{th} = -50 – -40$; $V_{max} = -35 – +25$	(Menelaou and McLean, 2019)
V2a-VB			$V_{th} = V_r + 20$-25; $V_{max} = V_{th} + 50$-60; $V_{reset} = V_r + 15$-20	(Kimura and Higashijima, 2019)

Table 6. The minimum-maximum range of each parameter fed to the GA algorithms.

	A	B	c	C_m	d	k	V_{max}	V_r	V_t
dI6A	0.01 – 2.01	-5.27 – 2.02	-55	5.25 – 7.5	-10.01 – 10	0.01 – 1	-20 – -10	-60	-40 – -35
dI6B	-2.01 – 2.01	-5.01 – 2.02	-65	5.25 – 7.5	-10.01 – 10	0.01 – 1	- 10 – 10	-70	-50 – -45
pMN	-2.01 – 2.01	-10.01 – -6.15	-89 – -53	30.15 – 79.5	-10.01 – 10	0.51 – 1*	-5.6 – 13.6	-79 – -63	-38.2 – -33.8
sMN-m-type	0.01 – 10	0.01 – 20	-70.01 – -65	9.9 – 44.85	-10.01 – 10	0.01 – 1	0 – 20	-75.7 – -55.5	-48.01 – -23.01
sMN-ms-type	-2.01 – 2.01	-50 – 2.43	-65.01 – -55	11.85 – 32.4	-10.01 – 10	0.01 – 1	-10 – 10	-75.7 – -55.5	-48 – -23.01
sMN-s	-2.01 – 2.01	-51.35 – 1.175	-65.01 – -55	8.25 – 21.75	-10.01 – 10	0.01 – 1	-10 – 10	-75.7 – -55.5	-48 – -23.01
V0d	-2.01 – 2.01	-12.77 – 2.12	-46 – -45	5.25 – 7.5	-10.01 – 10	0.01 – 1	0 – 10	-54 – -54	-44 – -39
V0v-A&B	0.01 – 10	0.01 – 20	-40 – -38	3.75 – 9	-10.01 – 10	0.01 – 1	0 – 30	-50 – -40	-35 – -30
V0v-D	0.01 – 10	0.01 – 20	-40 – -38	3.75 – 9	-10.01 – 10	0.01 – 1	0 – 30	-50 – -40	-35 – -30
V1-Fast	0.01 – 2.01	-16.67 – 1.28	-62.1 – -50.9	3.75 – 6.75	-10.01 – 10	0.01 – 1	-32.1 – -20.9	-82.1 – -70.9	-54.1 – -42.9
V1-Hybrid	0.01 – 2	-16.67 – 1.28	-62.1 – -50.9	3.75 – 6.75	-10 – 10	0.01 – 1	-32.1 – -20.9	-82.1 – -70.9	-54.1 – -42.9
V1-Slow	0.01 – 2	-16.67 – 1.28	-62.1 – -50.9	3.75 – 6.75	-10 – 10	0.01 – 1	-32.1 – -20.9	-82.1 – -70.9	-54.1 – -42.9
V2a-Type-I-DH	-2.01 – 2.01	-22.58 – -5.72	-45.01 – -40	2.85 – 4.65	-10.01 – 10	0.51 – 0.8*	-20 – 40	-55 – -50	-36 – -25
V2a-Type-I-DL	-1.01 – 1.01	-1.01 – 0.5	-50 – -45.01	2.85 – 4.65	-10.01 – 10	0.01 – 1	-20 – 40	-55 – -50	-36 – -25
V2a-Type-I-DM	-10.01 – 10	-30 – 1.28	-45.01 – -40	2.85 – 4.65	-10.01 – 10	0.01 – 1	-20 – 40	-55 – -50	-36 – -25
V2a Type II	-2.01 – 2	-20.01 – 9.8	-68 – -60	4.2 – 6.3	-10.1 – 10	0.01 – 1	10 – 12	-70 – -70	-50 – -40
V2a-VB	-2.01 – 2.01	-23 – 1.81	-55 – -45	6.96 – 10.14	-10.01 – 10	0.01 – 1	-20 – -10	-60 – -60	-40 – -35
V2b-Gly & Mixed	-2.01 – 2	-30 – 0.86	-50 – -45	2.85 – 10.14	-10.01 – 10	0.01 – 1	-20 – 0	-55 – -50	-36 – -25

*For these cell types, the k range of 0.01–1 was split into smaller sections.

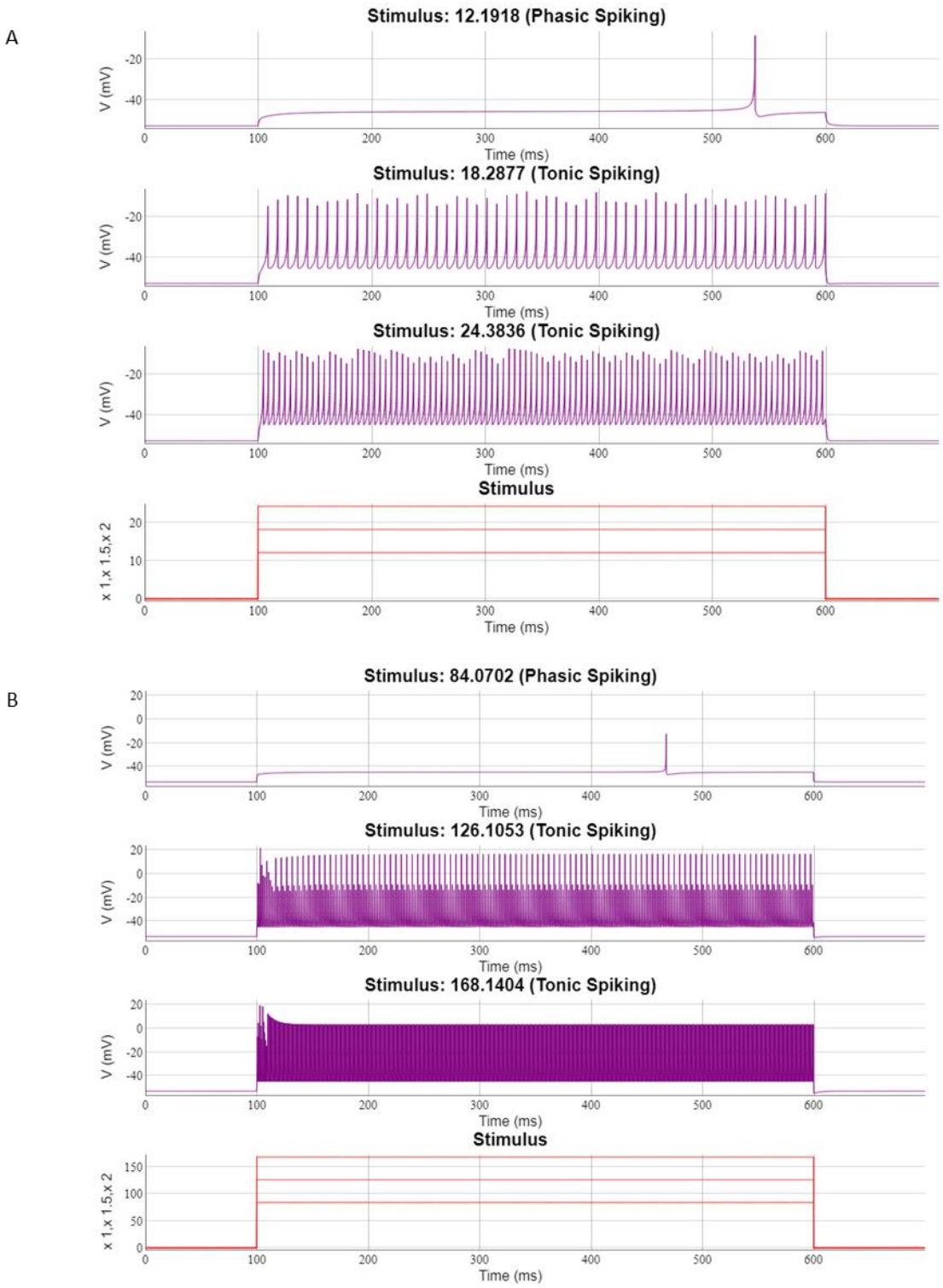

Figure 9. Firing pattern of two different k values.

Increasing the *k* parameter of the Izhikevich 9P model can create sudden peaks in the membrane potentials. (A) The firing pattern of a neuron with k = 0.24 and V_{max} = -15 mV at rheobase x 1, 1.1, and 1.2. (B) The firing pattern of the same neuron is changed by setting the *k* parameter to 1.24. The rheobase value changed, as well as its firing behaviour. The membrane potential reaches much higher than its V_{max} value.

Capacitance Calculations for the Parameter Fitting

The capacitance parameter is an important part of the model. Not many capacitance values are reported for zebrafish spinal neurons in the literature. Therefore, an approach was taken to determine the capacitance ranges using the cell sizes. For the cell types where soma size information was available but not any capacitance value, the capacitance was calculated using the formulation of C_m = 1 μF/cm^2 commonly used in the literature (Bui et al., 2008; Bui and Brownstone, 2015; Carlin et al., 2009; Hille, 2001; Stefanescu et al., 2013) (Table 7).

However, the result capacitance values were very small and did not generate proper parameter sets when fed into the genetic algorithm. The cell capacitance is impacted by the cell size, as well as the dendritic branches, nodes, and myelin content (Mainen et al., 1995). Therefore, the capacitance calculated using cell size was scaled with some of the capacitance values reported in the literature. For that, a cell type with both soma size and capacitance values reported was taken as a reference: the capacitance of motoneurons is given as 17.4 ± 1.3 (between 9-30 pF) (Buss et al., 2003). The capacitance value using the above formulation would come up with a range of [0.55, 2.99] for sMNs. Multiplying this range with 15 would bring the range closer to the reported capacitance values. Therefore, all the capacitance values calculated using the soma size were normalized by multiplying them by 15, as seen in the last two columns of Table 7.

Table 7. The soma size of the cell groups, the calculated and normalized capacitance values.

Type	Area Min (μm^2)	Area Max (μm^2)	C_m Min (pF)	C_m Max (pF)	Norm. Min (pF)	Norm. Max (pF)
pMN*	201	530	2.01	5.3	30.15	79.5
sMN-ms type*	79	216	0.79	2.16	11.85	32.4
sMN-m type*	66	299	0.66	2.99	9.9	44.85
sMN-s type*	55	145	0.55	1.45	8.25	21.75
dI6†,††	35	50	0.35	0.5	5.25	7.5
V0d†,††	35	50	0.35	0.5	5.25	7.5
V0v†	25	60	0.25	0.6	3.75	9
V0v slow††	46.4	67.6	0.464	0.676	6.96	10.14
V1†	25	45	0.25	0.45	3.75	6.75
V2a Type I¶	19	31	0.19	0.31	2.85	4.65
V2a Type II¶	28	42	0.28	0.42	4.2	6.3

*(Bello-Rojas et al., 2019)
† (McLean et al., 2007) reported as CoBL (dI6 and V0d), Multipolar commissural descending (McoD, V0v), and CiA (V1).
†† (Hale et al., 2001) reported as CoBL.
¶ (Menelaou and McLean, 2019)

3.1.2.2 Spatial Distribution

The number and spatial distribution of each cell pool were determined from the literature, either by directly using the reported values or deriving approximate values from published figures or plots (Table 9). When there are multiple subgroups of a single cell population, and their relative numbers are unknown based on the studies to date, the total number reported was distributed evenly among the subgroups. For example, there is no information on the number of dI6-A or dI6-B neurons, only dI6 neurons as ~20/hemisegment (Kishore et al., 2020). This number was divided into two to determine the number of dI6-As and dI6-Bs.

3.1.2.3 Muscle cells

Fast muscle cells have the ability to fire an action potential (Luna et al., 2015). Therefore, fast muscle cells were mathematically modelled as Leaky Integrate and Fire models. Slow muscle cells that do not fire action potentials are modelled as Leaky Integrators. The momentary tension of a muscle cell is calculated using the Boltzmann equation, where T_{max} is the maximum tension, T_a is the current tension, V_a is the voltage at T_a = 0.5 T_{max}, V_m is the membrane potential, and k_a is a slow factor (Dulhunty, 1992):

$$T_a = \frac{T_{max}}{1 + e^{(V_a - V_m)/k_a}}$$

T_{max} values were initially set to one but were later tweaked based on test results.

Table 8. Leaky Integrator parameters of the muscle cells.

Cell Group	Rheobase (pA)	C (pF)	k_a *	R† (GΩ)	T_{max}	V_a * (mV)	V_{max} * (mV)	V_r (mV)	V_{reset} (mV)	V_t (mV)
Muscle Fast AP	259.26	78 ± 2 [68-88]	6.2	0.108 ± 0.005	5	-13	30	-70	-70	-42
Muscle Slow	N/A	54 ± 3 [45-63]	6	0.12 ± 0.01	0.5	-24	30	-54		

*: derived from (Dulhunty, 1992)
†: derived using the values from (Bose et al., 2019) and (Buss and Drapeau, 2000).

Fast muscle cells were placed more medially, whereas slow muscle cells were on the lateral border of the musculoskeletal region (Devoto et al., 1996; Stellabotte and Devoto, 2007).

Table 9. Spatial distribution of each cell pool in the generated model.

The table does not include the rostrocaudal distribution, as it is assumed that all cell pools are uniformly distributed across the rostrocaudal axis of each somite.

Cell Group	# / Somite	Medial Lateral Distribution	Dorsal Ventral Distribution	Main Resources
dI6-A	10	Angular*: 0-80°	Radius*: 20-80%	(Kishore et al., 2020; Satou et al., 2020)
dI6-B	10	Angular*: 0-80°	Radius*: 20-80%	
Muscle Fast AP	20	Angular*: 45-135°	Radius*: 40-60%	(Devoto et al., 1996; Stellabotte and Devoto, 2007)
Muscle Slow	40	Angular*: 10-160°	Radius*: 95%	
pMN	4	Uniform: 40-50%	Gaussian: 45 ± 5	(Asakawa et al., 2021; Eisen et al., 1990; Liu and Westerfield, 1988)
sMN-m-type	20	Angular*: 90-180°	Radius*: 30-50%	(Asakawa et al., 2021; McLean et al., 2008; Svara et al., 2018)
sMN-ms-type	20	Angular*: 90-180°	Radius*: 30-50%	
sMN-s-type	20	Angular*: 90-180°	Radius*: 30-50%	
V0d	25	Uniform: 0-40%	Gaussian: 24±0.9	(Picton et al., 2022; Satou et al., 2012)
V0v-A	10	Uniform: 0-100%	55-70%	(McLean et al., 2008, 2007; Satou et al., 2012)
V0v-B	10	Uniform: 0-100%	55-70%	
V0v-D	10	Uniform: 0-100%	55-70%	
V1-Fast	10	Uniform: 0-100%	30-40%	(Higashijima et al., 2004a; Sengupta et al., 2021)
V1-Hybrid	10	Uniform: 0-100%	20-40%	
V1-Slow	10	Uniform: 0-100%	20-30%	
V2a-Type-I-DH	4	Uniform: 10-50%	Bimodal: 2:50 ± 2:5; 30 ± 5	(Kimura et al., 2006; McLean et al., 2008; Menelaou et al., 2014; Menelaou and McLean, 2012; Song et al., 2018)
V2a-Type-I-DL	4	Uniform: 30-80%	Bimodal: 2:50 ± 2:5; 30 ± 5	
V2a-Type-I-DM	4	Uniform: 30-80%	Bimodal: 2:50 ± 2:5; 30 ± 5	
V2a-Type-II-D	4	Uniform: 10-90%	Bimodal: 2:50 ± 2:5; 30 ± 5	
V2a-VB	4	Uniform: 10-90%	Gaussian: 55 ± 5	
V2b-Gly	10	Uniform: 10-90%	Gaussian: 40 ± 10	(Callahan et al., 2019)
V2b-Mixed	10	Uniform: 10-90%	Gaussian: 45 ± 10	

*: Angular distribution and radii range together define the medial-lateral and dorsal-ventral distribution. Angles and radii are randomly generated independently.

3.1.2.4 Motoneurons

Each hemisegment of larval zebrafish has 4-5 pMNs (Asakawa et al., 2021). These are middle primary (MiP), dorsal rostral primary (dRoP), ventral dorsal primary (vRoP), caudal primary (CaP), and variable primary (VaP) motoneurons based on their dorsal-ventral location and projection direction. These relatively larger MNs are distributed uniformly between 45-65% of the dorsoventral and 40-50% of the mediolateral axis of the spinal cord (Bello-Rojas et al., 2019; McLean et al., 2008; Svara et al., 2018).

In terms of neuronal dynamics, CaP has a rheobase of 300 pA and displays a tonic firing pattern at 1.5x rheobase (Menelaou and McLean, 2012). In embryonic zebrafish, there are differences in the electrical properties of CaP and MiP. CaP has a higher maximum membrane potential after an action potential (V_{max}) and a lower reset membrane potential (V_{reset}) (Moreno and Ribera, 2009). Despite the possible variability, due to a lack of information in the literature for the dynamics of other pMNs, a single pMN type was created in *Sili*Fish for simplicity with a uniform dorsoventral distribution covering 45-65% of the spinal cord. The CaP dynamics properties were used as a reference, and the Izhikevich parameter fitting was done using GA. The minimum-to-maximum ranges were captured from various experimental studies (Buss et al., 2003; Buss and Drapeau, 2001), and selected values are displayed in Table 5.

There are multiple classifications of sMNs based on their projections (Bello-Rojas et al., 2019; Menelaou and McLean, 2012). One study divides sMN into m-type (with medial projections to fast muscle cells), s-type (septal projections to slow muscle cells), and ms-type (both medial and septal projections to fast and slow muscle cells) (Bello-Rojas et al., 2019). S-type sMNs have lower thresholds and display burst firing. M-type sMNs have higher thresholds and display chattering firing. Another study classifies sMNs by the dorsoventral positions of their projections: dorsally projecting dS, ventrally projecting vS, and dvS covering a wider range (Menelaou and McLean, 2012). These sMNs have reported rheobase values of 35, 65, and 105 pA, respectively. The two classifications of sMNs were merged in the model. The sMN-m-type, s-type, and ms-type were created for the populations described by Bello-Rojas and colleagues (2019), which were also assumed to correspond to dvS, dS, and vS, respectively.

3.1.2.5 Interneurons

There are many subgroups of interneurons defined in the literature. All the subgroups involved in swimming speeds are generated in my model (Figure 1). However, the information on all these subgroups in the literature is incomplete. Therefore, some approximations and educated guesses were made to create the initial swim circuit model before testing and tweaking the parameter values.

dI6 Interneurons

There are three types of dI6 neurons in larval zebrafish (Satou et al., 2020). The high threshold dI6-C neurons exist in one/hemisegment and are involved in escape behaviour (Satou et al., 2020). The dI6-As and dI6-Bs constitute the remaining neurons of the 24 ± 4 dI6s / hemisegment (Satou et al., 2020). Due to the small number of dI6-C's and the lack of their involvement in regular swimming, only dI6-A and dI6-B were added to the model in equal numbers.

V0d Interneurons

V0ds can be glycinergic, GABAergic, or both (Lanuza et al., 2004). In adult zebrafish, different subgroups of V0ds are involved in slow, intermediate, and fast swimming (Picton et al., 2022). As the speed-dependent separation is not present at larval stages yet (Picton et al., 2022), and no detailed studies are available on V0ds with different neurotransmitter profiles, only one group of V0d was added to the model for simplicity.

Both dI6 and V0d neurons are part of CoBL neurons. Earlier studies that focused on CoBL neurons did not distinguish dI6 and V0ds, as the latter molecular classification had not occurred yet. The information reported was used as a source to generate both cell groups (Liao and Fetcho, 2008; McLean et al., 2007; Svara et al., 2018).

V0v Interneurons

There are three subgroups of V0v neurons with different projection patterns: V0v-A (ascending), V0v-D (descending), and V0v-B (bifurcating) (Satou et al., 2012). V0v-D neurons are active during slow swimming but are inhibited during fast swimming (Kimura et al., 2006; Satou et al., 2012). Early-born V0vs have ascending projections, whereas late-born V0vs have descending or bifurcating projections (Satou et al., 2012). In adult stages, V0vs are also grouped into slow, intermediate, and fast based on their recruitment at different swimming speeds

(Björnfors and El Manira, 2016); however, this separation has not yet been shown for larval zebrafish. Despite the lack of slow-fast separation in the larval zebrafish, all three subgroups of V0vs were created to benefit from different projection patterns: V0v-A, V0v-B, and V0v-D. With the general theme of early-born neurons being more involved in escape behaviour or faster swimming speeds, the rheobase range reported for V0vs, in general, was distributed such that V0v-As have the higher rheobase, and V0v-Ds have the lower rheobase. All V0v subgroups were placed within the same location, uniformly distributed across the medial-lateral axis, and had a dorsoventral distribution of 55-70% from the top.

V1 interneurons

In larval zebrafish, there are three subgroups of V1 neurons based on their recruitment at different swimming speeds: V1-Fast, V1-Hybrid, and V1-Slow (Kimura and Higashijima, 2019). In the literature, there is no information on the rheobase for these V1 neurons; however, the resistance of the V1 neurons increases going dorsally (McLean et al., 2007). Using the V2a rheobase values as a guide, V1-Fast, V1-Slow, and V1-Hybrid rheobase values were set to be in the range of 200, 5, and 50pA, respectively. As the rheobase values are inversely proportional to the resistance (Buss et al., 2003), the dorsoventral location was determined accordingly: V1-Fasts were placed more ventrally, V1-Slows were placed more dorsally, and V1-Hybrids across the range.

V2a Interneurons

Among the interneuron populations involved in larval zebrafish swimming speeds, V2as are the ones that are most studied, and all the available information was tried to be incorporated into the model to the best of my ability. V2as are shown to be necessary and sufficient for swimming in larval zebrafish (Eklöf-Ljunggren et al., 2012; Eklöf Ljunggren et al., 2014). Ventrally and dorsally located V2as are involved in slow and fast swimming, respectively (Kimura et al., 2006; Kimura and Higashijima, 2019). Dorsal V2as can further be divided into Type I and Type II V2as based on their roles and firing patterns (Menelaou and McLean, 2019). Type I V2as have a rheobase range of 2-200 pA, and high-order connections to other V2as and MNs and are involved in tail beat frequency (Menelaou and McLean, 2019). Type II V2as have a rheobase range of 60-600 pA, a conduction velocity of 0.5m/s, and last-order connections to MNs and are involved in tail beat amplitude (Menelaou and McLean, 2019).

Ventral V2as can also be divided into multiple subgroups based on their neuronal dynamics (McLean 2023, personal communication); however, as there is no published study to date with solid findings, only one type of cell group was created for ventral V2as: V2a-VB. As Type I V2a has a wide rheobase range (Menelaou and McLean, 2019), three subpopulations were generated with low, medium, and high rheobase: V2a-Type I DL, V2a-Type-I-DM, and V2a-Type-I-DH. Displaced V2as are also more dorsal than the rest and have more projections to larger pMNs (Svara et al., 2018). Assuming the V2as with the highest rheobase would be involved with the highest swimming speeds, V2a-Type-I-DH was considered to represent this displaced population. The spatial distribution of the rest of the V2as was derived from multiple studies (Kimura et al., 2006; McLean et al., 2008). There is no information to justify having different spatial distributions for the other V2a subgroups, so they were assigned the same spatial distribution.

Strictly by their projection patterns, V2as can also be divided into descending (V2a-D) and bifurcating (V2a-B) (Menelaou et al., 2014). Dorsal V2a-Ds have longer descending axons than the ventral V2a-Ds. Rather than creating subtypes for these two groups (D and B), this variability was embedded within the current classification. The V2as involved in slow swimming have descending projections only, whereas V2as involved in fast swimming have bifurcating projections (Björnfors et al., 2019). Therefore, V2a-Type-I-DL & DM were defined to have descending projections, and V2a-Type-I-DH, V2a-Type-II, and V2a-VB have both ascending and descending.

V2b Interneurons

V2as and V2bs are differentiated from the same progenitor domains, and each group has a similar number at each somite (Fetcho and Mclean, 2010). Half of V2bs release glycine only and are slightly located more dorsally (Callahan et al., 2019). The rest of the V2bs release both glycine and GABA. V2b-Gly and V2b-Mixed were created in the model to represent these two groups. Both subgroups are involved in speed control: V2b-Mixed during slow swimming and V2b-Gly during fast swimming (Callahan et al., 2019).

3.1.3 Projections, Gap Junctions, and Chemical Synapses

The experimental findings reported in the literature were used as the primary source when populating the projections and junctions between cells. The information reported generally fell into these categories: axon lengths and widths, junction type (electrical versus chemical),

conduction velocity, probability of connectivity, weight (conductance) of the junctions, and location of junction (soma versus dendrites). As cells are implemented as point neurons, axon size information or connection placements were not used. The lengths of the axons were implicitly implemented by the cell pool's ascending and descending axon length parameters without creating any structures for the axons.

3.1.3.1 Distance Calculations between Cells

There are two modes of distance calculation used in the generated model. Euclidean is the shortest distance between the two points, and Manhattan is the sum of the distances in all three coordinates. For contralateral projections and neurons with circumferential projections, Manhattan distance was used as a close estimate. For all others, Euclidean distance was used.

3.1.3.2 Synaptic Threshold Membrane Potential

The chemical synapse definition includes a threshold membrane potential to determine when the presynaptic neuron activity will impact the post-synaptic cell. At time *t*, the relevant time point *t'* is calculated using the pre-synaptic and post-synaptic cell coordinates and the pre-synaptic cell's conduction velocity. If the pre-synaptic cell's membrane potential at *t'* point is greater than this defined threshold, the synaptic transmission would take place, and the input current to the post-synaptic cell at *t* is calculated. The average of the pre-synaptic neuron's spiking threshold and maximum membrane potential was used to determine the synaptic threshold potential.

3.1.3.3 Synaptic Weights

When two cells project to each other, many factors may impact the conductance of the synapse or the gap junction in between. Creating the cell populations and their projections define the model only partially. The strength of those projections is crucial to how the model will behave. The literature provides only limited information on synaptic weights. To the best of my knowledge, the only information available related to larval zebrafish spinal circuits are some of the synaptic weights originating from V2bs (Callahan et al., 2019; Sengupta and Bagnall, 2022) or V1s (Sengupta et al., 2021).

The synaptic weights from V2bs to MNs are reported in the range of 97-174 pS (Callahan et al., 2019) or 0.5-2 nS (Sengupta and Bagnall, 2022). The synaptic weights from V1s to MNs are reported in the range of 0.2-2.1 nS (Sengupta et al., 2021). These synapses constitute only a small portion of the synapses that will be modelled in the speed circuits. The biological range of the

synaptic conductance values is reported as 0.6-1.5 nS for young tadpoles (Hull et al., 2016). So, the conductance values reported above between 0.1-2.1 nS can be a good candidate for the range of synaptic weights originating from spinal cord interneurons of the larval zebrafish. It is also known that conductance increases as the capacitance increases (Buss et al., 2003). Using this information and doing some basic algebra, initial synaptic weights were assigned to the outgoing chemical synapses of the neurons in the model proportional to the normalized capacitance values in Table 7. Being aware that this estimation is very broad, they were tweaked more generously than the actual values reported in the literature during the testing of the model.

Across development, zebrafish reliance on gap junctions slowly switches to chemical synapses instead (Drapeau et al., 2002; Knogler et al., 2014). Considering the developmental switch from gap junctions to chemical synapses, the fact that large gap junctions have a huge impact on the resting membrane potentials of the neighbouring cells, the lack of distinction in our model of soma-to-soma versus dendrite-to-axon gap junctions, which might change the strength of the gap junctions defined, the weights of gap junctions are kept small.

3.1.3.4 Conduction Velocity

As realistic dimensions of the larval spinal cord are used, the selection of conduction velocities will make a difference in the rostrocaudal delay of propagating contractile waves down the fish's body from head to tail.

Only a handful of conduction velocity information is provided in the literature for different neuronal groups. Type I and Type II V2a neurons have 0.2 and 0.5 m/s conduction velocities, respectively (Menelaou and McLean, 2019). Another computation study uses different conduction velocities for excitatory and inhibitory neurons for lampreys (Kozlov et al., 2014). A recent study states that the conduction velocity of V3 neurons (0.19 ± 0.07 m/s) is twice the velocity of dorsal oscillatory populations; however, there is no information on the identity of these dorsal populations (Böhm et al., 2022).

We can estimate the conduction velocity from the reported soma surface area, assuming that axonal width will be proportional to the soma size. A regression analysis using the V2a conduction velocities and soma sizes generated a formulation of CV = 0.013 * Size – 0.04, and an estimated conduction velocity was assigned to each cell group (Table 10).

Table 10. The conduction velocities of different cell groups are calculated by their average size.

Cell Group	Area Min (μm^2)	Area Max (μm^2)	Avg Size (μm^2)	Calculated CV (m/s)
dI6	35	50	42.5	0.51
pMN	201	530	365.5	4.71
sMN-m type	66	299	182.5	2.33
sMN-ms type	79	216	147.5	1.88
sMN-s type	55	145	100	1.26
V0d	35	50	42.5	0.51
V0v	66.1	102.3	84.2	1.05
V0v slow	46.4	67.6	57	0.70
V0v	25	60	42.5	0.51
V1	25	45	35	0.42
V2a Type I	19	31	19	0.21
V2a Type II	28	42	42	0.50
V2a-VB	46.4	67.6	57	0.70

3.1.3.5 Synaptic Delays

There is also a synaptic delay in synaptic transmissions that will delay the action potential firing in the postsynaptic neuron (Wen and Brehm, 2005). All the synapses, including gap junctions, have a delay field within their definition in *Sili*Fish. For pMN and sMN, synaptic delays of 0.69 and 1.43 were used, respectively (Wen et al., 2020). The synaptic delays of V1 to V0 projections are reported as 0.46±0.1, 0.63±0.08, 0.91±0.07 (Higashijima et al., 2004a). These numbers were used for synaptic delays from V1-Fast, V1-Hybrid, and V1-Slow to every commissural neuron. For all other chemical synapses, the default value of 0.5 ms was used (Uemura et al., 2020).

3.1.3.6 Generating Projections

Muscle Cells

During embryonic stages, slow muscle cells are connected to other slow muscle cells and fast muscle cells to other fast muscle cells by gap junctions. (Drapeau et al., 2002). The gap junctions between fast muscle cells reduce in number and become weaker from day 1 to day 3 (Drapeau et al., 2002; Luna and Brehm, 2006). During larval stages, there are gap junctions between slow muscle cells between and within somites (Luna and Brehm, 2006). Therefore, gap

junctions were created only between slow muscle cells with 0.6 probability, using the coupling coefficients in Luna & Brehm (2006).

MN Projections

A topographic innervation pattern is observed between MNs and muscle cells (Bello-Rojas et al., 2019; Menelaou and McLean, 2012). The pMNs project to fast muscle cells in a quadrant-dependent manner. Similarly, the gap junctions between pMNs within the dorsal or ventral quadrants of the spinal cord are twice as strong as the gap junctions between the dorsal and ventral (Bagnall and McLean, 2014). There are only 4-5 pMNs in a single somite (Bello-Rojas et al., 2019; Menelaou and McLean, 2012), so this quadrant-dependent connectivity may refer to the neighbouring somite. To mimic this constraint, pMNs are defined to have a single gap junction to a pMN in the neighbouring somite.

Muscle cells receive one input from pMNs and 1-3 inputs from sMNs (Wen et al., 2020; Westerfield et al., 1986). To represent this constraint, the maximum number of input projections to muscle cells was set to one from pMNs and two from sMNs.

Based on their muscle cell innervations found in the literature, projections from sMN-m-type to fast muscle cells, from sMN-s-type to slow muscle cells, and from sMN-ms-type to both fast and slow muscle cells were defined (Bello-Rojas et al., 2019). For sMNs, the gap junctions were limited to within and neighbouring somites ipsilaterally and within the same sMN groups.

Using the values reported in the literature, the decay tau values of the NMJs were set to 0.75 and 3 ms, and tau rise values were set to 0.25 and 0.33 for fast and slow muscle cells, respectively (Luna and Brehm, 2006).

There are also predictions that fast-type MNs inhibit slow circuits by activation inhibitory V1 neurons (Bello-Rojas et al., 2019); however, this prediction was not included in the current model.

V2a Projections

There are gap, synaptic, and slow junctions between different types of V2as (Menelaou and McLean, 2019). Slow junctions are assumed to be indirect electrical junctions. As the other multi-synaptic connections supposedly represent those junctions, they were not explicitly implemented in the model.

The probabilities of gap junctions and chemical synapses were derived using the information reported in the literature. The electrical connections between the dorsal V2as (Type I and Type II) are stronger among the same groups (Menelaou and McLean, 2019). A higher weight of 0.001 for gap junctions **within** Type I V2as (V2a DH/DM/DL), Type II V2as, and ventral V2as (V2a-VB), and a lower weight of 0.0005 in **between.**

During the embryonic stages, gap junctions exist between V2as and MNs (Kimura et al., 2006). The probability is 1/3 for dorsal V2as to sMNs, and ventral V2a to MN junctions are mostly electrical (Kimura et al., 2006). In larval zebrafish, a study claims no or little synaptic connections exist between dorsal V2as and pMNs (Bhatt et al., 2007). On the other hand, other studies are contradicting the previous statement (Menelaou and McLean, 2019)

Menelaou and McLean (Menelaou and McLean, 2019) provided the probability of projections between dorsal V2as and other dorsal V2as, pMNs, and V0ds, as well as their nature of connection (Table 11). The information reported in this study was merged to determine the probabilities of the outgoing V2a projections. For example, the projection probability from V2a Type I and V2a Type II was reported as 7/13 (~ 0.538). Type I to Type II junctions are descending: 45% glutamatergic, 45% mixed, and 10% slow (Menelaou and McLean, 2019). Mixed junctions have both gap junctions and chemical synapses. Combining these two pieces of information, 0.9*0.538 = 0.484 and 0.45*0.538 = 0.242 were used for synaptic and gap junction probabilities, respectively.

Table 11. Dorsal V2a outgoing projection types and probabilities. *

The values in parentheses represent the probability of any type of projection.

	V2a Type I	**V2a Type II**	**V0d**	**pMN**
V2a Type I	(12/12) 80% gap, rest mixed	(7/13) ~45% glutamatergic, ~45% mixed, ~10% slow Descending	(11/11) ~25% glutamatergic, ~20% mixed, ~55% gap	(38/38) ~80% glutamatergic, ~20% mixed
V2a Type II	(5/14) 35% glutamatergic, 50% slow Descending	(2/15) Mostly slow Descending	(10/17) ~40% slow, ~25%mixed, ~35% gap	(40/71) ~50% mixed, ~40% slow, ~10% electrical

*: Derived by using the information from (Menelaou and McLean, 2019)

When creating projections in between Type I V2as, for simplicity, only connections within the Type I V2as with similar rheobase were created: V2a-Type-I-DL to V2a-Type-I-DL, V2a-Type-I-DM to V2a-Type-I-DM, and V2a-Type-I-DH to V2a-Type-I-DH. The projections to pMNs were assumed to be from V2a-Type-I-DH. When generating projections between Type I and Type II V2as, as V2a-Type-I-DLs have very low rheobase, no projection was created between them.

In the same study, the peak EPSP amplitudes between V2a-Type-I to V2a-Type-I is two mV, V2a-Type-I to V2a-Type-II is five mV, and V2a-Type-II to V2a-Type-I is one mV (Menelaou and McLean, 2019). These values were used to normalize the synaptic weights of these junctions and start with 0.4, 1, and 0.2 nS.

Svara and colleagues (2018) also provide more information on V2a to MN projections based on the MN size. Displaced V2as make projections only to the largest of MNs and provide the majority of input to these MNs. Other dorsal V2as project mostly to large MNs but also to medium MNs. Ventral V2as project to both large and medium MNs based on proximity (Svara et al., 2018). Dorsal V2as have connections to all MNs (primary and secondary) (Menelaou et al., 2014).

The probabilities from V2as to sMNs were determined using the information in these studies, as shown in Table 12.

Table 12. The V2a to sMN gap junction and chemical synapse directions and probabilities used in the model*.

Source	Target	Junction Type	Axon Projection Pattern	Direction	Probability
V2a-Type-I-DL	All sMNs	Synapse	Ipsilateral	Descending	0.9
V2a-Type-I-DM	All sMNs	Synapse	Ipsilateral	Descending	0.9
V2a-VB	All sMNs	Synapse	Ipsilateral	Bifurcating	1
V2a-Type-I-DL	All sMNs	Gap	Ipsilateral	Descending	0.6
V2a-Type-I-DM	All sMNs	Gap	Ipsilateral	Descending	0.6
V2a-VB	All sMNs	Gap	Ipsilateral	Descending	0.2

*: Derived from (Svara et al., 2018)

To the best of my knowledge, the excitatory inputs to V0vs have not been studied. The V2as and V0vs are the only excitatory pools in the current model, so projections from V2as to V0vs were generated. As V0v-Ds are more involved in slow swimming, they received projections from V2a-VB and V2a-Type-I-DL subgroups. The other V0v populations received input from V2a-Type-I-DH and V2a-Type-I-DM subgroups.

dI6s and V1s are shown to be active during slow swimming (Kimura and Higashijima, 2019; Satou et al., 2020), but experimental evidence of their excitatory input is lacking. Descending projections and synaptic connections from low rheobase dorsal V2a and ventral V2a pools to every dI6 pool were created with 0.3 probability.

As explained above, the V1s are divided into three subgroups based on their recruitment patterns at different swimming speeds. Assuming they receive input from the V2as, projections from more dorsal V2as to V1-Fast, ventral V2as to V1-Slow, and V2as to V1-Hybrid were created.

Despite a surge in the studies on V2bs in recent years (Andrzejczuk et al., 2018; Callahan et al., 2019; Sengupta et al., 2021; Sengupta and Bagnall, 2022), the excitatory inputs driving their activity is not known. It is hypothesized that Type II V2as provide input to V2b neurons (Sengupta and Bagnall, 2022). However, as Type II V2as are more involved in the tail beat amplitude, I decided to generate Type I V2as to V2bs. Specifically, from V2a-Type-I-DH/DM to V2b-Gly, which are both active in fast swimming, and from V2a-Type-I-DL/DM to V2b-Mixed.

V2b Projections

Two main references were used for the V2b projections (Callahan et al., 2019; Sengupta and Bagnall, 2022). As some of the information did not separate the subgroups of V2bs, how V2b-Mixeds and V2b-Glys were differentially involved in speed circuits was considered when generating the projections.

Fast MN inhibition is mostly done by V2b-Glys, whereas slow MN inhibition is by V2b-Mixeds (Callahan et al., 2019). Descending projections of five somites were created from V2b-Gly to pMN and sMN-m-type MN, with 1.5 nS (midpoint of 1-2 nS range) and 0.75 nS (midpoint of 0.5-1 nS range) conductance weights, respectively (Sengupta and Bagnall, 2022) (Table 13). Similarly, descending projections of three somites were created from V2b-Mixed to sMN-ms-type and sMN-s-type MNs, with 0.75 nS conductance weights.

Table 13. Projection lengths and conductance values of V2b descending projections.*

<table>
<tr><th></th><th>V2b-Gly</th><th>V2b-Mixed</th><th>V1</th><th>dI6</th><th>V0</th><th>V2a</th><th>MN</th><th>pMN</th><th>sMN</th></tr>
<tr><td>V2b-Gly</td><td>One somite</td><td></td><td rowspan="2">Three somites 0.3-0.5 nS</td><td></td><td rowspan="2">Current somite</td><td rowspan="2">Seven somites 0.5-0.8 nS</td><td>Five somites</td><td rowspan="2">1-2 nS</td><td rowspan="2">0.5-1 nS</td></tr>
<tr><td>V2b-Mixed</td><td></td><td>One somite</td><td>Current somite</td><td>Three somites</td></tr>
</table>

*: Derived from (Sengupta and Bagnall, 2022)

V2b-Gly was projected to V1-Fast, and V2b-Mixed was projected to V1-Hybrid and V1-Slow, with descending projections of three somites and 0.4 nS conductance values (Sengupta and

Bagnall, 2022) (Table 13). Similarly, descending projections of seven somites from V2b-Gly to V2a-Type-I-DM/DH and V2a-Type-II-D, and V2b-Mixed to V2a-Type-I-DL and V2a-VB were generated with 0.65 nS conductance values.

For the rest of the V2b outgoing projections, the conductance value of 0.139 nS was used (Callahan et al., 2019). V2b-Mixed was projected to dI6-A, dI6-B, and V0v-D, and V2b-Gly was projected to V0d, V0v-A, and V0v-B within the current somite only.

dI6 Projections

dI6s are involved in contralateral inhibition and have ipsilateral projections to V2as (Satou et al., 2020). Both dI6-A and dI6-B have ascending and descending projections with different lengths (Satou et al., 2020). Other than their projection lengths, as there is no separation of dI6-A and dI6-B in the literature regarding other aspects of their projections, like conductance values of target cell populations, the same type of projections were generated for both.

Relying on the probabilities listed in a study by Satou and colleagues (2020), projections from dI6 to V2as, pMNs, sMNs, V1s, and other dI6s were defined.

V0v Projections

V0vs have projections and gap junctions to ventrally located sMNs (McLean et al., 2008). V0vs are involved in tail beat amplitude rather than rhythm generation (Jay and McLean, 2019). There is no literature that shows V0v projections to other INs; therefore, their projections were limited to MNs only. The weights were tweaked so that if there is only a left stimulus, the activation of the right side is less than the left. Ascending projection lengths of V0v-As and V0v-Bs were set to 14±7 and 5±5 somites, respectively (Satou et al., 2012). Descending projection lengths of V0v-Ds and V0v-Bs were set to 15±4 and 5±5 somites, respectively (Satou et al., 2012).

V0d Projections

V0d neurons have mostly contralateral and some ipsilateral projections (Satou et al., 2012).

V0ds are inhibitory and more active during fast swimming, so their projections were limited to sMNs rather than pMNs. V0d to V1 projections were also limited to V1-Slow only, which inhibits slow circuits for rhythm regulation (Wilson and Sweeney, 2023).

Using the axon lengths and probabilities reported in the literature, projections from V0ds to MNs, V2as, and V1s were defined with 3 ± 0.58 somites ascending and 2.7 ± 0.33 descending

lengths (Satou et al., 2020). V0d projects to both large and medium size MNs, so the projections to MNs included both pMNs and sMNs (Svara et al., 2018).

V1 Projections

V1s have stronger and longer ascending and shorter, weaker descending projections. (Higashijima et al., 2004a). Fast-type V1s are proposed to inhibit slow swimming circuits by shutting them down and inhibit fast swimming circuits for frequency regulation (Kimura and Higashijima, 2019). A similar inhibition between slow V1s and slow swimming circuits exists but is weaker (Kimura and Higashijima, 2019).

V1s provide inhibitory projections to MNs (Fidelin and Wyart, 2014). Slow MNs are inhibited by V1s during fast swimming (Bello-Rojas et al., 2019; Kimura and Higashijima, 2019). V1s have only ascending projections MNs (Sengupta et al., 2021). Considering the different recruitment of V1 subgroups at different speed circuits and their proposed roles, projections from V1-Fast to all MNs, from V1-Hybrid to all sMNs, and from V1-Slow to sMN-ms-type and sMN-s-type were created. The projection lengths to pMNs and sMNs were set as 2 and 3 somites, respectively (Sengupta et al., 2021). The conductance value of V1 to pMN is reported as 1.1-1.2 nS range (Sengupta et al., 2021). For projections to pMNs, 1.15 nS was used. V1 to sMN conductance value is reported as 0.3-0.6 nS range (Sengupta et al., 2021). This range was split equally into projections from different V1s: V1-Slow outgoing conductance was set to 0.3, V1-Hybrid was set to 0.45, and V1-Fast was set to 0.6 nS.

Both ascending and descending projections were created from V1s to V2as (Sengupta et al., 2021). These projections had three and two somite extensions, respectively (Sengupta et al., 2021). The V1 ascending projections are much weaker than their descending projections (Higashijima et al., 2004a; Sengupta et al., 2021). To implement this difference, ascending projections were assigned $1/5^{th}$ of their descending counterparts unless there is literature stating otherwise. The average of the reported 0.5-1 nS conductance value was used for the descending projections (Sengupta et al., 2021).

There are inhibitory projections from V1s to V2bs (Callahan et al., 2019). These projections are ascending only, reaching up to 3 somites, with 0.2-0.4 nS conductance (Sengupta et al., 2021).

Sengupta and colleagues give information from V1s to commissural premotor neurons (CoPr) as a whole (2021). These CoPr neurons can include dI6s, V0vs, and V0ds. The reported conductance range of 0.9-2.1 nS and the projection length of three segments were used for all three cell populations. As the only exception, considering V0d is more involved in fast swimming, V1-Slow to V0d projection was not created.

V1 to V1 projections exist only within the current segment (Sengupta et al., 2021). As there is no other information about their conductance values, an average value based on V1s other outgoing projections was used.

3.2 Simulation

After the model is created with the cell pools defined by the previous steps, the model can be tested by simulation. The simulation will test the system to observe how the intrinsic properties of the cells or the external stimuli can cause a chain reaction that ends up with swimming behaviour. The system is initialized such that every cell is at its resting membrane potential with zero incoming current. The simulation consists of iterating individual time points starting from zero with δt increments, and every cell's state is calculated using the incoming projections and applied stimuli.

3.2.1 Calculation of the incoming/outgoing currents

A cell's change in membrane potential depends on the current that passes through its ionic channels or gap junctions. In the case of a gap junction, the current is directly calculated by the membrane potential differences of the two cells. In the case of a chemical synapse, the current is calculated by the chemical synapse formulation, as explained in Chemical Synapses. At every time point of the simulation, the currents of all incoming synapses are summed up to be used in the change in the membrane potential calculation.

3.2.2 Calculation of membrane potentials

The membrane potential change depends on the amount and direction of the incoming current calculated, as explained above, and the cell's intrinsic properties, which are mathematically formalized as in Mathematical Models. At every time point *t*, the updated membrane potential values for every cell of the model are calculated to determine the new state of the model. The loop continues till the end of the simulation.

3.3 Full Model vs. Reduced Model

The first full model created comprised 30 somites and included the number of cells per somite reported in the literature for cell populations with available data. It contained 16K cells, >4M projections, and took close to two hours to run a 300 ms simulation. However, this level of complexity was hard to troubleshoot and tweak due in part to being memory intensive.

The model was simplified while maintaining relevant biological behaviour—the first simplification involved lowering the number of somites. However, axon lengths or projection limits are given in terms of somites. Therefore, the projection lengths were divided by three when the model was set to have ten somites instead of 30. The randomizations of the axon lengths were removed to enable troubleshooting easily. The number of cells per somite and the axon lengths of each cell group in the full model and the reduced model are displayed in Table 14.

Another method of simplification is to turn off/deactivate certain cell populations, for example, neurons involved in fast swimming, while testing the slow swimming circuits. However, some neurons can impact the whole system despite not firing an action potential due to gap junctions and different cell pools having different resting membrane potentials. Therefore, all of the cell pools and connections were always kept active. They were deactivated to replicate ablation studies only. Different stimuli to different cellular groups were used to trigger slow and fast networks rather than turning off a specific network.

The most impactful simplification in reducing simulation time involved reducing the number of cells. For each somite, the number of cells per cell pool per somite was set to one rather than the actual number. The single cell thus represented all of the cells belonging to a particular group in that somite. This simplification alone reduced the number of cells from 16K to 1.3K and the number of projections from 4M to 83K. (Table 14). The additional simplification of using ten somites rather than 30 reduced these numbers further at least by 1/3.

Assigning to each cell the role of representing every cell of the same group within a somite, some other adjustments had to be made. In the full model, projections had probabilities. However, using these probabilities creates issues when a single cell represents multiple cells. In reality, the probability of not having any connection from a cell group in one somite to another cell group in another somite would be slim. However, with one cell at each somite, this became an issue.

Therefore, in the reduced model, all probabilities were set to one. The probabilities in the full model are listed in Table 15 and Table 16.

Table 14. The number of cells per somite and their length of axonal branches in the Full and Reduced models.

In the reduced model, the uniform distributions (expressed as min-max) or normal distributions expressed (μ±SD) are replaced by their mean values. A single cell represents the whole population.

	Full Model			Reduced Model		
CellGroup	**Num/Somite**	**Descending Axon**	**Ascending Axon**	**Num/Somite**	**Descending Axon**	**Ascending Axon**
dI6-A	10*	2.3 ± 0.46†	4.6 ± 0.64†	1	0.77	1.53
dI6-B	10*	2 ± 0.66†	6.5 ± 0.66†	1	0.67	2.17
Muscle Fast AP	20			1		
Muscle Slow	40	1	1	1	0.33	0.33
pMN	4††	1	1	1	0.33	0.33
sMN-ms-type	20††	2	2	1	0.67	0.67
sMN-m-type	20††	2	2	1	0.67	0.67
sMN-s-type	20††	1	1	1	0.33	0.33
V0d	25§,¶	2.7 ± 0.33†	3 ± 0.58†	1	0.9	1
V0v-A	10§		13 ± 2§	1		4.67
V0v-B	10§	1-9§	1-9§	1	1.67	1.67
V0v-D	10§	11-21§		1	5	
V1-Fast	10	7 ± 2‖	10 ± 2‖	1	2.33	3.33
V1-Hybrid	10	7 ± 2‖	10 ± 2‖	1	2.33	3.33
V1-Slow	10	7 ± 2‖	10 ± 2‖	1	2.33	3.33
V2a Dis Type I DH	4	10-20#	2-6#	1	5	1.33
V2a-Type-I-DL	4	10-20#	2-6#	1	5	1.33
V2a-Type-I-DM	4	10-20#	2-6#	1	5	1.33
V2a-Type-II-D	4	10-20#	2-6#	1	5	1.33
V2a-VB	4	10-20#	2-6#	1	5	1.33
V2b-Gly	10	6.2 ± 2.7**		1	3	
V2b-Mixed	10	6.2 ± 2.7**		1	3	

*: (Kishore et al., 2020); †: (Satou et al., 2020); ††: (Asakawa et al., 2021); ¶: (Berg et al., 2023)
§: (Satou et al., 2012) ; ‖: (Sengupta et al., 2021); #: (Menelaou et al., 2014); **: (Callahan et al., 2019)

Table 15. Chemical synaptic probabilities in the full model.

Source	Target	Axon Projection Pattern	Direction	Full Model Prob.	Source
All dI6	All dI6	Contralateral	Bifurcating	0.286	(Satou et al., 2020)
All dI6	All MNs	Contralateral	Bifurcating	0.75	(Satou et al., 2020)
All dI6	All V1s	Contralateral	Bifurcating	0.5	(Satou et al., 2020)
All dI6	All V2as	Contralateral	Bifurcating	0.4	(Satou et al., 2020)
sMN-ms-type	All V1s	Ipsilateral	Bifurcating	0.5	
sMN-m-type	All V1s	Ipsilateral	Bifurcating	0.5	
Type I V2as	V0v-A	Ipsilateral	Descending	0.8	(Menelaou et al., 2014)
Type I V2as	V0v-B	Ipsilateral	Descending	0.8	(Menelaou et al., 2014)
Type I V2as	V2b-Gly	Ipsilateral	Descending	0.25	
V0d	All MNs	Contralateral	Bifurcating	0.538	(Satou et al., 2020)
V0d	All V2as	Contralateral	Bifurcating	0.75	(Satou et al., 2020)
V0d	V0d	Contralateral	Bifurcating	0.294	(Satou et al., 2020)
V0v-A	pMN	Contralateral	Ascending	0.3	
V0v-A	sMN-ms-type	Contralateral	Ascending	0.3	
V0v-A	V2a Dis Type I DH	Contralateral	Ascending	0.4	
V0v-A	V2a-Type-I-DM	Contralateral	Ascending	0.4	
V0v-B	sMN-ms-type	Contralateral	Bifurcating	0.3	
V0v-B	sMN-s-type	Contralateral	Bifurcating	0.3	
V0v-B	Type I V2as	Contralateral	Bifurcating	0.45	
V0v-D	sMN-s-type	Contralateral	Descending	0.3	
V0v-D	V2a-Type-II-D	Contralateral	Descending	0.25	
V0v-D	V2a-VB	Contralateral	Descending	0.25	
V2a Dis Type I DH	pMN	Ipsilateral	Descending	1	(Menelaou and McLean, 2019)
V2a Dis Type I DH	V2a Dis Type I DH	Ipsilateral	Descending	0.2	(Menelaou and McLean, 2019)
V2a Dis Type I DH	V2a Type II	Ipsilateral	Descending	0.48	(Menelaou and McLean, 2019)
V2a Type I	V0d	Ipsilateral	Descending	0.45	(Menelaou and McLean, 2019)
V2a-Type-I-DL	All sMNs	Ipsilateral	Descending	0.9	
V2a-Type-I-DL	dI6-A	Ipsilateral	Descending	0.3	(Menelaou et al., 2014)
V2a-Type-I-DL	dI6-B	Ipsilateral	Descending	0.3	(Menelaou et al., 2014)
V2a-Type-I-DL	V0v-D	Ipsilateral	Descending	0.8	(Menelaou et al., 2014)
V2a-Type-I-DL	V2a-Type-I-DL	Ipsilateral	Descending	0.2	(Menelaou and McLean, 2019)
V2a-Type-I-DL	V2a Type II	Ipsilateral	Descending	0.48	(Menelaou and McLean, 2019)
V2a-Type-I-DM	All sMNs	Ipsilateral	Descending	0.9	
V2a-Type-I-DM	V2a-Type-I-DM	Ipsilateral	Descending	0.2	(Menelaou and McLean, 2019)
V2a-Type-I-DM	V2a Type II	Ipsilateral	Descending	0.48	(Menelaou and McLean, 2019)
V2a Type II	pMN	Ipsilateral	Descending	0.5	(Svara et al., 2018)
V2a Type II	V2a Type I	Ipsilateral	Descending	0.12	(Menelaou and McLean, 2019)
V2a-Type-II-D	V0d	Ipsilateral	Descending	0.14	(Menelaou and McLean, 2019)
V2a-Type-II-D	V2b-Mixed	Ipsilateral	Descending	0.75	
V2a-VB	All dI6s	Ipsilateral	Descending	0.3	(Menelaou et al., 2014)
V2a-VB	All sMNs	Ipsilateral	Bifurcating	1	
V2a-VB	V0d	Ipsilateral	Descending	0.6	
V2a-VB	V0v-D	Ipsilateral	Descending	0.5	(Menelaou et al., 2014)
V2a-VB	V2a-VB	Ipsilateral	Bifurcating	0.7	
V2a-VB	V2b-Mixed	Ipsilateral	Descending	0.75	
V2b-Gly	V2b-Gly	Ipsilateral	Descending	0.80	
V2b-Mixed	V2b-Mixed	Ipsilateral	Descending	0.80	

Another adjustment was made to the synaptic weights with the lower number of cells and projection probabilities of one. The synaptic weights were normalized to represent the whole cell population with a single outgoing projection by multiplying the number of cells it is representing and the original probability values.

Table 16. Gap junction probabilities in the full model.

Source	Target	Axon Projection Pattern		Probability	Main Resource
Muscle Slow	Muscle Slow	Ipsilateral	Bifurcating	0.6	(Luna and Brehm, 2006)
V0v-A	sMN-ms-type	Contralateral	Ascending	0.3	
V0v-B	sMN-ms-type	Contralateral	Bifurcating	0.3	
V0v-B	sMN-s-type	Contralateral	Bifurcating	0.3	
V0v-D	sMN-s-type	Contralateral	Descending	0.3	
V2a Dis Type I DH	pMN	Ipsilateral	Descending	0.2	
V2a Dis Type I DH	V2a Dis Type I DH	Ipsilateral	Descending	1	(Menelaou and McLean, 2019)
V2a Dis Type I DH	V2a Type II	Ipsilateral	Descending	0.24	(Menelaou and McLean, 2019)
V2a Type I	V0d	Ipsilateral	Descending	0.75	(Menelaou and McLean, 2019)
V2a-Type-I-DL	All sMNs	Ipsilateral	Descending	0.6	
V2a-Type-I-DL	V2a-Type-I-DL	Ipsilateral	Descending	1	(Menelaou and McLean, 2019)
V2a-Type-I-DL	V2a-Type-II-D	Ipsilateral	Descending	0.24	(Menelaou and McLean, 2019)
V2a-Type-I-DL	V2a-VB	Ipsilateral	Descending	0.7	
V2a-Type-I-DM	All sMNs	Ipsilateral	Descending	0.6	
V2a-Type-I-DM	V2a-Type-I-DM	Ipsilateral	Descending	1	(Menelaou and McLean, 2019)
V2a-Type-I-DM	V2a-Type-II-D	Ipsilateral	Descending	0.24	(Menelaou and McLean, 2019)
V2a-Type-I-DM	V2a-VB	Ipsilateral	Descending	0.7	
V2a Type II	pMN	Ipsilateral	Descending	0.6	(Svara et al., 2018)
V2a Type II	V0d	Ipsilateral	Descending	0.35	(Menelaou and McLean, 2019)
V2a-Type-II-D	V2a-Type-II-D	Ipsilateral	Descending	0.001	(Menelaou and McLean, 2019)
V2a-Type-II-D	V2a-VB	Ipsilateral	Descending	0.7	
V2a-VB	All sMNs	Ipsilateral	Descending	0.2	
V2a-VB	V2a-VB	Ipsilateral	Descending	0.7	

3.4 Generating Speed Networks

The model was designed to incorporate circuitry to generate swimming at different speeds (slow, intermediate, and fast). To the best of my knowledge, there is no literature on the neuronal bases of the gliding period of the beat and glide swimming pattern. Therefore, only the beat portion of the beat and glide swimming was taken into consideration. With this constraint, a swimming

episode which consists of multiple beat and glide periods cannot be modelled. In this document, an episode refers to the time period when there is an external stimulus that triggers the behaviour observed.

3.4.1 Determining Supraspinal Input

Many hindbrain and midbrain neurons project to the spinal cord, some extending to the caudal positions (Kimmel et al., 1982).

There are descending neurons from the medial longitudinal fasciculus (MLF) region of the midbrain to both pMN and sMNs of larval zebrafish (Wang and McLean, 2014). Some of the MLF neurons are shown to be differentially active at different swimming speeds with in-phase activation with the tail movements (Severi et al., 2014). In adult zebrafish, the firing frequency of the MLF neurons changes based on the swimming speed (Berg et al., 2023).

Similarly, the presence of hindbrain (HB) V2as that are rhythmically active and in sync with the ventral root is shown (Kinkhabwalaa et al., 2011). As the swim frequency increases, more ventral HB populations become active (Kinkhabwalaa et al., 2011). Another study showed that there is both tonic and rhythmic excitation in the HB during swimming (Kimura et al., 2013). A correlation between glycinergic hindbrain neurons with tail bends is also shown (Severi et al., 2018).

The early-born hindbrain V2as project directly to caudal early pMNs to create crude behaviours observed in early development and escape behaviour (Pujala and Koyama, 2019). The intermediate-born HB neurons project to caudal pMNs, sMNs, and V2as, whereas late-born HB neurons extend only to the rostral V0vs (Pujala and Koyama, 2019). Both intermediate and late-born HB V2as create multi-synaptic connections to MNs with slower conductance (Pujala and Koyama, 2019).

The supraspinal input may be important in determining the swimming speeds in larval zebrafish. Therefore, three different hindbrain neuronal populations were created to represent the early-born, intermediate-born, and late-born HB neurons, and projections to a selected set of excitatory INs of rostral or caudal somites were created. However, the intrinsic properties of the HB neurons also became a crucial part of the system. As this project focuses on the spinal control

of the larval zebrafish swimming speeds, I decided to represent the supraspinal input as a step current stimulus rather than activation by the neurons.

To represent the input from late-born, intermediate-born, and early-born HB neurons, a step current stimuli to rostral V2a-VB and V0v-D (slow mode), caudal V2a-Type-I-DL and V2a-Type-I-DM (intermediate mode), and caudal V2a-Type-I-DH (fast mode) were created, respectively. The HB inputs to the MNs were not included to focus on the CPG properties of the spinal cord. In the rest of the document the slow, intermediate and fast mode terms will be used to indicate which cell populations receive the excitatory stimuli.

The amount of stimulus current for each group was determined by testing out a range starting from the rheobase of the target cells up to 10-fold and picking a range that would give the most probable suitable amount. This scale test was referred to frequently in case any change in the model would make another stimulus range more meaningful.

In zebrafish, unilateral activation of the MLR causes bilateral activation in the hindbrain (Carbo-Tano et al., 2022). Similarly, in lampreys, unilateral MLR activation causes bilateral activation in the reticulospinal neurons (Dubuc et al., 2008). In the Xenopus tadpole, it was shown that there is about a 20 ms delay between the left and right reticulospinal inputs that drive locomotion (Buhl et al., 2015). Using this information from various vertebrate models, a bilateral stimulus with a contralateral and rostrocaudal delay was applied to the target cell pools. The contralateral delay was set to 10, 15, and 20 ms for fast, intermediate, and slow swimming. The conduction velocity of the early, intermediate, and late-born HB neurons are 3.5, 1.5, and 0.75 m/s, respectively (Pujala and Koyama, 2019). To mimic the delay that would be generated from the HB projections to the target neurons at different somites, 0.09, 0.2, and 0.4 ms rostrocaudal delays per somite were used for fast, intermediate, and slow swimming, respectively.

3.4.2 Testing the Generated Model

The reduced model has 440 cells and more than 8K projections between these cells. None of the components are completely independent of the rest. Tweaking the model and trying to find the right values for different parameters was quite a challenging task. The behavioural checks were done at every stage of the model change, as listed below. Depending on the test results, various parameters were updated.

The number of parameters that can be tweaked is enormous. At any point, the decision was made to determine which parameter is preferable to modify. For example, if a neuron has too little or too much activity, its Izhikevich parameters were updated to bring the neuron's rheobase to a more desirable value. If one neuron's impact on another neuron was too little or too much, the conductance value was played around with. If the impact of one neuron on multiple cell groups is not as preferred, the neuron's conductance velocity was reviewed.

When these parameters were fine-tuned, the range of allowed values depended on how the value was set in the first place. The parameter was more conservatively tweaked if there was strong literature support behind it. If an approximation was made, as in using the cell sizes to calculate its estimated conduction velocity, there was no hesitation in making more liberal changes.

3.4.2.1 Behavioural checks of the cell groups

The summary of the expected recruitments of different cell pools at different speeds is summarized in Table 3. A visual check was done to see which cellular pools showed firing behaviour whenever a model parameter was updated. For example, when a slow network is active, there should not be any activity in the pMNs. If there is, using the plots provided by the software, the cause was found by going backward from the pMNs to the source input. Below is the checklist that was visually tested to decide whether the generated model can be statistically analyzed.

The pMNs are mostly involved in escape behaviour and during the fastest swimming (Ampatzis et al., 2013; Wen et al., 2020). There is incremental recruitment of sMN as the speed increases (Svara et al., 2018). Therefore, the sMN-s-type should be active at all speeds, whereas the sMN-ms-type and sMN-m-type should be recruited starting at intermediate and fast speeds, respectively.

V2as are active before MNs (Ampatzis et al., 2014). This timing difference was checked by the activity times of these neurons at each somite during the simulation.

V1s show in-phase activity with MNs during swimming (Higashijima et al., 2004a). The firing patterns of sMN-s-type and V1-Slow/Hybrid during slow swim, pMN/sMN-m-type and V1-Fast during fast swim, and sMN-ms-type and V1-Hybrid during intermediate swim were observed to test the in-phase activity.

The late-born slow V1s are active during slow swimming, inhibiting slow swimming circuits to regulate swimming frequency (Kimura and Higashijima, 2019). The early-born V1-Fasts are active during fast swimming and turn off the slow swimming circuits. The V1-Hybrids are active for all swimming speeds (Kimura and Higashijima, 2019). V1-Fast, V1-Hybrid, and V1-Slow activity were tested across different swimming speeds.

3.4.2.2 Output behaviour: MN-based activity/Muscle activity/Tail activity

The proper way to measure the tail beat frequency is to measure the locomotion of the tail tip. However, the formulization of the tail beat is a simplification by itself, excluding certain criteria that could affect the output behaviour, like inertia. Considering the ventral root activity is frequently used to report motor output, referring to MN activity can be a good approximation to determine the tail behaviour (Kawano et al., 2022; Kimura et al., 2013; Menelaou et al., 2014; Satou et al., 2020, 2009; Talpalar et al., 2013; Wilson et al., 2010; Zhang et al., 2011). Therefore, both tail movement and MN activity at each somite were considered when testing the model.

The MN or the muscle at the most caudal somites does not have to show any activity for the tip of the tail to show swimming behaviour due to the contraction in more rostral somites. So, to use MN membrane potential change as an indicator of the ventral root activity, the last somite with relevant MN activity should be considered. Considering the late-born hindbrain V2as projects to the middle of the spinal cord (Pujala and Koyama, 2019), the MNs situated around the middle somites of the body were taken as the representative of spinal cord-generated swimming activity.

3.4.3 Experimental Scenarios

The literature provides information on how larval zebrafish swimming changes when a certain cell group is activated or inhibited by optogenetic stimulation, laser ablation, or chemical treatments. These experimentally observed changes were used to constrain and fine-tune our model.

3.4.3.1 Optogenetic Stimulation

A current stimulus was applied to the target cell populations to imitate optogenetic stimulation. As there is no direct correlation between the light intensity and the current representing that light intensity, various current values were tested to find the most appropriate range.

Test 1a – Optogenetic stimulation of glutamatergic neurons

Based on a study done by optogenetic stimulation of all glutamatergic neurons on the rostral region of the spinalized larval zebrafish, the fish displays different behaviours based on the optic intensity (Wahlstrom-Helgren et al., 2019). At a specific range of light intensity, this behaviour is similar to beat and glide swimming. This optogenetic stimulation was represented in *Sili*Fish as a stimulus applied to all V2a and V0v neurons between the second and fifth somites. Different stimulus amounts were tested to find the right range to imitate similar behaviour observed in the study.

Test 2a – Optogenetic stimulation of V2a neurons

Based on a study done by optogenetic stimulation of all V2a neurons on ½ of the somites, spinalized larval zebrafish display different swim-like behaviour (Eklöf Ljunggren et al., 2014). This optogenetic stimulation was represented in *Sili*Fish as a stimulus applied to all V2a and V0v neurons between the first and fifth somites. Different stimulus amounts were tested to find the right range to imitate similar behaviour observed in the study.

3.4.3.2 Glycine Inhibition

To simulate the experiments where a glycine inhibitor is applied, the connections of the glycinergic neurons were updated. In particular, the synaptic junctions of glycinergic neurons (dI6 and V2b-Gly) were deactivated. When a neuron is both glycinergic and GABAergic (as in V1, V0d, and V2b-Mixed), the synaptic weights were lowered to represent the GABAergic part only. The tau values of those synapses were also updated as glycine receptors have faster decay times than the GABA receptors (Moore and Trussell, 2017).

Test 1b – Glycine inhibition after optogenetic stimulation of glutamatergic neurons

Applying strychnine, a glycine inhibitor, prevents the left and right alternation caused after the optogenetic stimulation (Wahlstrom-Helgren et al., 2019). This scenario was tested in *Sili*Fish, making the changes to represent glycine inhibition.

Test 1b – Glycine inhibition after optogenetic stimulation of glutamatergic neurons

Similar to the above study, applying strychnine prevents the left and right alternation caused after the optogenetic stimulation of only V2as as well (Eklöf Ljunggren et al., 2014). This scenario was also tested in *Sili*Fish, making the changes to represent glycine inhibition.

3.4.3.3 Ablation or Suppression

To imitate the ablation studies, the ablated cell groups were deactivated. For the suppression studies, three different approaches were taken: deactivating the cell groups that are being suppressed, lowering the synaptic conductance values of the cell group's outgoing projections, or applying a negative current to all of the cells in that particular group throughout the simulation duration.

Test 3a – V2b suppression

V2b suppression causes faster swimming (Callahan et al., 2019). This study was replicated by using the three approaches of suppression explained above.

Test 4 – V1 ablation

V1s are shown to be involved in the inhibition of slow INs and slow MNs during fast swimming (Bello-Rojas et al., 2019; Kimura and Higashijima, 2019). Ablation of V1s causes MNs and V2s that are normally active at slow speeds to be active at fast speeds as well (Kimura and Higashijima, 2019). This behaviour was tested by deactivating the V1s and running the model in fast mode, using a stimulus range of 500-900 pA.

3.4.3.4 Activation

For the activation studies, two different approaches were taken: increasing the synaptic conductance values of the cell group's outgoing projections or applying a positive current to all of the cells in that particular group throughout the simulation duration. The amount of current was selected to be slightly above their rheobase values.

Test 3b – V2b activation

V2b activation lowers the swimming frequency (Callahan et al., 2019). This study was replicated by using the two approaches of activation explained above.

Tests that cannot be done with the reduced model

The ablation of V1s prolongs the swimming duration, which is more prominent in fast swimming. As my model implements only the beat part of the beat and glide, not the glide portion, this behaviour cannot be tested with the current model.

The resolution of the reduced model is not enough to test partial ablation studies. For example, a laser ablation study targeted less than 10% of the V0vs in part of the spinal cord

(Kawano et al., 2022). With only one cell in a single somite, this level of testing is beyond the reduced model's capability.

3.5 Troubleshooting

*Sili*Fish provides different types of plots that make detailed data inspection possible. An example is displayed in Figure 10. In this case, there was an irregularity in the bursting behaviour and the left-right alternation of the neurons on a somite that was inspected. Looking into the full dynamics of a single neuron in the V2b-Mixed group, the source was suspected to be from a high activation of V2b-Mixeds by V2a-Type-I-DLs. When the conductance was lowered, and the same simulation was run, the tail movement and the alternation of all the neurons improved.

This example is a case where a simple decision was enough to resolve the issue. In most cases, multiple steps had to be taken, sometimes reversing a previous decision. It was important to test the whole picture after any parameter fitting. Zooming in and out was the main approach during the testing process.

3.6 Statistical Analysis

All statistical analysis was done with IBM SPSS Version 29.0 (IBM Corp., 2023)

All values indicated as ± represent the standard deviation of the mean. Medians and interquartile ranges (IQR) are reported as [Median] (IQR [1st quartile]- [3rd quartile]), such as 25 (IQR 20-27). Outliers are the values greater than the third quartile + 1.5 * IQR and smaller than the first quartile – 1.5 * IQR and are displayed as a circle on the boxplots. Extreme outliers are the values greater than the third quartile + 3 * IQR and smaller than the first quartile – 3 * IQR and are displayed as an asterisk on the boxplots.

The data did not show normality, so the Kruskal Wallis non-parametric test was used for comparisons.

A

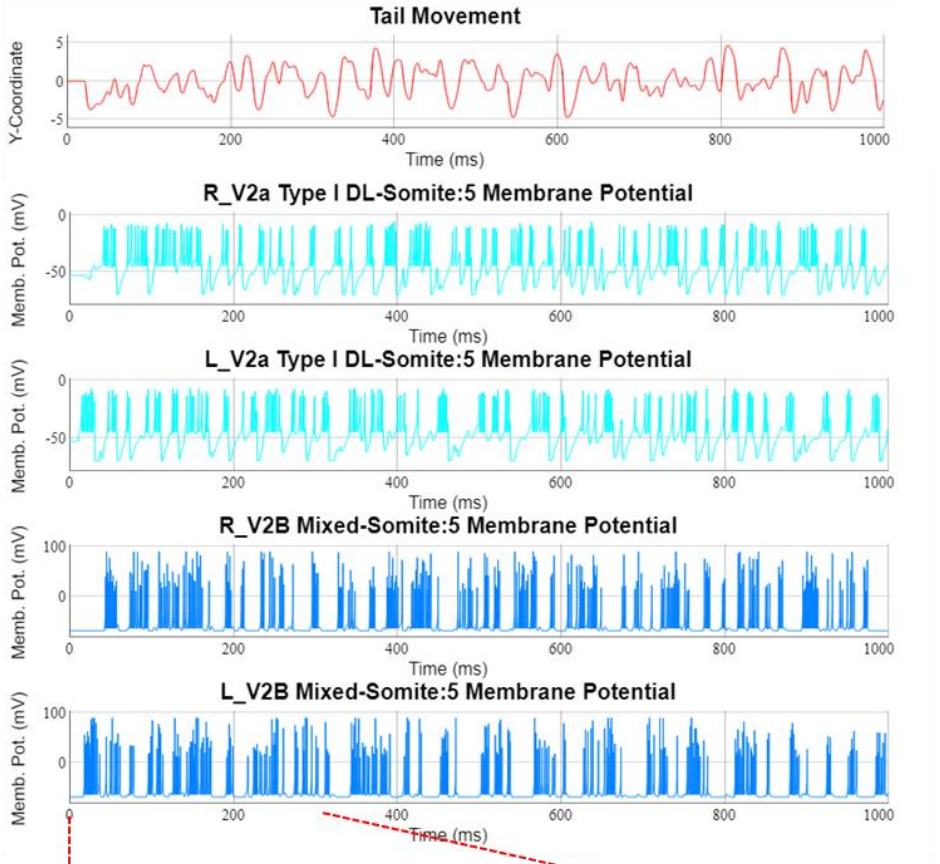

B

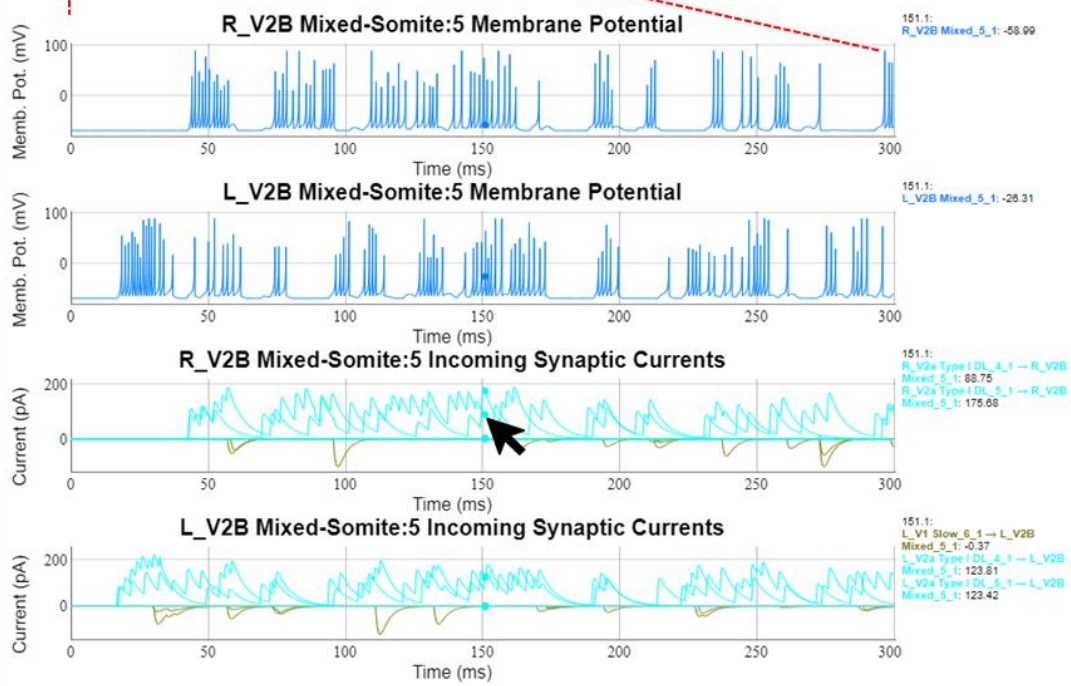

(Figure continues the next page)

C

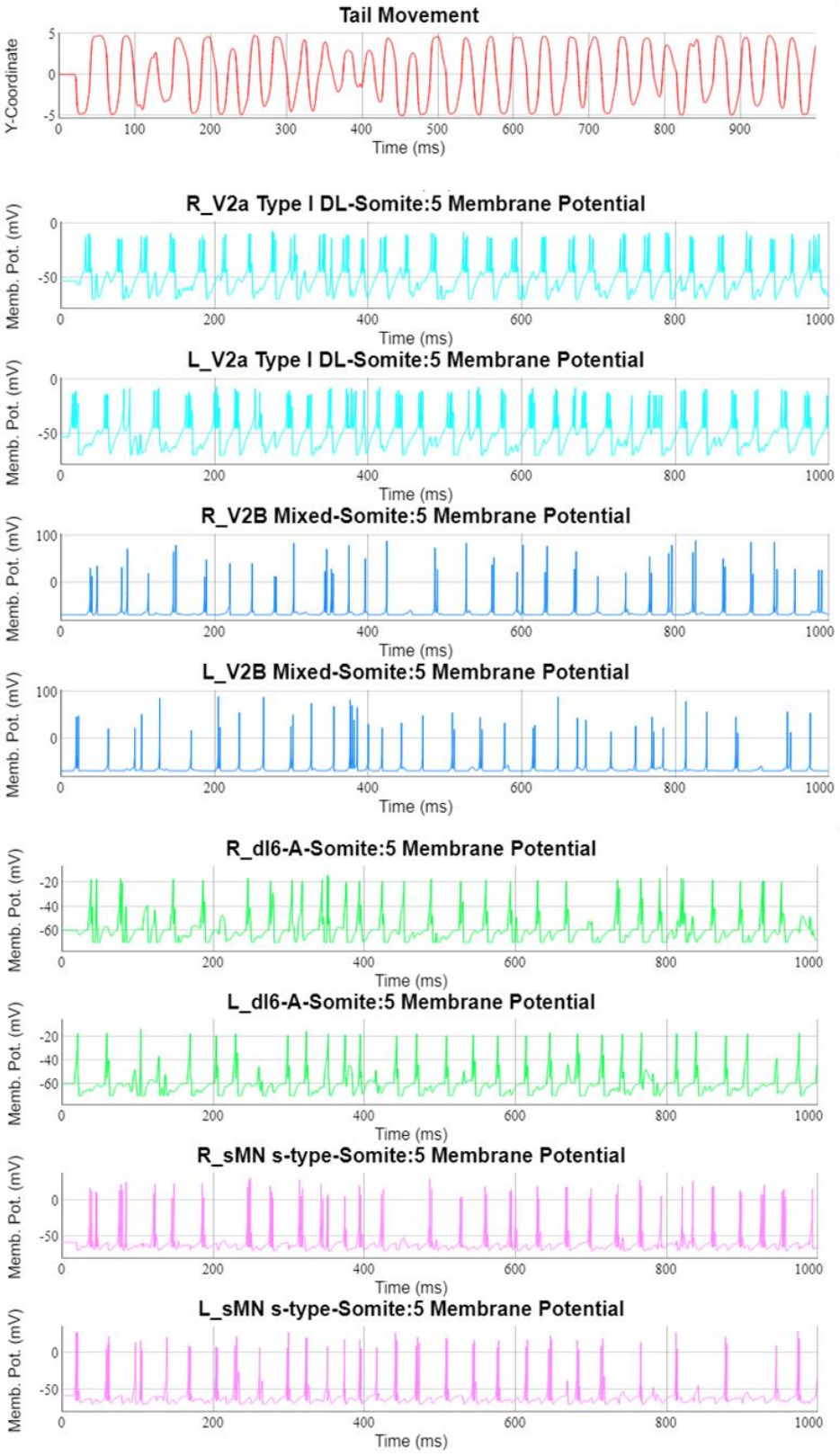

(Figure legend on the next page)

Figure 10. The *Sili*Fish features can help in troubleshooting.

(A) The tail movement shows some irregularity. When the activity of two neurons in the fifth somite was observed on both sides of the spinal cord—V2a-Type-I-DL and V2b-Mixed—no clear left-right alternation was observed. (B) Plotting the full dynamics of V2b-Mixed on the fifth right somite and zooming in to the first 300 ms of the activity shows all the synaptic currents it receives. It was observed that there is high activation of V2b-Mixed by the V2a-Type-I-DLs. Moving the pointer over the plot shows all the values on that time point as a list on the right-hand side of the plot. (C) After running the same simulation after changing V2a-Type-I-DL to V2b-Mixed conductance from 0.5 to 0.2 nS, a much cleaner tail movement and left and right alternation of the neuronal activity was observed. The activity of the four neurons on the fifth somite for the whole period plotted in (A) is displayed.

Chapter 4. Results

4.1 The Network

The reduced model is composed of 22 cell types, 440 cells, and around 8K projections. The 2D and 3D renderings of the model are displayed in Figure 11 & Figure 12. The full model initially generated had the same 2D rendering as the cellular populations did not change; however, the 3D rendering was overly complicated to understand and excessively resource-intensive to generate.

Two main parameter sets were the subject of fitting when generating the swimming networks: the Izhikevich parameters that define the intrinsic properties of the cells and the conductance values of the gap junctions and chemical synapses. The Izhikevich parameters of each cell population are listed in Table 17. The Izhikevich parameter fitting was done using GA and manually updated based on the test results. Conductance values of the gap junctions and chemical synapses are listed in Supplementary Tables S1-S5.

Table 17. Parameters of each cell population that define their intrinsic properties.

The rheobase values are calculated using the Izhikevich parameters (columns *a* to V_t) determined by GA. CV: Conduction Velocity.

Cell Group	CV (m/s)	Rheobase (pA)	*a*	*b*	*C* (mV)	C_m (pF)	*d*	*k*	V_{max} (mV)	V_r (mV)	V_t (mV)
dI6-A	0.5	53.54	0.18	0.56	-55	6.41	-8.43	0.3	-20	-60	-35
dI6-B	0.5	51.71	0.01	2.02	-65	5.25	10	0.31	-10	-70	-45
pMN	4.7	265.69	0.03	1.87	-78	68.11	-3.98	0.55	8.5	-77	-35.6
sMN-m-type	2.3	101.15	0.01	-5.69	-69.02	19.36	2.55	0.92	20	-55.5	-29.16
sMN-ms-type	1.9	67.37	0.02	2.43	-55	11.85	10	0.3	10	-75.7	-48
sMN-s-type	1.3	29.34	1.85	-7.088	-65.01	8.25	6.28	0.83	2	-58.7	-38.27
V0d	0.5	33.75	0.01	1	-46	6	10	0.91	10	-54	-42
V0v-A	0.5	23.65	0.56	2.9	-38	5.58	-10	0.69	27	-41	-33
V0v-B	0.5	14.85	8.53	1.04	-40	8.12	3.6	0.89	9	-41	-34
V0v-D	0.5	11.07	0.38	1.51	-38	3.75	10	0.47	27	-40	-33
V1-Fast	0.4	229.67	0.01	1.28	-69.1	5.87	10	0.67	-28.6	-82.1	-45.3
V1-Hybrid	0.4	63.75	0.12	1.12	-61.9	6.33	4	0.2	-31.1	-77.9	-46
V1-Slow	0.4	8.46	0.71	-1.69	-61.8	3.75	10	0.16	-20.9	-70.9	-45.8
V2a-Type-I-DH	0.2	190.27	0.55	0.7	-44.64	4.65	-3.45	0.8	8	-55	-25
V2a-Type-I-DL	0.2	12.19	0.2	-0.66	-45.01	2.85	10	0.24	-15	-53	-36
V2a-Type-I-DM	0.2	59.24	10	1.28	-45.01	4.65	-10	0.22	20	-50	-23
V2a-Type-II-D	0.5	155.72	0.02	4.62	-62	6.3	10	0.7	12	-70	-41
V2a-VB	1.2	19.92	0.162	0.483	-55	2.85	20	0.16	-10	-60	-40
V2b-Gly		64.00	1	3	-65	10	10	1	10	-70	-57
V2b-Mixed		43.40	0.04	0.36	-65	6	10	1	10	-70	-57

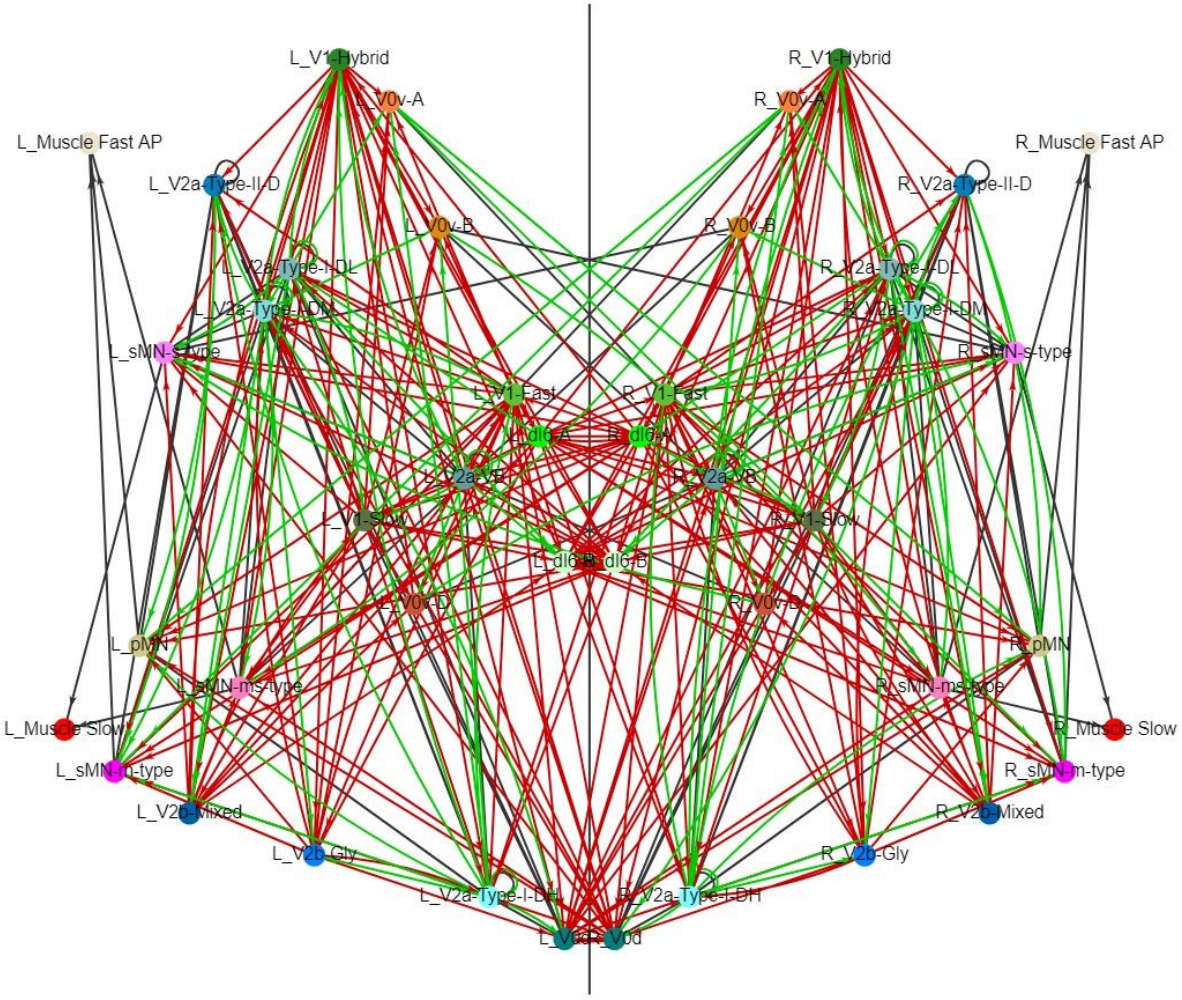

Figure 11. The 2D-rendering of the reduced model shows the cellular groups and how they are connected.

The colour of the nodes is defined by the user. The black, red, and green arrows represent electrical, inhibitory, and excitatory projections. The positioning of the nodes does not represent the actual spatial positioning, as a single node can represent one or many cells.

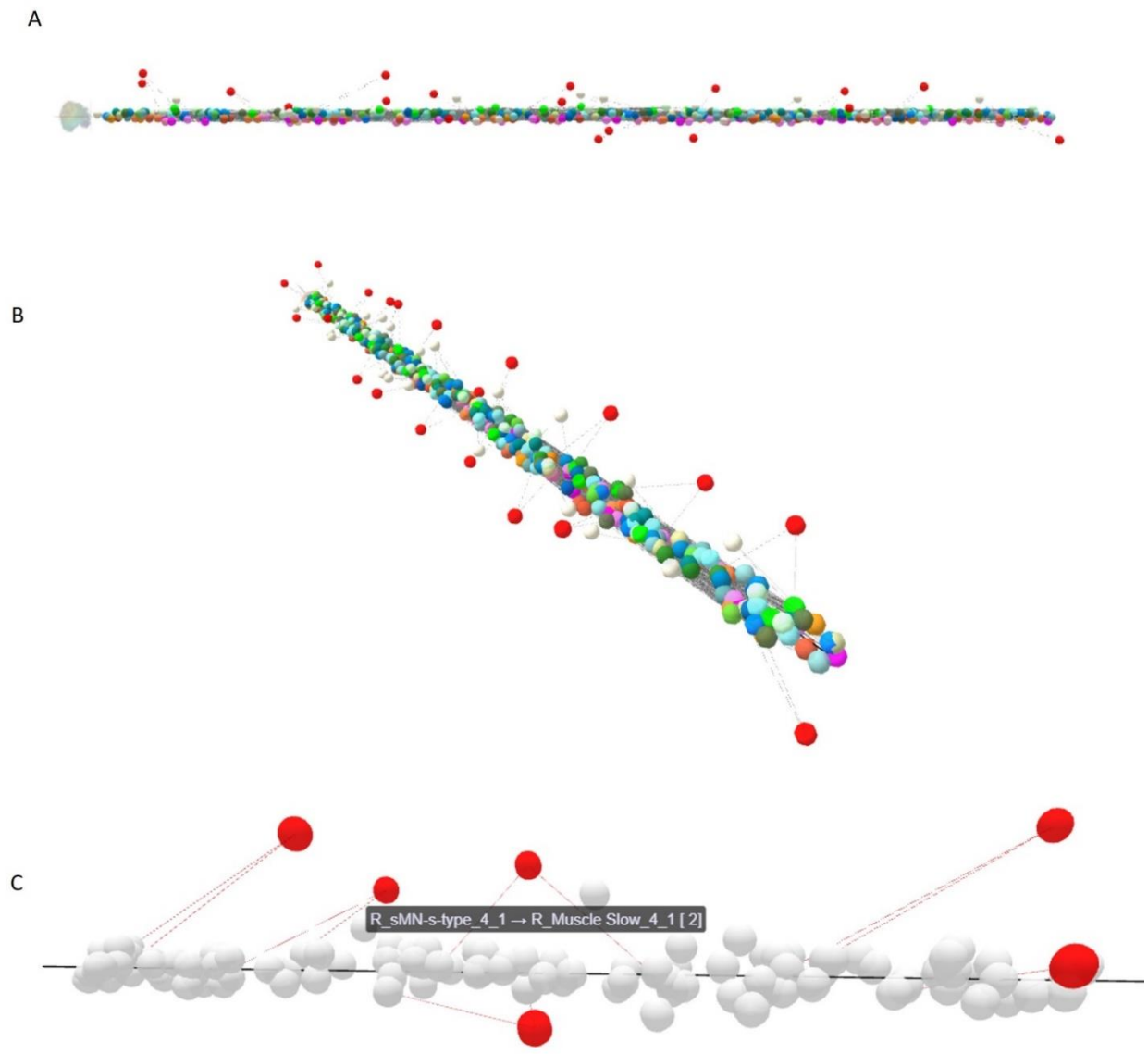

Figure 12. The 3D-Rendering of the reduced model shows the individual cells and how they are connected.

(A) Each node represents a single cell. The spatial positioning is the actual coordinates in the model. (B) The rendering is user-interactive and allows rotations in all directions and zooming. (C) Various features were implemented to simplify the outputs to a more digestible format, like displaying only a selection of somites, a single cell pool, and hiding projections with electrical or chemical synapses.

The simulations were run in two basic modes for two different goals: “Model Generation and Testing” and “Statistical Analysis.” Model generation and testing were done with various stimuli levels and shorter simulation durations. Statistical analyses were done with a single stimulus level and longer simulation durations. This section presents the results of the modes listed in Table 18. A consecutive step current stimulus of 500 ms, which will be called an episode, with 300 ms breaks in between, was applied for each mode. The stimuli's target and the current amount dictated the modes. The intermediate mode of statistical analyses was split into three simulations due to many cell groups with very different intrinsic properties expected to be activated. In addition, a cap was applied to the V2a-Type-I-DL input current stimulus due to its low rheobase.

Table 18. The test modes with the amount and target of current stimuli applied.

	Mode	**# of episodes**	**Target cell population**	**Current amount (pA)**
Model Generation and Testing	Slow-Scale	5	V0v-D, V2a-VB	21 – 30
	Intermediate-Scale	5	V2a-Type-I-DL V2a-Type-I-DM	50 – 150 50 – 450
	Fast-Scale	5	V2a-Type-I-DH	500 – 900
Statistical Analysis	Slow	20	V0v-D, V2a-VB	23
	Inter-I	20	V2a-Type-I-DL V2a-Type-I-DM	50 50
	Inter-II	20	V2a-Type-I-DL V2a-Type-I-DM	100 100
	Inter-III	20	V2a-Type-I-DL V2a-Type-I-DM	150 450
	Fast	20	V2a-Type-I-DH	1000

The data analysis was done after pooling all five simulations listed under Statistical Analysis. There was a clear change in the spike count and frequency for all cell populations across the three swim modes (Figure 13 & S1). As the number of cell groups and wide range of spike count and frequency values make it hard to understand these plots, the spike frequency plots for slow, intermediate, and fast swim modes are drawn separately for clarity in the individual network’s results section (Figures 19, 24, and 30).

Rather than individual spike frequencies for each cell for the three swim modes simulated, the average spiking frequency for each cell group was plotted against the actual TBF measured (Figure 14B). Across all three swim modes, the TBF ranged between 20.70-65.16 Hz (37.73 ± 12.51 Hz). These ranges were 20.70-23.52 Hz (22.14 ± 0.96 Hz), 24.42-42.71 Hz (35.01 ± 4.79 Hz), and 53.69-65.16 Hz (58.34 ± 3.03 Hz) for slow, intermediate, and fast modes, respectively.

The TBF range of intermediate mode was very close to slow mode frequencies (Figure 14A). Below, these three modes will be analyzed separately as representative of the slow, intermediate, and fast networks.

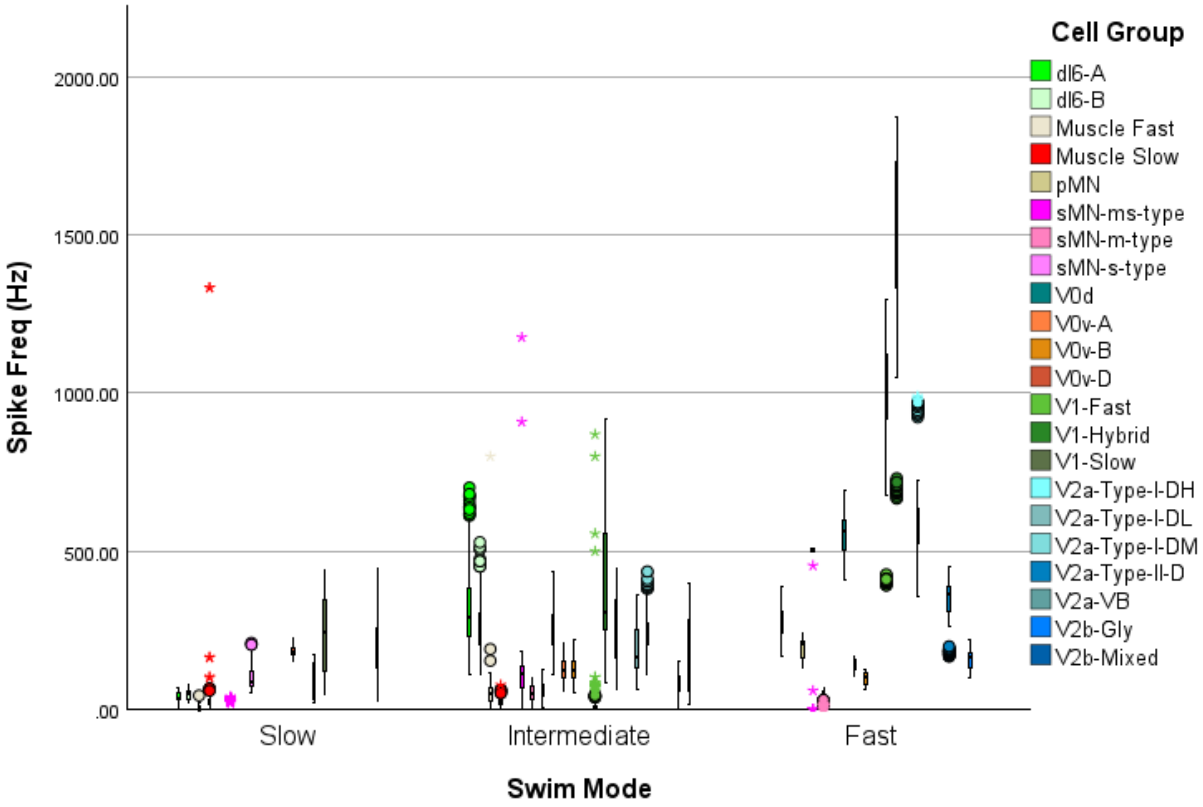

Figure 13. Activation of cell groups differs across the swimming modes.

The distributions of the spiking frequencies of each cell group in slow, intermediate, and fast swim modes are shown. The boxes show the median and 25-75 IQR. Circles and asterisks are outliers and extreme outliers. N = 20 for each swim mode.

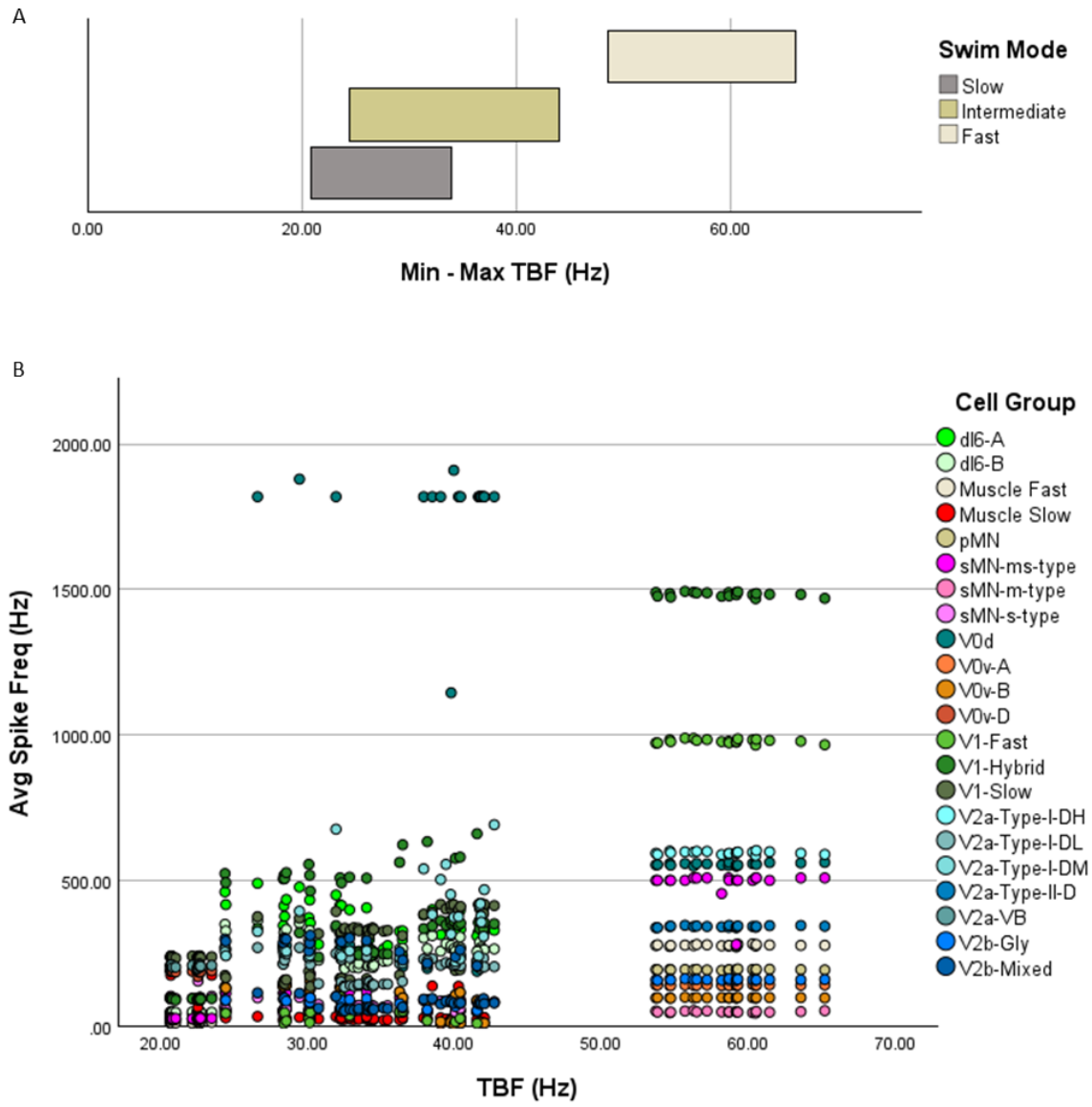

Figure 14. The range of TBFs for each swim mode, and the average spike frequencies of each cell group across the TBF measured are shown.

(A) The TBF ranges observed during the slow, intermediate, and fast modes. Both model generation and statistical analysis run results are included (Table 18). N = 21 for slow and fast modes; N = 61 for intermediate modes. (B) Cell groups showed an increased spiking frequency as the TBF increased. Their spiking pattern shows greater consistency for faster TBF greater than ~55 Hz. Two records of V0d with spike frequency > 3 kHz were removed from the plot to increase clarity. Only statistical analysis simulation results are included. N=100.

4.2 Slow Network

The cell populations that were active during the slow mode are shown in Figure 15. A series of 500 ms step stimuli (episodes) with 300 ms breaks in between were applied to excitatory V2a-VBs and V0v-Ds (Figure 16A, Table 18-Model Generation and Testing). The individual steps ranged between 21-30 pA, had 0.4 ms rostrocaudal delay, and a delay of 20 ms between left and right. A TBF range of 23.46-33.92 Hz was observed (Figure 16B).

The subset of active cell populations aligned with what the literature supports (Table 3, Figure 15). The wide range of activity was due to different cells on different somites having different activity levels (Figures S2-S9). Among the excitatory neurons, V0v-Ds and V2as activity per episode of 500 ms stimulation had an average of 87.52 ± 7.86 and 94.34 ± 58.47 spikes (Figure S10). V1-Slow and V1-Hybrid had higher activity levels than dI6-A and dI6-B inhibitory neurons (111.04 ± 62.13 and 42.59 ± 24.44 versus 17.65 ± 8.29 and 21.54 ± 8.14 spikes/episode) (Figure S12). Only sMN-s-type MNs showed spiking activity (Figure 17 & Figure 18).

Despite the stimulus not having a rhythmic property, rhythmic activity was observed across all of the cell populations, which generated the tail-beating behaviour (Figure 16B, S10-S13). The spiking activity of all cell groups is displayed in Figure 19. The left and right alternation of each cell group was visible (Figure 17, S11, and S13).

For further analysis, a series of twenty current step stimuli with 300 ms breaks in between were applied to excitatory V2a-VBs and V0v-Ds (Table 18-Statistical Analysis).

The most active MN group was sMN-s-type, with 88.69 Hz (IQR 72.21-121.94 Hz) spiking frequency (Figure 19A). The only other active MN group was sMN-ms-type, with 24.43 Hz (IQR 24.35-24.66 Hz) spiking frequency. Slow muscle activity was 22.06 Hz (IQR 16.66-39.59 Hz).

Despite this network generating TBFs in the slow swimming range, some random activities of fast muscle cells were also observed, with a maximum of five spikes for 500 ms episode (Figure 19B).

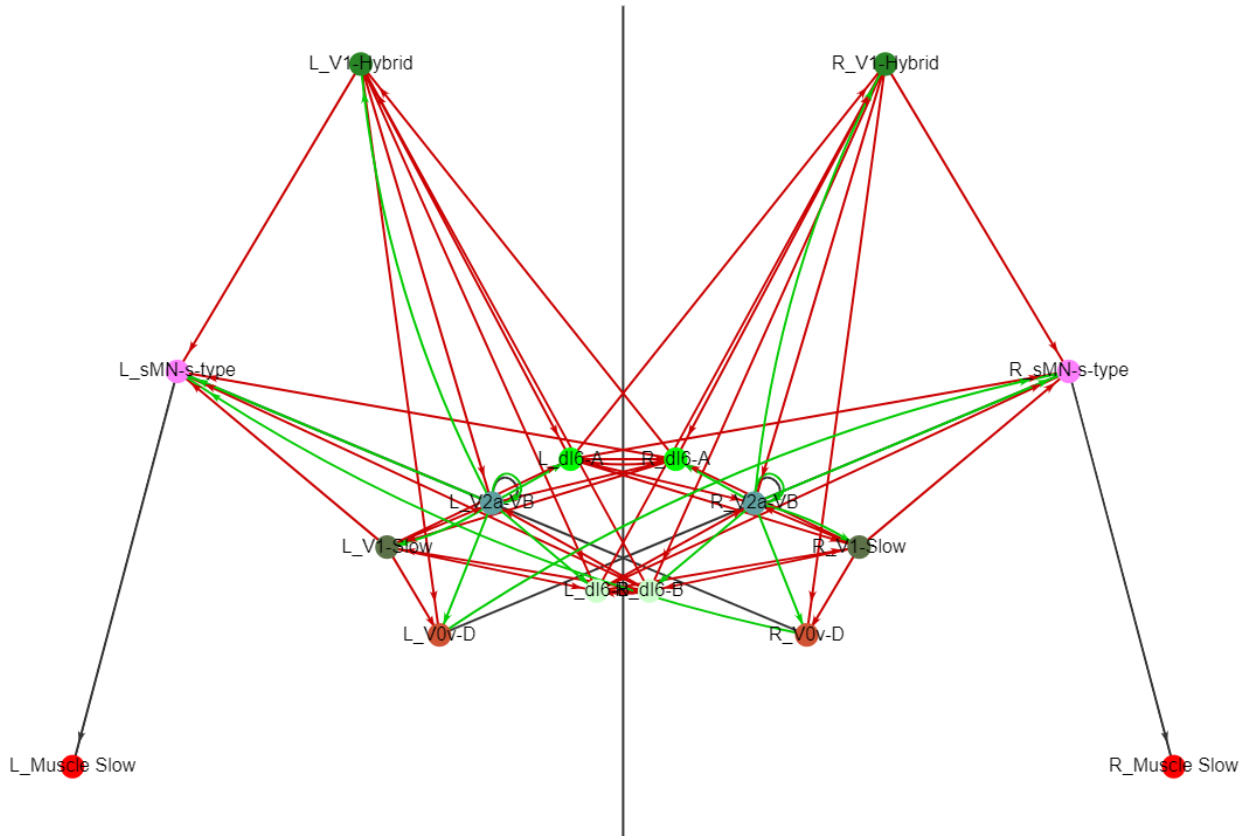

Figure 15. 2D-rendering of the cell populations forming the slow network.

Only spiking cellular populations are included in this figure. Slow muscle cells do not have spiking capacity but are included as they show activity. Despite the presence of other cellular populations (Muscle Fast AP, pMN, sMN-m-type/ms-type, V0d, V1-Fast, V0v-A/B, V2a-Type-I-DH/DM/DL, V2a-Type-II-D, V2b-Gly/Mixed), they are not activated enough to generate a spike.

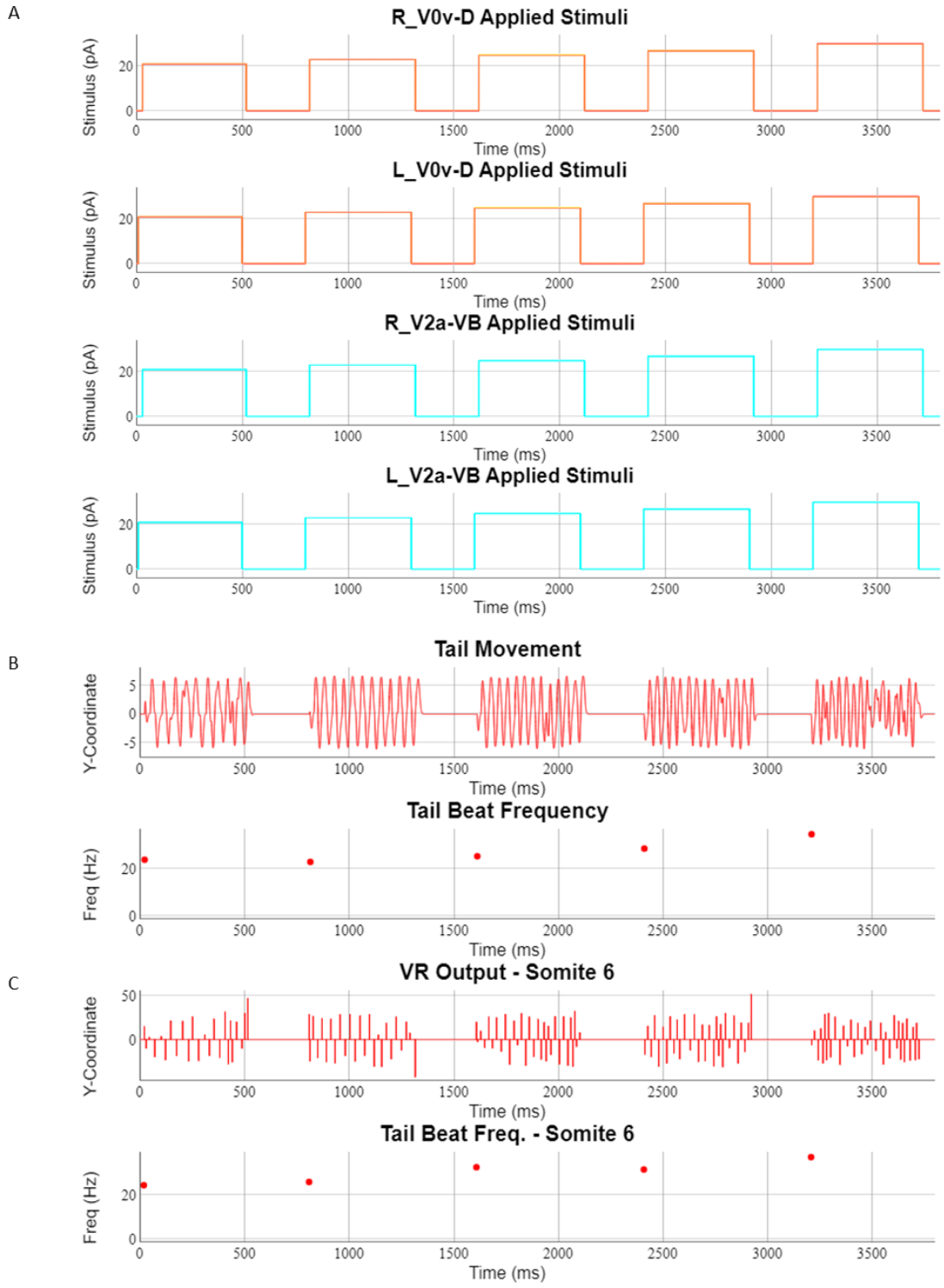

Figure 16. Current stimulus to V0v-Ds and V2a-VBs generate 23-34 Hz TBF.

(A) A stimulus consisting of rectangular pulses ranging from 21 to 30 pA was applied to the rostral V0v-D and V2a-VB populations. (B) The TBF was measured as the movement of the tip of the tail (23.52, 22.6, 24.95, 28.15, 34.12 Hz). (C) The TBF was measured by the sum of left and right MN activity at somite six, representing the middle section of the spinal cord (24.15, 25.61, 32.18, 31.15, 36.69 Hz).

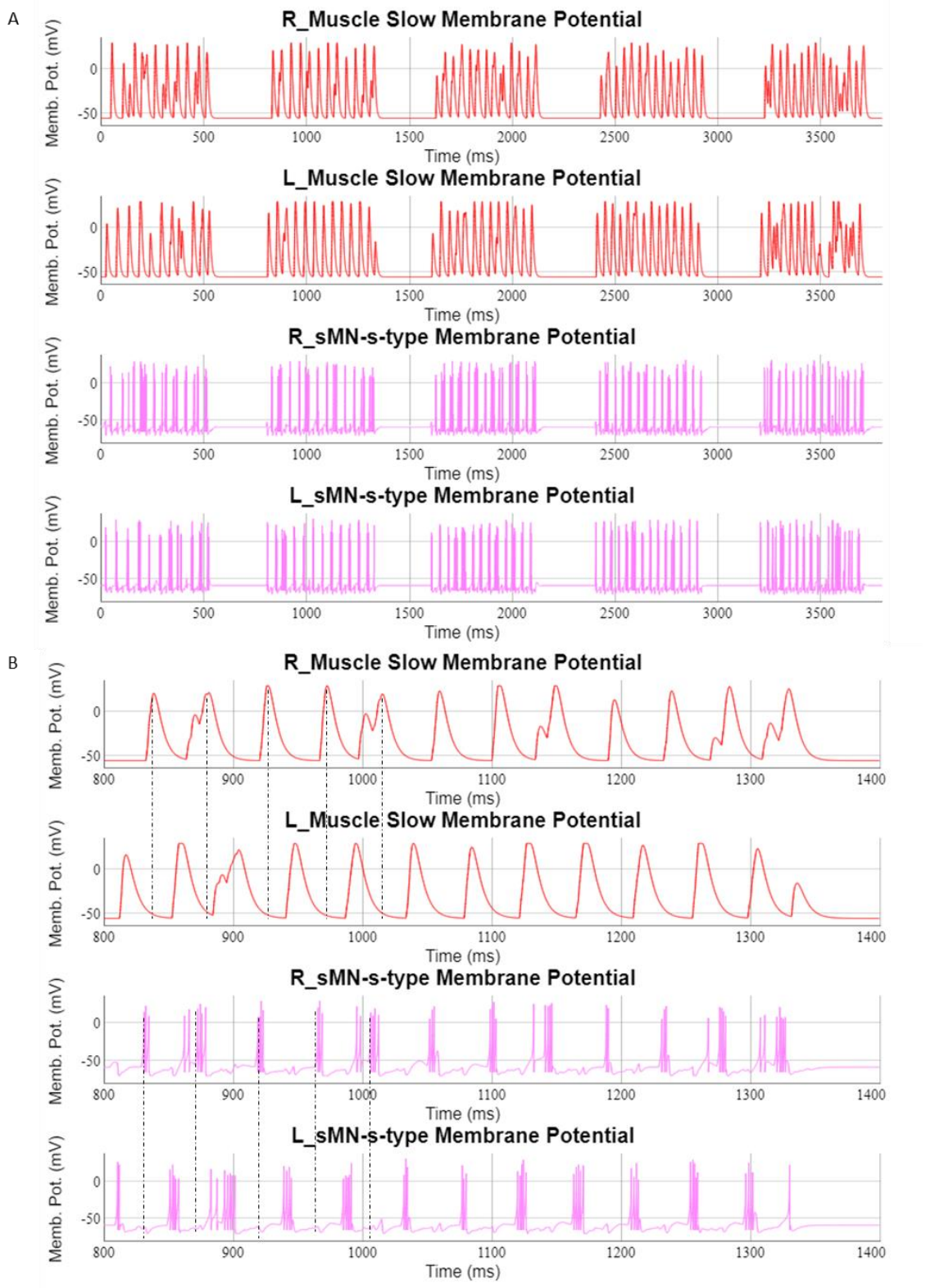

Figure 17. The muscle cell and motoneuron activity display left-right alternation.

(A) Slow muscle cells and sMN-s-type MNs displayed activity. The cells on the third somite are shown. (B) Zoomed-in activity for both cells to show the left and right alternation. Dashed lines are added to denote the peak of the cell activity on the right side of the spinal cord.

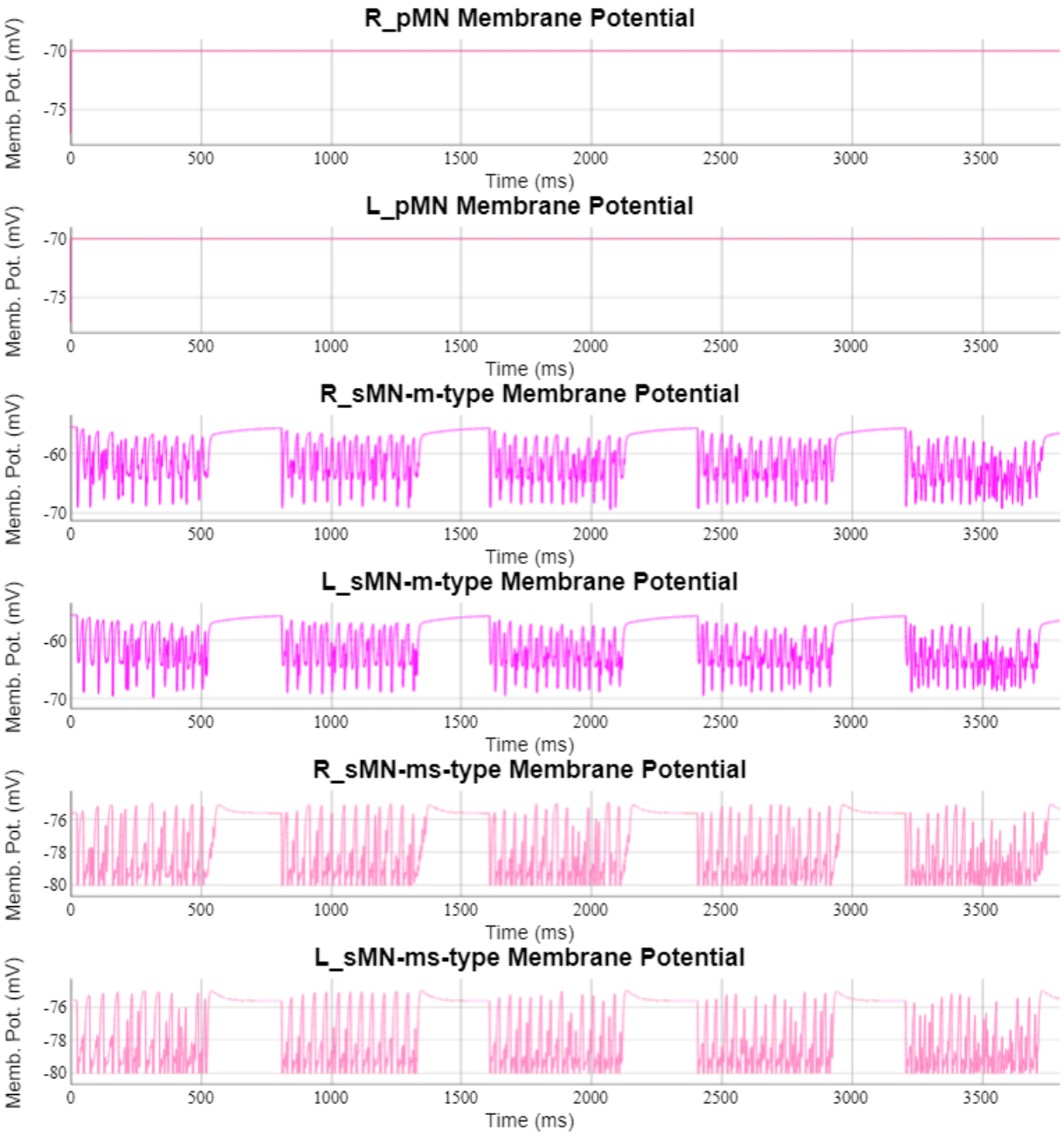

Figure 18. pMNs and sMNs that have projections to fast muscle cells are not active in slow mode.

All three groups of MNs on somite six show slight, mostly inhibitory, changes in their membrane potentials. The y-axis scale is zoomed in to the voltage change of each cell.

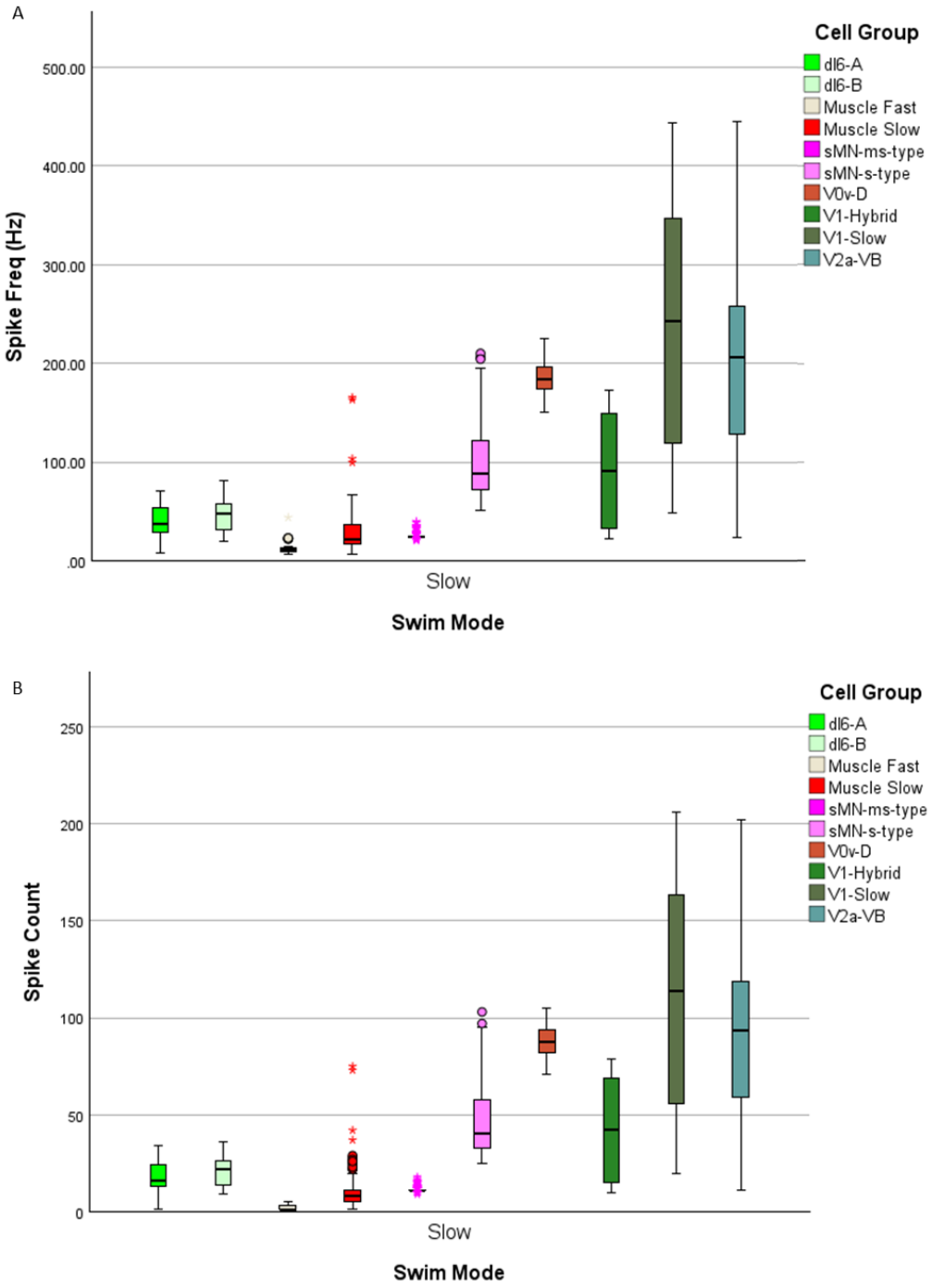

Figure 19. The distribution of spike frequencies and counts for each cell pool during slow mode.

(A) Zoomed in version of Figure 13. Only cells with spikes are plotted. As activity from every somite is plotted, there is a wide range of activity within each group. The boxes show the median and 25-75% IQR. Circles are outliers; asterisks are extreme outliers. One extreme outlier N = 20. dI6-A: 37.49 (IQR 29.02-53.14); dI6-B: 48.1 (IQR 27.86-58.63); Muscle Fast: 11.06 (IQR 8.78-13.56); Muscle Slow: 22.06 (IQR 16.66-39.59); sMN-ms-type: 24.43 (IQR 24.35-24.66); sMN-s-type: 88.69 (IQR 72.21-121.94); V0v-D: 183.24 (IQR 174.47-196.78); V1-Hybrid: 90.83 (IQR 33.21-149.05); V1-Slow: 242.98 (IQR 88.64-364.98); 205.86 (IQR 128.71-257.19); (B) Spike counts of the same cellular groups in the swim mode. Despite the similarity to the spike frequency plot, the spike count plot is presented to show the low number of fast muscle cell activity.

4.3 Intermediate Network

The cell populations that were active during the intermediate mode are shown in Figure 20.

For the initial analyses listed below, a series of 500 ms step stimuli with 300 ms breaks in between were applied to excitatory V2a-Type-I-DLs and V2a-Type-I-DMs (Figure 21, Table 18-Model Generation and Testing). The individual steps ranged between 50-150 pA for V2a-Type-I-DLs and 50-450 pA for V2a-Type-I-DMs. The input of V2a-Type-I-DLs was capped at 150 pA because, at higher levels, they were showing tonic activity and causing unstable behaviour. All the stimuli had 0.2 ms rostrocaudal delay and a delay of 15 ms between left and right. A TBF range of 35.47-43.98 Hz was observed (Figure 22).

Despite the stimulus not having a rhythmic property, rhythmic activity was observed across all of the cell populations, which generated the tail-beating behaviour (Figure 23, S14-19). The level of activity was not homogeneous across different stimulus amounts. As the current increased, new neuronal populations—sMN-ms-type and sMN-m-type MNs (Figure S15), V0vs (Figure S16), V0ds (Figure S17), and V2b-Glys (not shown)—started to show spiking activity. All other cell populations were active throughout the testing period (Figures S14-S15, S17-S18).

For the rest of the analysis, a train of 500 ms step current stimuli with 300 ms breaks in between was applied. The amounts of currents are listed in Table 18 (Statistical Analysis). There was spiking activity across all cell populations at various levels (Figure 24). Some neuronal populations displayed high levels of variability, like V1-Hybrids (Figures 24, S18). This variability was due to the intermediate test having a large range of stimulus amounts. The distributions of spike activities for three different intermediate modes are displayed in Figure S20.

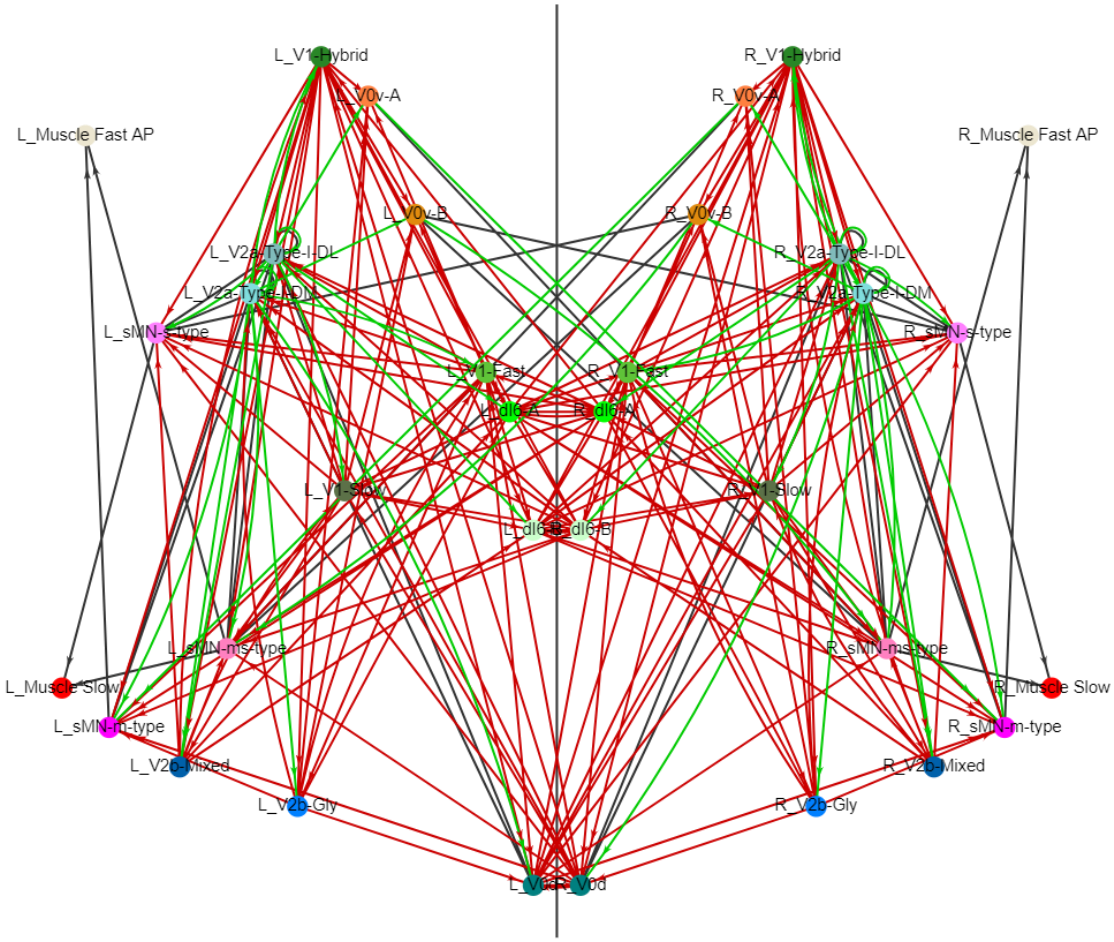

Figure 20. 2D-rendering of the cell populations forming the intermediate network.

The majority of the cell populations were part of the intermediate network.

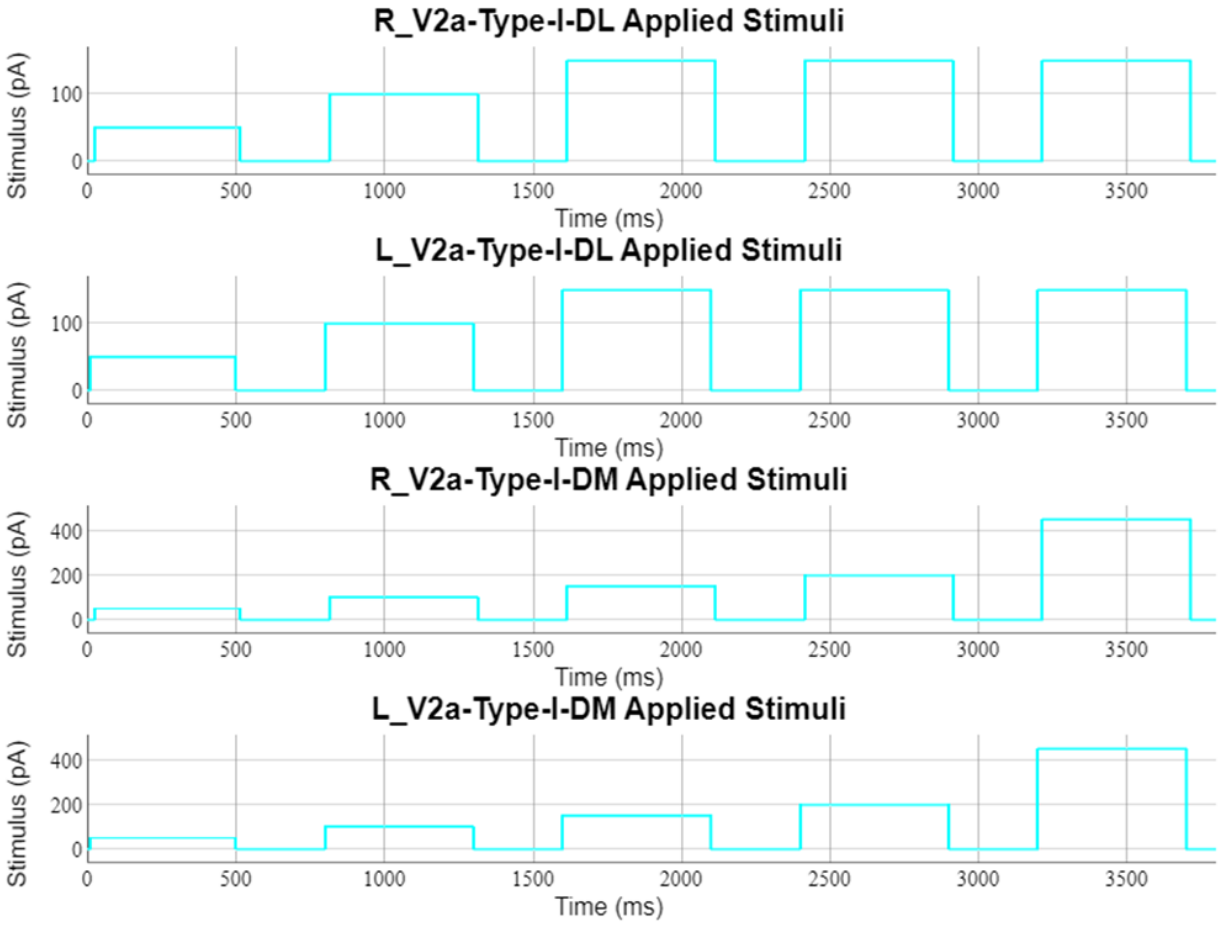

Figure 21. Stimuli applied during intermediate swimming.

An increasing amount of 500 ms current step stimuli were applied with 300 ms breaks in between. V2a-Type-I-DL received between 50-150 pA, whereas V2a-Type-I-DM received between 50-450 pA current stimuli.

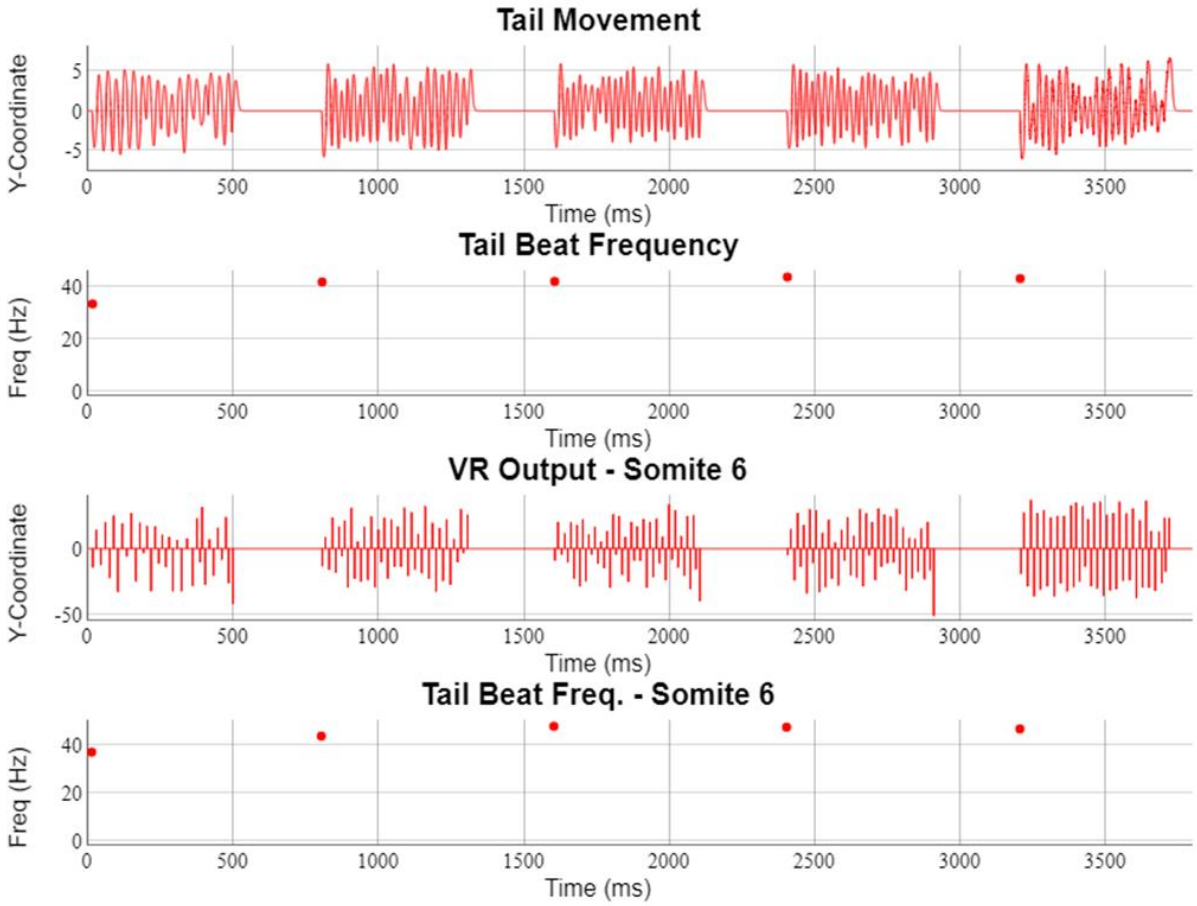

Figure 22. Tail movement and summarized MN activity of the sixth somite during the intermediate mode.

The TBFs observed by the tip of the tail are 33.66, 42.06, 42.28, 43.97, and 43.37 Hz. The frequency of left and right MN populations' peak activity is 37.09, 43.75, 47.82, 47.44, and 46.71 Hz.

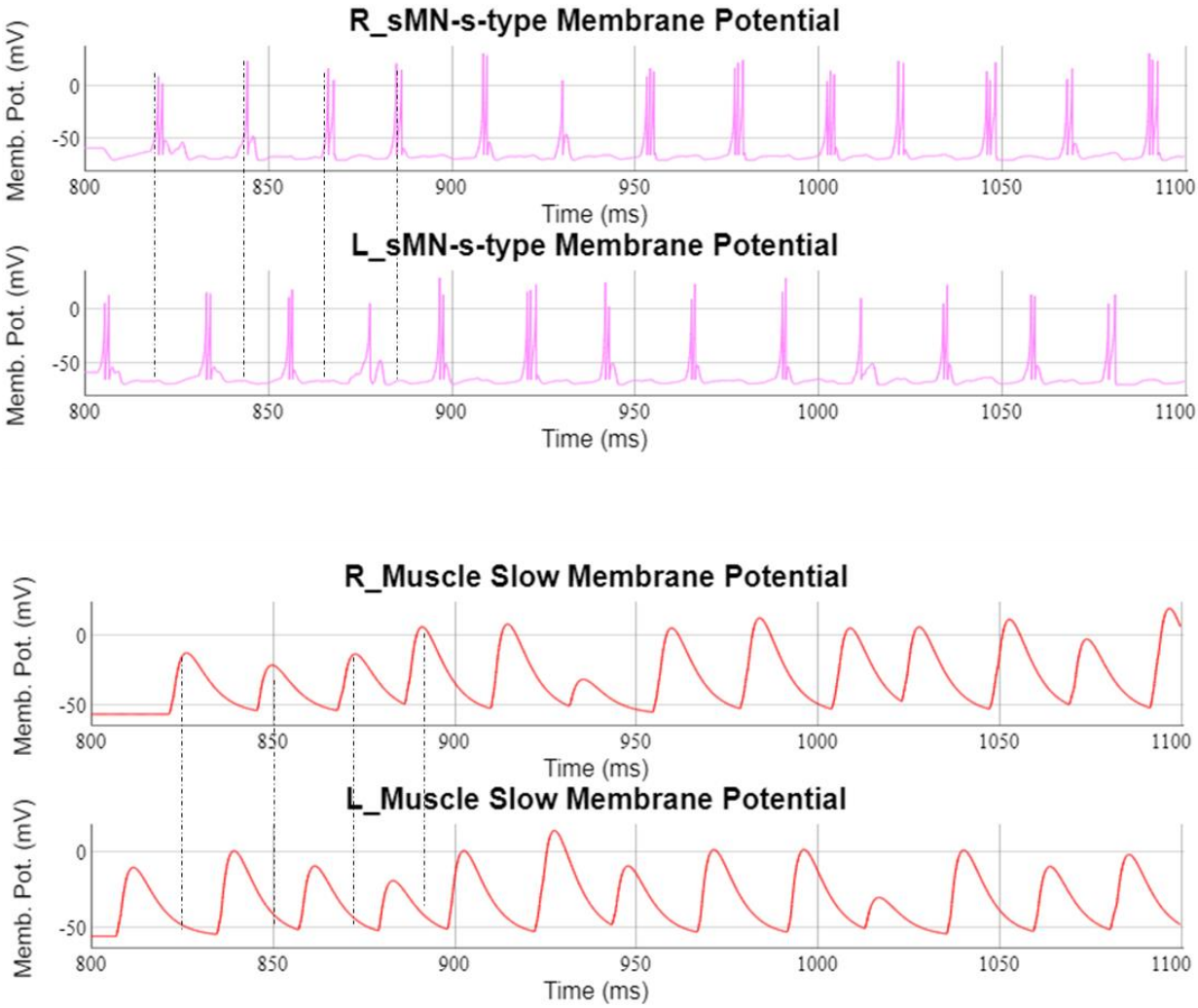

Figure 23. Left and right alternation was observed across all cell groups in the intermediate mode.

The zoomed-in activity of left and right sMN-s-type neurons and slow muscle cells on somite six shows clear left and right alternation.

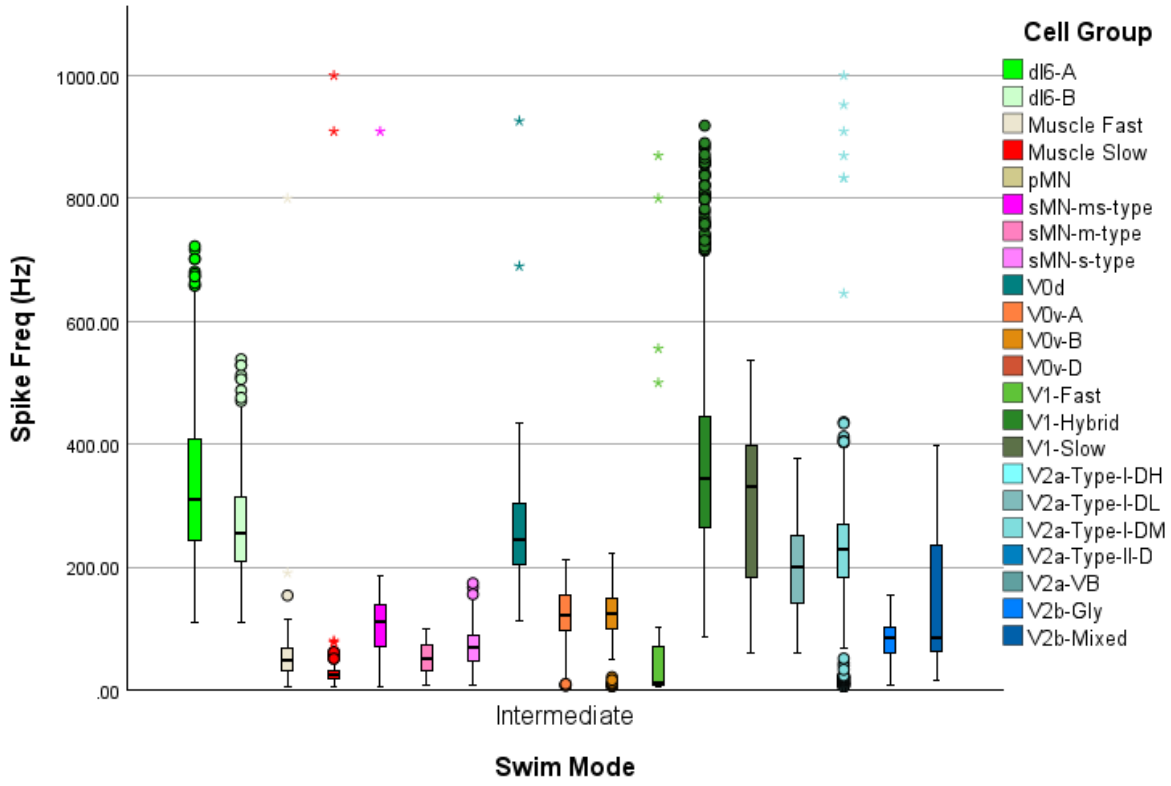

Figure 24. Spike frequency distribution of all the cells when the model was tested in the intermediate mode.

The zoomed-in version of Figure 13. As activity from every somite is plotted, there is a wide range of activity within each group. The boxes show the median and 25-75% IQR. Circles and asterisks are outliers and extreme outliers. Extreme outliers over 1000 Hz are removed for clarity. N = 20.

4.4 Fast Network

The cell populations that were active during the intermediate mode are shown in Figure 25.

For the initial analyses listed below, a series of 500 ms step stimuli with 300 ms breaks in between were applied to excitatory V2a-Type-I-DHs (Figure 26, Table 18-Model Generation and Testing). The individual steps ranged between 500-900 pA. All the stimuli had 0.09 ms rostrocaudal delay and a delay of 10 ms between left and right. A TBF range of 48.51-66.01 Hz was observed (Figure 26).

Despite the stimulus not having a rhythmic property, rhythmic activity was observed across all of the cell populations, which generated the tail-beating behaviour (Figure 26). The level of left and right alternation was not as clear as in slow and intermediate modes (Figures 27, 29, and S21). In general, it required a longer time for the left and right alternation to stabilize (Figure 29).

For the rest of the analysis, a train of 500 ms step current stimuli with 1000 pA amplitude with 300 ms breaks in between was applied (Table 18-Statistical Analysis). The distribution of the spiking activity across different call groups is displayed in Figure 30. Interestingly, the activity of V1-Hybrids was much higher than any other cell population's activity (Figure 30.)

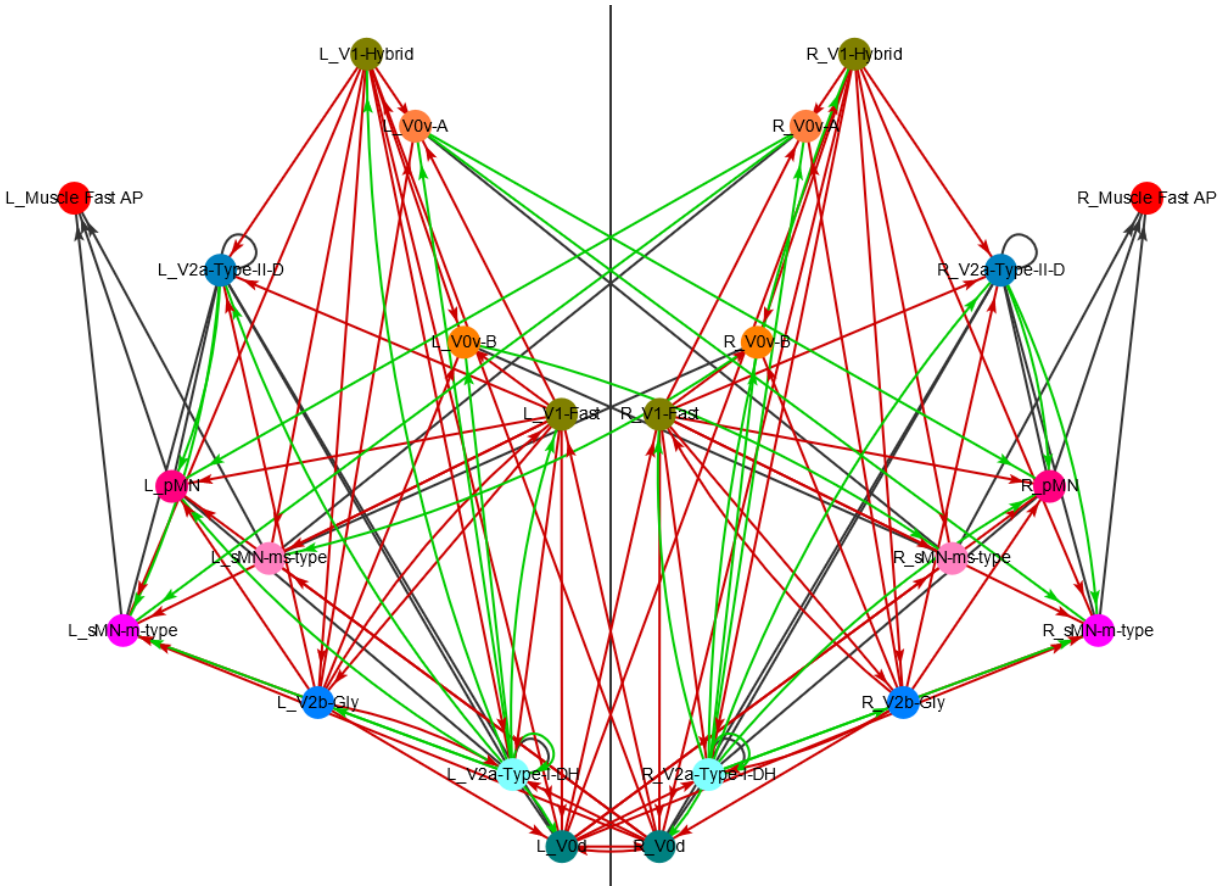

Figure 25. 2D-rendering of the cell populations forming the fast network.

There is no spiking activity observed in dI6s, slow muscle cells, V0v-Ds, V1-Slows, V2a-VBs, V2a-Type-I-DL/DMs, sMN-s-type MNs, and V2b-Mixeds despite their presence and functionality in the network.

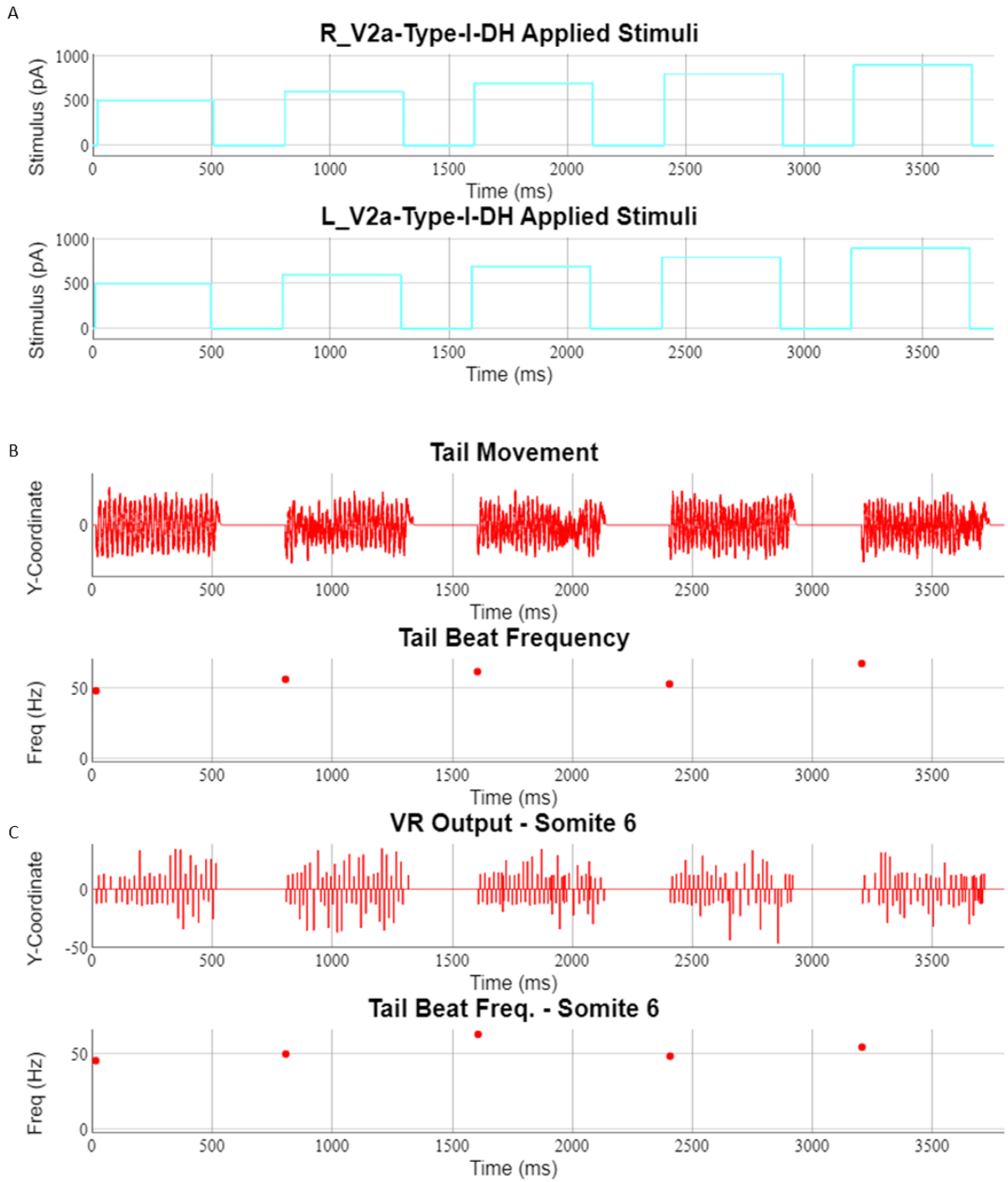

Figure 26. The stimulus applied and the behaviour observed during the fast mode testing.

(A) An increasing amount of 500 ms current step stimuli, ranging between 500-900 pA, were applied with 300 ms breaks in between. (B) Tail beat behaviour, and (C) the alternating MN activity on somite six was observed. TBF of the tail movement: 48.51, 56.67, 62.12, 53.35, and 67.9 Hz. TBF based on MN activity: 44.54, 49.93, 62.92, 48.52, and 54.57 Hz.

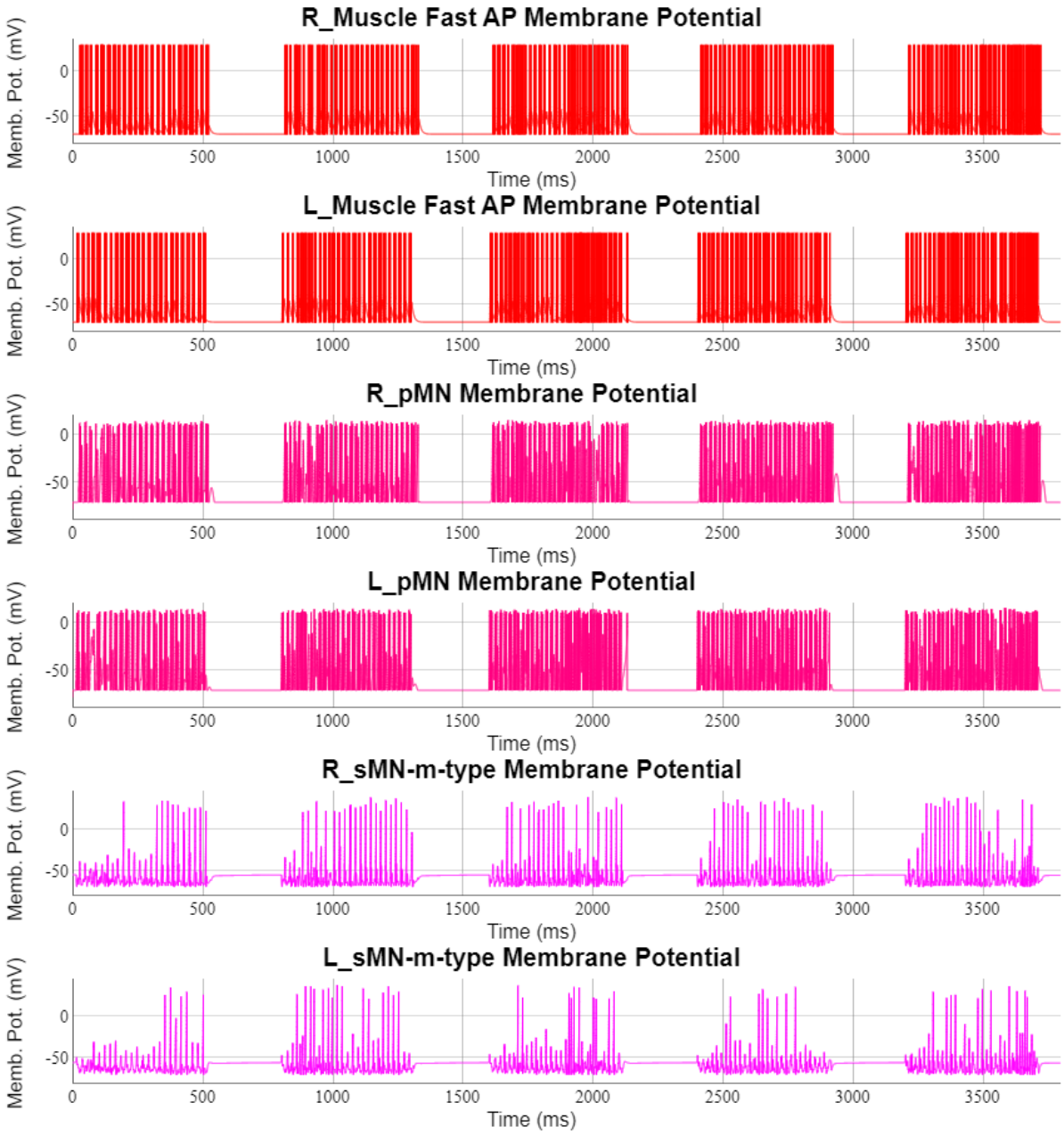

Figure 27. MNs and muscle cells in the fast mode.

Related to Figure 26. The activities of the muscle cells and MNs on the sixth somite are shown.

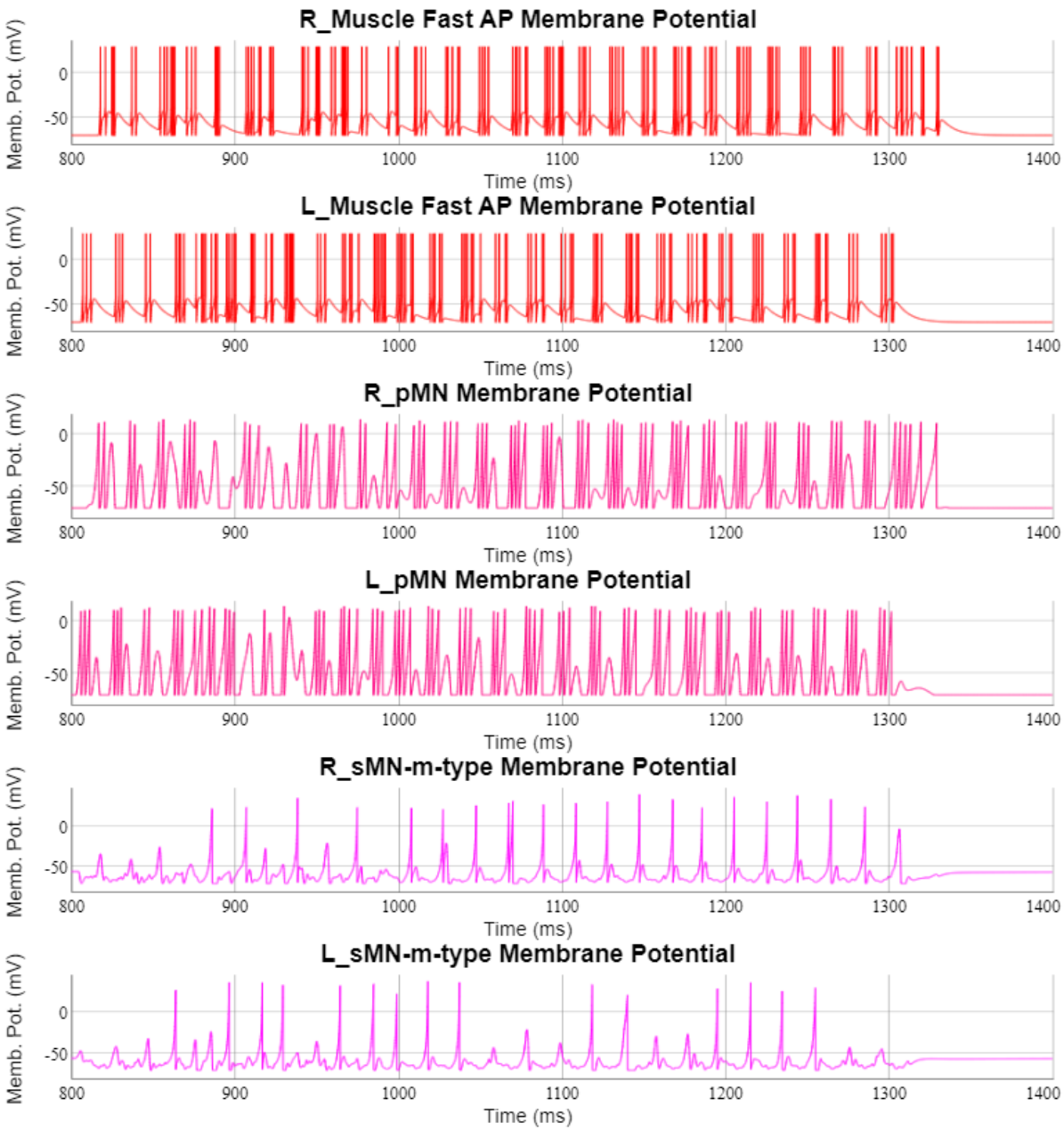

Figure 28. The zoomed-in activities of muscle cells and MNs in the fast mode are shown.

Related to Figure 27. Zoomed-in activity to the muscle cells and MNs showed a high level of activity.

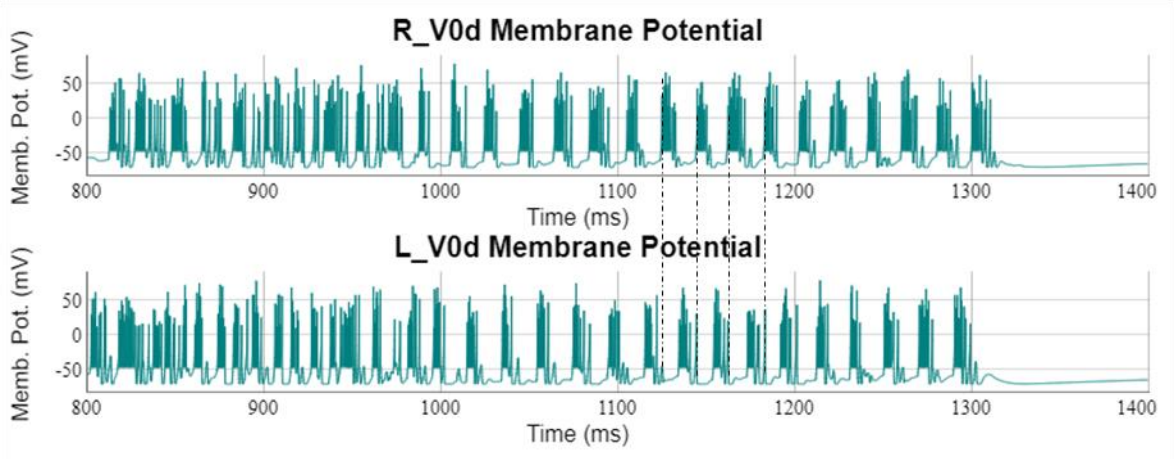

Figure 29. V0d activity on the sixth somite during the fast mode.

Left and right alternation was observed; however, it took longer for the model to stabilize.

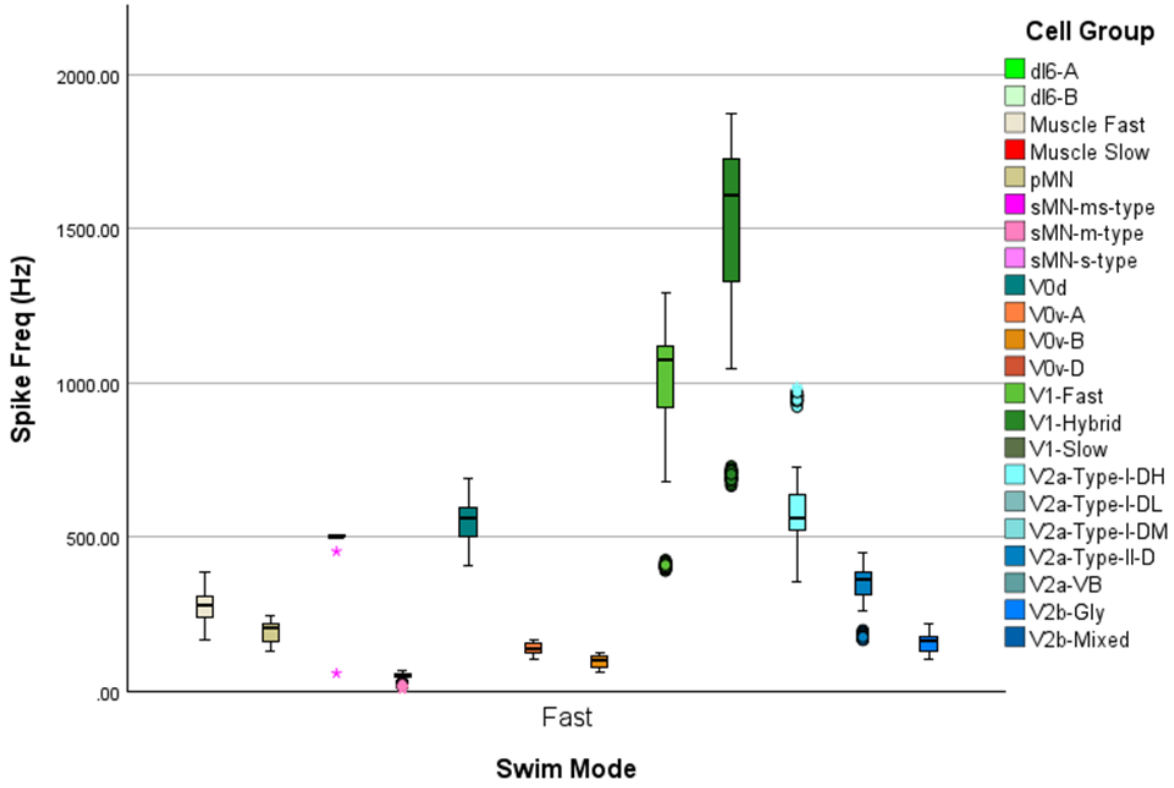

Figure 30. Spike frequency distribution of all the cells when the model was tested in fast mode.

The zoomed-in version of Figure 13. As activity from every somite is plotted, there is a wide range of activity within each group. The boxes show the median and 25-75% IQR. Circles and asterisks are outliers and extreme outliers. N = 20.

4.5 Experimental Tests

The model parameters were tweaked such that the expected cellular populations were activated at each mode (slow, intermediate, and fast), and a range of TBF was observed. However, there can be many ways to create a model to generate a required behaviour. For the model to be representative of the organism it is modelling, it should also replicate a range of published experimental data compiled on the actual organism.

4.5.1 Simulation of Optogenetic Stimulation

Wahlstrom-Helgren et al. (2019) showed that by applying various amounts of optic light to the 1/3rd of the spinal cord of a genetic line of zebrafish sensitive to blue light, swim-like behaviour can be observed. In this study, they targeted the glutamatergic neurons. To simulate their results, various current stimuli were applied to the glutamatergic neurons in somites 2-5 (Figure 31). Since some light intensities were better than others in generating alternating tail beats (Wahlstrom-Helgren et al., 2019), a wide range of current stimuli was tested with the current model; a selected range is displayed in Figure 31. A two-millisecond sagittal delay and no rostrocaudal delay were applied to the stimuli. The 40, 60, and 80 pA stimulus generated left and right tail beats over 30 Hz. Left-right alternation was observed in all the activated cellular populations (Figure 32, S22A, and S23A).

A similar optogenetic stimulation study targeting only V2as was also imitated (Eklöf Ljunggren et al., 2014) (Figure 33). Stimulating only V2as was more challenging in terms of finding the right stimulus amount required to observe tail beat behaviour. Various amounts between 10-400 pA were tested, and 90 pA was picked as the most promising candidate. In Figure 33, the response to multiple-step stimuli of 90 pA is displayed. Similar to the previous study, there was left-right alternation in the bursting activity of all neuronal populations, a selection of them displayed in Figures 33A and 34A.

4.5.2 Simulation of Glycine Inhibition after Optogenetic Stimulation

Both studies mentioned in the previous section also tested the effects of blocking glycinergic transmission, which resulted in disruption in the left-right alternation of activity (Eklöf Ljunggren et al., 2014; Wahlstrom-Helgren et al., 2019). In *Sili*Fish, glycinergic synapses were inhibited by deactivating glycinergic projections and manipulating the glycine-GABA mixed

junctions (by lowering their conductance values and changing their decay constants to slower GABA decay times). When the above tests were replicated after glycine inhibition, a clear disruption to left-right alternation was observed (Figure 31-Figure 36, S22-23). The TBFs were also greatly reduced (Figure 31C and Figure 33C). V1s can be both glycinergic and GABAergic (Fetcho and Mclean, 2010; Higashijima et al., 2004a). Therefore, removing the glycine from the system does not fully prevent the inhibition. The presence of tail beats, despite lacking synaptic inhibition by glycine, can be explained by the presence of GABA.

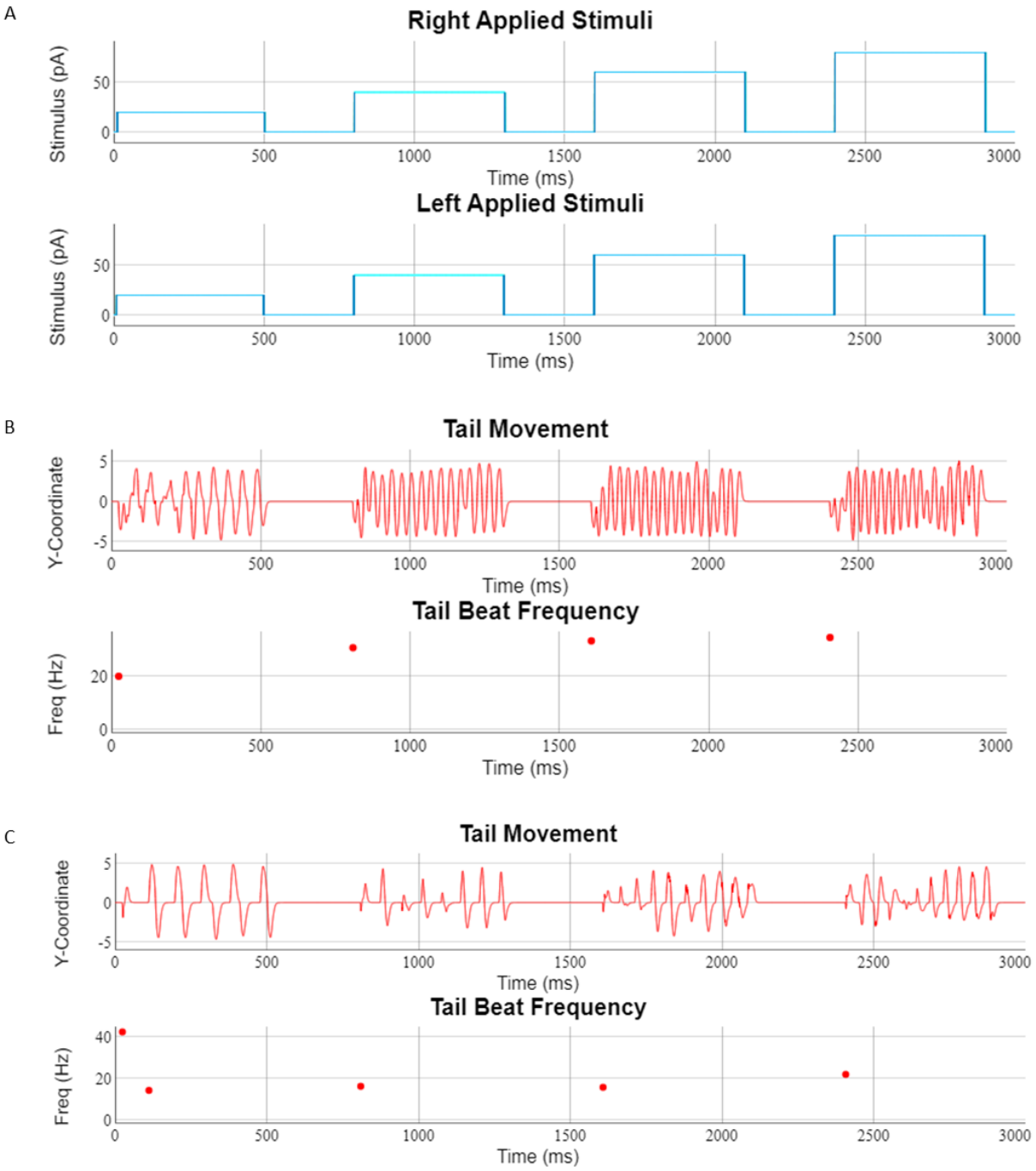

Figure 31. Applying current stimulus to all glutamatergic neurons creates a swim like behaviour that is disrupted by glycine inhibitor.

(A) Rectangular pulses ranging between 20-80 pA were applied to the glutamatergic neurons of somites 2-5. (B) Tail beats were present across all four stimulus steps. (TBFs displayed: 20.16, 30.09, 33.48, 34.74 Hz) (C) Deactivating glycinergic synapses generated more irregular tail beats with lower frequencies (Frequencies displayed: 42.55 & 11.86, 14.43, 15.92, 22.13 Hz - the first 42.55 Hz considers only two beats without merging it to the next series of beats, due to two successive right beats.)

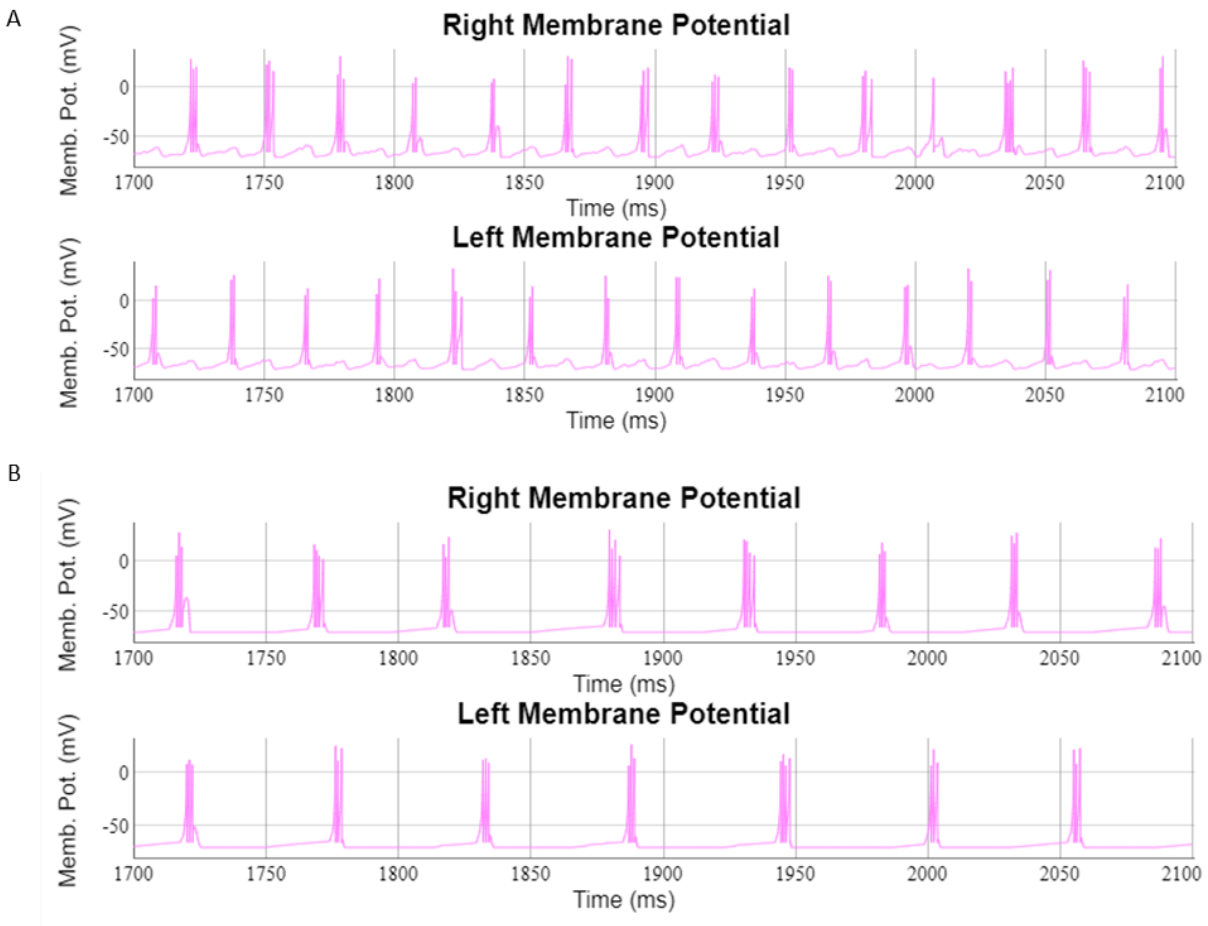

Figure 32. Inhibiting glycine activity disrupted the left-right alternation of the MNs.

Related to Figure 31. (A) The zoomed-in sMN activity when all cells and projections were fully functional is shown. (B) When glycinergic synapses were deactivated, the left-right alternation was disrupted, and the bursting frequency was lowered.

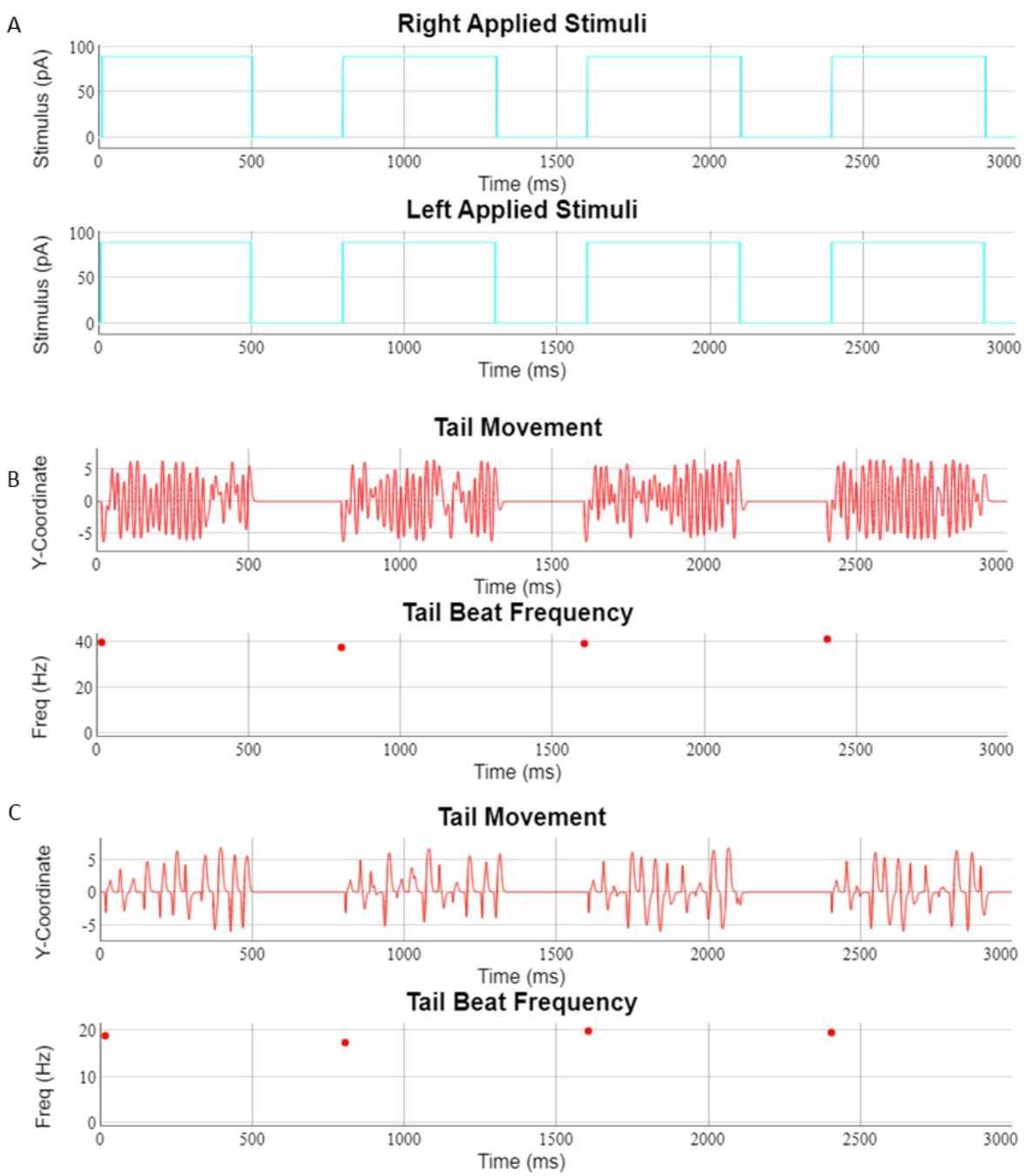

Figure 33. Applying the current stimulus to all V2as creates a swim-like behaviour that is disrupted by glycine inhibitors.

(A) Rectangular pulses of 90 pA were applied to all V2as. (B) Tail beats were observed with some irregularities, such as successive tail beats on one side without passing through the midline in between. (Frequencies displayed: 40.02, 37.8, 39.5, 41.47 Hz) (C) Inactivation of the glycinergic projections increased the irregularities and lowered the TBFs. (Frequencies displayed: 18.78, 17.29, 19.81, 19.47 Hz)

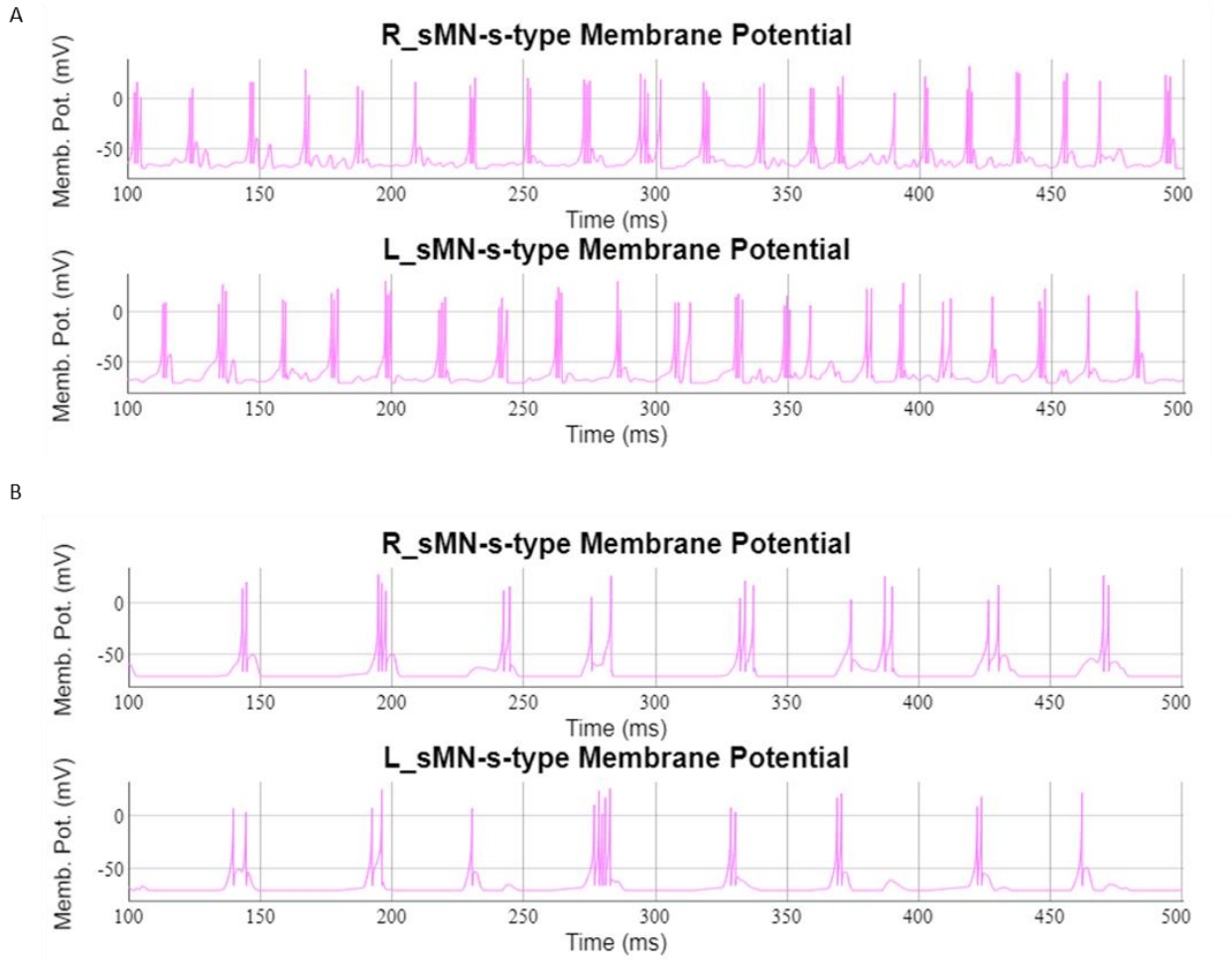

Figure 34. The left-right alternation of MNs was disrupted by deactivating glycinergic projections.

Related to Figure 33. (A) The zoomed-in activity of sMN-s-type MNs on the sixth somite when the network is fully functional is shown. (B) When glycinergic synapses were deactivated, the left-right alternation was disrupted, and the bursting frequency was lowered.

A

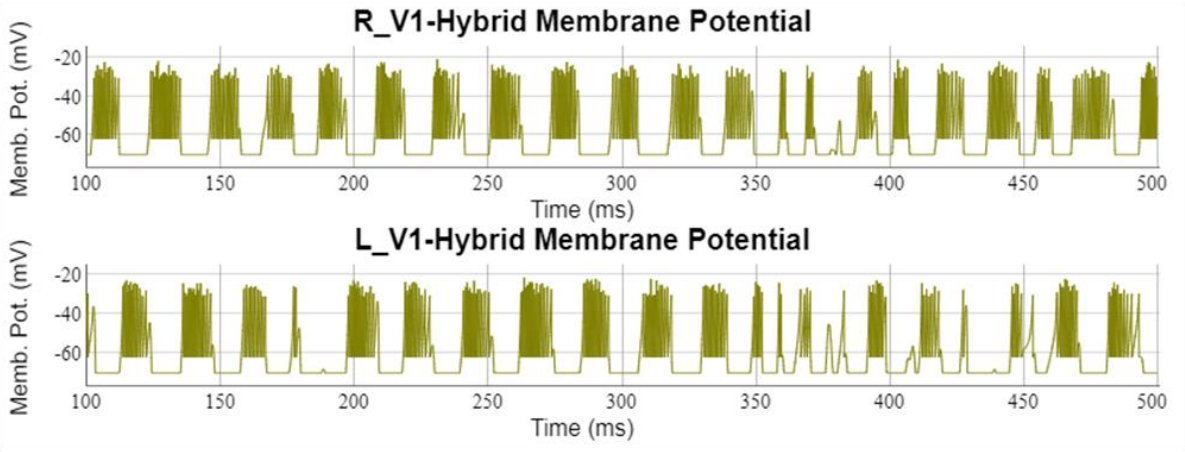

B

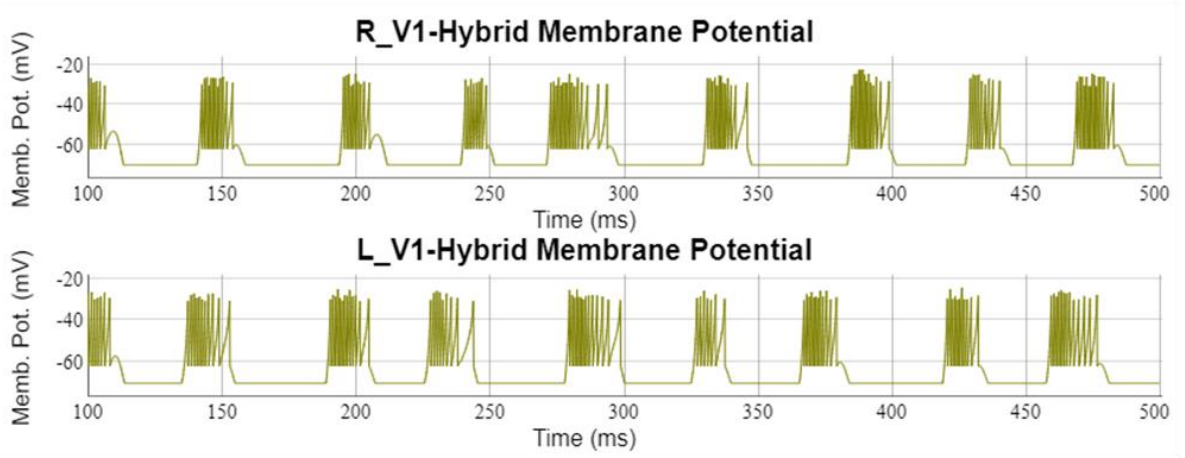

Figure 35. The left-right alternation of inhibitory neurons was disrupted by deactivating glycinergic projections.

Related to Figure 33. (A) The zoomed-in activity of V1s on the sixth somite when the network is fully functional is shown. (B) When glycinergic synapses were deactivated, the left-right alternation was disrupted, and the bursting frequency was lowered.

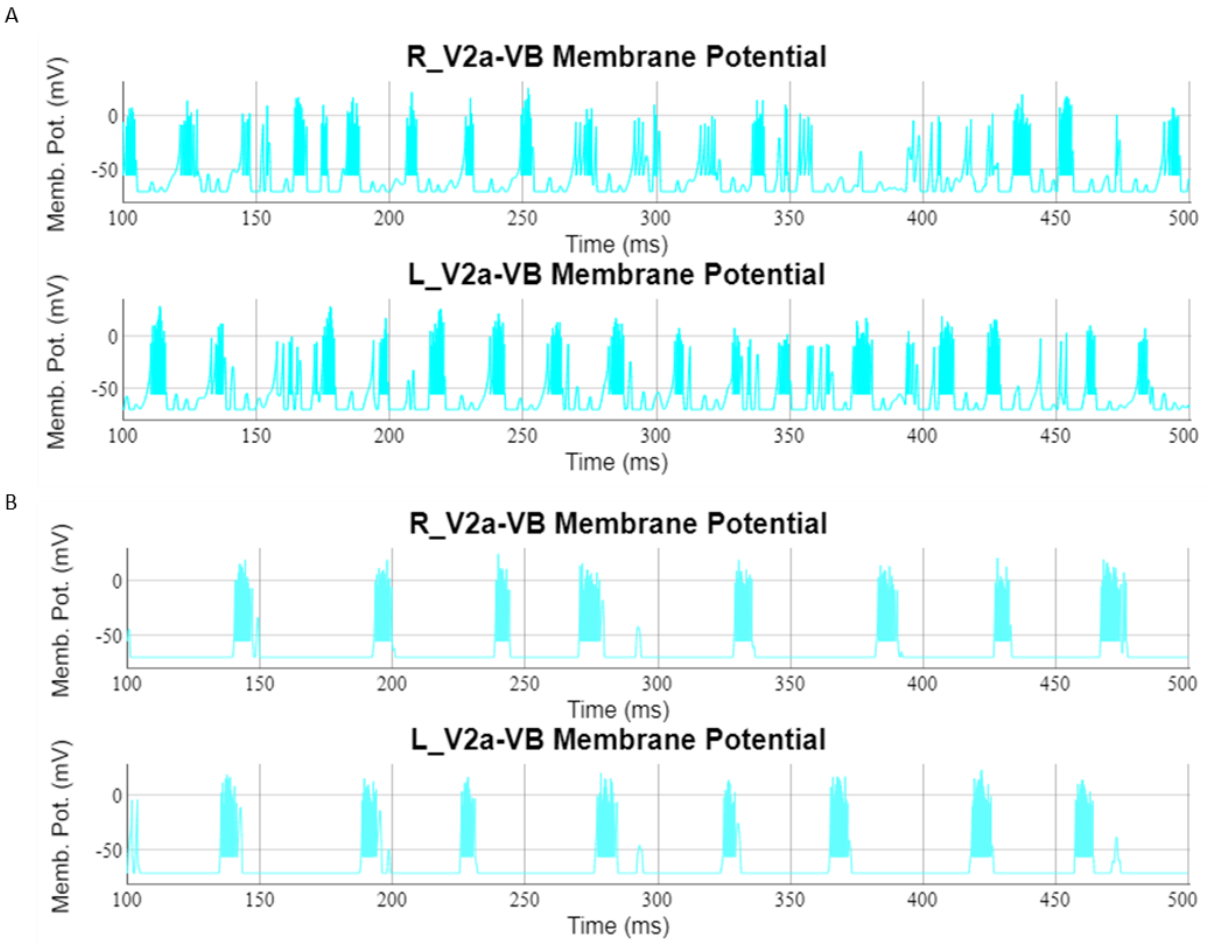

Figure 36. The left-right alternation of excitatory neurons was disrupted by deactivating glycinergic projections.

Related to Figure 33. (A) The zoomed-in activity of V2a-VBs on the sixth somite when the network is fully functional is displayed. (B) When glycinergic synapses were deactivated, the left-right alternation was disrupted, and the bursting frequency was lowered.

4.5.3 Suppression or activation of V2bs did not generate the expected results.

V2bs are shown to have an effect on the tail beats of larval zebrafish, such that the activation of V2bs lowers, whereas their suppression increases the TBF (Callahan et al., 2019).

These findings were tested with the current model. To suppress V2bs, three approaches were tried: deactivating the V2bs, lowering the conductance values of the outgoing projections by half, or applying a negative current stimulus to the V2b populations. To activate V2bs, two similar approaches were used: doubling the conductance values of the outgoing projections or applying a positive current stimulus to the V2b populations. Figure 37 shows the response of the model when a series of slow, intermediate, and fast mode test stimuli were applied under normal conditions. The bursting frequency of all of the neuronal populations on somite six and tail behaviour is displayed for comparison. Contrary to Callahan *et al.*'s conclusions, there was no consistent change in the TBF during the slow, intermediate, or fast swimming when a positive (Figure 38) or negative (Figure 39) current was applied to all V2bs throughout the simulation. There was no visual consistent change in the bursting frequency, TBF, or MN activity. Similar inconclusive results were obtained when V2b suppression was done by changing their outgoing projection weights or deactivating them (data not shown).

4.5.4 V1 ablation did not generate the expected results.

When V1s were deactivated and the fast mode was run with various stimulus amounts, the expected results of slow V2as and MNs to be activated were not observed. On the contrary, the resulting behaviour was far away from swimming behaviour (Figure 40). Motoneuron activation was strictly unilateral rather than a rhythmic left and right alternation (Figure 41). When the animation was generated, the behaviour looked like stretching rather than swimming.

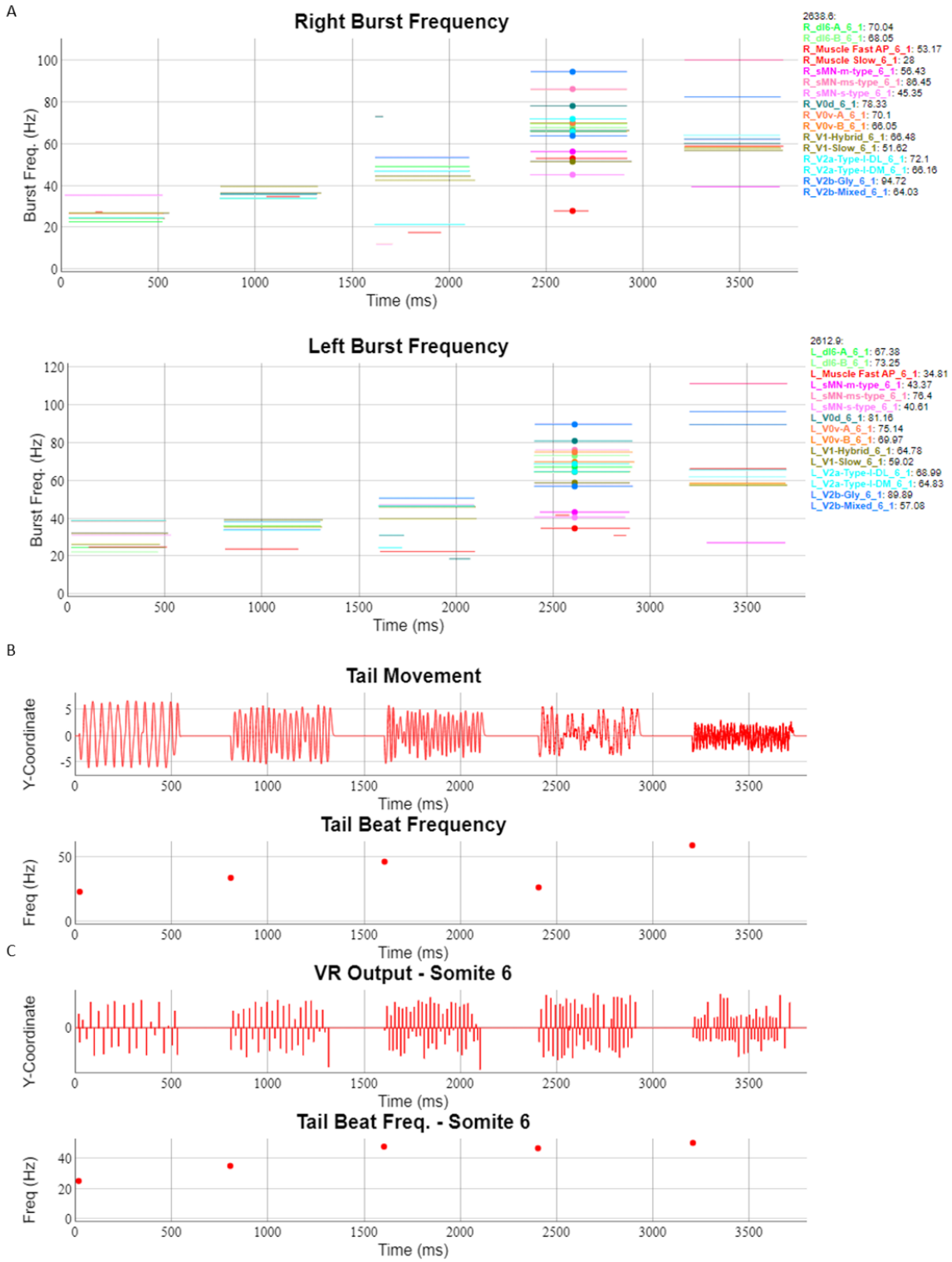

Figure 37. The bursting frequency of all cellular pools on somite six and observed behaviour to a series of tests are shown.

(A) The slow, three intermediate, and fast modes are run back to back, and the bursting frequencies of cellular pools are displayed. The list on the right-hand side of the top plots shows which cellular pools the colour corresponds to and the value on the cursor. The circles on the plot shows which time point the cursor is pointing to. (B) The tail movement observed is shown. (C) The MN activity on somite six is shown.

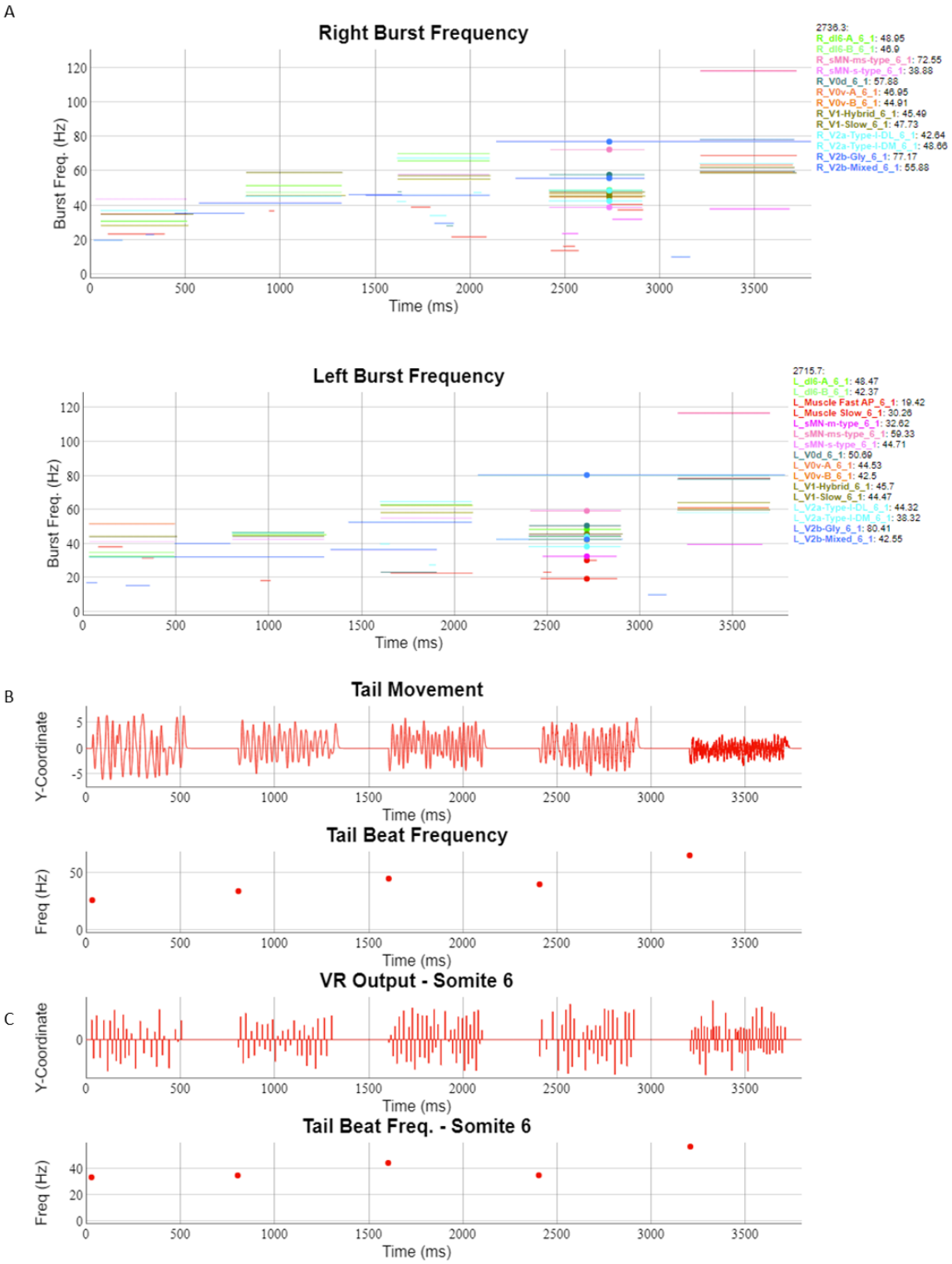

Figure 38. V2b activation by positive current did not generate the expected results.

Related to Figure 37. A step stimulus throughout the testing period was applied. The amount of current was a little higher than the rheobase of the target cell populations. (A) The slow, three intermediate, and fast modes are run back to back, and the bursting frequencies of cellular pools are displayed. (B) The tail movement observed is shown. (C) The MN activity on somite six is shown.

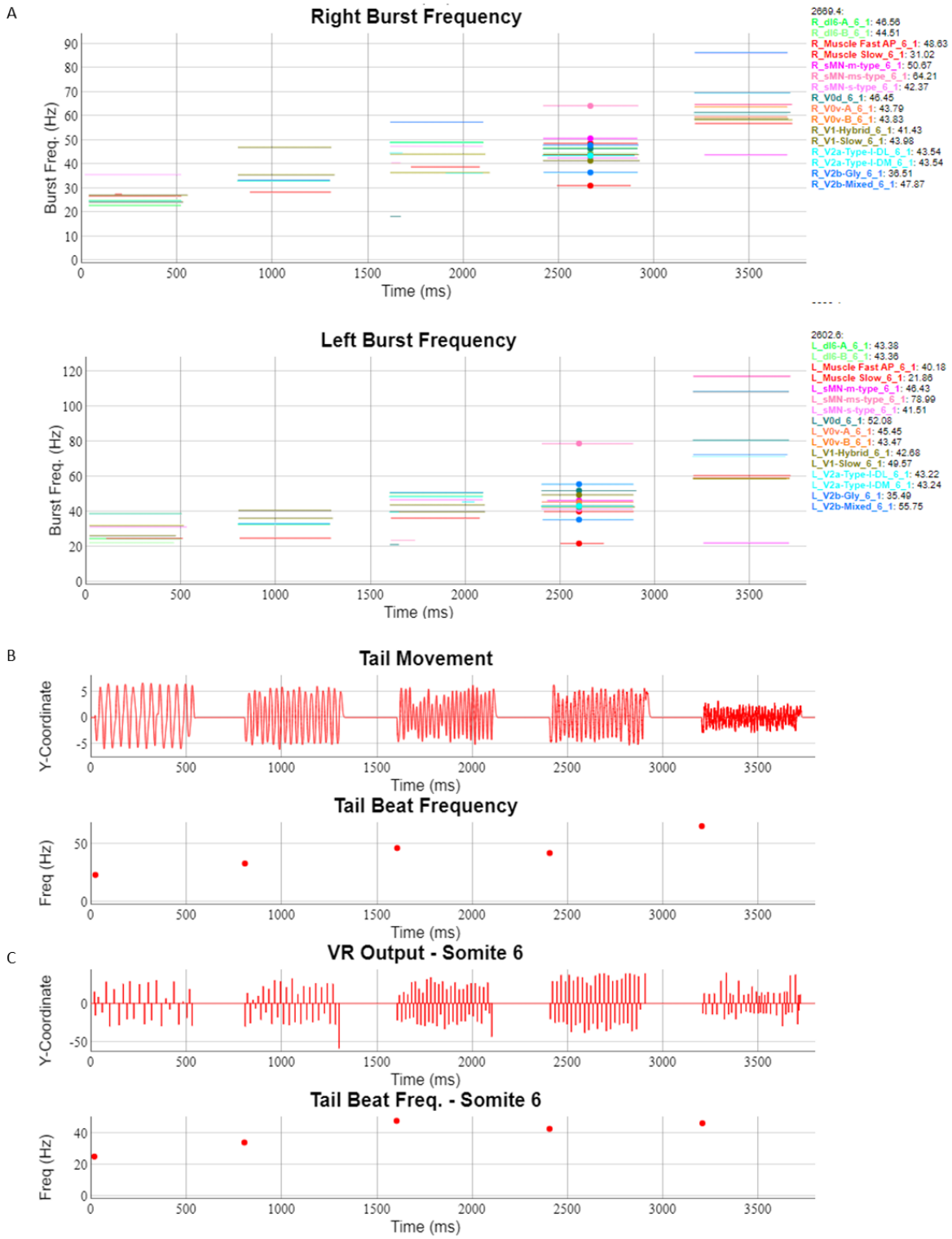

Figure 39. V2b suppression by negative current did not generate the expected results.

Related to Figure 37. A step stimulus throughout the testing period was applied. The amount of current was slightly higher than the rheobase of the target cell populations, only negative. (A) The slow, three intermediate, and fast modes are run back to back, and the bursting frequencies of cellular pools are displayed. (B) The tail movement observed is shown. (C) The MN activity on somite six is shown.

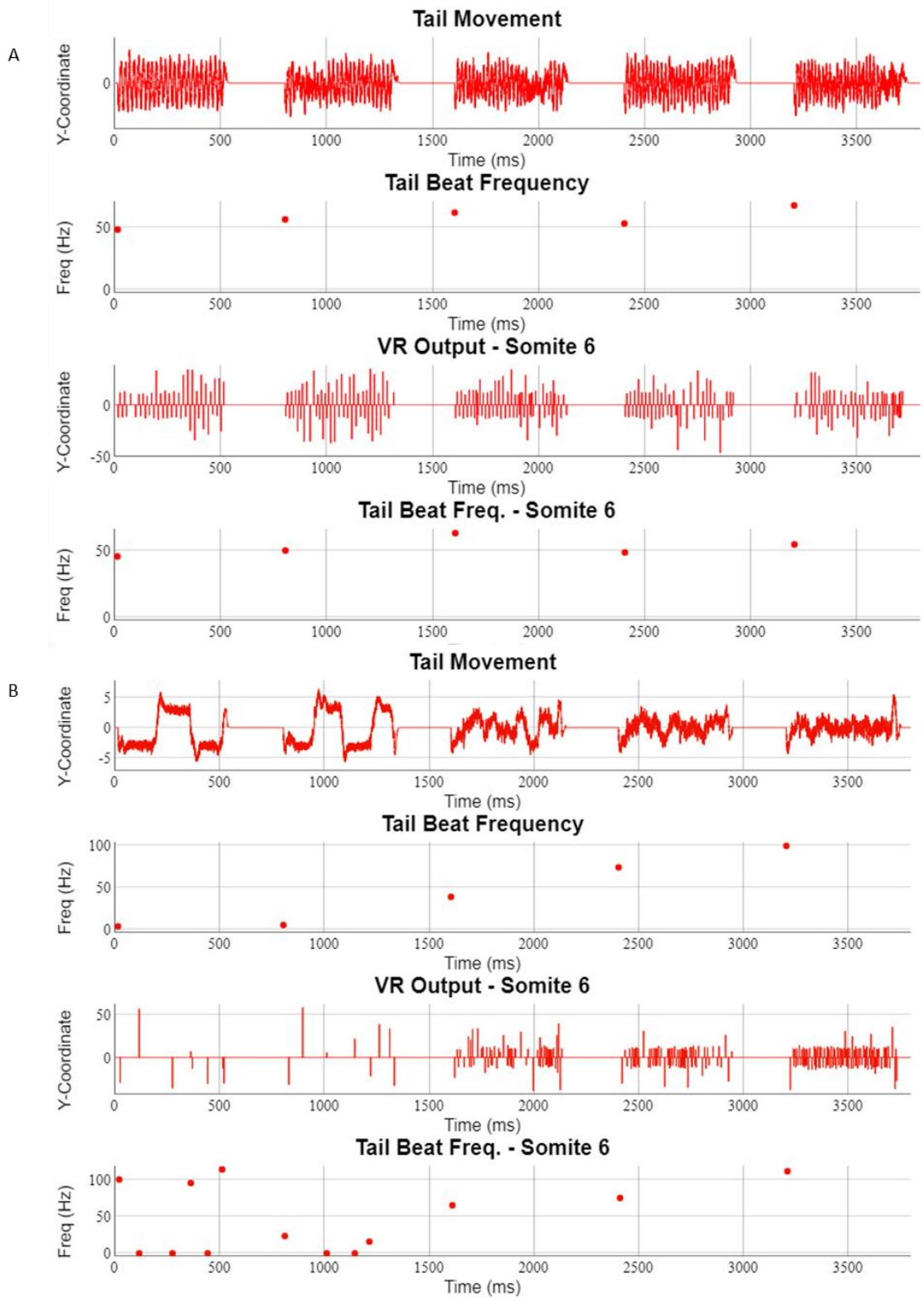

Figure 40. Tail movement after V1 suppression was not similar to tail-beating behaviour.

(A) Under normal conditions, the fast scale mode stimulus is applied to see tail-beating behaviour. (B) When V1s were deactivated, the tail movements were greatly disrupted.

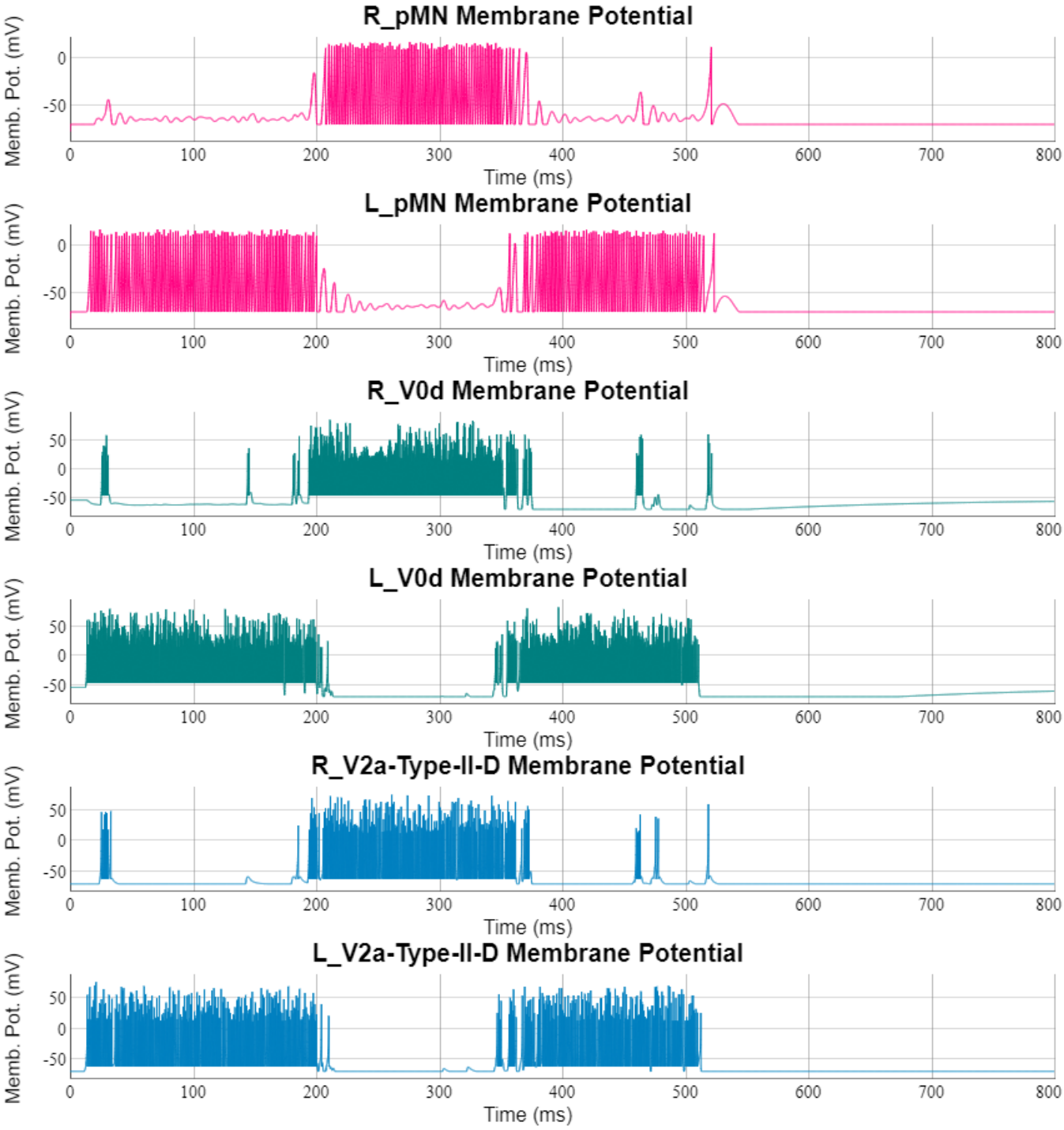

Figure 41. V1suppresion caused unilateral activation of the neurons rather than alternating.

A representative motor, inhibitory, and excitatory neuron activity on somite six is displayed.

4.6 Impact of the Stimulation Duration

The tests above were run with a train of stimulus episodes, each lasting 500 ms. To see the impacts of the episode duration, the slow mode simulation was replicated with twenty successive step stimuli of 500 ms, 1 s, 2 s, 3 s, and 10 s. The break between the 500 ms and 10 s stimulus episodes was 300 and 1000 ms, respectively. The difference in the long gap for the 10 s test was to allow the system to stabilize after a long stimulation. It was observed that long gaps were unnecessary for stabilization (not displayed); therefore, the remaining tests of 1-3 s stimuli episodes were run with 200 ms gaps in between to expedite the testing process. For each test, a single TBF was calculated for every episode, generating twenty TBF values. The distribution of TBF across different tests is displayed in Figure 42A.

The TBF values across the test groups were different than each other (Kruskal-Wallis, $p < 0.001$). A pairwise comparison showed that 1-3 s episodes and 500 ms and 10s episodes showed similarity (Figure 42B). Despite the pairwise differences, all TBF values are close to each other. The full ranges observed were [20.70-23.52 Hz], [22.26-25.56 Hz], [22.36-24.43 Hz], [22.86-24.93 Hz], and [22.13-22.21 Hz] for 500 ms, 1 s, 2 s, 3 s, 10 s episodes, respectively.

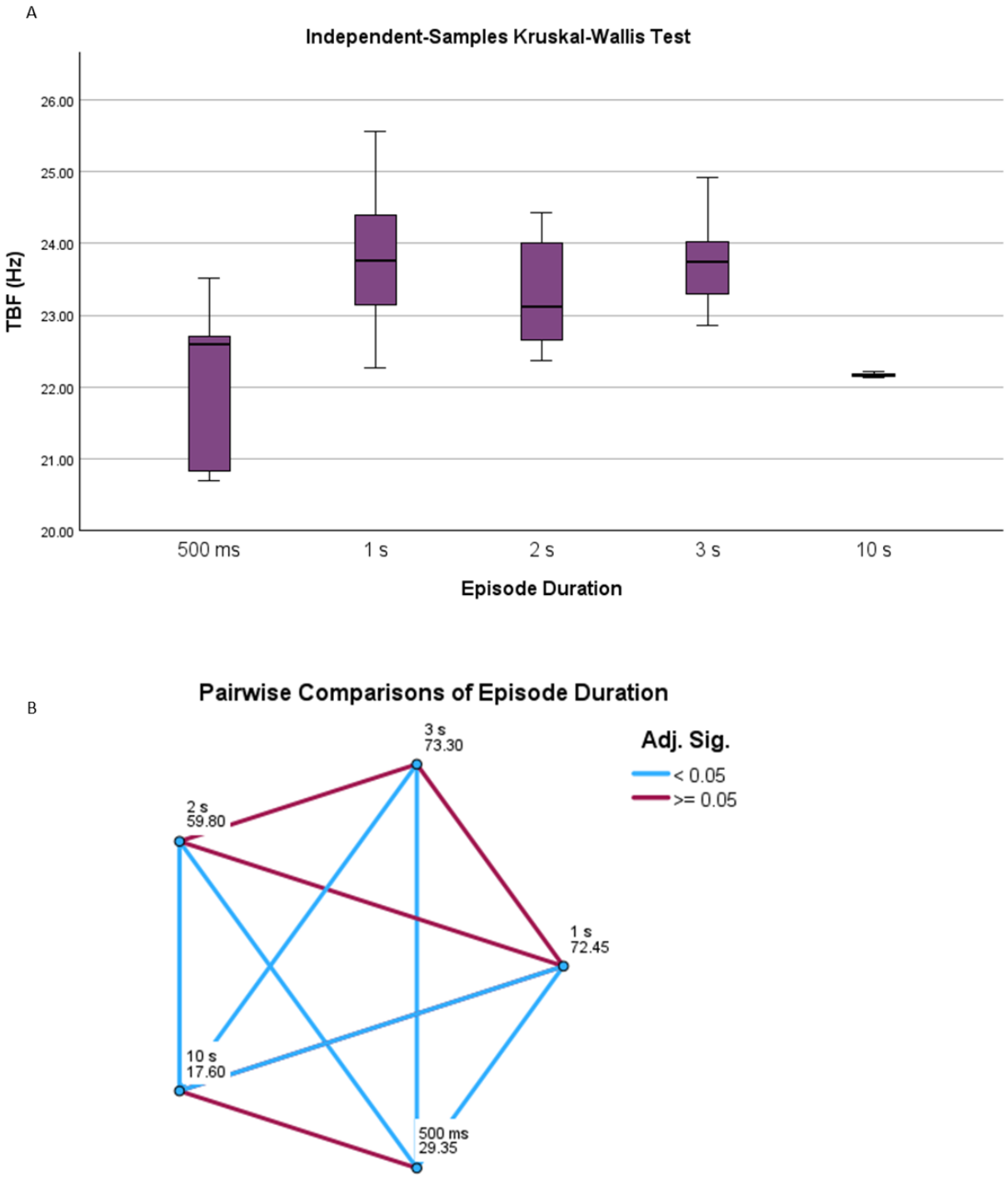

Figure 42. The distribution of TBF values for different episode lengths and their pairwise comparisons.

(A) The TBF values were 22.59 (IQR 20.8-22.7), 23.76 (IQR 22.96-24.39), 23.13 (IQR 22.66-24.05), 23.75 (IQR 23.29-24.08), and 22.16 (IQR 22.14-22.18) Hz for 500 ms, 1s, 2s, 3s, 10s episodes, respectively. N=20. (B) The episodes of 1s, 2s, and 3s were not significantly different. Similarly, the episodes of 500 ms and 10 s were significantly similar. (Kruskal Wallis, p = 1, adjusted by the Bonferroni correction). The numbers on the nodes represent the sample average rank required for non-parametric tests.

4.7 MN activity versus tail beat

When the TBFs at each test were determined, the tail tip movement and the sixth somite MN activity—as an approximation to mid-body ventral root activation— were visually observed. A pairwise comparison was performed to determine whether the sixth somite is a valid approximation (Figure 43). The TBF measured by the tip of the tail was similar to TBFs measured by the MN activity on somites 3 and 6 (Kruskal Wallis, adj. p = .662 and .058) (Figure S24A). However, N numbers were 100 for the tail tip and somite six, but only 84 on the third somite.

When the same analysis was repeated by separating the data by the five swim modes tested, the tail continued to show similarity to the sixth somite in the slow and Inter-I modes (Kruskal Wallis, adj. p = 0.135) (Figures S25-S26). However, in the remaining swim modes (Inter-II, Inter-III, and Fast), the tail tip showed similarity to more rostral somites (Figures S25-S26).

4.8 Impact of the target somites

Due to an experimental error, the fast mode was run by applying the stimulus to the caudal somites only rather than the full body. The results were unexpected and contrary to my previous tests. Therefore, a simple test was run by using the same amount of current stimulus in the fast mode and applying the stimulus to the whole, rostral half, or the caudal half of the spinal cord. The rostral half as the target was visually similar to the full-body stimulation (Figure 44). The propagation of the excitatory signals was sufficient to generate similar results. In the case of caudal stimulation only, the frequency of neuronal activity was not different (not shown); however, the tail tip movement was not prominent enough to consider a tail beat depending on the selected kinematics settings.

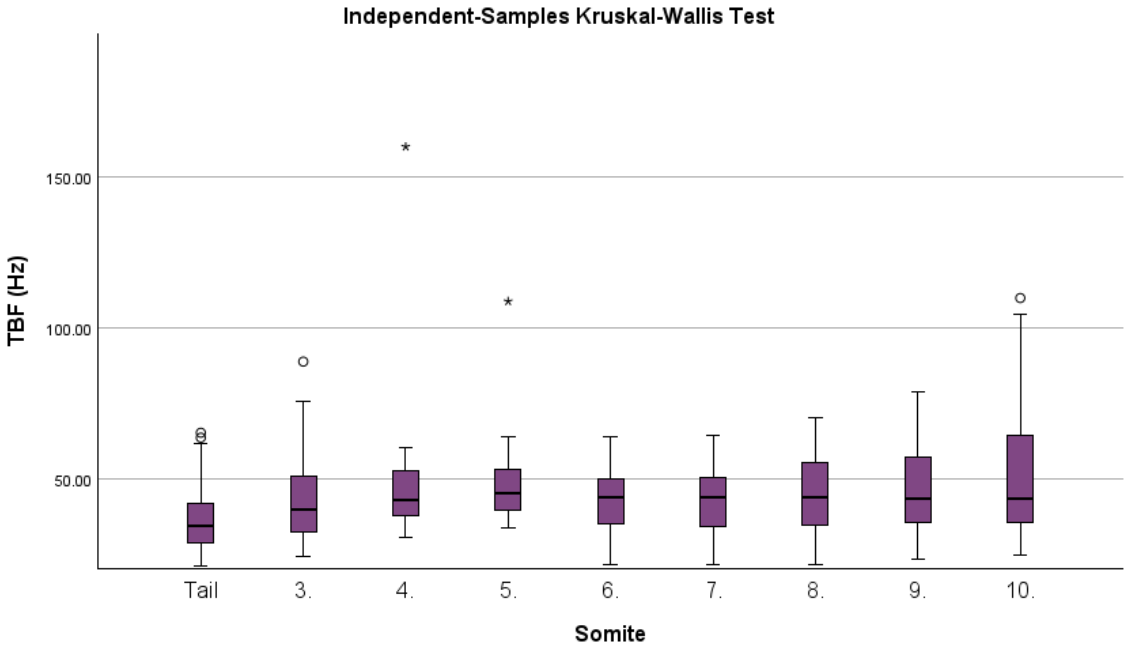

Figure 43. The distribution of TBFs calculated by the tail tip movement and MN activity on different somites are shown.

The first two somites were excluded from the comparison. (Tail: 34.31 (IQR 28.39-41.8), N = 100; Somite 3: 39.51 (IQR 32.16-51.22), N = 84; Somite 4: 42.83 (IQR 37.68-52.34), N = 82; Somite 5: 44.97 (IQR 39.13-52.97), N = 81; Somite 6: 43.8 (IQR 34.65-49.86), N = 100; Somite 7: 43.6 (IQR 34.09-50.22), N = 100; Somite 8: 43.58 (IQR 34.52-55.41), N = 100; Somite 9: 43.48 (IQR 35.33-57.1), N = 100; Somite 10: 43.28 (IQR 35.23-64.33), N = 100)

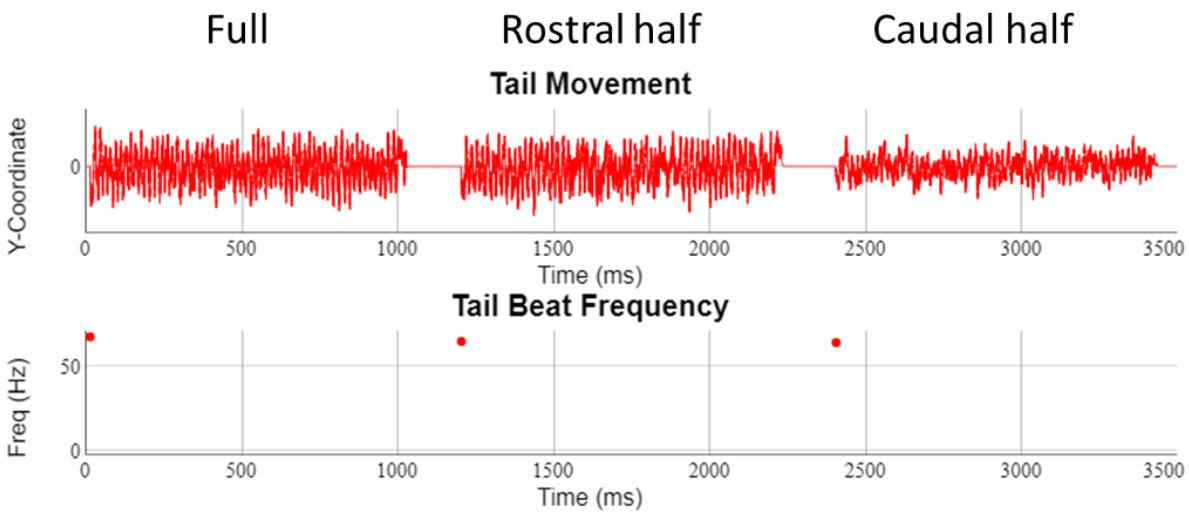

Figure 44. Tail movements observed with different target somites are shown.

Despite the same amount of current stimulus being applied, the tail movement differed when the target somites differed. The TBFs on the plot are 68.08 Hz for the full body stimulation and 65.27 and 63.63 Hz for the rostral and caudal half stimulation.

Chapter 5. Discussion

5.1 The Complexity

It is not *that* simple.

The literature strongly supports the presence of speed microcircuits in the zebrafish spinal cord (Ampatzis et al., 2014; Ausborn et al., 2012; McLean et al., 2008). These microcircuits probably consist of multiple subgroups of the same cellular populations with differing intrinsic properties and connectivity patterns (Figure 1, Table 2). Therefore, it was necessary to define the cell types and their projections which were studied and shown to be involved in swimming speeds.

As a result, 22 cell types with a total of 240 parameters were created. There are 172 chemical synapse definitions with nine parameters and 33 gap junction definitions with five parameters each. In total, close to 2000 parameters can be tweaked, resulting in a different model behaviour.

Clearly, changing manually all 2000 parameters to do testing is not practical. There were many simplifications done. For example, rather than 172 different tau decay and tau rise values for the chemical synapses, only eleven and six unique values were used for each. Regardless, when troubleshooting an unexpected behaviour, all of the parameters were in my reach to change, and I had to decide whether to change a single value or a group of values. For example, if I noticed that the conductance value of a synapse was low, I decided whether I should increase only one synapse conductance that I am specifically investigating or all the conductance values that I set with a similar approximation I have done (e.g., using the cell sizes.)

Moving on from the model template to the running model that the simulations are run on: when the model was generated using the blueprint (the model template), the full model was composed of ~16K cells and 4M synapses. When the model was simplified by reducing the number of somites and the number of cells per somite, the final numbers became 440 cells and 8058 synapses. This simplification, however, does not simplify the model. The number of parameters in the previous paragraph still exists. However, the reduced model extensively lowered memory usage, allowing far faster trials and tests.

Another challenge arises because none of these parameters are mutually exclusive. There is high connectivity within the circuit, and any change in a single parameter can have multiple side effects other than what I am going for. One fix can easily impact the previous fixes. So, it is very possible that a change previously made had to be reverted. The fine-tuning required to focus on the details but also retest the big picture simultaneously.

Despite multiple attempts to simplify the model for easy testing, the end result was still far from simple. I did not want to compromise the goal of representing the fish to the best of my ability; therefore, all cell populations were kept, but only a reduction in numbers was made from the model initially designed.

5.2 *Sili*Fish

At juvenile stages, 17 months post-fertilization.

The complexity detailed above requires a powerful tool to work with. Despite the time required to develop *Sili*Fish, it brought multiple advantages.

The most important one is the ability to create test scenarios, have fast-run simulations, and inspect the results to the level of current passing through a single synapse detail. Depending on the simulation duration, it required only seconds to minutes to test the model. In rare cases of testing the system for tens of thousands of milliseconds, it took multiple hours to run a simulation, but those cases were run for data analysis rather than model creation or testing.

The most time-intensive part was investigating what expected and unexpected behaviours were observed. After pinpointing the suspected cell population that acts contrary to the expectation, the cause of that behaviour and how it can be fixed had to be determined. There can be multiple causes for the unexpected behaviour, and some may not be obvious. Therefore, this cycle had to be repeated countless times, which enforced the need for a powerful tool.

Many features have been added to *Sili*Fish during the last two years. Whenever I noticed a repetition in a task that I was doing, I looked for a way to simplify it—for example, exporting components of the model to a comma-delimited text (.csv) file allowed bulk updating. I could export all the chemical synapses of a single neural pool and modify their tau decay values using Excel in one shot, reimport the file, and run the simulation with the updated parameters in a matter of seconds.

The UI was also expanded to make the software's usage more efficient. For example, it is possible to plot the current information of a synapse by just selecting a synapse from the list in the UI and selecting an item on the context menu. There are many other shortcuts added that would be hard to put into words, but the idea was to choose to spend some time on coding so that I would not need to spend time on repetitive tasks afterward.

One of the important features incorporated into *Sili*Fish was the usage of genetic algorithms (GA) for parameter fitting of the Izhikevich parameters (2.2.4.3 Genetic Algorithms). It simplified the process of parameter fitting, but not without consequences. It was easy to get blinded to the process, not interfere with the procedure, and use the results that passed the initial visual tests without further thought. Later, I realized that not all parameter combinations are created equal, and I should not be completely blind and have some control over the GA. That was when I added the extra controls explained in Additional Range Checks for the Parameter Fitting.

The success of GA also depended on how well the fitness functions were defined (Genetic Algorithms). Several algorithms were developed to determine the firing patterns from a given array of membrane potential values. These algorithms used several settings of their own, as listed in Table 19.

These settings were tweaked during the initial testing and revisited multiple times during the Izhikevich parameter fitting process. However, some cell firing patterns show they are still not perfect. For example, the infographic of V1-Slow (see Infographics document) shows a tonic firing behaviour, but the algorithm describes it as tonic bursting. As I do not see all the trials that the GA is going through (thankfully), it is hard to gauge the impact of such errors. It may be possible that I missed the Izhikevich parameter combinations that are better suited to my firing goals.

These settings bring another level of complexity to the model generation. One alternative to eliminating these errors is using machine learning to determine the firing patterns rather than relying on the new algorithms that I developed. This option was shortly considered; however, whether it would create a more desirable output is not known with certainty. Therefore, I determined it would not be worthwhile to include it as part of my master's project.

Table 19. The settings of the firing pattern detection algorithms.

Setting	Value
Burst Break	100
In ms. The duration to be used as a break while calculating bursting frequency.	
Chattering Irregularity	0.1
The 'SD/Avg Interval' ratio for a burst sequence to be considered chattering.	
Max Burst Interval - no spread	5
In ms, the maximum Interval two spikes can have to be considered as part of a burst. Used if the intervals between spikes are not increasing with time.	
Max Burst Interval - spread	30
In ms, the maximum Interval two spikes can have to be considered as part of a burst. Used if the intervals between spikes are increasing with time.	
One Cluster Multiplier	2
Centroid2 (average duration between bursts) < Centroid1 (average duration between spikes) * One Cluster Multiplier means there is only one cluster (all spikes are part of a burst).	
Spike Break	10
In ms. The duration to be used as a break while calculating spiking frequency.	
Tonic Padding	1
In ms. The range between the last spike and the end of the current to be considered as tonic firing.	

Implementing a software tool takes time. *Sili*Fish developed gradually since the beginning, and it helped me tremendously in generating and testing the model. However, there is much more to be done. Writing software for one's own use or the general public has different requirements. *Sili*Fish is available for any researcher who does computational modelling; therefore, great attention was paid to making the UI user-friendly and intuitive. Nevertheless, due to the time limitation of a master's program, many shortcuts had to be taken, and many features were added to the list of "future improvements."

5.3 Speed Networks

Some fish swim slow.

5.3.1 Swimming Speeds

The swimming speed of larval and zebrafish, measured as tail beat frequencies (TBF), are divided into slow, intermediate, and fast speeds in the literature (Ampatzis et al., 2014; Kimura and Higashijima, 2019; Song et al., 2020) (Table 1). However, these ranges may not be as distinct as we are making them.

Depending on the study, different TBF ranges can be put into different swimming speed categories (Ampatzis et al., 2014; Berg et al., 2023; Björnfors et al., 2019; Budick and O'Malley, 2000; Portugues and Engert, 2011). For example, for adult zebrafish, a 7.5 Hz can be considered as intermediate (Ampatzis et al., 2014; Björnfors et al., 2019) or fast (Berg et al., 2023) swimming, depending on the study. The intermediate swimming TBF range of larval zebrafish becomes specifically hard to determine, as not all studies use the three different categories but rather differentiate only slow and fast swimming (Kimura and Higashijima, 2019; Severi et al., 2014). Furthermore, in the majority of the studies, there is a continuation of TBF that goes from slow to intermediate ranges (Kawano et al., 2022; McLean and Fetcho, 2009; Menelaou and McLean, 2019; Müller and Van Leeuwen, 2004; Severi et al., 2014)

Despite multiple studies focusing on larval stages of the fish, there can be differences in their results due to fish's age and developmental differences. A wide range of four to nine dpf animals are used in many larval zebrafish studies (Asakawa et al., 2021, 2013; Bello-Rojas et al., 2019; Böhm et al., 2022; Budick and O'Malley, 2000; Buss and Drapeau, 2001; Dou et al., 2008; Eklöf Ljunggren et al., 2014; Higashijima et al., 2004a, 2004b; Kishore et al., 2014; McLean and Fetcho, 2009; Menelaou et al., 2014; Menelaou and McLean, 2012; Myers et al., 1986; Portugues and Engert, 2011; Roussel et al., 2020; Satou et al., 2020, 2012). It is also expected to have individual differences between animals such that one zebrafish can generally swim faster than another conspecific. Even a single animal can show a variety in swimming speeds in a multi-trial experiment (Callahan et al., 2019), which could make determining the cut-off line between two speeds more challenging.

Despite all the unclarity in determining the speed categories, as having the goal of modelling the speed microcircuits, an approximation was made using these multiple sources as a reference for my tests. The 20-40 Hz, 40-60 Hz, and 60-80 Hz were accepted as the ranges to be aimed to achieve with the model (Table 1). A serious effort was spent to give these results while fine-tuning the model parameters. Despite the effort, the ranges produced were only 20.70-33.92 Hz, 24.42-43.98 Hz, and 48.51-66.01 Hz (Figure 14A). The slow mode had the TBF on the lowest end of the spectrum. The intermediate mode covered most of the slow swimming range, extending to the intermediate swimming range only slightly. The fast mode covered the high end of the intermediate swimming and the low end of the fast-swimming ranges.

There may be multiple reasons for this mismatch. As mentioned, there may be individual differences among fish regarding how fast they swim. In the current model, each cell group and synapse were defined with a unique set of parameters that were the same across the spinal cord. These parameter combinations might as well have a limit on the TBF they can generate. For example, the pMN firing frequency in Figure 27 shows very little inter-burst intervals (IBI). Increasing the excitation to those neuronal groups was causing a tonic firing with no clear breaks, which prevented the left-right alternation (data not shown). This may be due to the intrinsic properties of the pMNs or the weights and patterns of the incoming projections to the pMNs. These were all tweaked, of course, during the testing process. However, with the current level of complexity, a lower level of accuracy than desired was accepted as ‘good enough’ many times during the testing process.

Another reason for the small TBFs may be due to the simplification of the model. Maybe having ten somites instead of 30, having one cell instead of the actual number of cells per somite of each group (which varied from 4 to 40, Table 14) might have caused the body to be stiffer, less flexible, and therefore less able to create frequent tail beats. If we were to look at the MN activity, the stiff body would not explain the issue. In this case, the input synaptic conductance approximation may be to blame. The conductance values were multiplied by the probability of the synapse and the number of cells the presynaptic cell represents, as explained in the Methods section. This approximation is also very simplistic. The idea was to be able to capture, let us say, ten chemical synapses a pMN is getting from ten V0v-As with 30% probability (Table 14 & Table 15). It may capture the total effect, but it does not capture the difference in the timing of the activity

on these synapses. If the actual number of cells and synaptic weights were to be used, the impact of those synapses could be more subtle rather than having them active all at once.

The large overlap of the slow and intermediate mode swimming does not necessarily point to an issue either. The speed circuits in the zebrafish spinal cord may not work as in a relay race but rather have some redundancy in the behaviour they generate by incorporating different circuits. After all, redundancy is observed in biology and encoded even in our genes. It may be possible that different networks generate similar swimming speeds. It may also be possible that different networks are recruited at different times, like from slow to fast swimming or from fast to slow swimming. The current model does not yet cover these types of transitions, so this is only a speculation. However, it would be interesting to come back to these overlapping ranges after the model is further improved.

5.3.2 Recruitment of different cellular groups

During slow, intermediate, or fast swimming, there are certain expectations on which neuronal pools will be active and which pools will not (Table 3). Similar results were observed when the model was run on different slow, intermediate, and fast modes to potentially trigger their corresponding speed circuits.

5.3.2.1 V0vs and V2as

The V0vs and V2as are recruited at different swimming speeds (McLean et al., 2008). However, there are multiple subtypes of both neuronal groups, so the separation of their recruitment may not be that sequential. For example, V0vs have slow, intermediate and fast subgroups that may have different roles at different swimming speeds (Kishore et al., 2014; Satou et al., 2012). Therefore, the model was designed so that slow rheobase V0v-Ds should be active during slow swimming, whereas V0v-As and V0v-Bs should be activated during intermediate and fast swimming. The results aligned with the design, and V0v-Ds showed activity only during slow swimming, whereas V0v-As and V0v-Bs were recruited during intermediate and fast modes (Figures 19, 24, and 30).

The lack of activity of V0v-Ds during fast mode was not solely due to lack of activation but rather their inhibition, as suggested by literature (Kimura et al., 2006; McLean et al., 2008; Satou et al., 2012). When the model received a stimulus that would trigger both the slow and fast

modes, the excitatory input V0v-Ds were insufficient for them to show spiking activity due to the inhibitory processes involved in fast mode (data not shown).

The level of activity V0v-As and V0v-Bs displayed were very similar. Surprisingly, the activity across different somites showed higher variability in the intermediate mode than in the fast mode (Figure S3). This difference is worth further investigation. V0vs receive inhibitory inputs from V1s, and one test to replicate a V1 ablation study was unsuccessful (V1 ablation did not generate the expected results.). There can be possible propagation of error of V1 activity to the V0v activity, which creates this variability.

V2a-Type-I-DH and V2a-Type-II-D showed activity only during the fast mode, V2a-VB during the slow mode, and V2a-Type-I-DL and V2a-Type-I-DM during the intermediate mode (Figures 19, 24, and 30). This was not surprising, as these neuronal populations directly received stimulation in their respective swimming modes. V2a-Type-I-DH and V2a-Type-II-D populations having high rheobase values were sufficient for them not to be triggered in slower swim modes. V2a-VBs have a low rheobase and can be activated easily. However, the inhibition they received from almost every inhibitory neuronal group in the model was a guarantee that they were completely silenced in the fast modes.

The optic stimulation tests where both V2as and V0vs, or only V2as, were simultaneously activated were successful and generated swimming-like behaviour (Simulation of Optogenetic Stimulation). These tests are very similar to the swimming tests that were run, with two major differences. The first one is that the swim tests have selective activations to imitate the supraspinal inputs, triggering different swimming speeds. In neither slow, intermediate, or fast swim modes were all excitatory neurons stimulated simultaneously. The second difference is that there was no rostrocaudal delay in the optogenetic stimulation test modes, whereas a delay was added to swim test modes to imitate the delay from the supraspinal regions. Despite these differences, the results were similar: a rostrocaudal delay was intrinsically generated by the neuronal connections, and tail-beating behaviour was observed (Figure 31B, Figure 33B). These tests can be considered as an indicator of the robustness of the network that different patterns of excitations can produce similar behavioural results.

5.3.2.2 dI6s versus V0ds

V0vs and V2as are the only excitatory neuronal populations in the model. Their selective excitation was enough to generate activity, resulting in tail-beating behaviour. However, inhibition is the main contributor to the left and right alternation and rhythmicity. Fine-tuning the connectivity patterns of the inhibitory neurons turned out to be more complicated than working with excitatory neurons.

Among the inhibitory neuronal groups, dI6s and V0ds are recruited at different swimming speeds (Picton et al., 2022; Satou et al., 2020). dI6s are involved in contralateral inhibition during slow and intermediate swimming, whereas V0ds during fast swimming. The results observed from my model were consistent with these expectations (Figures 19, 24, and 30). dI6s were active during slow and intermediate swimming but completely silent during fast swimming. V0ds, on the other hand, were completely silent during slow mode but active at variable degrees during the intermediate and fast modes.

As can be seen, there was a big overlap in the activity of dI6s and V0ds. Furthermore, the activity of dI6 increases during the intermediate modes at the same time V0ds get into the picture (Figure 24). To the best of my knowledge, whether there is an overlapping activity of these two populations exists is not clear. To make things more complicated, dI6s and V0ds can both be studied under the name of CoBL without a distinction (Liao and Fetcho, 2008; McLean et al., 2007; Svara et al., 2018), which makes fine-tuning the activities of these inhibitory neuronal groups more challenging.

On another aspect, there was no dI6 spiking activity in fast modes, as expected (Figure 30). However, this was not due to dI6 inhibition, as suggested in the literature (Satou et al., 2020), but rather the lack of activation (data not shown). They were silent, but they were not silenced. They receive strong inhibition from V1s, which shows no purpose in the model. Therefore, there is an apparent lack of excitatory input to these neuronal pools at the model's current state.

On a positive note, the glycine inhibition study replication where dI6 outgoing projections were deactivated and V0d outgoing projections were updated to reflect GABA release only gave the expected results of disrupted left-right alternation (Figure 31C, Figure 33C).

Overall, dI6 and V0d populations were successful in creating the desired output. However, there are still places for improvement behind the scenes.

5.3.2.3 V1s and V2bs

V1 subgroup activations observed were in line with what was expected based on the literature: V1-Slows were active during the slow mode, V1-Fasts were active during the fast mode, and V1-Hybrids were active across the board (Table 3) (Kimura and Higashijima, 2019; Wilson and Sweeney, 2023). The model was able to imitate their activation pattern successively. However, their impact on the model was not as promising, as can be seen by the V1 ablation test results (Figure 40).

A similar success and failure pattern was observed with the V2b population recruitment and roles. V2b-Mixeds were recruited during the intermediate mode, whereas V2b-Glys were activated during both intermediate and fast modes (Figures 19, 24, and 30). Their involvement during intermediate swimming is unclear (Callahan et al., 2019); therefore, these results can be considered as expected. However, replicating the V2b ablation study did not generate the desired output (Figures 38 and 39). Higher and lower activity of V2bs did not result in lower and higher TBFs as expected (Callahan et al., 2019). The results were inconclusive; TBFs were lowered in some modes but increased in others.

However, the differences in measurement between the replicated study and *Sili*Fish require some attention. Callahan *et al.* (2019) focused on the change of first inter-burst intervals (IBI) when they activated the V2bs. The remaining IBIs also showed a reduction but were not as prominent. The TBF values generated by *Sili*Fish do not have detailed information on how the TBF changes across an episode. A single value is calculated for the whole episode unless there is an apparent time gap between the tail beats. Furthermore, in reality, the fish switches from one swim mode to another in a single episode (McLean et al., 2008), which is not currently incorporated in the model. It may not be possible, or fair, to try to replicate some of these studies with the current model.

One of the major handicaps of using *Sili*Fish is that the ease of using its features makes it preferable to limit the analysis to what is provided in the software. It is possible to export the spiking data and calculate the rolling TBFs across an episode rather than an individual number; however, given the vast amount of data and possible tests, it would be a much better alternative to expand *Sili*Fish to include this feature. These types of needs brought the state of *Sili*Fish to what it is now. There are no boundaries on what more can be done.

Despite the differences in the data interpretation from the two failed tests of V1 inhibition and V2b activity manipulations, it is apparent that the model needs more tweaking, especially in the involvements of the inhibitory neuronal groups.

5.3.2.4 MNs and Muscle cells

Slow muscle cells were only active during slow and intermediate swimming, and no activity was observed during fast swimming (Figures 19, 24, and 30). However, some activity is also expected to be observed during the fast swimming, even though reduced (Buss and Drapeau, 2002). This discrepancy may be due to the low activation of the sMN-ms-type MNs in fast mode (Figure 30, S7-C). There was some presence of sMN-ms-type activation, which has projections to both slow and fast muscle cells; however, it was not enough to trigger activity in the slow muscle cells in the fast mode. Furthermore, the activation of these MNs seems to be limited to the most caudal somite (Figure S7-C).

The analyses of spike frequency or spike count values can tell different stories on the success of cell recruitments (Figure 19). When we look at the spiking frequencies of fast muscle cells during slow mode when they should be silent, there is 11.06 Hz (IQR 8.78-13.56) activity (Figure 19A). However, the number of spikes is slim if we look at the spike count per episode. During the slow mode, the fast muscle cells on the most caudal somites show two to a maximum of five spikes in some episodes (data not shown).

Therefore, focusing only on the spike counts, we can see that pMN recruitment is only during fast mode, which aligns with the literature (Liu and Westerfield, 1988; McLean et al., 2007). sMN-m-type MNs showed higher activity in the intermediate mode compared to the fast, which seems to be inconsistent with the literature (Bello-Rojas et al., 2019; Fetcho and Mclean, 2010; Kishore et al., 2014; Knafo et al., 2017; McLean et al., 2007). They should have shown little, if any, activity during the intermediate mode and much higher activity during fast swimming. However, looking at the difference in firing behaviour of sMN-m-type MNs and pMNs (Figure 27), it is easy to see that looking at the spike count may not be the right measure for such comparisons. The bursting frequency may be a better indicator. The reason why burst count or burst frequency was not used in the data analysis was due to possible errors in firing pattern determination, as mentioned above.

Moving on, the expected neuronal populations of sMN-s-type and sMN-ms-type were recruited in slow mode. This is not surprising, as the slow mode comprises a low-level stimulation only to a small subset of excitatory neurons, and there is not much opportunity for the network to go haywire. The model works in a low gear, just enough to activate a selective group of neurons in the spinal cord and let the others wait their turns.

Overall, visually studying the plots of activities in *Sili*Fish, the recruitment patterns were similar to what was expected. However, when I started looking at other measures like spike frequency or spike count, the details I could catch by visual inspection were lost, and the results became inconclusive. This is a good indicator of better analysis features that should be incorporated to determine the recruitment levels of cellular groups.

5.4 Statistical Analysis Results

Statistical versus biological significance.

5.4.1 Impact of the Stimulation Duration

With such an extensive number of parameters, expediting the testing process and trying many different models quickly was crucial. Therefore, 500 ms was used for the stimulus episode duration for fast simulations. The model showed robustness and no visual differences during each episode. However, it was still important to double-check what the results would be if the episodes were, in fact, longer. Therefore, a comparison between twenty episodes of various lengths between 500 ms – 10 s was made (Figure 42).

Statistically, the 500 ms and 10 s episode tests formed one group, and 1, 2, and 3 s episode tests formed another group (Figure 42B). However, the statistical difference may not be that relevant in this case due to the range of TBF numbers and how they were calculated in the first place.

With 500 ms episodes and 1 s episodes, the ranges were [20.70-23.52 Hz] and [22.13-22.21 Hz]. Specifically, the range for 1 s episodes was tight, and that is probably due to the way TBF is calculated. As mentioned above, currently, *Sili*Fish does not provide the running TBF values across an episode but rather calculates a single number. This way of calculation would hide the variability across the episode; therefore, having a tight range across twenty trials is not surprising.

As the TBF values were not normally distributed, we can look at their median values for comparison. The medians were 22.59, 23.76, 23.13, 23.75, and 22.16 Hz for the five durations mentioned above. There is only a 7% difference between the highest and lowest TBF values. Considering the 20 Hz range used to determine the swimming mode (Table 1), this statistical significance can be considered biologically insignificant.

5.4.2 MN activity versus tail beat

Based on how other studies use the ventral root activity at the midpoint of the spinal cord to determine motor behaviour (Kawano et al., 2022; Kimura et al., 2013; Menelaou et al., 2014; Satou et al., 2020, 2009; Talpalar et al., 2013; Wilson et al., 2010; Zhang et al., 2011). With a similar approach, the MN activity on the sixth somite was observed during my visual inspections. To decide whether the tip of the tail movement and MN activity on the sixth somite are correlational, a pairwise comparison was made using the Kruskal-Wallis test (Figure 43, S24, S25, and S26). The tail and sixth somite activity were not significantly different from each other when all modes were pooled, as well as Slow and Inter-I modes. However, they were significantly different in the faster modes: Inter-II, Inter-III, and Fast (Figure S26).

Looking deeper into their median and IQR of the modes that show significant differences between the tail and the sixth somite: the Fast mode statistics are 58.65 (IQR 55.82-60.42) and 50.59 (IQR 48.3-53.18) for the tail and sixth somite. There is no overlap between these ranges, and TBF measured by the tail is 16% larger than the one measured by the MN activity on the sixth somite. The Inter-II mode statistics are 40.12 (IQR 38.64-41.8) and 43.84 (IQR 43.3-45.06) for the tail and sixth somite. Again, there is no overlap between these ranges and TBF measured by the tail is 8% smaller than the MN activity calculated results this time. The highest difference was observed in the Inter-III mode, with 31.22 (IQR 28.43-36.44) and 52.99 (IQR 48.96-57.71) for the tail and sixth somite. The TBF measured by the tail was smaller than the MN-measured TBF by a whopping 41%.

This discrepancy would probably be biologically significant. Further investigation is necessary to understand how a frequent left-right alternation on the sixth somite MN activity is not converted to tail beats properly. I was focused on generating the expected TBF ranges and activating certain cellular groups at each mode, and I could not reach the point of investing in such questions.

5.4.3 Impact of the target somites

I decided to include this section in my thesis, because it is an indicator of how easy it was to make a mistake. Initially, the fast mode stimulation was only to the rostral regions. I was able to generate a model that was generating TBFs, even though in the lower end, in the fast-swimming speed ranges. After several modifications, the model was not able to generate high TBFs. A serious amount of time was spent on regenerating the previous results until I figured that the real problem is not the network parameters, but how it is stimulated.

Even though experimental errors like this are time-consuming, there are lessons learned from them. There are also features born by them. A feature was implemented to compare different models to see what modifications have been done from one to another. This feature is not a complicated feature that would compare two unrelated models. Rather, it compares two different versions of the same models during the fine-tuning process. I had spent many hours on experimental errors like these, but the additional features lowered the number of such occurrences.

5.5 Limitations

"For I was conscious that I knew practically nothing..." - Plato.

The approach in creating the model for the speed microcircuits was to replicate what is already known so that the model would be a good representation of the larval zebrafish. There are many studies working on zebrafish; however, the information available is far from complete.

Adult zebrafish information can be, and sometimes was, used; however, it comes with some caveats. There are many developmental changes from larval to juvenile/adult zebrafish, which could negatively impact the model behaviour if a substitution of information is done (Björnfors et al., 2019; Svara et al., 2018). For example, the contribution of V0v is different at the larval and adult stages (Björnfors et al., 2019). Therefore, usage of knowledge of the adult zebrafish was kept to a minimum.

The existing knowledge was tried to be completed in various ways, such as approximations or deductions, as explained in the Methods section. Some of these deductions were far-fetched. For example, to derive the conductance velocity from the soma sizes, the conductance values of only two V2a-type neurons and the soma sizes from a totally different source were used. The

validity of this approach is questionable. Knowing this, these types of approximations were still done rather than starting with random numbers.

5.6 Possible Improvements (to the model and *Sili*Fish)

No rest for the wicked.

Many models can be created to generate a desired output. The model's success relies on its representation of the many aspects of the organism it is modelling, not only the output.

As seen in the tests that attempted to replicate the studies in the literature, the results were sometimes promising and other times disappointing. It is apparent that the model has to be tweaked more, so that it would pass the tests that are tried and others that have not yet been tried.

After the model is brought to a state that passes these study replications, some proposed connectivities can also be tested. For example, one study predicts there is an excitation of V1s by m-type and ms-type sMNs (Bello-Rojas et al., 2019). V1 activation by MNs was not implemented as it is merely a prediction with no information on the connectivity patterns and parameters. Regardless, it would be interesting to add this connectivity to the model and observe its impacts.

Another addition that could be added to the model is the contribution of V3 neurons to the swim amplitude (Wiggin et al., 2022). V3s have both ipsilateral and contralateral projections to MNs, which is different from any cell groups in the current model (Böhm et al., 2022; Fetcho and Mclean, 2010).

Moving further, it is also possible to model the supraspinal inputs to the current model. *Sili*Fish was expanded to include the supraspinal region, with the plan of including the supraspinal inputs to swim control. It was later removed to lower the complexity; however, it would be an important extension to the speed microcircuits.

As was initially planned, the model's complexity can also be increased gradually until the biological numbers per somite are used. The projection probabilities can be put back in place, and synaptic conductance values can be reverted doing the opposite of the approach taken during creating the reduced model. Out of curiosity, a quick and dirty attempt was made to convert the current model to full mode and run the simulation for a short time (as long-time simulations are resource-intensive). The results were not similar to the reduced model (data not shown). In fact,

they were more like the beginning stages of the reduced model, showing that a new series of fine-tuning steps had to be taken. I would suspect this new fine-tuning process would not be as challenging, and it will really be “fine” tuning, but with this level of complexity, I would not be surprised if I am mistaken.

Increasing the level of complexity would require some modifications to the software as well. The simulation speed relies on the processor of the computer used, and there is not much to be done to make the simulation run faster other than making some hardware investments. However, the memory requirement can be reduced. As mentioned in 2.2.5, two major time-dependent parameters take up memory space during the simulation. One of them is the membrane potential values of the cells, and the other is the current information passing through each synapse. The membrane potential information is crucial to see the output of the simulation, so it was always kept in the memory. The current information, on the other hand, was not kept and recreated if and when the user wanted to visualize it on a plot after the simulation was completed. Removing the current information reduced the memory requirement drastically.

To be able to handle the memory requirement of a more complex model, a better approach must be taken for the membrane potentials as well. It is not practical to have the same approach for the membrane potentials as done with the currents, as the membrane potential information is used in a window frame rather than at a specific instance only. So, it may be possible to keep only the values within that window frame, i.e. the longest time it would take for a membrane potential change in a cell to be propagated to another cell it is projecting to. This time frame would be easy to calculate by taking the projection lengths and the conduction velocities of each cell. This approach would require a more complex algorithm of reviewing the memory and cleaning up as time goes, and also would require recreating the data every time a plot is generated This is not practical and would definitely make the testing process even slower than before.

Another approach to minimize memory usage is using a database to keep the data rather than the memory. Using the database would add time to the simulation time, but at least it would increase the complexity of possible models that can be tested. The usage of the database after a certain threshold of complexity of the simulation, which can easily be calculated by the simulation time and number of cells and synapses, would be the best solution. This would allow faster

simulations for simple models, and even though slower, would make more complex models possible.

One major handicap of *Sili*Fish is its platform dependence. Only Windows users can currently use the tool. However, its architecture was created with the idea that the core functionalities could be converted to a library format later in the future. The main engine is cross-platform. One of the most important improvements that can be made to *Sili*Fish is converting it to a library so that it will be accessible to more researchers.

5.7 Significance

My hope is…

Despite the differences among different animals and how these different roles are distributed and maintained, studying simpler animals brings us closer to understanding the more complex mechanisms. Speed circuits are shown to be present in multiple organisms; however, their mechanism is not fully understood. A computational model can allow the testing of different hypotheses that may not be possible with the current experimental techniques and help understand various mechanisms.

*Sili*Fish provides an easy-to-use user interface for the researcher to generate and test spinal cord models quickly and easily. It being open-source and publicly available, its further development or usage is not limited to a specific person or institution.

5.8 Conclusion

Long story short…

Despite the technological advancements of the past decades, there are still many limitations in observing the neuronal activity in a free-swimming zebrafish. The differences in goals, perspectives and approaches of different studies make it difficult to create a complete knowledge base of neuronal architecture. Using a computational model and having the flexibility of testing different hypotheses to fill in the gaps that are not yet covered by animal studies. A computational model can be created to generate any behaviour. Therefore, it is important to base a model using actual data and continuously tweak it with the newly published research results. With more focus on the software tool development, little time was left for the model creation and analysis, which

requires extensive fine-tuning of the model parameters and tool settings for the right data analysis. The model explained in this thesis was generated using the data available to date. It has space for improvement; however, it offers a good point to start.

There were many mini hypotheses along the way. Anytime there was inconsistency, unclarity, or a lack of information available, educated guesses had to be made for various parameters without any direct link to a study. As new research becomes available, these parameter values need to be reset, and the model needs to be re-tweaked for it to be beneficial.

Bibliography

Ampatzis, K., Song, J., Ausborn, J., El Manira, A., 2013. Pattern of innervation and recruitment of different classes of motoneurons in adult zebrafish. J. Neurosci. 33, 10875–10886. https://doi.org/10.1523/JNEUROSCI.0896-13.2013

Ampatzis, K., Song, J., Ausborn, J., ElManira, A., 2014. Separate Microcircuit Modules of Distinct V2a Interneurons and Motoneurons Control the Speed of Locomotion. Neuron 83, 934–943. https://doi.org/10.1016/j.neuron.2014.07.018

Andrzejczuk, L.A., Banerjee, S., England, S.J., Voufo, C., Kamara, K., Lewis, K.E., 2018. Tal1, Gata2a, and Gata3 have distinct functions in the development of V2b and cerebrospinal fluid-contacting KA spinal neurons. Front. Neurosci. 12, 1–24. https://doi.org/10.3389/fnins.2018.00170

Antanas, Martynas, Gediminas, Ty, Paul, Anthony, Alan, 2022. amCharts 5.

Arber, S., 2012. Motor Circuits in Action: Specification, Connectivity, and Function. Neuron 74, 975–989. https://doi.org/10.1016/j.neuron.2012.05.011

Arber, S., Costa, R.M., 2018. Connecting neuronal circuits for movement. Science (80-.). 360, 1403–1404. https://doi.org/10.1126/science.aat5994

Asakawa, K., Abe, G., Kawakami, K., 2013. Cellular dissection of the spinal cord motor column by BAC transgenesis and gene trapping in zebrafish. Front. Neural Circuits 7, 100. https://doi.org/10.3389/fncir.2013.00100

Asakawa, K., Handa, H., Kawakami, K., 2021. Illuminating ALS Motor Neurons With Optogenetics in Zebrafish. Front. Cell Dev. Biol. 9, 1–8. https://doi.org/10.3389/fcell.2021.640414

Asturiano, V., 2022a. force-graph. https://doi.org/https://github.com/vasturiano/force-graph

Asturiano, V., 2022b. 3d-force-graph.

Ausborn, J., Mahmood, R., El Manira, A., 2012. Decoding the rules of recruitment of excitatory interneurons in the adult zebrafish locomotor network. Proc. Natl. Acad. Sci. U. S. A. 109. https://doi.org/10.1073/pnas.1216256110

Bagnall, M.W., McLean, D.L., 2014. Modular Organization of Axial Microcircuits in Zebrafish. Science (80-.). 343, 197–200. https://doi.org/10.1126/science.1245629

Batista, M.F., Jacobstein, J., Lewis, K.E., 2008. Zebrafish V2 cells develop into excitatory CiD and Notch signalling dependent inhibitory VeLD interneurons. Dev. Biol. 322, 263–275. https://doi.org/10.1016/j.ydbio.2008.07.015

Bello-Rojas, S., Istrate, A.E., Kishore, S., McLean, D.L., 2019. Central and peripheral innervation

patterns of defined axial motor units in larval zebrafish. J. Comp. Neurol. 527, 2557–2572. https://doi.org/10.1002/cne.24689

Berg, E.M., Björnfors, E.R., Pallucchi, I., Picton, L.D., El Manira, A., 2018. Principles Governing Locomotion in Vertebrates: Lessons From Zebrafish. Front. Neural Circuits 12, 1–18. https://doi.org/10.3389/fncir.2018.00073

Berg, E.M., Mrowka, L., Bertuzzi, M., Madrid, D., Picton, L.D., Berg, E.M., Mrowka, L., Bertuzzi, M., Madrid, D., Picton, L.D., El Manira, A., 2023. Brainstem circuits encoding start, speed, and duration of swimming in adult zebrafish. Neuron 111, 372-386.e4. https://doi.org/10.1016/j.neuron.2022.10.034

Bhatt, D.H., McLean, D.L., Hale, M.E., Fetcho, J.R., 2007. Grading Movement Strength by Changes in Firing Intensity versus Recruitment of Spinal Interneurons. Neuron 53, 91–102. https://doi.org/10.1016/j.neuron.2006.11.011

Björnfors, E.R., El Manira, A., 2016. Functional diversity of excitatory commissural interneurons in adult zebrafish. Elife 5, 1–15. https://doi.org/10.7554/eLife.18579

Björnfors, E.R., Picton, L.D., Song, J., El Manira, A., 2019. Diversity of neurons and circuits controlling the speed and coordination of locomotion. Curr. Opin. Physiol. 8, 170–176. https://doi.org/10.1016/j.cophys.2019.02.006

Böhm, U.L., Kimura, Y., Kawashima, T., Ahrens, M.B., Higashijima, S. ichi, Engert, F., Cohen, A.E., 2022. Voltage imaging identifies spinal circuits that modulate locomotor adaptation in zebrafish. Neuron 110, 1211-1222.e4. https://doi.org/10.1016/j.neuron.2022.01.001

Bose, P., Armstrong, G.A.B., Drapeau, P., 2019. Neuromuscular junction abnormalities in a zebrafish loss-of-function model of TDP-43. J. Neurophysiol. 121, 285–297. https://doi.org/10.1152/jn.00265.2018

Bott, E., Stinson, C., 2019. Windows 10 inside out. Microsoft Press.

Bouvier, J., Caggiano, V., Leiras, R., Caldeira, V., Bellardita, C., Balueva, K., Fuchs, A., Kiehn, O., 2015. Descending Command Neurons in the Brainstem that Halt Locomotion. Cell 163, 1191–1203. https://doi.org/10.1016/j.cell.2015.10.074

Box, G.E.P., 1979. Robustness in the Strategy of Scientific Model Building. Robustness Stat. 201–236. https://doi.org/10.1016/b978-0-12-438150-6.50018-2

Brown, T.G., 1911. The Intrinsic Factors in the Act of Progression in the Mammal. Proc. R. Soc. London 84, 308–319.

Brownstone, R.M., Bui, T. V., 2010. Spinal interneurons providing input to the final common path during locomotion, Progress in Brain Research. Elsevier B.V. https://doi.org/10.1016/B978-0-444-53613-6.00006-X

Buchanan, J.T., Sten, G., 1987. Newly Identified ` Glutamate Interneurons ' and their Role in

Locomotion in the Lamprey Spinal Cord Author (s): James T . Buchanan and Sten Grillner Source : Science , New Series , Vol . 236 , No . 4799 (Apr . 17 , 1987), pp . 312-314 Published by : A. Adv. Sci. 236, 312–314.

Budick, S.A., O'Malley, D.M., 2000. Locomotor repertoire of the larval zebrafish: Swimming, turning and prey capture. J. Exp. Biol. 203, 2565–2579. https://doi.org/10.1242/jeb.203.17.2565

Buhl, E., Soffe, S.R., Roberts, A., 2015. Sensory initiation of a co-ordinated motor response: Synaptic excitation underlying simple decision-making. J. Physiol. 593, 4423–4437. https://doi.org/10.1113/JP270792

Bui, T. V., Brownstone, R.M., 2015. Sensory-evoked perturbations of locomotor activity by sparse sensory input: A computational study. J. Neurophysiol. 113, 2824–2839. https://doi.org/10.1152/jn.00866.2014

Bui, T. V., Grande, G., Rose, P.K., 2008. Relative location of inhibitory synapses and persistent inward currents determines the magnitude and mode of synaptic amplification in motoneurons. J. Neurophysiol. 99, 583–594. https://doi.org/10.1152/jn.00718.2007

Bui, T. V., Stifani, N., Akay, T., Brownstone, R.M., 2016. Spinal microcircuits comprising dI3 interneurons are necessary for motor functional recovery following spinal cord transection. Elife 5, 1–20. https://doi.org/10.7554/eLife.21715

Buss, R.R., Bourque, C.W., Drapeau, P., 2003. Membrane properties related to the firing behavior of zebrafish motoneurons. J. Neurophysiol. 89, 657–664. https://doi.org/10.1152/jn.00324.2002

Buss, R.R., Drapeau, P., 2002. Activation of Embryonic Red and White Muscle Fibers During Fictive Swimming in the Developing Zebrafish. J. Neurophysiol. 87, 1244–1251. https://doi.org/10.1152/jn.00659.2001

Buss, R.R., Drapeau, P., 2001. Synaptic drive to motoneurons during fictive swimming in the developing zebrafish. J. Neurophysiol. 86, 197–210. https://doi.org/10.1152/jn.2001.86.1.197

Buss, R.R., Drapeau, P., 2000. Physiological Properties of Zebrafish Embryonic Red and White Muscle Fibers During Early Development. J. Neurophysiol. 84, 1545–1557. https://doi.org/https://doi.org/10.1152/jn.2000.84.3.1545

Cabelguen, J.M., Bourcier-Lucas, C., Dubuc, R., 2003. Bimodal locomotion elicited by electrical stimulation of the midbrain in the salamander Notophthalmus viridescens. J. Neurosci. 23, 2434–2439. https://doi.org/10.1523/jneurosci.23-06-02434.2003

Callahan, R.A., Roberts, R., Sengupta, M., Kimura, Y., Higashijima, S.I., Bagnall, M.W., 2019. Spinal V2b neurons reveal a role for ipsilateral inhibition in speed control. Elife 8, 1–27. https://doi.org/10.7554/eLife.47837

Capelli, P., Pivetta, C., Esposito, M.S., Arber, S., 2017. Locomotor speed control circuits in the caudal brainstem. Nature 551, 373–377. https://doi.org/10.1038/nature24064

Carbo-Tano, M., Lapoix, M., Jia, X., Thouvenin, O., Pascucci, M., Auclair, F., Quan, F.B., Albadri, S., Aguda, V., Farouj, Y., Hillman, E.M.C., Portugues, R., Del Bene, F., Thiele, T.R., Dubuc, R., Wyart, C., 2023. The mesencephalic locomotor region recruits V2a reticulospinal neurons to drive forward locomotion in larval zebrafish. Nat. Neurosci. 26, 1775–1790. https://doi.org/10.1038/s41593-023-01418-0

Carbo-Tano, M., Mathilde, L., Jia, X., Auclair, F., Dubuc, R., Wyart, C., 2022. Functional coupling of the mesencephalic locomotor region and V2a reticulospinal neurons driving forward locomotion. bioRxiv 1–42. https://doi.org/https://doi.org/10.1101/2022.04.01.486703

Carlin, K.P., Bui, T. V., Dai, Y., Brownstone, R.M., 2009. Staircase currents in motoneurons: Insight into the spatial arrangement of calcium channels in the dendritic tree. J. Neurosci. 29, 5343–5353. https://doi.org/10.1523/JNEUROSCI.5458-08.2009

Choi, T.Y., Choi, T.I., Lee, Y.R., Choe, S.K., Kim, C.H., 2021. Zebrafish as an animal model for biomedical research. Exp. Mol. Med. 53, 310–317. https://doi.org/10.1038/s12276-021-00571-5

Dal Maschio, M., Donovan, J.C., Helmbrecht, T.O., Baier, H., 2017. Linking Neurons to Network Function and Behavior by Two-Photon Holographic Optogenetics and Volumetric Imaging NeuroResource Linking Neurons to Network Function and Behavior by Two-Photon Holographic Optogenetics and Volumetric Imaging. Neuron 94, 774-789.e5. https://doi.org/10.1016/j.neuron.2017.04.034

Del Pozo, A., Manuel, R., Gonzalez, A.B.I., Koning, H.K., Habicher, J., Zhang, H., Allalou, A., Kullander, K., Boije, H., 2020. Behavioral characterization of dmrt3a mutant zebrafish reveals crucial aspects of vertebrate locomotion through phenotypes related to acceleration. eNeuro 7, 1–13. https://doi.org/10.1523/ENEURO.0047-20.2020

Demin, K.A., Meshalkina, D.A., Volgin, A.D., Yakovlev, O. V., de Abreu, M.S., Alekseeva, P.A., Friend, A.J., Lakstygal, A.M., Zabegalov, K., Amstislavskaya, T.G., Strekalova, T., Bao, W., Kalueff, A. V., 2019. Developing zebrafish experimental animal models relevant to schizophrenia. Neurosci. Biobehav. Rev. 105, 126–133. https://doi.org/10.1016/j.neubiorev.2019.07.017

Devoto, S.H., Melançon, E., Eisen, J.S., Westerfield, M., 1996. Identification of separate slow and fast muscle precursor cells in vivo, prior to somite formation. Development 122, 3371–3380. https://doi.org/10.1242/dev.122.11.3371

Dou, Y., Andersson-Lendahl, M., Arner, A., 2008. Structure and function of skeletal muscle in zebrafish early larvae. J. Gen. Physiol. 131, 445–453. https://doi.org/10.1085/jgp.200809982

Downes, G.B., Granato, M., 2006. Supraspinal input is dispensable to generate glycine-mediated locomotive behaviors in the zebrafish embryo. J. Neurobiol. 66, 437–451. https://doi.org/10.1002/neu.20226

Drapeau, P., Saint-Amant, L., Buss, R.R., Chong, M., McDearmid, J.R., Brustein, E., 2002. Development of the locomotor network in zebrafish, Progress in Neurobiology. https://doi.org/10.1016/S0301-0082(02)00075-8

Dubuc, R., Brocard, F., Antri, M., Fénelon, K., Gariépy, J.F., Smetana, R., Ménard, A., Le Ray, D., Viana Di Prisco, G., Pearlstein, É., Sirota, M.G., Derjean, D., St-Pierre, M., Zielinski, B., Auclair, F., Veilleux, D., 2008. Initiation of locomotion in lampreys. Brain Res. Rev. 57, 172–182. https://doi.org/10.1016/j.brainresrev.2007.07.016

Dulhunty, A.F., 1992. The Voltage-Activation of Contraction in Skeletal Muscle. Prog. Biophys. Mol. Biol. 57, 181–223.

Eisen, J.S., Pike, S.H., Romacier, B., 1990. An Identified Motoneuron with Variable Fates in Embryonic Zebrafish. J. Neurosci. 10, 34–43.

Eklöf-Ljunggren, E., Haupt, S., Ausborn, J., Dehnisch, I., Uhleń, P., Higashijima, S.I., El Manira, A., 2012. Origin of excitation underlying locomotion in the spinal circuit of zebrafish. Proc. Natl. Acad. Sci. U. S. A. 109, 5511–5516. https://doi.org/10.1073/pnas.1115377109

Eklöf Ljunggren, E., Haupt, S., Ausborn, J., Ampatzis, K., El Manira, A., 2014. Optogenetic activation of excitatory premotor interneurons is sufficient to generate coordinated locomotor activity in larval zebrafish. J. Neurosci. 34, 134–139. https://doi.org/10.1523/JNEUROSCI.4087-13.2014

Fetcho, J.R., Higashijima, S. ichi, McLean, D.L., 2008. Zebrafish and motor control over the last decade. Brain Res. Rev. 57, 86–93. https://doi.org/10.1016/j.brainresrev.2007.06.018

Fetcho, J.R., Mclean, D.L., 2010. Some principles of organization of spinal neurons underlying locomotion in zebrafish and their implications. Ann. N. Y. Acad. Sci. 1198, 94–104. https://doi.org/10.1111/j.1749-6632.2010.05539.x

Fidelin, K., Djenoune, L., Stokes, C., Prendergast, A., Gomez, J., Baradel, A., Del Bene, F., Wyart, C., 2015. State-dependent modulation of locomotion by GABAergic spinal sensory neurons. Curr. Biol. 25, 3035–3047. https://doi.org/10.1016/j.cub.2015.09.070

Fidelin, K., Wyart, C., 2014. Inhibition and motor control in the developing zebrafish spinal cord. Curr. Opin. Neurobiol. 26, 103–109. https://doi.org/10.1016/j.conb.2013.12.016

Fuiman, L.A., Webb, P.W., 1988. Ontogeny of routine swimming activity and performance in zebra danios (Teleostei: Cyprinidae). Anim. Behav. 36, 250–261. https://doi.org/10.1016/S0003-3472(88)80268-9

Gabriel, J.P., Ausborn, J., Ampatzis, K., Mahmood, R., Eklöf-Ljunggren, E., El Manira, A., 2011. Principles governing recruitment of motoneurons during swimming in zebrafish. Nat. Neurosci. 14, 93–100. https://doi.org/10.1038/nn.2704

Gerstner, W., Kistler, W.M., Naud, R., Paninski, L., 2014. Neuronal Dynamics, From Single Neurons to Networks and Models of Cognition.

Getting, P.A., Lennard, P.R., Hume, R.I., 1980. Central pattern generator mediating swimming in Tritonia. I. Identification and synaptic interactions. J. Neurophysiol. 44, 151–164. https://doi.org/10.1152/jn.1980.44.1.151

Giacomelli, D., 2022. GeneticSharp.

Gosgnach, S., Lanuza, G.M., Butt, S.J.B., Saueressig, H., Zhang, Y., Velasquez, T., Riethmacher, D., Callaway, E.M., Kiehn, O., Goulding, M., 2006. V1 spinal neurons regulate the speed of vertebrate locomotor outputs. Nature 440, 215–219. https://doi.org/10.1038/nature04545

Goulding, M., 2009. Circuits controlling vertebrate locomotion: Moving in a new direction. Nat. Rev. Neurosci. 10, 507–518. https://doi.org/10.1038/nrn2608

Grillner, S., El Manira, A., 2020. Current principles of motor control, with special reference to vertebrate locomotion. Physiol. Rev. 100, 271–320. https://doi.org/10.1152/physrev.00015.2019

Grillner, S., McClellan, A., Perret, C., 1981. Entrainment of the spinal pattern generators for swimming by mechano-sensitive elements in the lamprey spinal cord in vitro. Brain Res. 217, 380–386. https://doi.org/10.1016/0006-8993(81)90015-9

Grillner, S., Wallén, P., Saitoh, K., Kozlov, A., Robertson, B., 2008. Neural bases of goal-directed locomotion in vertebrates-An overview. Brain Res. Rev. 57, 2–12. https://doi.org/10.1016/j.brainresrev.2007.06.027

Hale, M.E., Ritter, D.A., Fetcho, J.R., 2001. A confocal study of spinal interneurons in living larval zebrafish. J. Comp. Neurol. 437, 1–16. https://doi.org/10.1002/cne.1266

Hejlsberg, A., Wiltamuth, S., Golde, P., 2003. C\# language specification. Addison-Wesley Longman Publishing Co., Inc.

Higashijima, S.I., Masino, M.A., Mandel, G., Fetcho, J.R., 2004a. Engrailed-1 expression marks a primitive class of inhibitory spinal interneuron. J. Neurosci. 24, 5827–5839. https://doi.org/10.1523/JNEUROSCI.5342-03.2004

Higashijima, S.I., Schaefer, M., Fetcho, J.R., 2004b. Neurotransmitter properties of spinal interneurons in embryonic and larval zebrafish. J. Comp. Neurol. 480, 19–37. https://doi.org/10.1002/cne.20279

Hille, B., 2001. Ion Channels of Excitable Membranes, 3rd ed. Sinauer Associates, Inc.

Hirata, H., Iida, A. (Eds.), 2018. Zebrafish, Medaka, and Other Small Fishes, Zebrafish, Medaka, and Other Small Fishes. Springer. https://doi.org/10.1007/978-981-13-1879-5

Hoo, J.Y., Kumari, Y., Shaikh, M.F., Hue, S.M., Goh, B.H., 2016. Zebrafish: A Versatile Animal Model for Fertility Research. Biomed Res. Int. 2016. https://doi.org/10.1155/2016/9732780

Howe, K., Clark, M.D., et al, _, 2013. The zebrafish reference genome sequence and its

relationship to the human genome. Nature 496, 498–503. https://doi.org/10.1038/nature12111

Hsu, L.J., Bertho, M., Kiehn, O., 2023. Deconstructing the modular organization and real-time dynamics of mammalian spinal locomotor networks. Nat. Commun. 14, 873. https://doi.org/10.1038/s41467-023-36587-w

Huang, K.H., Ahrens, M.B., Dunn, T.W., Engert, F., 2013. Spinal projection neurons control turning behaviors in zebrafish. Curr. Biol. 23, 1566–1573. https://doi.org/10.1016/j.cub.2013.06.044

Hull, M.J., Soffe, S.R., Willshaw, D.J., Roberts, A., 2016. Modelling Feedback Excitation, Pacemaker Properties and Sensory Switching of Electrically Coupled Brainstem Neurons Controlling Rhythmic Activity. PLoS Comput. Biol. 12, 1–19. https://doi.org/10.1371/journal.pcbi.1004702

IBM Corp., 2023. IBM SPSS Statistics for Windows.

Izhikevich, E.M., 2007. Dynamical Systems in Neuroscience, Dynamical Systems in Neuroscience. The MIT Press. https://doi.org/10.7551/mitpress/2526.001.0001

Izhikevich, E.M., 2003. Simple model of spiking neurons. IEEE Trans. Neural Networks 14, 1569–1572. https://doi.org/10.1109/TNN.2003.820440

Jay, M., McLean, D.L., 2019. Reconciling the functions of even-skipped interneurons during crawling, swimming, and walking. Curr. Opin. Physiol. 8, 188–192. https://doi.org/10.1016/j.cophys.2019.02.003

Juvin, L., Grätsch, S., Trillaud-Doppia, E., Gariépy, J.F., Büschges, A., Dubuc, R., 2016. A Specific Population of Reticulospinal Neurons Controls the Termination of Locomotion. Cell Rep. 15, 2377–2386. https://doi.org/10.1016/j.celrep.2016.05.029

Kawano, K., Kato, K., Sugioka, T., Kimura, Y., Tanimoto, M., Higashijima, S., 2022. Long descending commissural V0v neurons ensure coordinated swimming movements along the body axis in larval zebrafish. Sci. Rep. 12, 1–12. https://doi.org/10.1038/s41598-022-08283-0

Kiehn, O., 2016. Decoding the organization of spinal circuits that control locomotion. Nat. Rev. Neurosci. 17, 224–238. https://doi.org/10.1038/nrn.2016.9

Kimmel, C.B., Powell, S.L., Metcalfe, W.K., 1982. Brain Neurons Which Project to the Spinal Cord in Young Larvae of the Zebrafish. J. Comp. Neurol. 127, 112–127. https://doi.org/10.1002/cne.902050203

Kimura, Y., Higashijima, S. ichi, 2019. Regulation of locomotor speed and selection of active sets of neurons by V1 neurons. Nat. Commun. 10, 1–12. https://doi.org/10.1038/s41467-019-09871-x

Kimura, Y., Okamura, Y., Higashijima, S.I., 2006. alx, a zebrafish homolog of Chx10, marks ipsilateral descending excitatory interneurons that participate in the regulation of spinal locomotor circuits. J. Neurosci. 26, 5684–5697. https://doi.org/10.1523/JNEUROSCI.4993-05.2006

Kimura, Y., Satou, C., Fujioka, S., Shoji, W., Umeda, K., Ishizuka, T., Yawo, H., Higashijima, S.I., 2013. Hindbrain V2a neurons in the excitation of spinal locomotor circuits during zebrafish swimming. Curr. Biol. 23, 843–849. https://doi.org/10.1016/j.cub.2013.03.066

Kinkhabwalaa, A., Riley, M., Koyama, M., Monen, J., Satou, C., Kimura, Y., Higashijima, S.I., Fetcho, J., 2011. A structural and functional ground plan for neurons in the hindbrain of zebrafish. Proc. Natl. Acad. Sci. U. S. A. 108, 1164–1169. https://doi.org/10.1073/pnas.1012185108

Kishore, S., Bagnall, M.W., McLean, D.L., 2014. Systematic shifts in the balance of excitation and inhibition coordinate the activity of axial motor pools at different speeds of locomotion. J. Neurosci. 34, 14046–14054. https://doi.org/10.1523/JNEUROSCI.0514-14.2014

Kishore, S., Cadoff, E.B., Agha, M.A., McLean, D.L., 2020. Orderly compartmental mapping of premotor inhibition in the developing zebrafish spinal cord. Science (80-.). 370, 431–436. https://doi.org/10.1126/science.abb4608

Knafo, S., Fidelin, K., Prendergast, A., Tseng, P.E.B., Parrin, A., Dickey, C., Böhm, U.L., Figueiredo, S.N., Thouvenin, O., Pascal-Moussellard, H., Wyart, C., 2017. Mechanosensory neurons control the timing of spinal microcircuit selection during locomotion. Elife 6, 1–21. https://doi.org/10.7554/eLife.25260

Knogler, L.D., Ryan, J., Saint-Amant, L., Drapeau, P., 2014. A hybrid electrical/chemical circuit in the spinal cord generates a transient embryonic motor behavior. J. Neurosci. 34, 9644–9655. https://doi.org/10.1523/JNEUROSCI.1225-14.2014

Kozlov, A.K., Kardamakis, A.A., Kotaleski, J.H., Grillner, S., 2014. Gating of steering signals through phasic modulation of reticulospinal neurons during locomotion. Proc. Natl. Acad. Sci. U. S. A. 111, 3591–3596. https://doi.org/10.1073/pnas.1401459111

Laliberte, A.M., Goltash, S., Lalonde, N.R., Bui, T.V., 2019. Propriospinal Neurons: Essential Elements of Locomotor Control in the Intact and Possibly the Injured Spinal Cord. Front. Cell. Neurosci. 13, 1–16. https://doi.org/10.3389/fncel.2019.00512

Lanuza, G.M., Gosgnach, S., Pierani, A., Jessell, T.M., Goulding, M., 2004. Genetic identification of spinal interneurons that coordinate left-right locomotor activity necessary for walking movements. Neuron 42, 375–386. https://doi.org/10.1016/S0896-6273(04)00249-1

Leiras, R., Cregg, J.M., Kiehn, O., 2022. Brainstem Circuits for Locomotion. Annu. Rev. Neurosci. 45, 63–85. https://doi.org/10.1146/annurev-neuro-082321-025137

Liao, J.C., Fetcho, J.R., 2008. Shared versus specialized glycinergic spinal interneurons in axial motor circuits of larval zebrafish. J. Neurosci. 28, 12982–12992.

https://doi.org/10.1523/JNEUROSCI.3330-08.2008

Lieschke, G.J., Currie, P.D., 2007. Animal models of human disease: Zebrafish swim into view. Nat. Rev. Genet. 8, 353–367. https://doi.org/10.1038/nrg2091

Liu, D.W., Westerfield, M., 1988. Function of Identified Motoneurones and Co-ordination of Primary and Secondary Motor Systems During Zebra Fish Swimming. J. Physiol. 403, 73–89.

Luna, V.M., Brehm, P., 2006. An electrically coupled network of skeletal muscle in zebrafish distributes synaptic current. J. Gen. Physiol. 128, 89–102. https://doi.org/10.1085/jgp.200609501

Luna, V.M., Daikoku, E., Ono, F., 2015. "Slow" skeletal muscles across vertebrate species. Cell Biosci. 5. https://doi.org/10.1186/s13578-015-0054-6

Mainen, Z.F., Joerges, J., Huguenard, J.R., Sejnowski, T.J., 1995. A Model of Spike Initiation in Neocortical Pyramidal Neurons. Neuron 15, 1427–1439. https://doi.org/10.1016/0896-6273(95)90020-9

Marder, E., Taylor, A.L., 2011. Multiple models to capture the variability in biological neurons and networks. Nat. Neurosci. 14, 133–138. https://doi.org/10.1038/nn.2735

Masino, M.A., Fetcho, J.R., 2005. Fictive swimming motor patterns in wild type and mutant larval zebrafish. J. Neurophysiol. 93, 3177–3188. https://doi.org/10.1152/jn.01248.2004

McDearmid, J.R., Drapeau, P., 2006. Rhythmic motor activity evoked by NMDA in the spinal zebrafish larva. J. Neurophysiol. 95, 401–417. https://doi.org/10.1152/jn.00844.2005

McLean, D.L., Fan, J., Higashijima, S.I., Hale, M.E., Fetcho, J.R., 2007. A topographic map of recruitment in spinal cord. Nature 446, 71–75. https://doi.org/10.1038/nature05588

McLean, D.L., Fetcho, J.R., 2009. Spinal interneurons differentiate sequentially from those driving the fastest swimming movements in larval zebrafish to those driving the slowest ones. J. Neurosci. 29, 13566–13577. https://doi.org/10.1523/JNEUROSCI.3277-09.2009

McLean, D.L., Masino, M.A., Koh, I.Y.Y., Lindquist, W.B., Fetcho, J.R., 2008. Continuous shifts in the active set of spinal interneurons during changes in locomotor speed. Nat. Neurosci. 11, 1419–1429. https://doi.org/10.1038/nn.2225

Menelaou, E., McLean, D.L., 2019. Hierarchical control of locomotion by distinct types of spinal V2a interneurons in zebrafish. Nat. Commun. 10, 1–12. https://doi.org/10.1038/s41467-019-12240-3

Menelaou, E., McLean, D.L., 2012. A gradient in endogenous rhythmicity and oscillatory drive matches recruitment order in an axial motor pool. J. Neurosci. 32, 10925–10939. https://doi.org/10.1523/JNEUROSCI.1809-12.2012

Menelaou, E., Vandunk, C., McLean, D.L., 2014. Differences in the morphology of spinal V2a neurons reflect their recruitment order during swimming in larval Zebrafish. J. Comp. Neurol. 522, 1232–1248. https://doi.org/10.1002/cne.23465

Microsoft, 2022. Microsoft Visual Studio Community 2022.

Montgomery, J.E., Wahlstrom-Helgren, S., Vanpelt, K.T., Masino, M.A., 2021. Repetitive optogenetic stimulation of glutamatergic neurons: An alternative to NMDA treatment for generating locomotor activity in spinalized zebrafish larvae. Physiol. Rep. 9, 1–13. https://doi.org/10.14814/phy2.14774

Moore, L.A., Trussell, L.O., 2017. Corelease of inhibitory neurotransmitters in the mouse auditory midbrain. J. Neurosci. 37, 9453–9464. https://doi.org/10.1523/JNEUROSCI.1125-17.2017

Moreno, R.L., Ribera, A.B., 2009. Zebrafish motor neuron subtypes differ electrically prior to axonal outgrowth. J. Neurophysiol. 102, 2477–2484. https://doi.org/10.1152/jn.00446.2009

Müller, U.K., Van Leeuwen, J.L., 2004. Swimming of larval zebrafish: Ontogeny of body waves and implications for locomotory development. J. Exp. Biol. 207, 853–868. https://doi.org/10.1242/jeb.00821

Myers, P.Z., Eisen, J.S., Westerfield, M., 1986. Development Zebrafish and Axonal Outgrowth of Identified Motoneurons in the. J. Neurosci. 6, 2278–2289.

Naganawa, Y., Hirata, H., 2011. Developmental transition of touch response from slow muscle-mediated coilings to fast muscle-mediated burst swimming in zebrafish. Dev. Biol. 355, 194–204. https://doi.org/10.1016/j.ydbio.2011.04.027

Nakanishi, S.T., Whelan, P.J., 2012. A decerebrate adult mouse model for examining the sensorimotor control of locomotion. J. Neurophysiol. 107, 500–515. https://doi.org/10.1152/jn.00699.2011

Pallucchi, I., Bertuzzi, M., Michel, J.C., Miller, A.C., El Manira, A., 2022. Transformation of an early-established motor circuit during maturation in zebrafish. Cell Rep. 39, 110654. https://doi.org/10.1016/j.celrep.2022.110654

Peng, C.Y., Yajima, H., Burns, C.E., Zon, L.I., Sisodia, S.S., Pfaff, S.L., Sharma, K., 2007. Notch and MAML Signaling Drives Scl-Dependent Interneuron Diversity in the Spinal Cord. Neuron 53, 813–827. https://doi.org/10.1016/j.neuron.2007.02.019

Picton, L.D., Bertuzzi, M., Pallucchi, I., Fontanel, P., Dahlberg, E., Björnfors, E.R., Iacoviello, F., Shearing, P.R., El Manira, A., 2021. A spinal organ of proprioception for integrated motor action feedback. Neuron 109, 1188-1201.e7. https://doi.org/10.1016/j.neuron.2021.01.018

Picton, L.D., Björnfors, E.R., Fontanel, P., Pallucchi, I., Bertuzzi, M., El Manira, A., 2022. Developmental switch in the function of inhibitory commissural V0d interneurons in zebrafish. Curr. Biol. 32, 1–14. https://doi.org/10.1016/j.cub.2022.06.059

Portugues, R., Engert, F., 2011. Adaptive locomotor behavior in larval zebrafsh. Front. Syst. Neurosci. 5, 1–11. https://doi.org/10.3389/fnsys.2011.00072

Pujala, A., Koyama, M., 2019. Chronology-based architecture of descending circuits that underlie the development of locomotor repertoire after birth. Elife 8, 1–47. https://doi.org/10.7554/eLife.42135

Roberts, A., Li, W.C., Soffe, S.R., 2008a. Roles for inhibition: Studies on networks controlling swimming in young frog tadpoles. J. Comp. Physiol. A Neuroethol. Sensory, Neural, Behav. Physiol. 194, 185–193. https://doi.org/10.1007/s00359-007-0273-3

Roberts, A., Li, W.C., Soffe, S.R., Wolf, E., 2008b. Origin of excitatory drive to a spinal locomotor network. Brain Res. Rev. 57, 22–28. https://doi.org/10.1016/j.brainresrev.2007.06.015

Rossignol, S., Frigon, A., 2011. Recovery of locomotion after spinal cord injury: Some facts and mechanisms. Annu. Rev. Neurosci. 34, 413–440. https://doi.org/10.1146/annurev-neuro-061010-113746

Roussel, Y., Gaudreau, S.F., Kacer, E.R., Sengupta, M., Bui, T. V, 2021. Modeling spinal locomotor circuits for movements in developing zebrafish. Elife 10. https://doi.org/10.7554/elife.67453

Roussel, Y., Paradis, M., Gaudreau, S.F., Lindsey, B.W., Bui, T. V., 2020. Spatiotemporal transition in the role of synaptic inhibition to the tail beat rhythm of developing larval zebrafish. eNeuro 7, 1–18. https://doi.org/10.1523/ENEURO.0508-18.2020

Sagner, A., Briscoe, J., 2019. Establishing neuronal diversity in the spinal cord: A time and a place. Dev. 146. https://doi.org/10.1242/dev.182154

Saint-Amant, L., 2010. Development of motor rhythms in zebrafish embryos, Progress in Brain Research. Elsevier B.V. https://doi.org/10.1016/B978-0-444-53613-6.00004-6

Saint-Amant, L., Drapeau, P., 1998. Time course of the development of motor behaviors in the zebrafish embryo. J. Neurobiol. 37, 622–632. https://doi.org/10.1002/(SICI)1097-4695(199812)37:4<622::AID-NEU10>3.0.CO;2-S

Satou, C., Kimura, Y., Higashijima, S., 2012. Generation of multiple classes of V0 neurons in Zebrafish spinal cord: Progenitor heterogeneity and temporal control of neuronal diversity. J. Neurosci. 32, 1771–1783. https://doi.org/10.1523/JNEUROSCI.5500-11.2012

Satou, C., Kimura, Y., Kohashi, T., Horikawa, K., Takeda, H., Oda, Y., Higashijima, S.I., 2009. Functional role of a specialized class of spinal commissural inhibitory neurons during fast escapes in zebrafish. J. Neurosci. 29, 6780–6793. https://doi.org/10.1523/JNEUROSCI.0801-09.2009

Satou, C., Sugioka, T., Uemura, Y., Shimazaki, T., Zmarz, P., Kimura, Y., Higashijima, S., 2020. Functional Diversity of Glycinergic Commissural Inhibitory Neurons in Larval Zebrafish. Cell Rep. 30, 3036-3050.e4. https://doi.org/10.1016/j.celrep.2020.02.015

Sengupta, M., Bagnall, M.W., 2023. Spinal Interneurons: Diversity and Connectivity in Motor Control. Annu. Rev. Neurosci. 46, 79–99. https://doi.org/10.1146/annurev-neuro-083122-025325

Sengupta, M., Bagnall, M.W., 2022. V2b neurons act via multiple targets in spinal motor networks. bioRxiv 016413, 2022.08.01.502410.

Sengupta, M., Daliparthi, V., Roussel, Y., Bui, T. V., Bagnall, M.W., 2021. Spinal V1 neurons inhibit motor targets locally and sensory targets distally. Curr. Biol. 31, 3820-3833.e4. https://doi.org/10.1016/j.cub.2021.06.053

Severi, K.E., Böhm, U.L., Wyart, C., 2018. Investigation of hindbrain activity during active locomotion reveals inhibitory neurons involved in sensorimotor processing. Sci. Rep. 1–11. https://doi.org/10.1038/s41598-018-31968-4

Severi, K.E., Portugues, R., Marques, J.C., O 'malley, D.M., Orger, M.B., Engert, F., O'Malley, D.M., Orger, M.B., Engert, F., 2014. Neural Control and Modulation of Swimming Speed in the Larval Zebrafish. Neuron 83, 692–707. https://doi.org/10.1016/j.neuron.2014.06.032

Song, J., Dahlberg, E., El Manira, A., 2018. V2a interneuron diversity tailors spinal circuit organization to control the vigor of locomotor movements. Nat. Commun. 9, 1–14. https://doi.org/10.1038/s41467-018-05827-9

Song, J., Pallucchi, I., Ausborn, J., Ampatzis, K., Bertuzzi, M., Fontanel, P., Picton, L.D., El Manira, A., 2020. Multiple Rhythm-Generating Circuits Act in Tandem with Pacemaker Properties to Control the Start and Speed of Locomotion. Neuron 105, 1048-1061.e4. https://doi.org/10.1016/j.neuron.2019.12.030

Stefanescu, R.A., Shivakeshavan, R.G., Khargonekar, P.P., Talathi, S.S., 2013. Computational Modeling of Channelrhodopsin-2 Photocurrent Characteristics in Relation to Neural Signaling. Bull. Math. Biol. 75, 2208–2240. https://doi.org/10.1007/s11538-013-9888-4

Stellabotte, F., Devoto, S.H., 2007. The teleost dermomyotome. Dev. Dyn. 236, 2432–2443. https://doi.org/10.1002/dvdy.21253

Svara, F.N., Kornfeld, J., Denk, W., Bollmann, J.H., 2018. Volume EM Reconstruction of Spinal Cord Reveals Wiring Specificity in Speed-Related Motor Circuits. Cell Rep. 23, 2942–2954. https://doi.org/10.1016/j.celrep.2018.05.023

Talpalar, A.E., Bouvier, J., Borgius, L., Fortin, G., Pierani, A., Kiehn, O., 2013. Dual-mode operation of neuronal networks involved in left-right alternation. Nature 500, 85–88. https://doi.org/10.1038/nature12286

Thiele, T.R., Donovan, J.C., Baier, H., 2014. Descending Control of Swim Posture by a Midbrain Nucleus in Zebrafish. Neuron 83, 679–691. https://doi.org/10.1016/j.neuron.2014.04.018

Topcu, E., Roussel, Y., Bui, T. V., 2023. SiliFish: A desktop application to model swimming behavior in developing zebrafish (Danio rerio). STAR Protoc. 4, 101973.

https://doi.org/10.1016/j.xpro.2022.101973

Uemura, Y., Kato, K., Kawakami, K., Kimura, Y., Oda, Y., Higashijima, S.I., 2020. Neuronal Circuits That Control Rhythmic Pectoral Fin Movements in Zebrafish. J. Neurosci. 40, 6678–6690. https://doi.org/10.1523/JNEUROSCI.1484-20.2020

Vanderkam, D., 2022. DyGraph.

Wahlstrom-Helgren, S., Montgomery, J.E., Vanpelt, K.T., Biltz, S.L., Peck, J.H., Masino, M.A., 2019. Glutamate receptor subtypes differentially contribute to optogenetically activated swimming in spinally transected zebrafish larvae. J. Neurophysiol. 122, 2414–2426. https://doi.org/10.1152/jn.00337.2019

Wang, W.C., McLean, D.L., 2014. Selective Responses to Tonic Descending Commands by Temporal Summation in a Spinal Motor Pool. Neuron 83, 708–721. https://doi.org/10.1016/j.neuron.2014.06.021

Wen, H., Brehm, P., 2005. Paired motor neuron-muscle recordings in zebrafish test the receptor blockade model for shaping synaptic current. J. Neurosci. 25, 8104–8111. https://doi.org/10.1523/JNEUROSCI.2611-05.2005

Wen, H., Eckenstein, K., Weihrauch, V., Stigloher, C., Brehm, P., 2020. Primary and secondary motoneurons use different calcium channel types to control escape and swimming behaviors in zebrafish. PNAS 117, 26429–26437. https://doi.org/10.1073/pnas.2015866117

Westerfield, M., Mcmurray, V., Eisen, J.S., 1986. Identified Motoneurons and Their Innervation of Axial Muscles in the Zebrafish. J. Neurosci. 6, 2267–2277.

Whelan, P.J., 1996. Control of locomotion in the decerebrate cat. Prog. Neurobiol. 49, 481–515. https://doi.org/10.1016/0301-0082(96)00028-7

Wiggin, T.D., Anderson, T.M., Eian, J., Peck, J.H., Masino, M.A., 2012. Episodic swimming in the larval zebrafish is generated by a spatially distributed spinal network with modular functional organization. J. Neurophysiol. 108, 925–934. https://doi.org/10.1152/jn.00233.2012

Wiggin, T.D., Montgomery, J.E., Brunick, A.J., Peck, J.H., Masino, M.A., 2022. V3 Interneurons Are Active and Recruit Spinal Motor Neurons during In Vivo Fictive Swimming in Larval Zebrafish. eNeuro 9. https://doi.org/https://doi.org/10.1523/ENEURO.0476-21.2022 1Department

Wiggin, T.D., Peck, J.H., Masino, M.A., 2014. Coordination of fictive motor activity in the larval zebrafish is generated by non-segmental mechanisms. PLoS One 9. https://doi.org/10.1371/journal.pone.0109117

Wilson, A.C., Sweeney, L.B., 2023. Spinal cords: Symphonies of interneurons across species. Front. Neural Circuits 17. https://doi.org/10.3389/fncir.2023.1146449

Wilson, B.Y.D.M., 1961. The Central Nervous Control of Flight in a Locust. J. Exp. Biol. 38, 471–490.

Wilson, J.M., Blagovechtchenski, E., Brownstone, R.M., 2010. Genetically defined inhibitory neurons in the mouse spinal cord dorsal horn: A possible source of rhythmic inhibition of motoneurons during fictive locomotion. J. Neurosci. 30, 1137–1148. https://doi.org/10.1523/JNEUROSCI.1401-09.2010

Wu, M.Y., Carbo-Tano, M., Mirat, O., Lejeune, F.X., Roussel, J., Quan, F.B., Fidelin, K., Wyart, C., 2021. Spinal sensory neurons project onto the hindbrain to stabilize posture and enhance locomotor speed. Curr. Biol. 31, 3315-3329.e5. https://doi.org/10.1016/j.cub.2021.05.042

Yokoyama, H., Ogawa, T., Kawashima, N., Shinya, M., Nakazawa, K., 2016. Distinct sets of locomotor modules control the speed and modes of human locomotion. Sci. Rep. 6, 1–14. https://doi.org/10.1038/srep36275

Zhang, H.Y., Issberner, J., Sillar, K.T., 2011. Development of a spinal locomotor rheostat. Proc. Natl. Acad. Sci. U. S. A. 108, 11674–11679. https://doi.org/10.1073/pnas.1018512108

Zhang, Y., Narayan, S., Geiman, E., Lanuza, G.M., Velasquez, T., Shanks, B., Akay, T., Dyck, J., Pearson, K., Gosgnach, S., Fan, C.M., Goulding, M., 2008. V3 Spinal Neurons Establish a Robust and Balanced Locomotor Rhythm during Walking. Neuron 60, 84–96. https://doi.org/10.1016/j.neuron.2008.09.027

Appendices

Appendix 1. Supplementary Material

The Network

Table S1. Conductance values and outreach types of the gap junctions

Source	Target	Axon Reach Mode	Projection	Conductance (nS)	Dist. Mode	Max Out	Max In
Muscle Slow	Muscle Slow	Ipsilateral	Bifurcating	0.024	Euclidean		
pMN	pMN	Ipsilateral	Bifurcating	0.0004	Euclidean	1	1
sMN-m-type	sMN-m-type	Ipsilateral	Bifurcating	0.002	Euclidean		
sMN-ms-type	sMN-ms-type	Ipsilateral	Bifurcating	0.002	Euclidean		
sMN-s-type	sMN-s-type	Ipsilateral	Bifurcating	0.002	Euclidean		
V0v-A	sMN-ms-type	Contralateral	Ascending	0.001	Manhattan		
V0v-B	sMN-ms-type	Contralateral	Bifurcating	0.001	Manhattan		
V0v-B	sMN-s-type	Contralateral	Bifurcating	0.001	Manhattan		
V0v-D	sMN-s-type	Contralateral	Descending	0.001	Manhattan		
V2a-Type-I-DH	pMN	Ipsilateral	Descending	0.0024	Manhattan		
V2a-Type-I-DH	V0d	Ipsilateral	Descending	0.0003	Manhattan		
V2a-Type-I-DH	V2a-Type-I-DH	Ipsilateral	Descending	0.008	Manhattan		
V2a-Type-I-DH	V2a-Type-I-DM	Ipsilateral	Descending	0.002364	Manhattan		
V2a-Type-I-DH	V2a-Type-II-D	Ipsilateral	Descending	0.000482	Manhattan		
V2a-Type-I-DH	V2a-VB	Ipsilateral	Descending	0.001182	Manhattan		
V2a-Type-I-DL	sMN-m-type	Ipsilateral	Descending	0.0012	Manhattan		
V2a-Type-I-DL	sMN-ms-type	Ipsilateral	Descending	0.0012	Manhattan		
V2a-Type-I-DL	sMN-s-type	Ipsilateral	Descending	0.0012	Manhattan		
V2a-Type-I-DL	V0d	Ipsilateral	Descending	0.0003	Manhattan		
V2a-Type-I-DL	V2a-Type-I-DL	Ipsilateral	Descending	0.002002	Manhattan		
V2a-Type-I-DL	V2a-VB	Ipsilateral	Descending	0.001116	Manhattan		
V2a-Type-I-DM	sMN-m-type	Ipsilateral	Descending	0.0012	Manhattan		
V2a-Type-I-DM	sMN-ms-type	Ipsilateral	Descending	0.0012	Manhattan		
V2a-Type-I-DM	sMN-s-type	Ipsilateral	Descending	0.0012	Manhattan		
V2a-Type-I-DM	V0d	Ipsilateral	Descending	0.0003	Manhattan		
V2a-Type-I-DM	V2a-Type-I-DM	Ipsilateral	Descending	0.004004	Manhattan		
V2a-Type-I-DM	V2a-Type-II-D	Ipsilateral	Descending	0.000482	Manhattan		
V2a-Type-I-DM	V2a-VB	Ipsilateral	Descending	0.001182	Manhattan		
V2a-Type-II-D	pMN	Ipsilateral	Bifurcating	0.0041	Manhattan		
V2a-Type-II-D	sMN-m-type	Ipsilateral	Bifurcating	0.0036	Manhattan		
V2a-Type-II-D	V0d	Ipsilateral	Descending	0.00014	Manhattan		
V2a-Type-II-D	V2a-Type-II-D	Ipsilateral	Descending	0.001	Manhattan		
V2a-VB	V2a-VB	Ipsilateral	Descending	0.001472	Manhattan		

Table S2. Conductance values and outreach types of the NMJs

Source \ Target	**Muscle Fast AP**	**Muscle Slow**
pMN	↑↓ G = 5 nS	
sMN-m-type	↑↓ G = 4 nS	
sMN-ms-type	↑↓ G = 2.5 nS	↑↓ G = 0.6 nS
sMN-s-type		↑↓ G = 2 nS

↑: Ipsilateral ascending
↓: Ipsilateral descending

Table S3. Conductance values and outreach types of the chemical synapses to MNs.

All conductance values are in nS.

Source \ Target	**pMN**	**sMN-m-type**	**sMN-ms-type**	**sMN-s-type**
dI6-A	↗↘ 5.58	↗↘ 5.58	↗↘ 5.58	↗↘ 5.58
dI6-B	↗↘ 5.58	↗↘ 5.58	↗↘ 5.58	↗↘ 5.58
V0d	↗↘ 8	↗↘ 16.01	↗↘ 16.01	↗↘ 16.01
V0v-A	↗ 0.1875	↗ 0.375		
V0v-B			↗↘ 0.375	
V0v-D				↘ 0.15
V1-Fast	↑ 5.5	↑ 3	↑ 3	↑ 4.5
V1-Hybrid		↑ 2.25	↑ 2.25	↑ 2.25
V1-Slow			↑ 1.5	↑ 1.5
V2a-Type-I-DH	↑↓ 1.5	↓ 0.345		
V2a-Type-I-DL				↓ 1.035
V2a-Type-I-DM		↓ 0.828	↓ 0.9	
V2a-Type-II-D	↑↓ 0.3602	↑↓ 0.4825		
V2a-VB				↑↓ 0.7275
V2b-Gly	↓ 7	↓ 3.75		
V2b-Mixed			↓ 3.75	↓ 3.75

↗: Contralateral ascending
↘: Contralateral descending

Table S4. Conductance values and outreach types of the chemical synapses to inhibitory neurons.

All conductance values are in nS.

Source \ Target	dI6-A	dI6-B	V0d	V1-Fast	V1-Hybrid	V1-Slow	V2b-Gly	V2b-Mixed
dI6-A	↗↘ 2.13			↗↘ 3.73	↗↘ 20	↗↘ 3.73		
dI6-B		↗↘ 2.13		↗↘ 3.73	↗↘ 20	↗↘ 3.73		
V0d			↗↘ 1.5	↗↘ 10	↗↘ 10	↗↘ 29.76		
V1-Fast	↑ 7.5	↑ 7.5	↑ 7.5	↑ 1.15			↑ 2	
V1-Hybrid	↑ 7.5	↑ 7.5	↑ 7.5		↑ 0.85		↑ 1.5	↑ 1.5
V1-Slow	↑ 7.5	↑ 7.5				↑ 0.5		↑ 1.5
V2a-Type-I-DH			↓ 4	↓ 1.2	↓ 0.7		↓ 0.2	
V2a-Type-I-DL	↓ 2.5	↓ 2.5			↓ 0.6	↓ 0.4		↓ 0.2
V2a-Type-I-DM			↓ 0.996	↓ 0.1	↓ 0.326		↓ 0.1	↓ 0.2
V2a-Type-II-D								
V2a-VB	↓ 0.436	↓ 0.436		↓ 0.134	↓ 0.134			
V2b-Gly	↓ 0.695		↓ 0.695	↓ 2			↓ 0.695	
V2b-Mixed	↓ 0.695	↓ 0.695			↓ 2	↓ 2		↓ 0.695

Table S5. Conductance values and outreach types of the chemical synapses to excitatory neurons.

All conductance values are in nS.

Source \ Target	V0v-A	V0v-B	V0v-D	V2a-Type-I-DH	V2a-Type-I-DL	V2a-Type-I-DM	V2a-Type-II-D	V2a-VB
dI6-A				↗↘ 2.98	↗↘ 0.55875	↗↘ 0.745		↗↘ 2.98
dI6-B				↗↘ 2.98	↗↘ 0.55875	↗↘ 2.98		↗↘ 2.98
V0d				↗↘ 3	↗↘ 20	↗↘ 1.5		↗↘ 2.232
V1-Fast	↑ 0.75	↑ 0.75	↑ 8	↑ 3.75 ↓ 1	↑ 3.75 ↓ 0.75	↑ 3.75 ↓ 0.75	↑ 5 ↓ 1	↑ 3.75 ↓ 0.75
V1-Hybrid	↑ 0.75	↑ 0.75	↑ 3	↑ 3.75 ↓ 0.75	↑ 5 ↓ 1	↑ 3.75 ↓ 0.75	↑ 5 ↓ 1	↑ 3.75 ↓ 0.75
V1-Slow	↑ 0.75	↑ 0.75	↑ 2	↑ 3.75 ↓ 0.75	↑ 2.5 ↓ 0.5	↑ 3.75 ↓ 0.75	↑ 3.75 ↓ 0.75	↑ 3.75 ↓ 0.75
V2a-Type-I-DH	↓ 0.275	↓ 0.2		↑↓ 1			↑↓ 1.5	
V2a-Type-I-DL					↑↓ 0.5	↑↓ 0.1		
V2a-Type-I-DM	↓ 0.2	↓ 0.2				↑↓ 0.3	↑↓ 0.25	
V2a-VB		↓ 0.91					↑↓ 1.34	
V2b-Gly	↓ 0.695	↓ 0.695		↓ 3.25		↓ 3.25	↓ 4	
V2b-Mixed			↓ 0.695				↓ 3.25	↓ 3.25

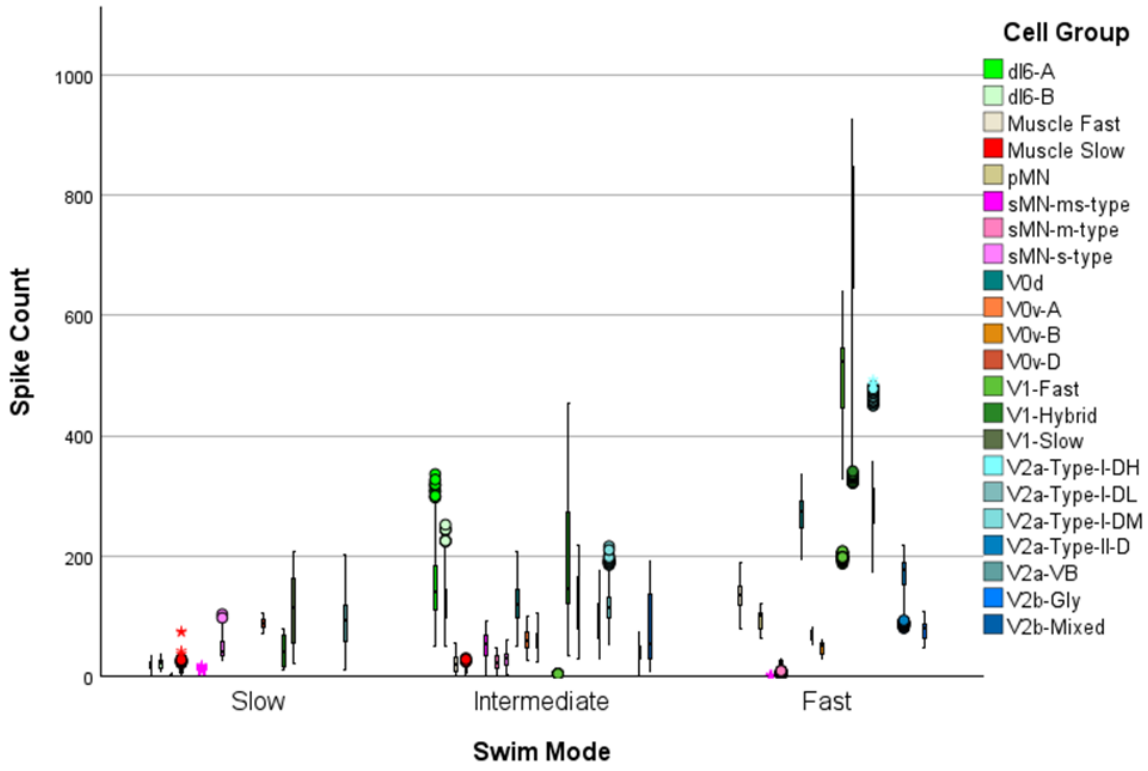

Figure S1. Activation of cell groups differs across the swimming modes.

Related to Figure 13. The distribution of the spiking counts of each cell group in slow, intermediate, and fast swim modes. The boxes show the median and 25-75 IQR. Asterixes are the outliers. N = 20 for the slow and fast swim modes and 60 for the intermediate mode.

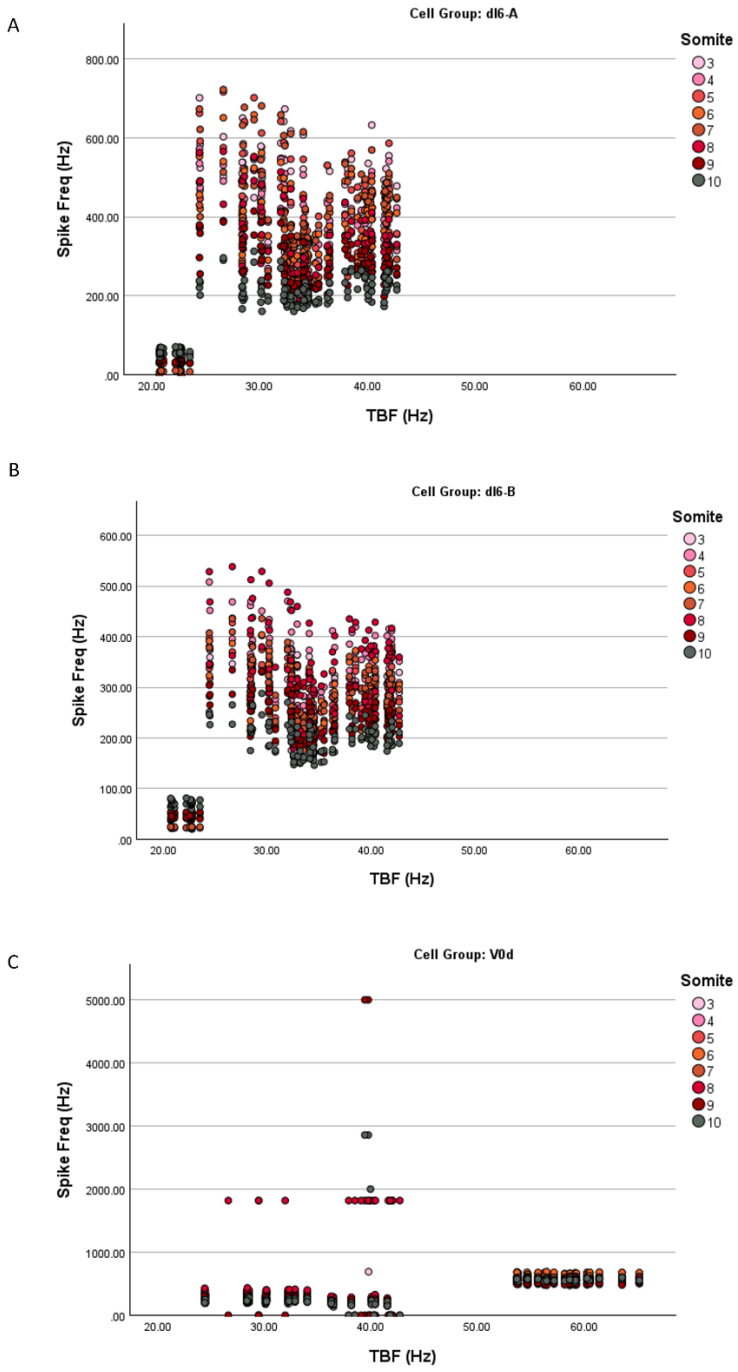

Figure S2. The spiking frequency of dI6s and V0ds plotted against the TBF observed.

Different somites are displayed in different colours. The first two somites were excluded for clarity. The plotted data includes all five testing modes (Table 18 - Statistical Analysis) with a train of twenty 500 ms step stimuli with 300 ms breaks in between. (A) dI6-A, (B) dI6-B, (C) V0d. (N = 100).

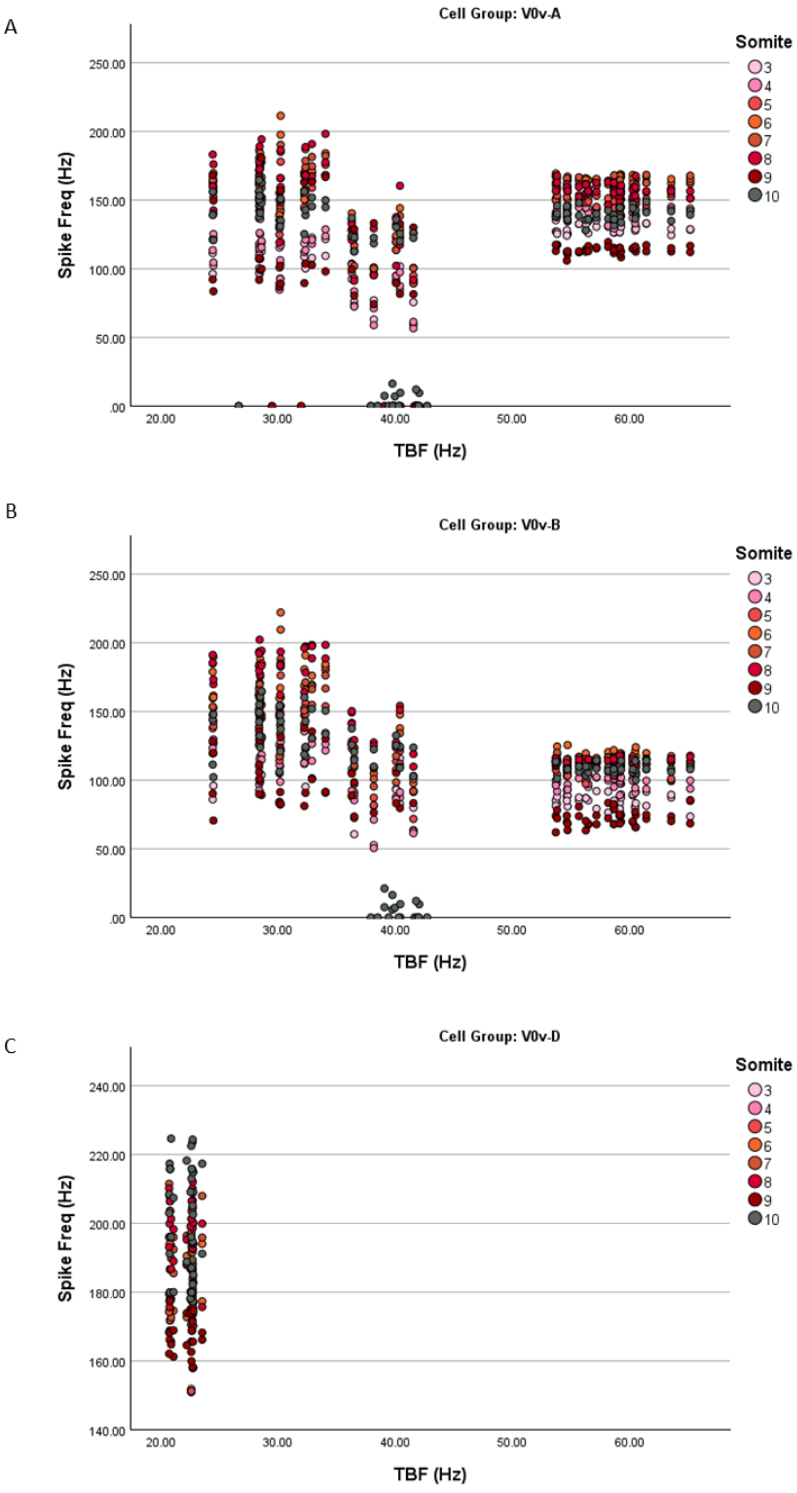

Figure S3 The spiking frequency of V0v subgroups plotted against the TBF observed.

Continuing from Figure S2. (A) V0v-A, (B) V0v-B, (C) V0v-D.

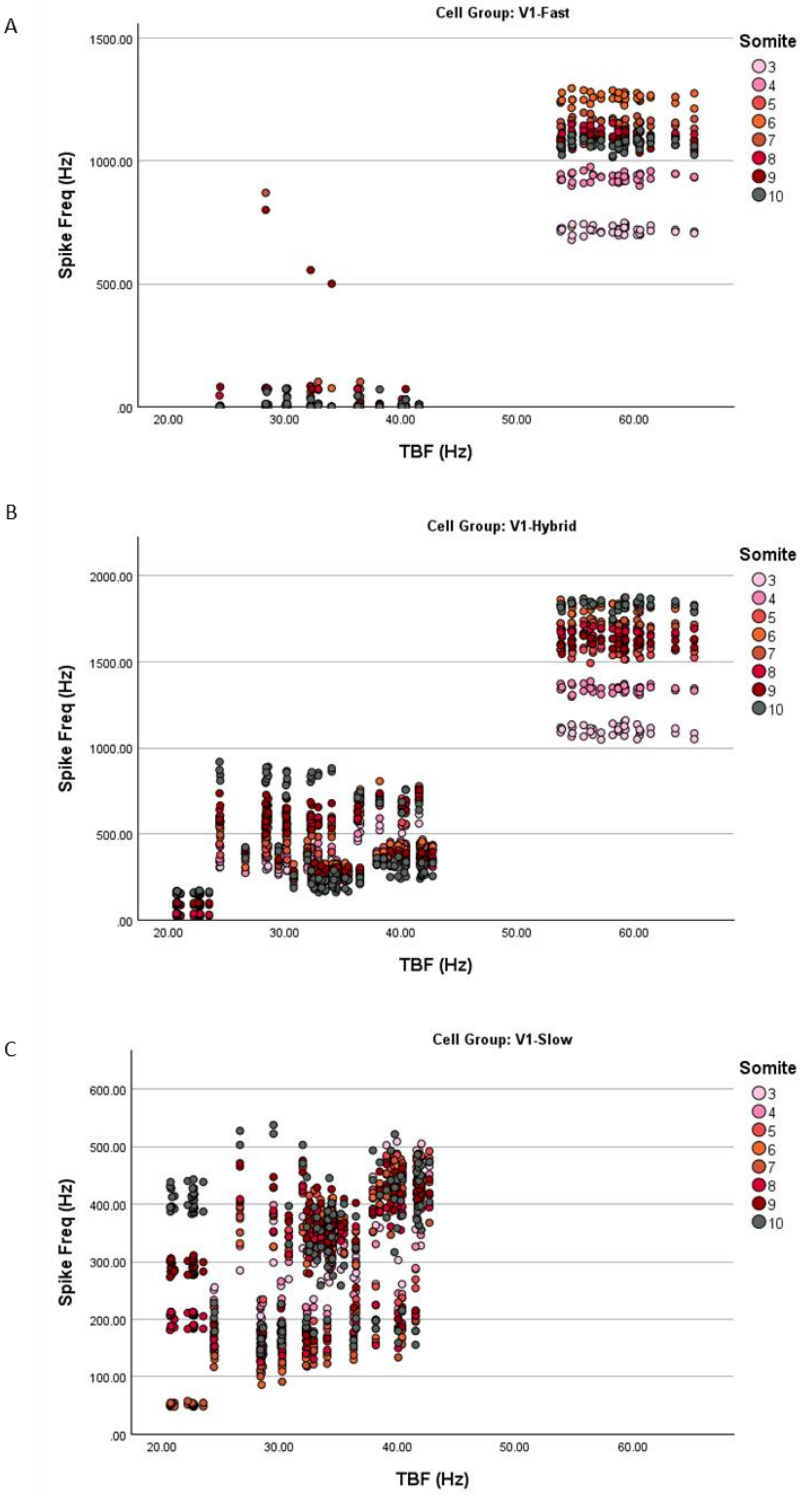

Figure S4. The spiking frequency of V1 subgroups plotted against the TBF observed.

Continuing from Figure S2. (A) V1-Fast, (B) V1-Hybrid, (C) V1-Slow.

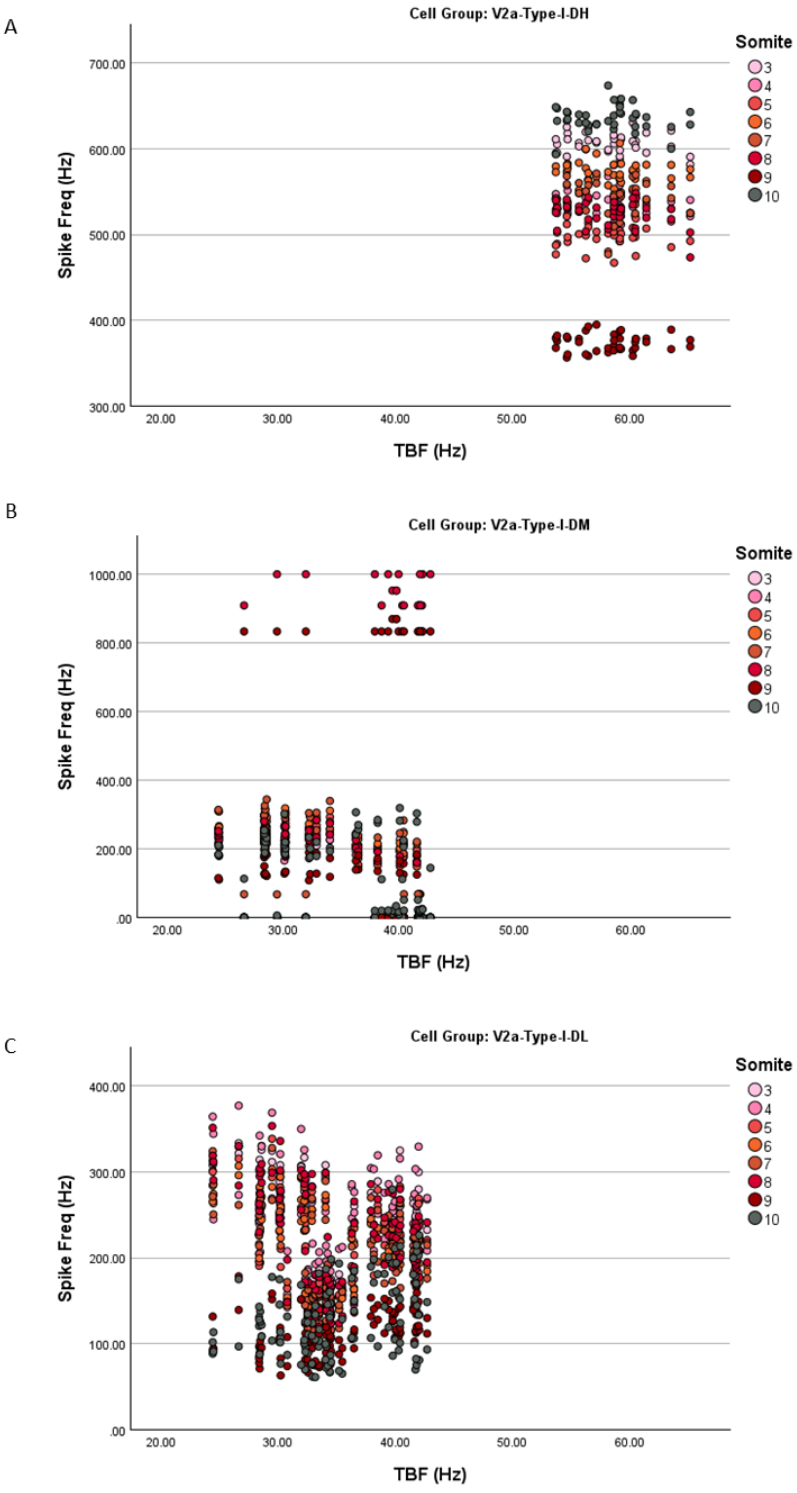

Figure S5. The spiking frequency of Type I V2a subgroups plotted against the TBF observed.

Continuing from Figure S2. (A) V2a-Type-I-DH, (B) V2a-Type-I-DM, (C) V2a-Type-I-DL.

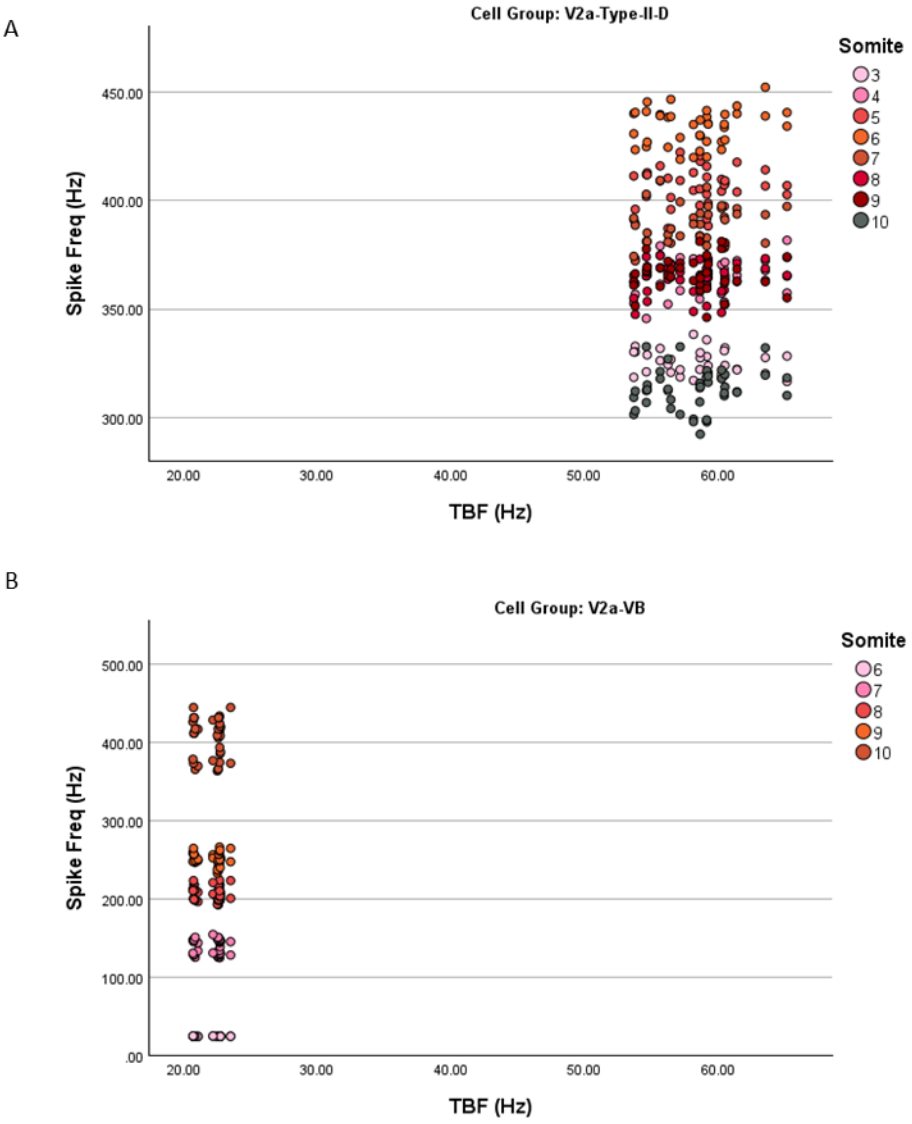

Figure S6. The spiking frequency of ventral V2a and Type II dorsal V2a subgroups plotted against the TBF observed.

Continuing from Figure S2. (A) V2a-Type-II-D, (B) V2a-VB.

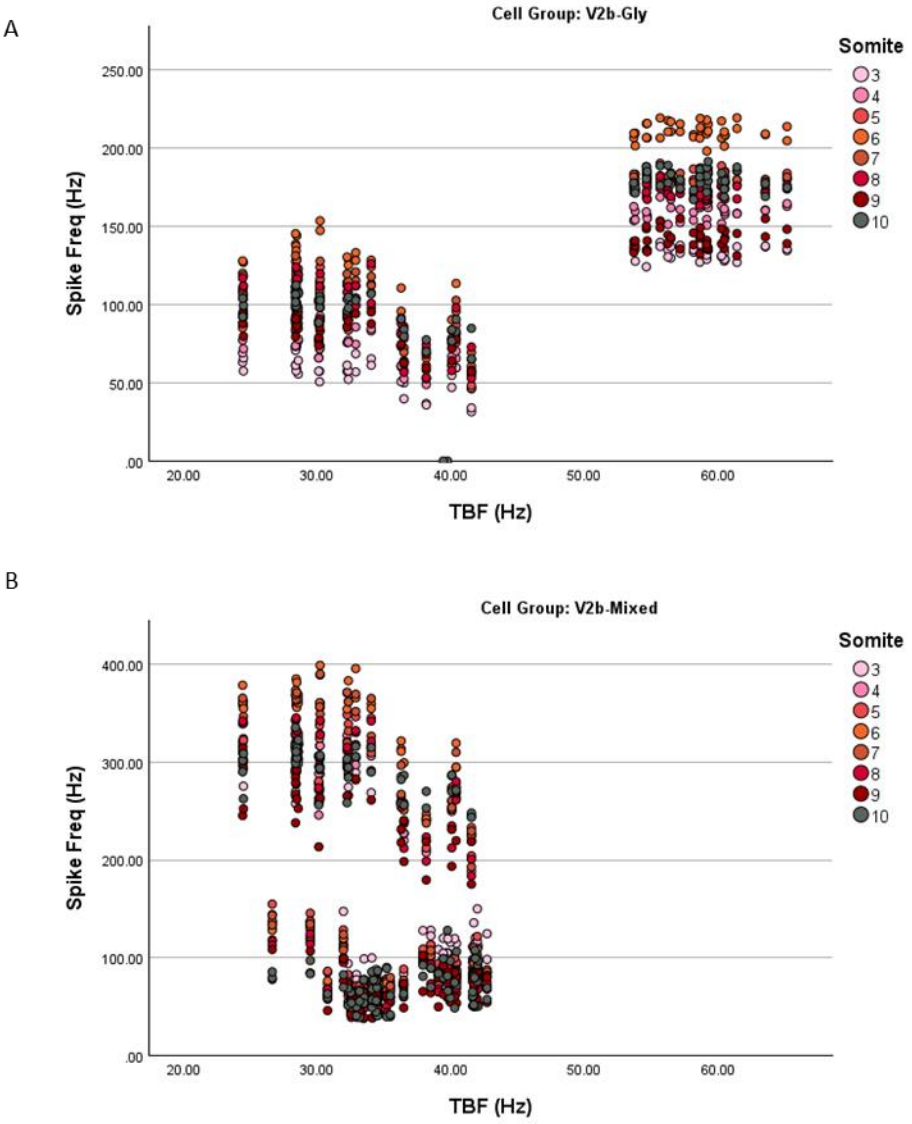

Figure S7. The spiking frequency of V2b subgroups plotted against the TBF observed.

Continuing from Figure S2. (A) V2b-Gly, (B) V2b-Mixed.

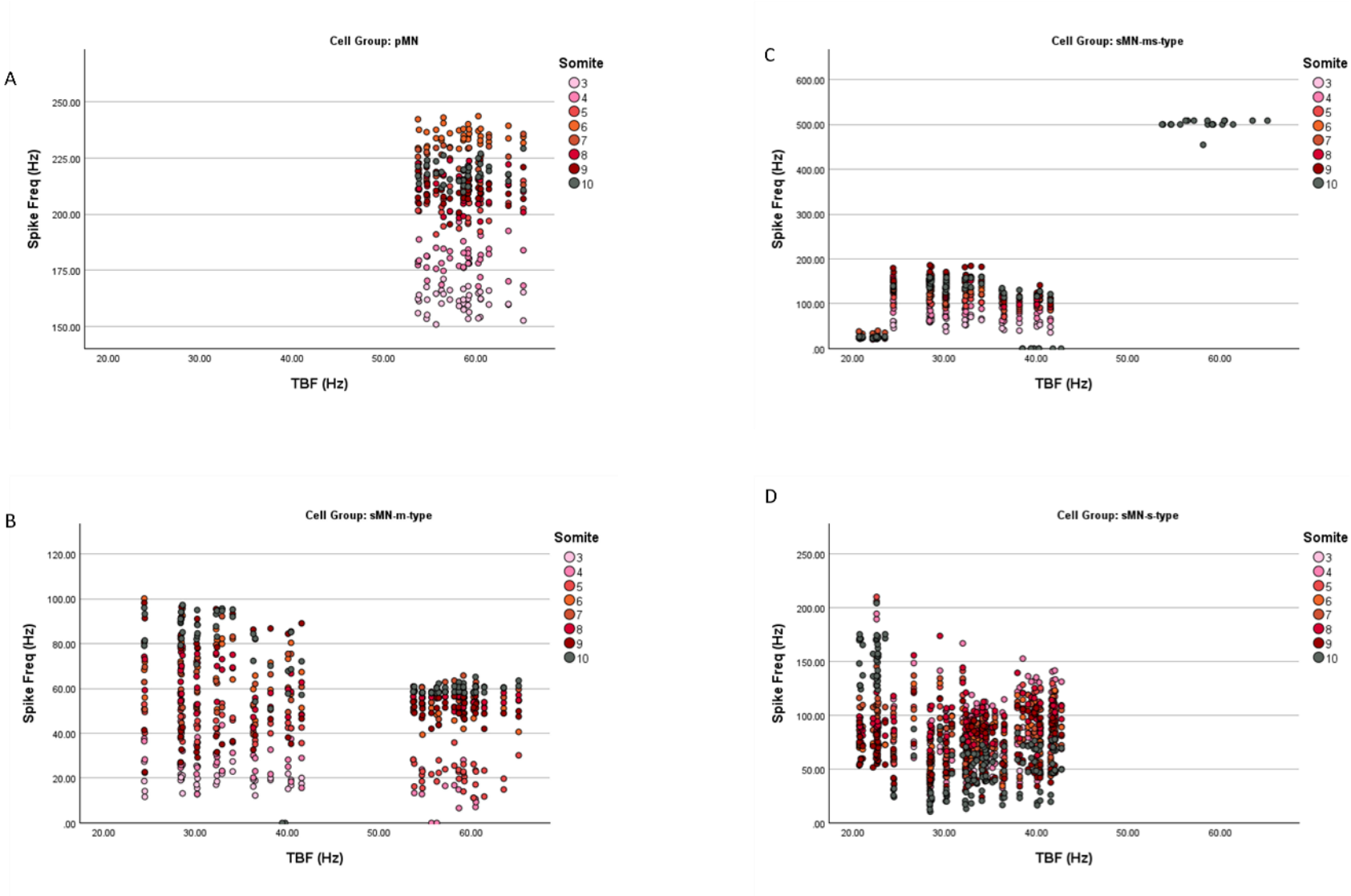

Figure S8. The spiking frequency of all MN subgroups plotted against the TBF observed.

Continuing from Figure S2. (A) pMN, (B) sMN-s-type, (C) sMN-ms-type, (D) sMN-s-type.

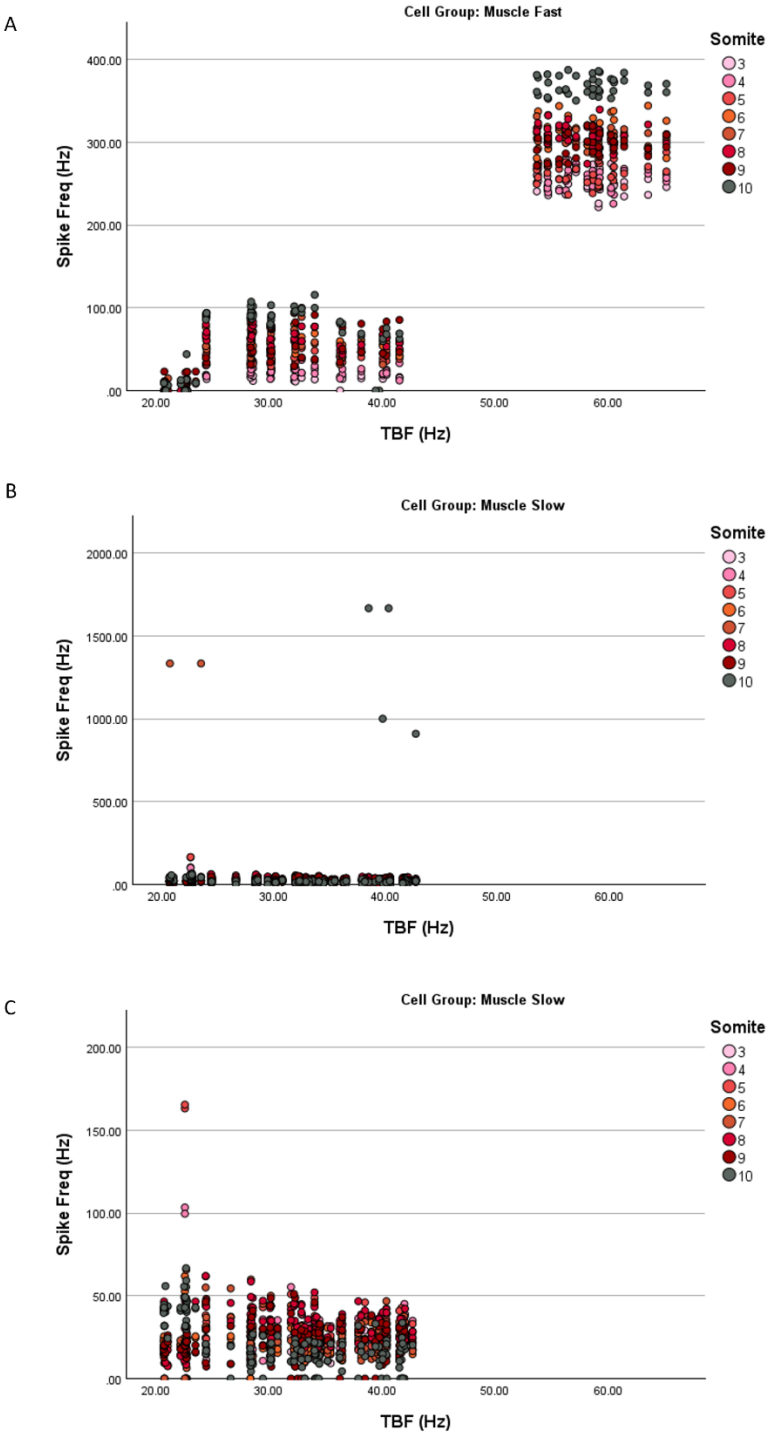

Figure S9. The spiking frequencies of muscle cells plotted against the TBF observed are shown.

Continuing from Figure S2. (A) Fast muscle cells showed activity across a wide range of TBF, with higher spiking frequency at higher swimming speeds. (B) Slow muscle cells were active during slow and intermediate swimming modes. (C) Zoomed in version of the plot in (B), where the outlier spiking frequencies over 500 Hz were removed for clarity.

Slow Network

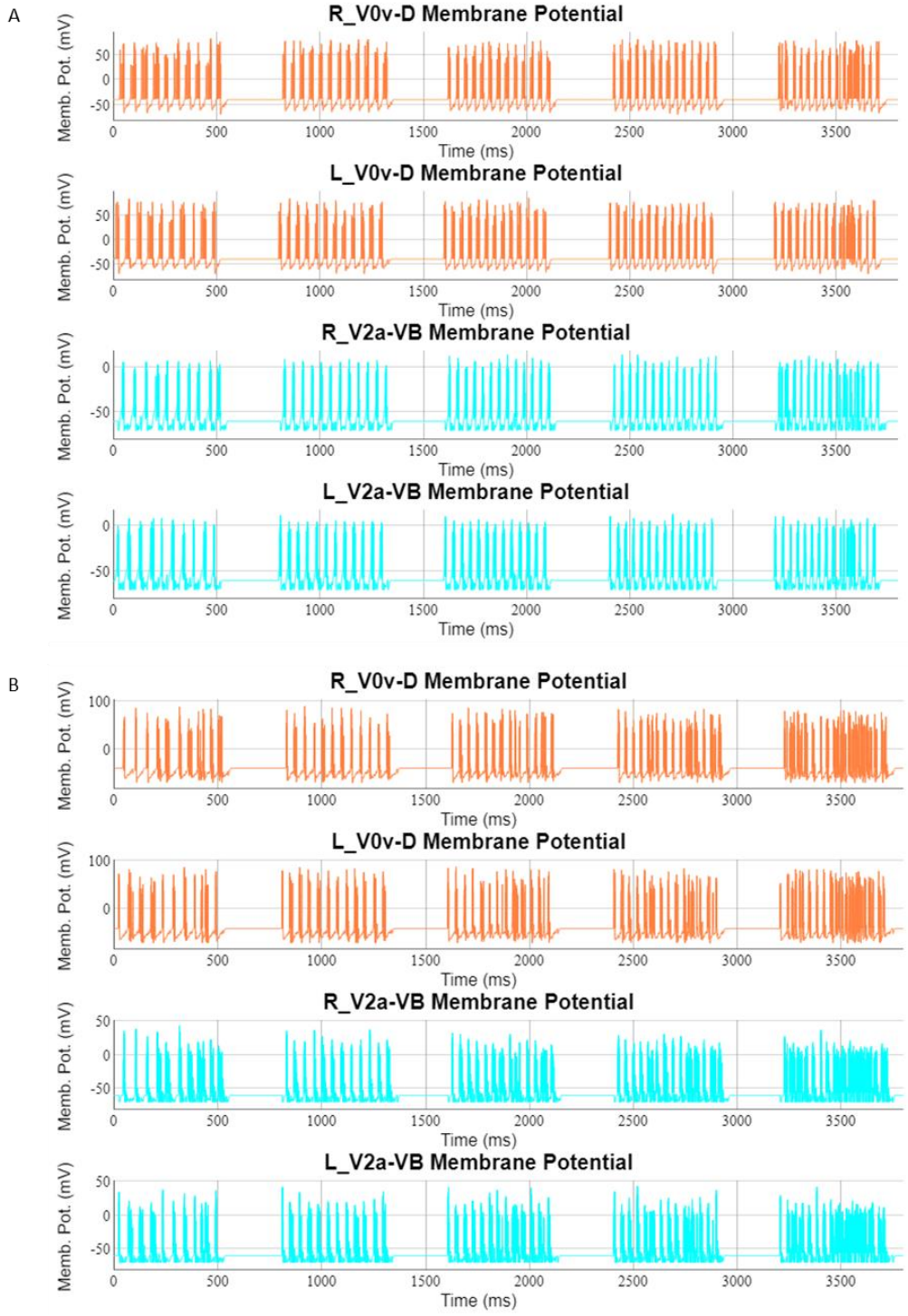

Figure S10. The excitatory neurons displayed rhythmic behaviour in the slow mode.

Related to Figure 16. The activity on the third (A) and ninth (B) somites show similar activity. The third somite receives stimulation, whereas the ninth somite does not. The slow network is capable of transferring the activation caudally.

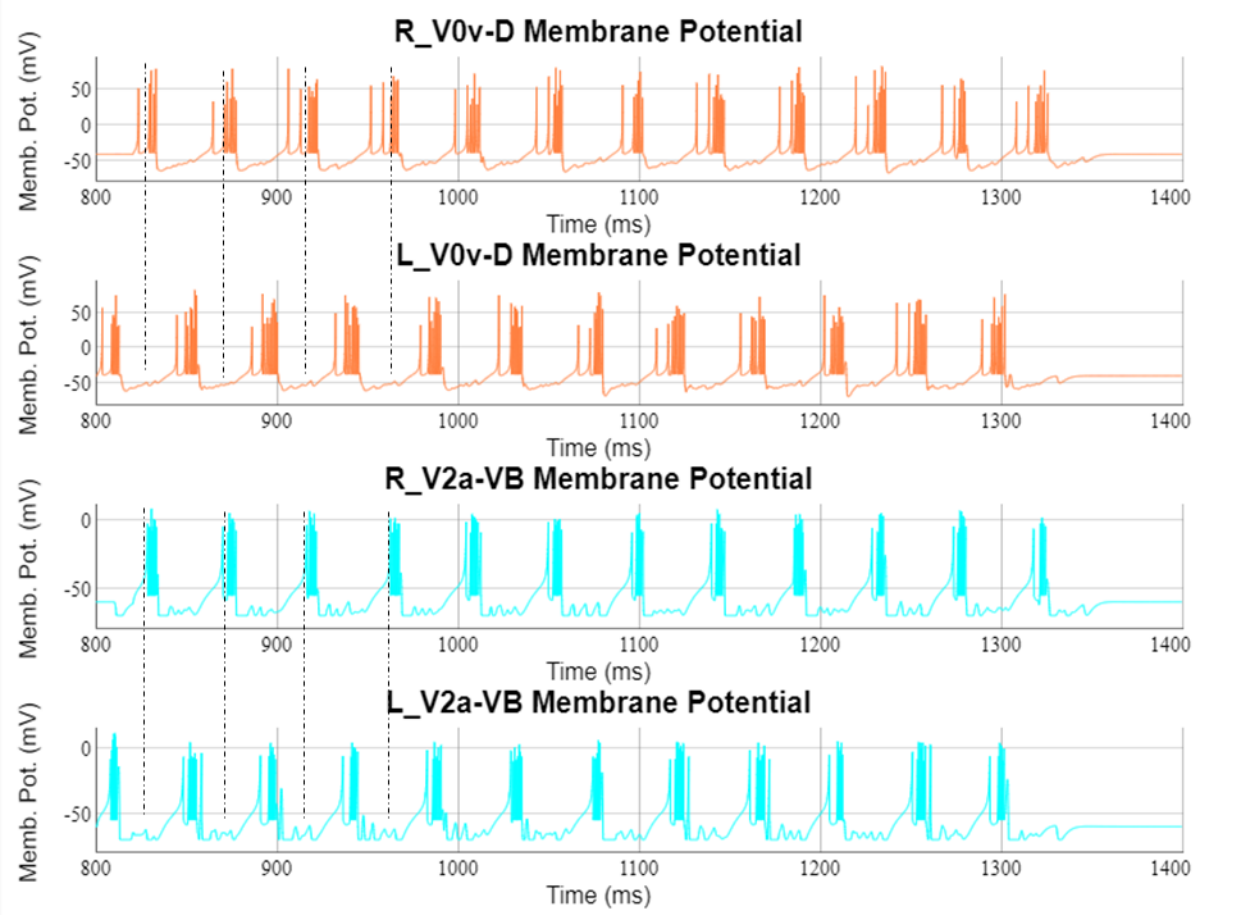

Figure S11. Left and right alternation of the excitatory neurons in the slow mode is shown.

Zoomed-in activity for the cells plotted in Figure S10A shows the left and right alternation. Dashed lines are added to reflect the peak of the cell activity on the right side of the spinal cord activity to the left side.

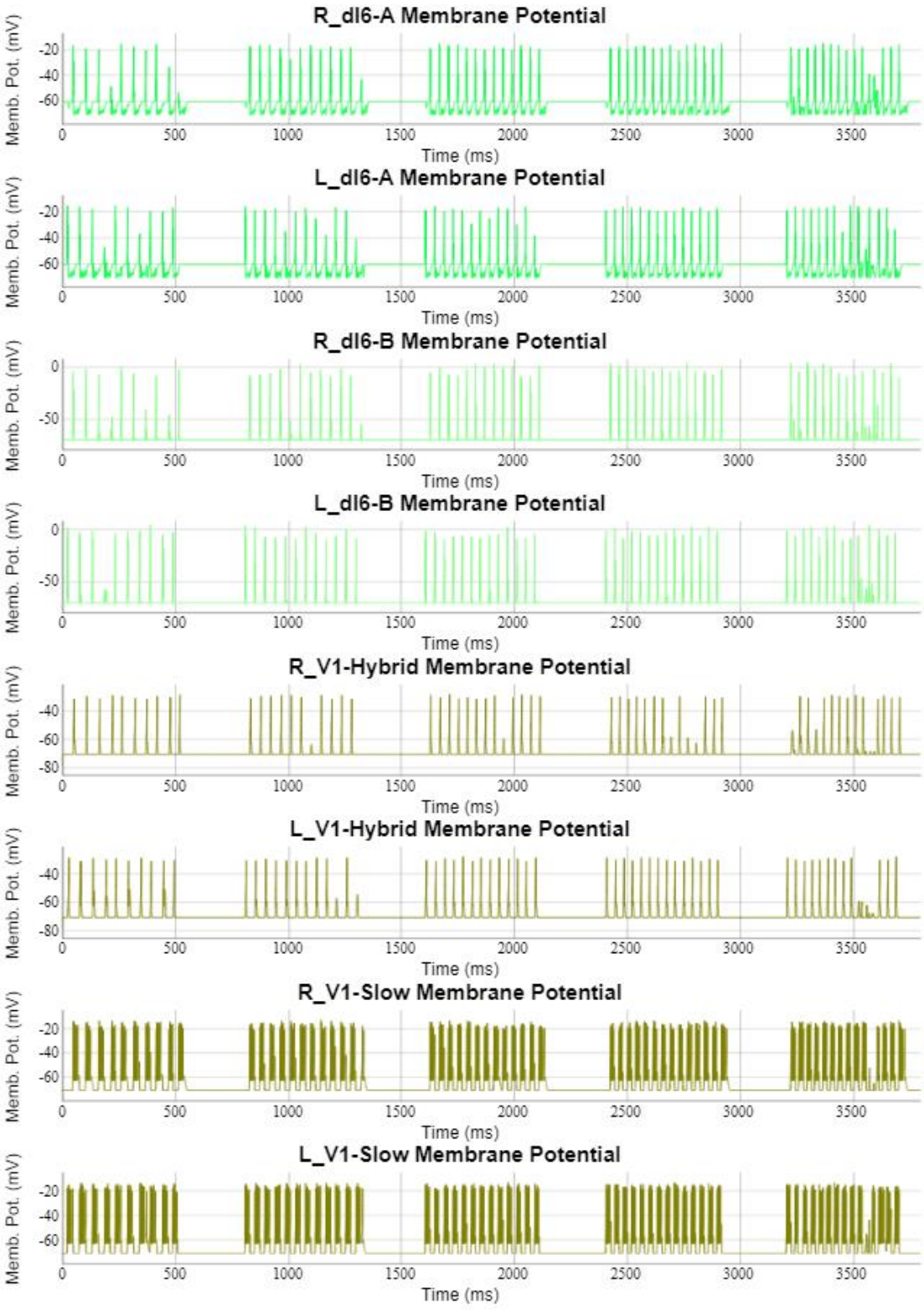

Figure S12. The inhibitory neurons displayed rhythmic behaviour in the slow mode.

The activity of the inhibitory neurons on the third somite is shown, which is related to Figure16. dI6-A, dI6-B, V1-Slow, and V1-Hybrids showed activity across the applied stimulus range.

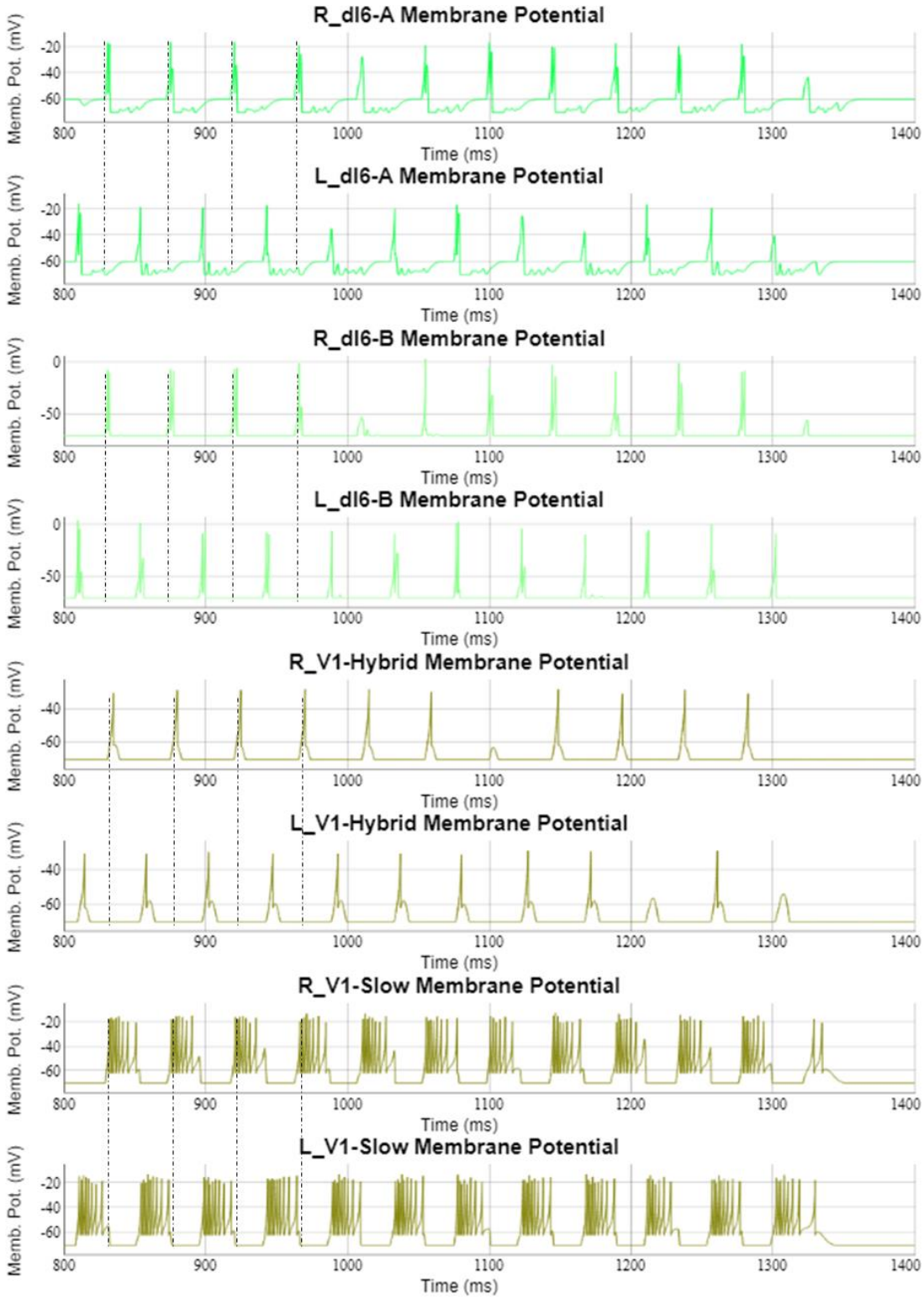

Figure S13. Inhibitory neurons showed left-right alternation in the slow mode.

Related to Figure S12. Zoomed-in activity for the inhibitory cells on the third somite to show the left and right alternation. Dashed lines are added to reflect the peak of the cell activity on the right side of the spinal cord activity to the left side.

Intermediate Network

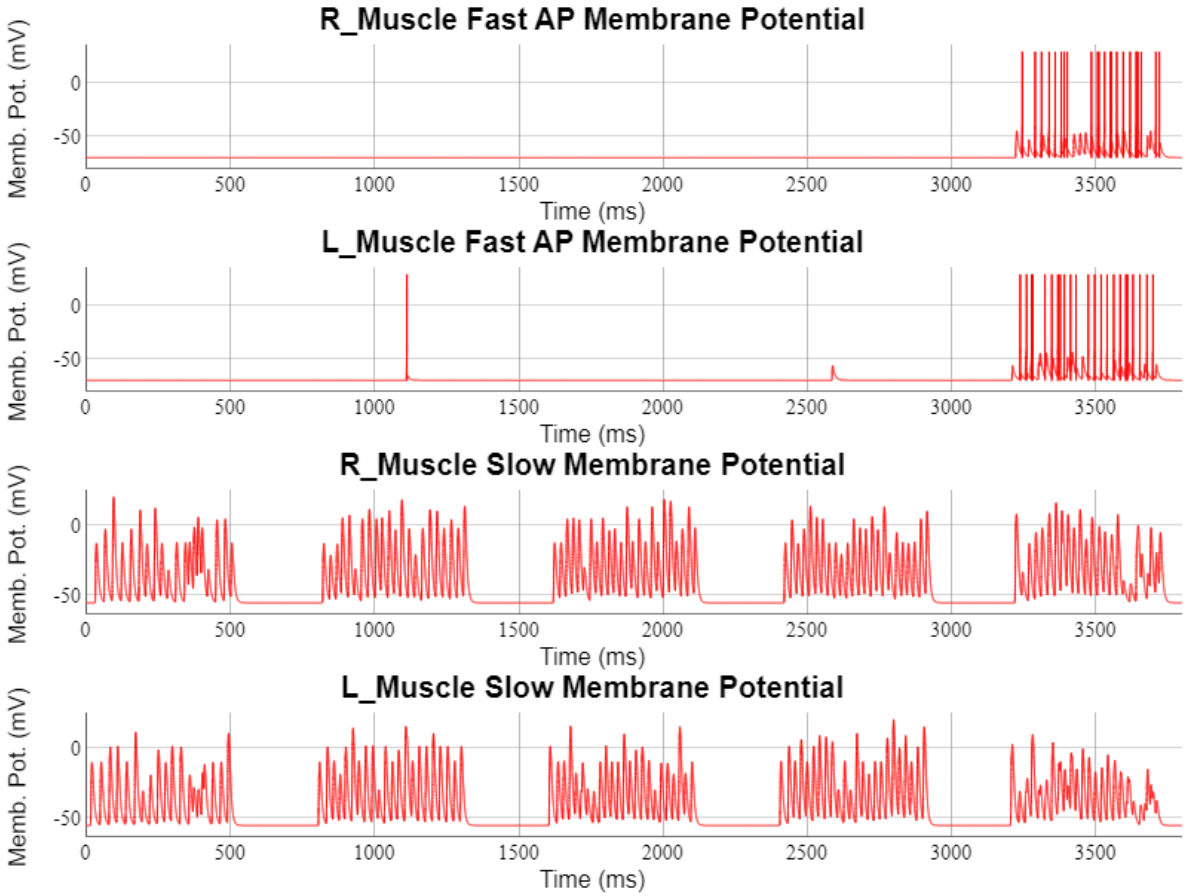

Figure S14. Changing activity levels of muscle cells during the intermediate mode.

Related to Figure 22. Fast muscle cells do not show activity during low stimulus amounts. As the stimulation increases, they start to get activated. The displayed cell is located on somite six.

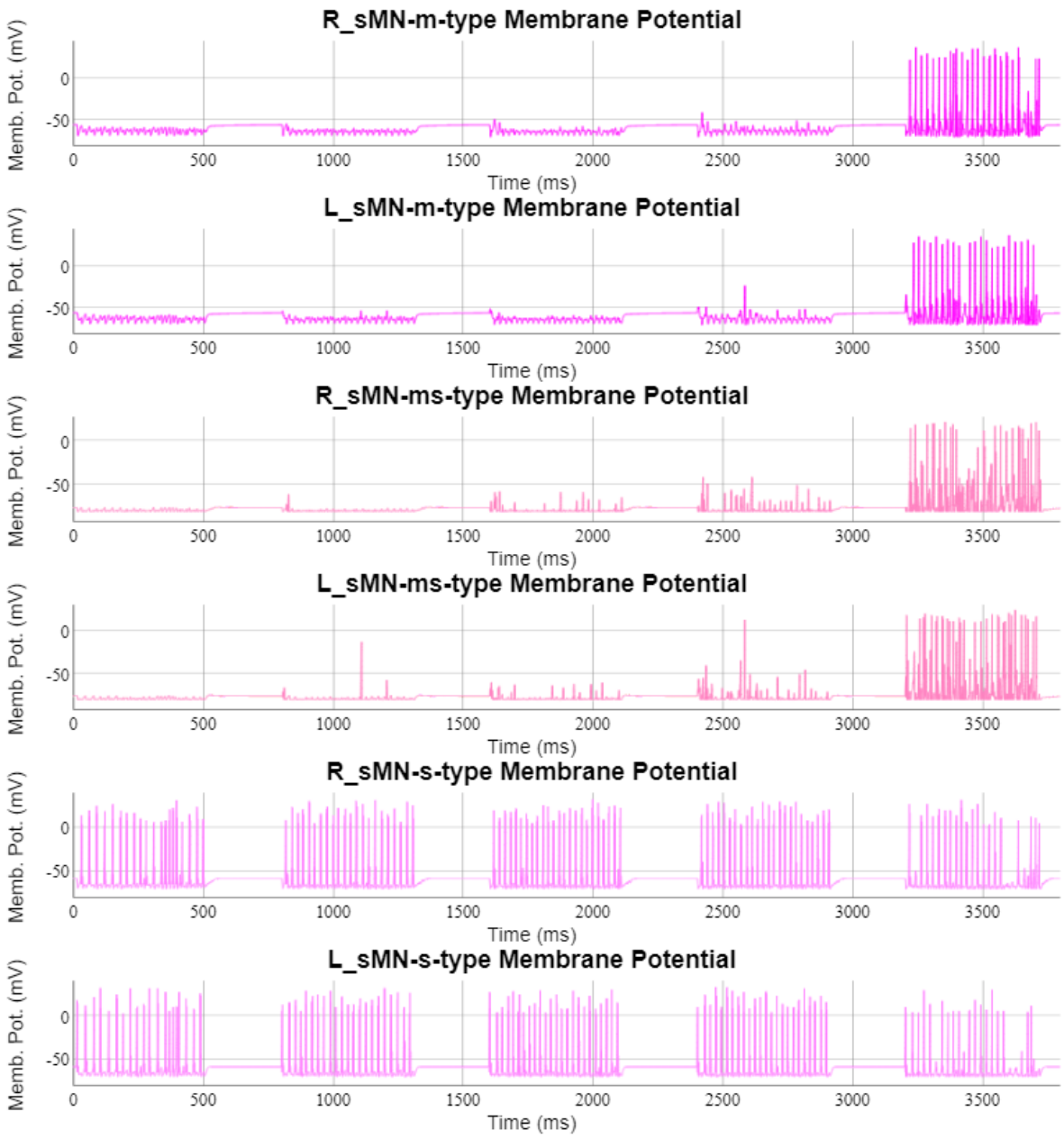

Figure S15. Activity levels of sMNs in the intermediate mode.

Related to Figure 22. sMN-ms-type and sMN-s-type MNs do not show activity during low stimulus amounts. As the stimulation increases, they start to get activated. The MNs shown are located on somite six.

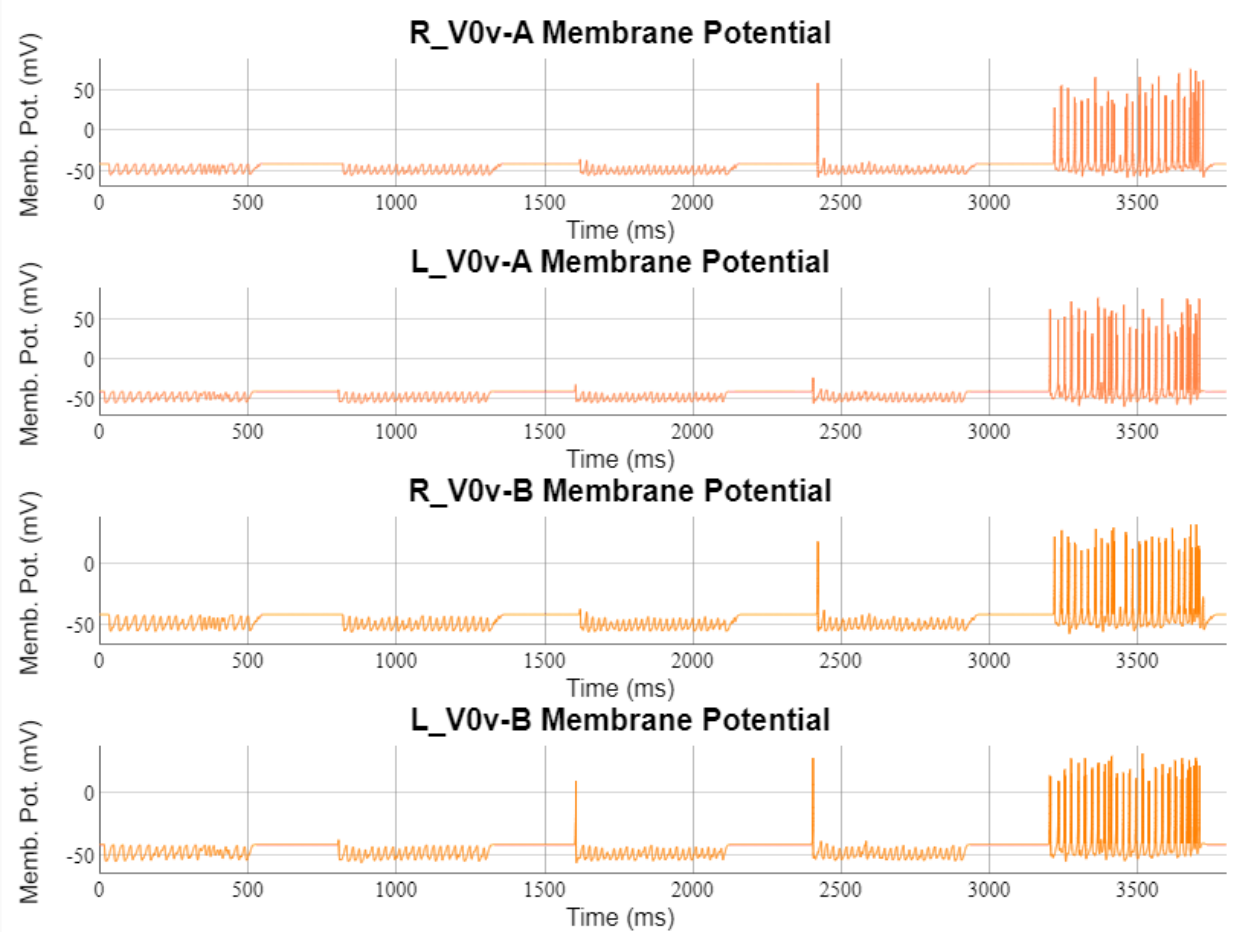

Figure S16. Changing activity levels of V0vs in the intermediate mode.

Related to Figure 22. V0v-As and V0v-Bs do not show activity during slow and intermediate swimming with low stimulus amounts. As the stimulation increases, both groups start to get activated. The V0vs shown are located on somite six.

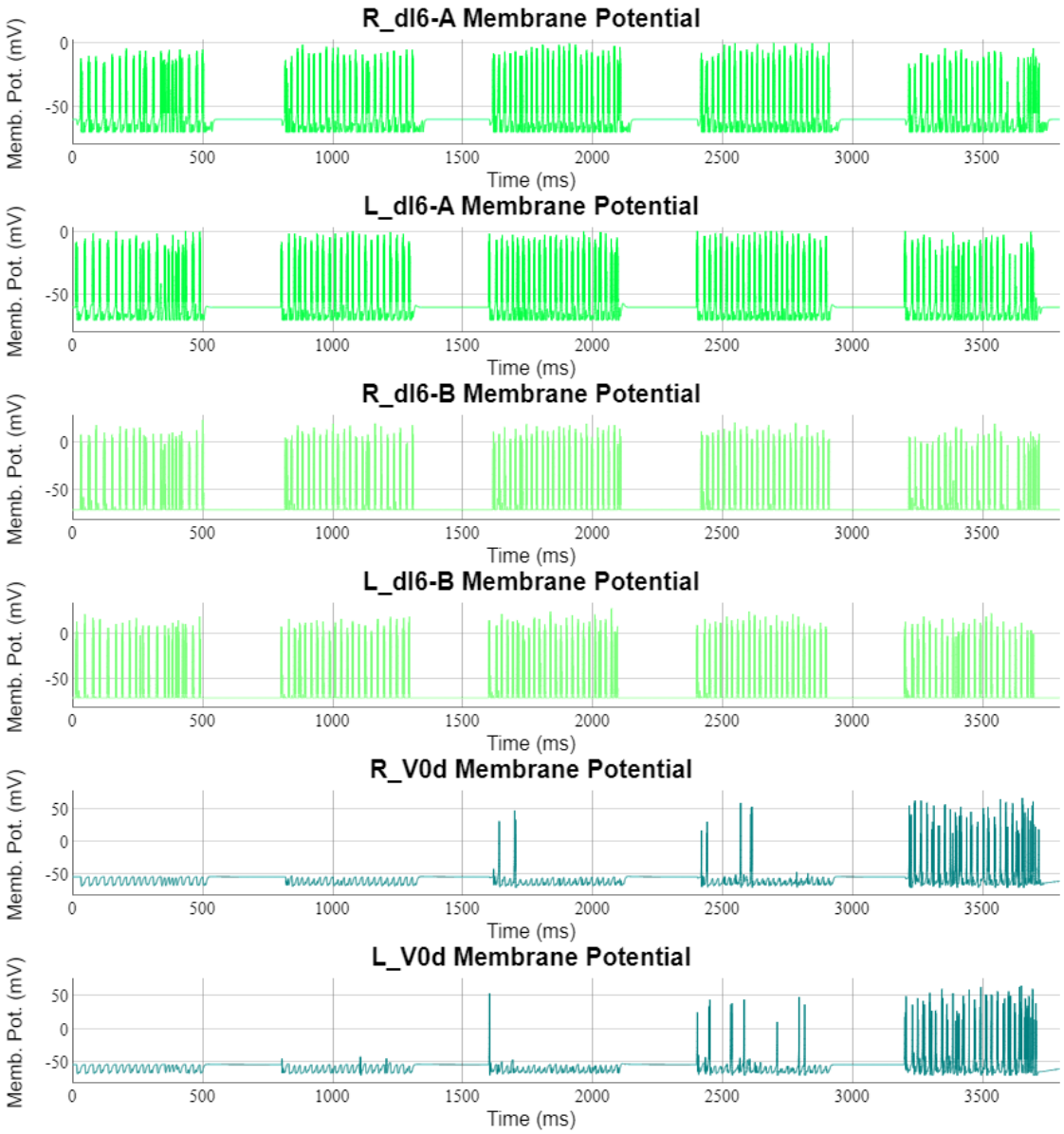

Figure S17. Activity levels of dI6s and V0ds changed based on the stimulus amount in the intermediate mode.

Related to Figure 22. dI6s show activity at all levels of stimuli. On the other hand, V0ds get into the picture only at a high level of stimulation. The inhibitory neurons shown are located on somite six.

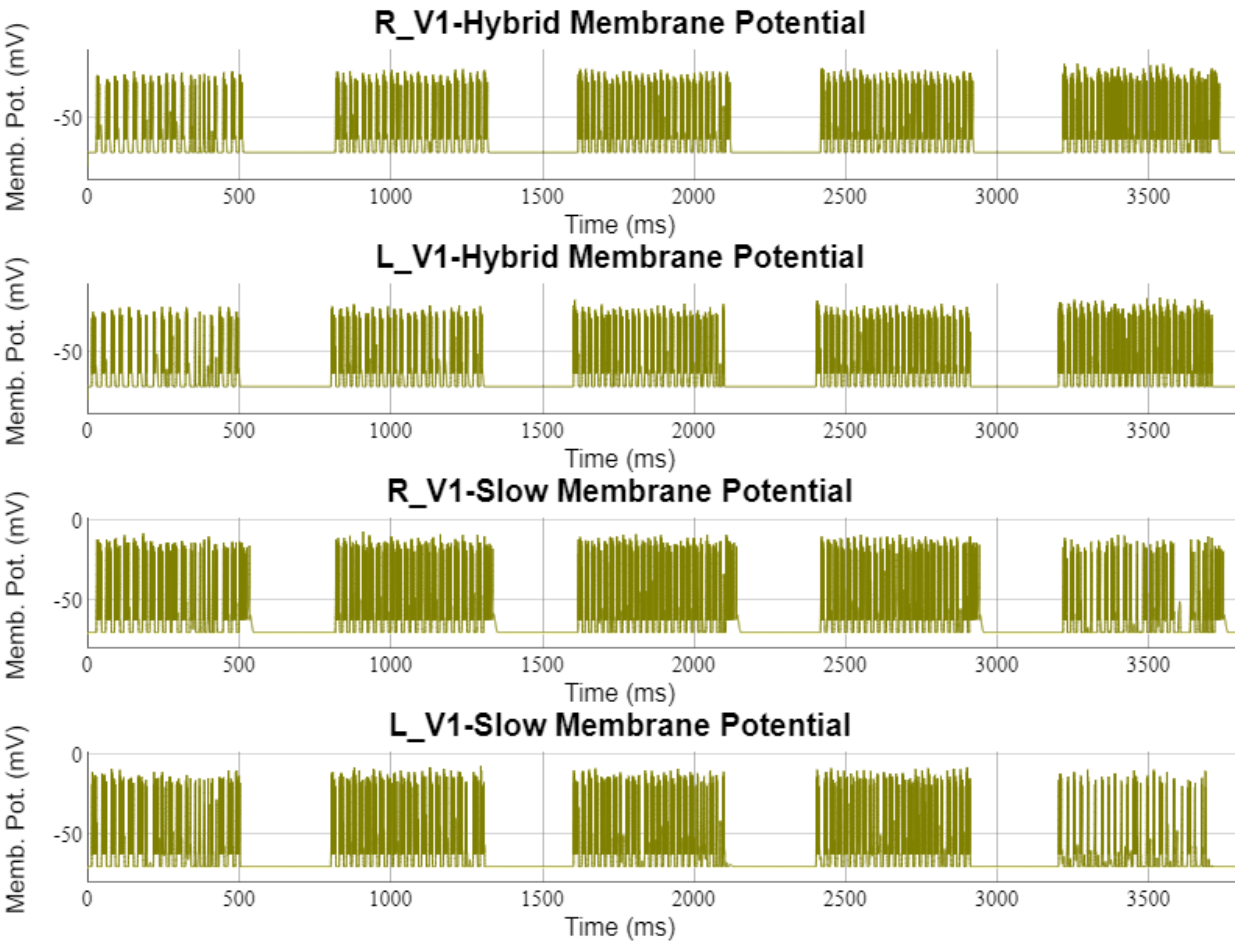

Figure S18. V1-Slows and V1-Hybrids displayed rhythmic behaviour in the intermediate mode.

Related to Figure 22. Both V1-Slow and V1-Hybrid inhibitory neurons showed activity across all levels of stimulus levels applied. V1-Fast activity is not displayed as they had only several spikes at the maximum stimulus period. The V1s shown are located on somite six.

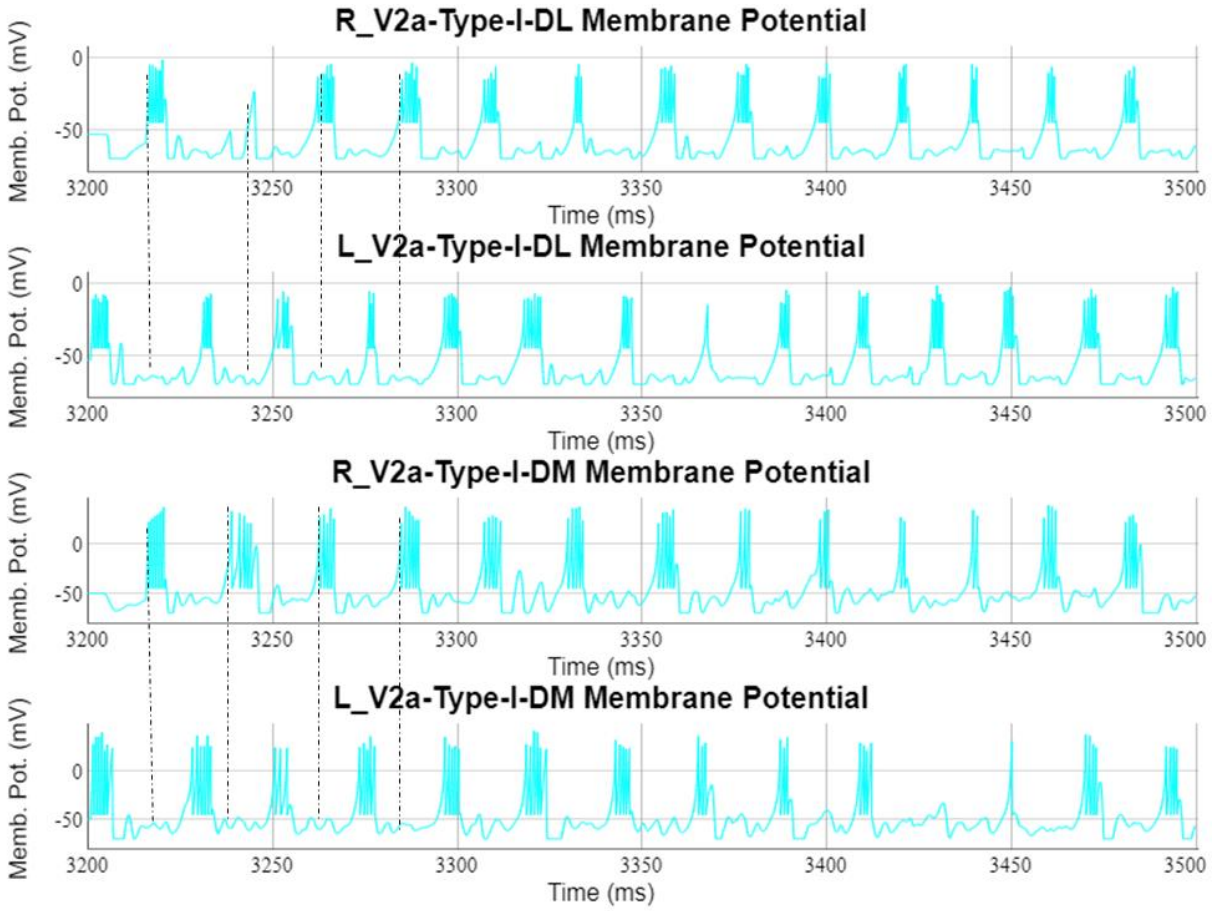

Figure S19. Left and right alternation of excitatory neuron activity in the intermediate mode.

Related to Figure 22. The zoomed-in activity of left and right V2as on somite six shows clear left and right alternation.

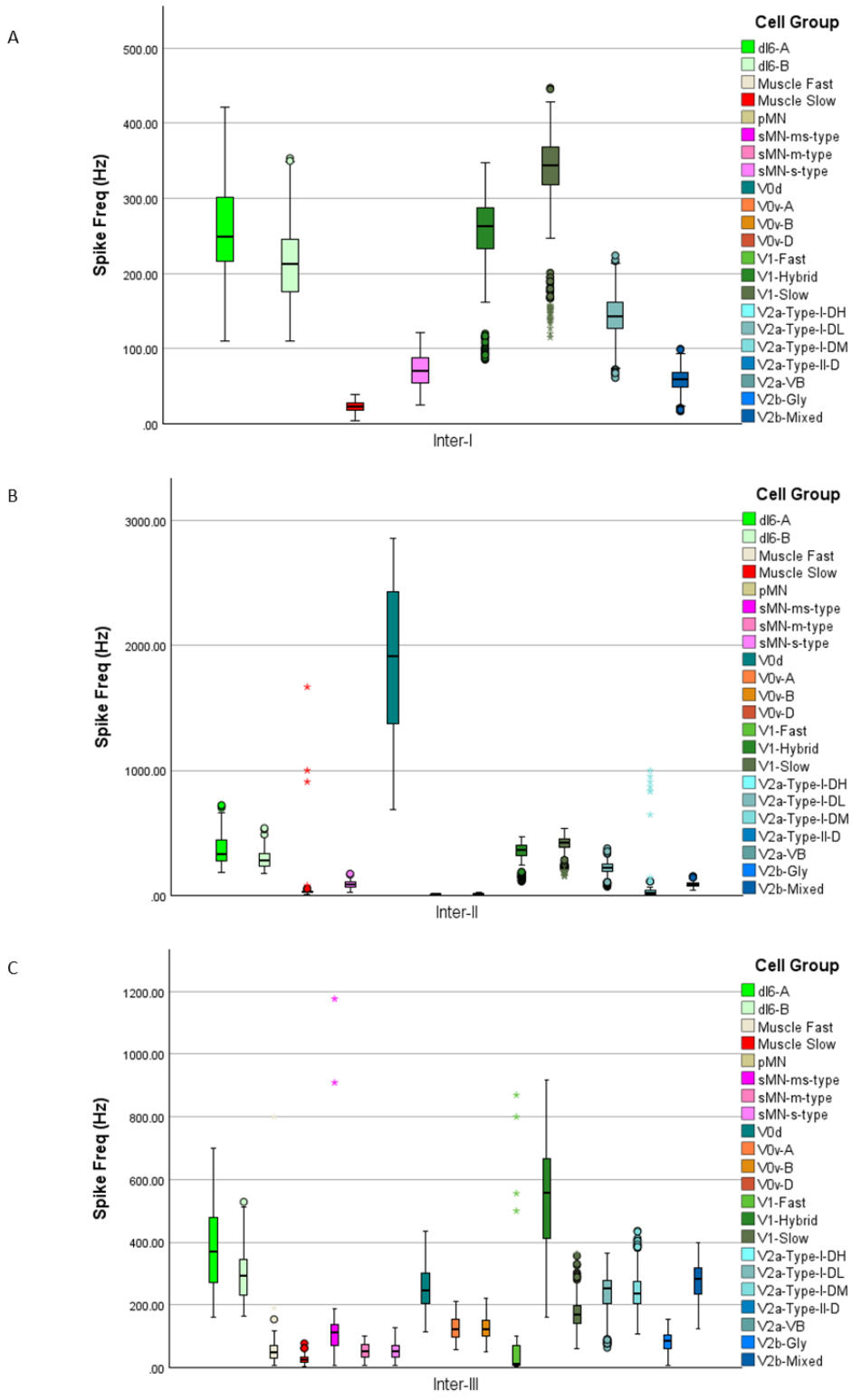

Figure S20. The Spike count distribution of the cell groups in intermediate mode, separated by stimulus quantity.

Related to Figure 24. Notice that the y-axis scales are different. Inter-I (A), Inter-II (B), and Inter-III (C) modes received 50-50 pA, 100-100 pA, and 150-450 pA current stimulation to V2a-Type-I-DL and V2a-Type-I-DM populations.

Fast Network

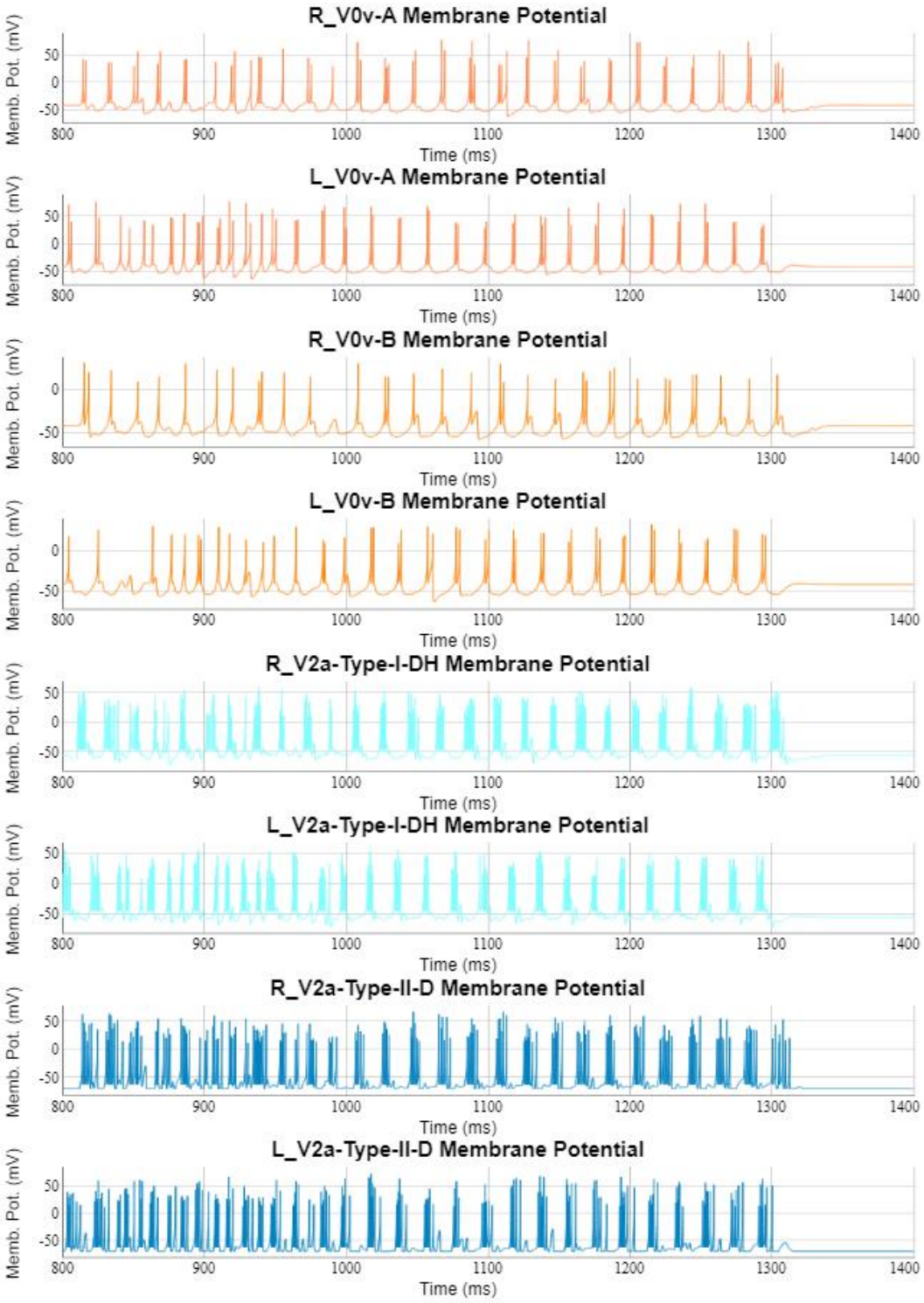

Figure S21. Left-right alternation in the excitatory neurons of the fast mode.

Related to Figure 26.

Optogenetic Stimulation

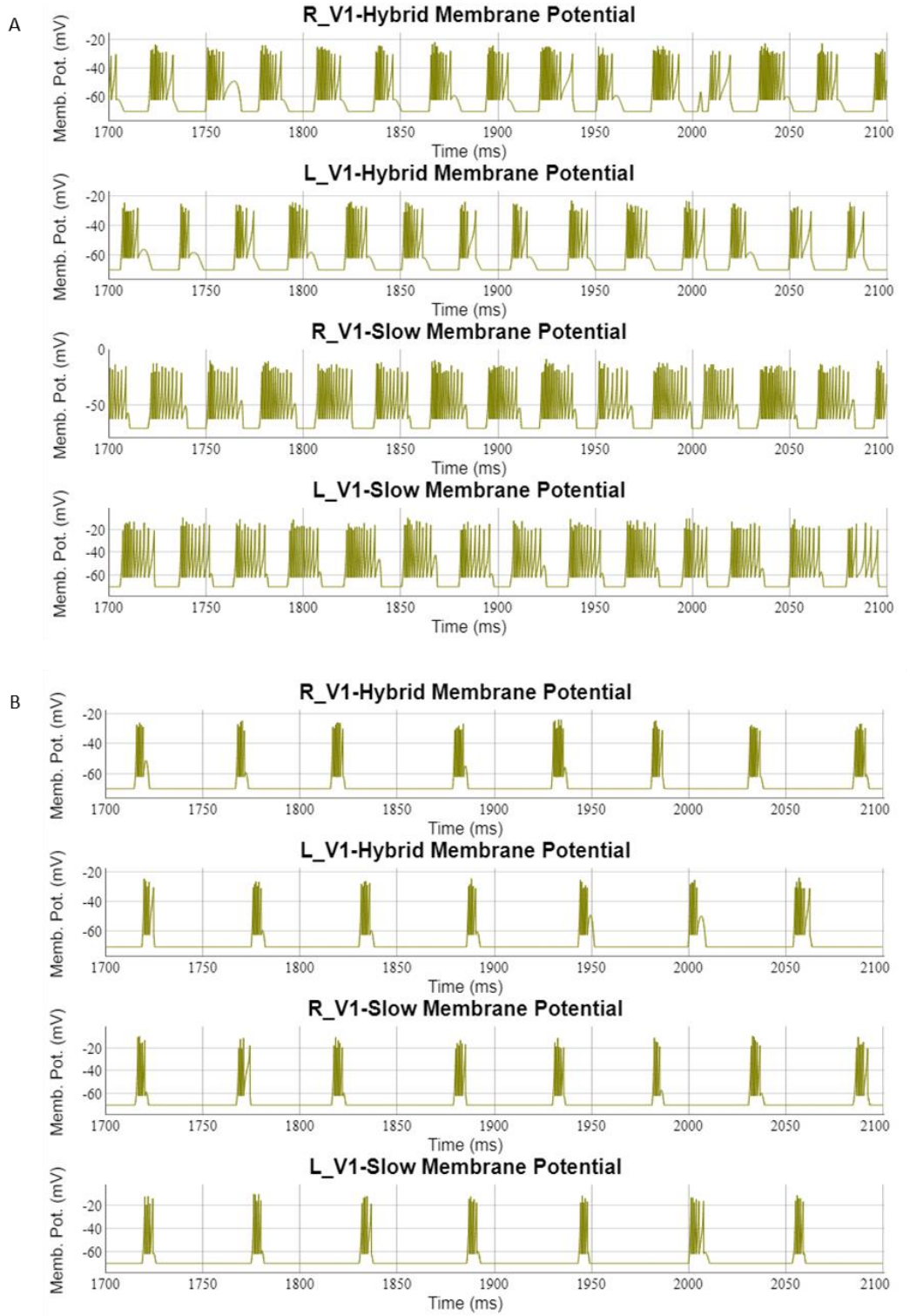

Figure S22. The activity of the V1s with the optogenetic stimulation experiment.

Related to Figures 31-32. (A) The activity of V1s on the sixth somite. (B) The left-right alternation is disrupted, and frequency is lowered when glycinergic synapses are deactivated.

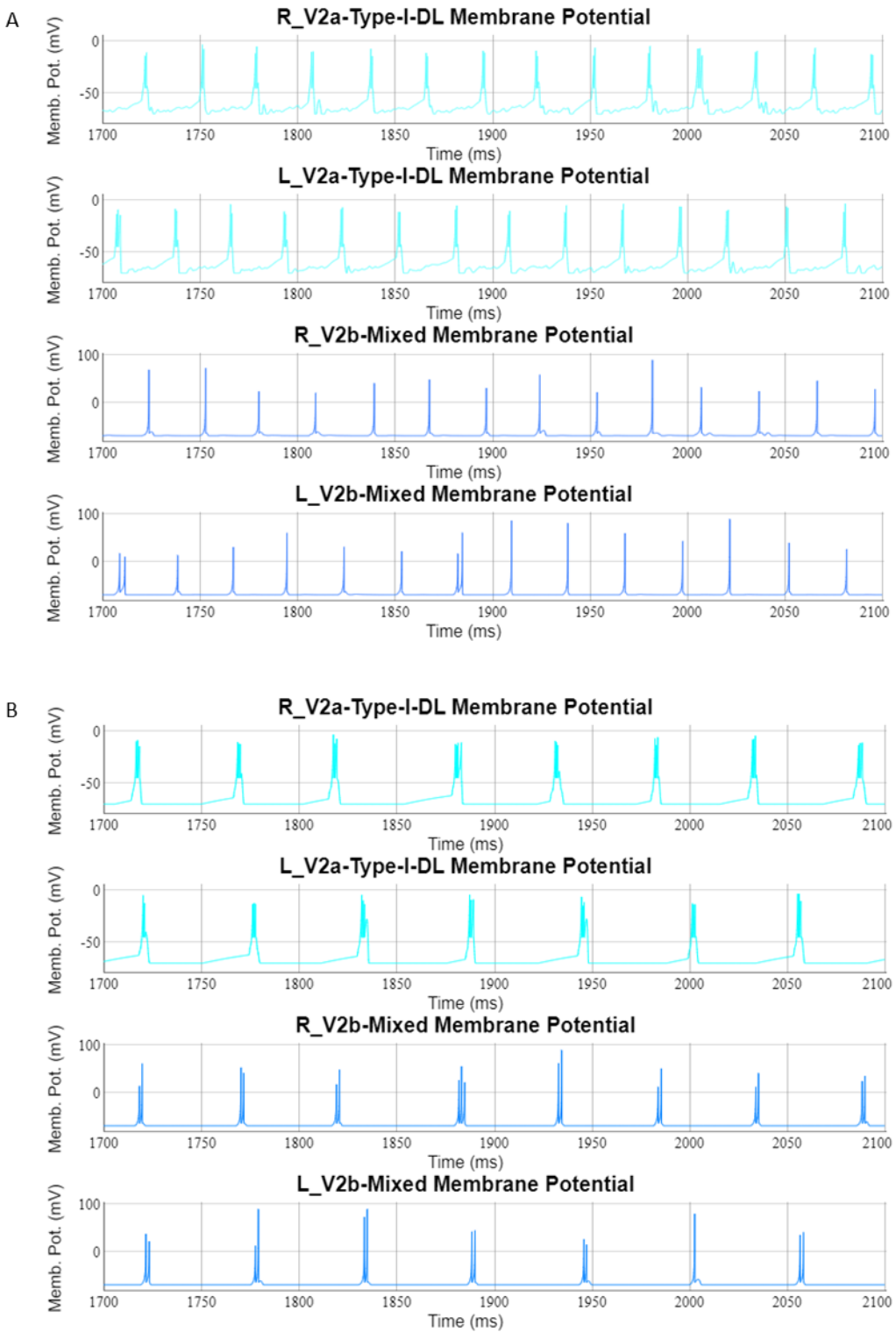

Figure S23. The activity of the V2as and V2bs with the optogenetic stimulation experiment.

Related to Figures 33-36. (A) The activity of V2as and V2bs on the sixth somite. (B) The left-right alternation is disrupted, and frequency is lowered when glycinergic synapses are deactivated.

MN activity versus tail beat

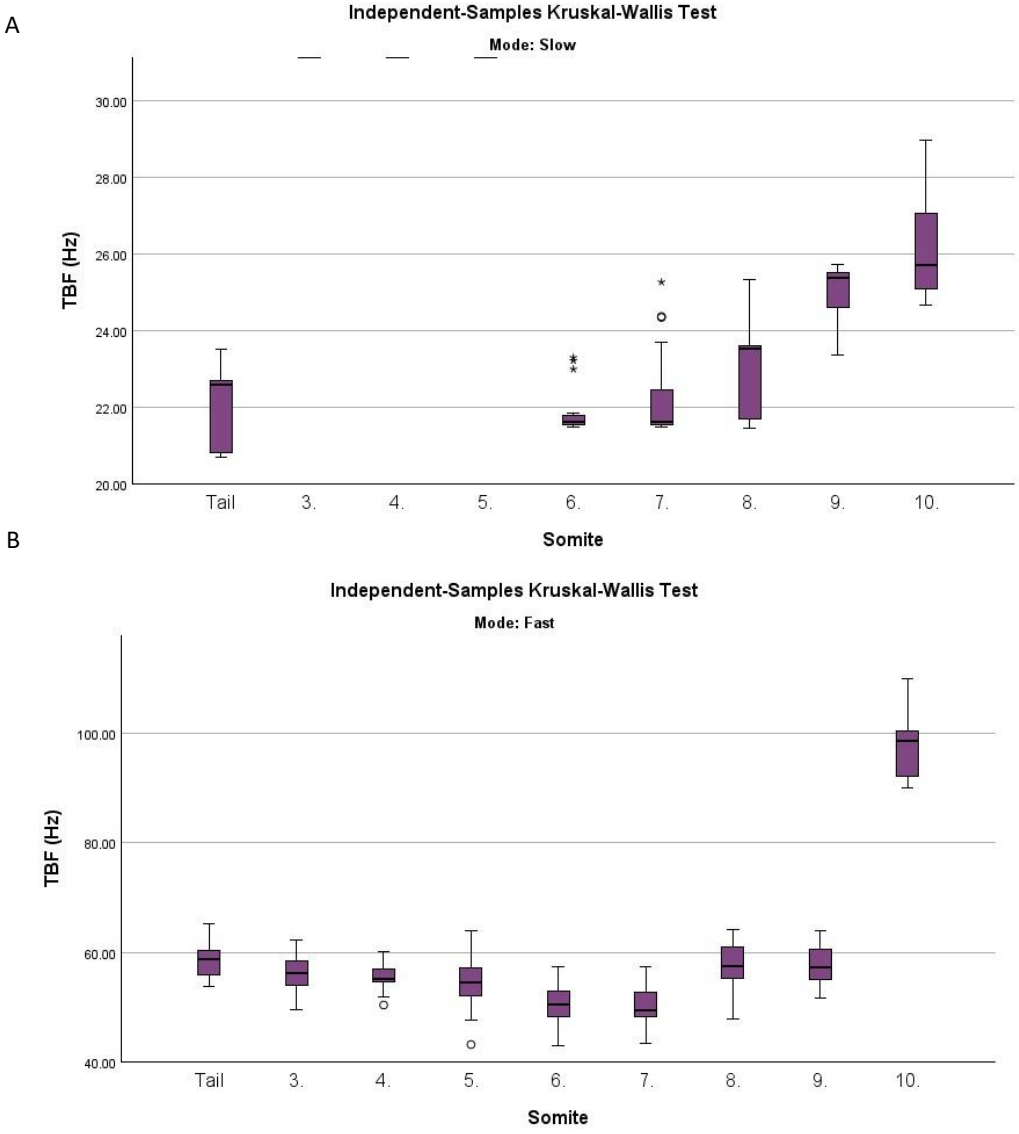

Figure S24. The comparison of the distribution of TBFs calculated by the tail tip movement and MN activity on different somites in slow and fast modes is shown.

Related to Figure 43. The first two somites were excluded from the comparison. (A) Slow mode. The y-axis of the slow mode was scaled to better focus on the more caudal somites. Somites 3-5 are off the chart. (Tail: 22.59 (IQR 20.8-22.7), N = 20; Somite 3: 88.79 (IQR 88.79-1), N = 1; Somite 4: 160.17 (IQR 160.17-1), N = 1; Somite 5: 108.82 (IQR 108.82-20), N = 1; Somite 6: 21.62 (IQR 21.55-21.83), N = 20; Somite 7: 21.61 (IQR 21.54-22.74), N = 20; Somite 8: 23.53 (IQR 21.62-23.59), N = 20; Somite 9: 25.39 (IQR 24.55-25.51), N = 20; Somite 10: 25.7 (IQR 25.08-27.09), N = 20), (B) Fast mode (Tail: 58.65 (IQR 55.82-60.42), N = 20; Somite 3: 56.13 (IQR 53.96-58.58), N = 20; Somite 4: 55.22 (IQR 54.71-57.19), N = 20; Somite 5: 54.6 (IQR 51.98-57.41), N = 20; Somite 6: 50.59 (IQR 48.3-53.18), N = 20; Somite 7: 49.51 (IQR 48.1-52.88), N = 20; Somite 8: 57.59 (IQR 55.31-61.11), N = 20; Somite 9: 57.32 (IQR 54.89-60.48), N = 20; Somite 10: 98.56 (IQR 91.94-100.66), N = 20)

A

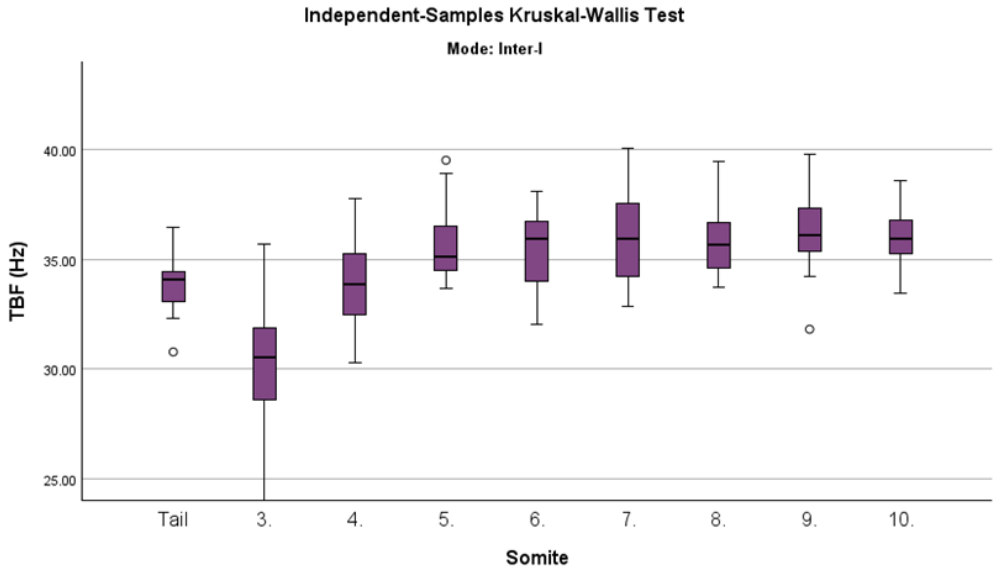
Independent-Samples Kruskal-Wallis Test
Mode: Inter-I
TBF (Hz)
40.00
35.00
30.00
25.00
Tail
3.
4.
5.
6.
7.
8.
9.
10.
Somite

B

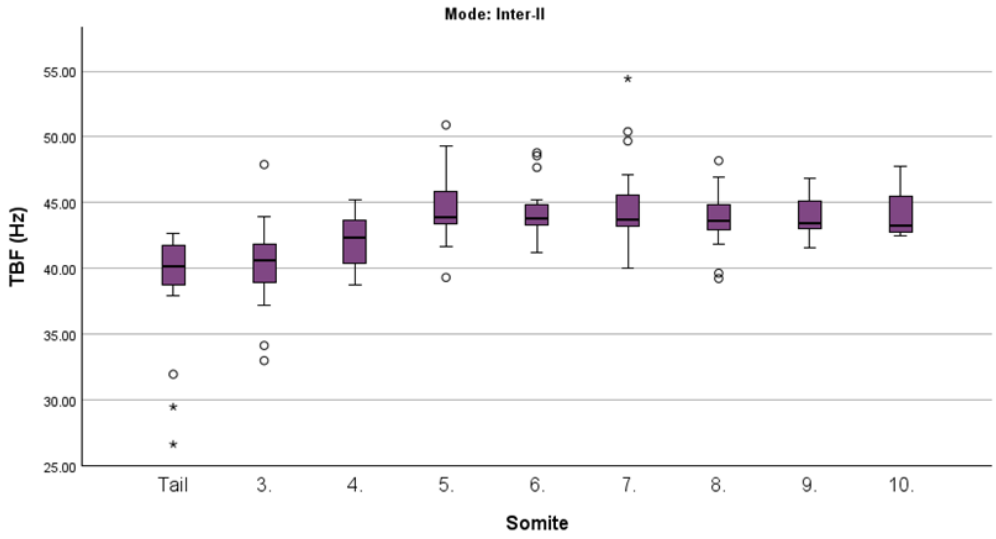
Mode: Inter-II
TBF (Hz)
55.00
50.00
45.00
40.00
35.00
30.00
25.00
Tail
3.
4.
5.
6.
7.
8.
9.
10.
Somite

C

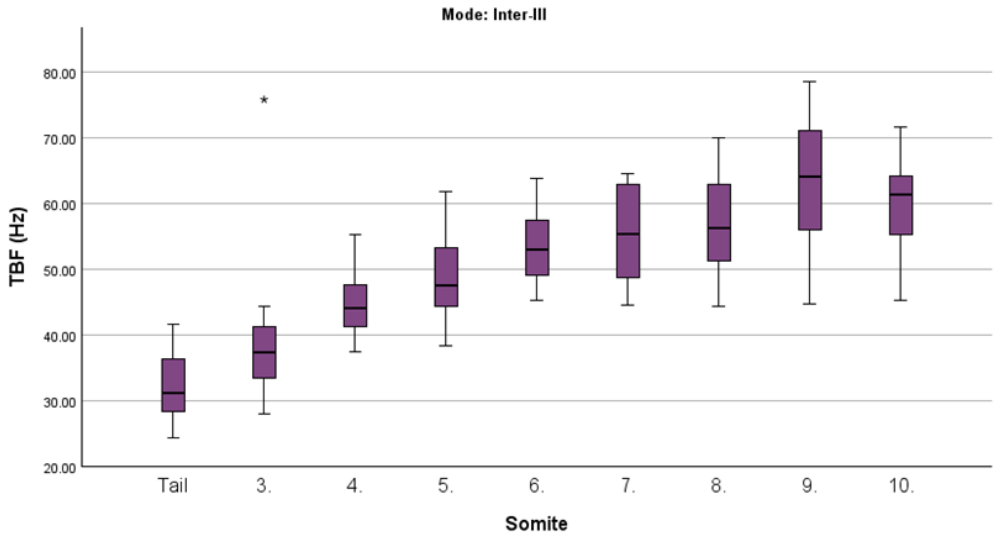
Mode: Inter-III
TBF (Hz)
80.00
70.00
60.00
50.00
40.00
30.00
20.00
Tail
3.
4.
5.
6.
7.
8.
9.
10.
Somite

Figure S25. The comparison of the distribution of TBFs calculated by the tail tip movement and MN activity on different somites in intermediate modes is shown.

Related to Figure 43. The first two somites were excluded from the comparison. (A) Inter-I Mode (Tail: 34.09 (IQR 32.99-34.45), N = 20; Somite 3: 30.51 (IQR 28.54-31.87), N = 20; Somite 4: 33.86 (IQR 32.39-35.27), N = 20; Somite 5: 35.13 (IQR 34.38-36.68), N = 20; Somite 6: 35.91 (IQR 33.77-36.71), N = 20; Somite 7: 35.96 (IQR 34.09-37.63), N = 20; Somite 8: 35.64 (IQR 34.52-36.7), N = 20; Somite 9: 36.12 (IQR 35.33-37.37), N = 20; Somite 10: 35.96 (IQR 35.23-36.9), N = 20), (B) Inter-II Mode (Tail: 40.12 (IQR 38.64-41.8), N = 20; Somite 3: 40.64 (IQR 38.91-42.02), N = 21; Somite 4: 42.37 (IQR 40.05-43.69), N = 20; Somite 5: 43.86 (IQR 43.36-46.02), N = 20; Somite 6: 43.84 (IQR 43.3-45.06), N = 20; Somite 7: 43.76 (IQR 43.23-45.79), N = 20; Somite 8: 43.58 (IQR 42.98-44.92), N = 20; Somite 9: 43.48 (IQR 43.01-45.39), N = 20; Somite 10: 43.28 (IQR 42.75-45.48), N = 20;), (C) Inter-III Mode (Tail: 31.22 (IQR 28.43-36.44), N = 20; Somite 3: 37.35 (IQR 33.4-41.68), N = 22; Somite 4: 43.98 (IQR 41.18-48.18), N = 21; Somite 5: 47.45 (IQR 44.01-53.29), N = 20; Somite 6: 52.99 (IQR 48.96-57.71), N = 20; Somite 7: 55.4 (IQR 48.02-62.97), N = 20; Somite 8: 56.27 (IQR 51.27-63.11), N = 20; Somite 9: 63.96 (IQR 55.63-71.92), N = 20; Somite 10: 61.29 (IQR 55.13-64.33), N = 20;).

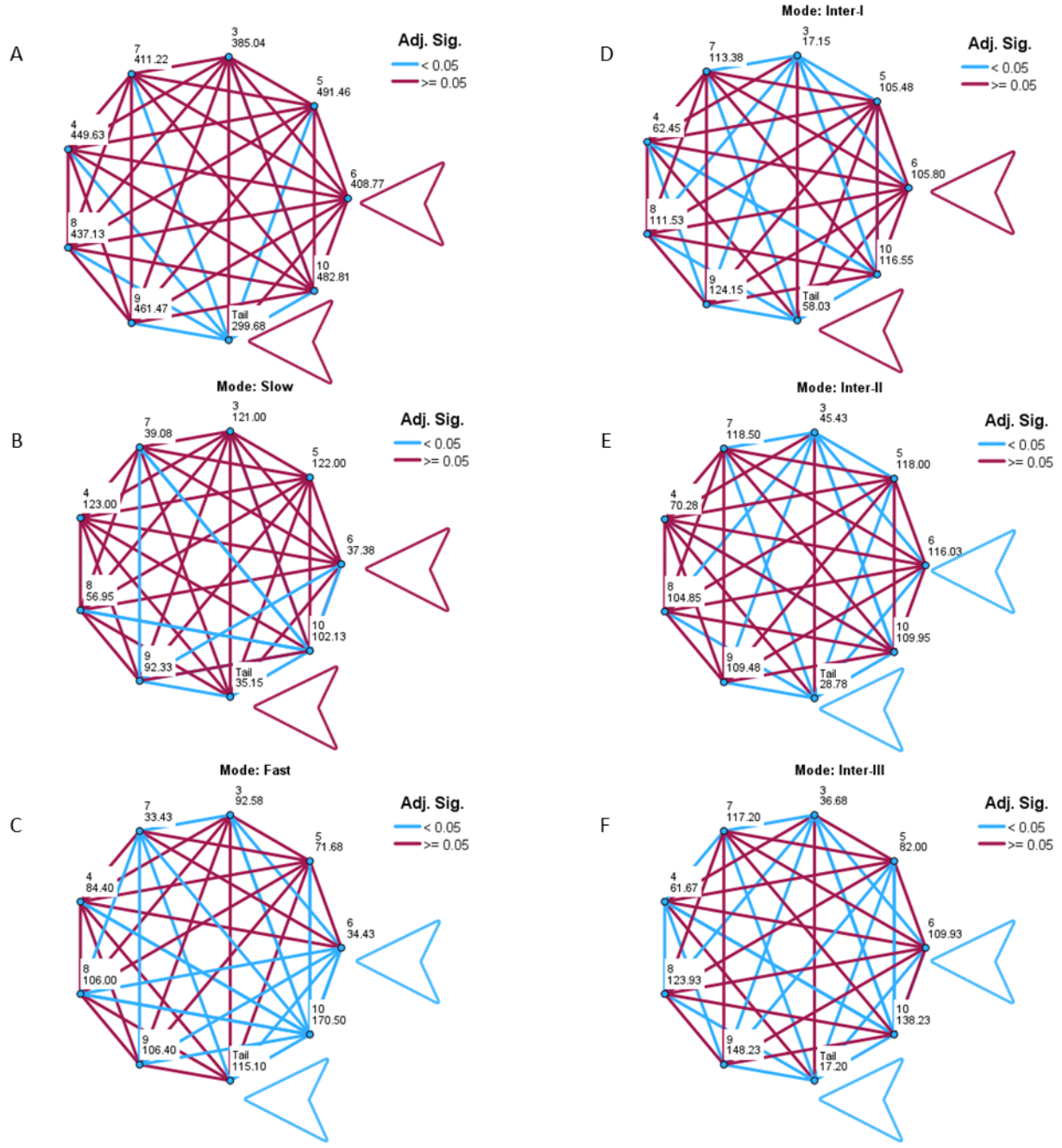

Figure S26. Pairwise comparisons of the TBFs measured by tail tip movement and MN activity of the somites are shown.

Pairwise comparisons of the pooled (A) and separated by the swim mode (B-F) TBFs are displayed. The nodes representing the tail and the sixth somite are pointed by an arrow header. The colour of the arrow header indicates whether they are significantly different (blue) or not (bordeaux).

Appendix 2. Infographics

MN Motoneurons

Projection: Bifurcating / Ipsilateral

Neurotransmitter: ACh

pMN

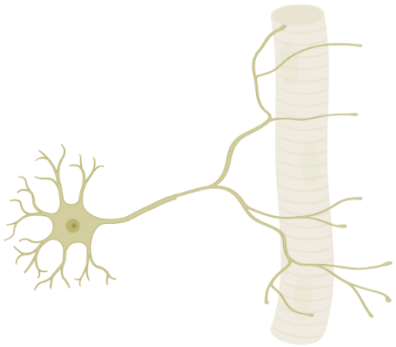

sMN-ms-type

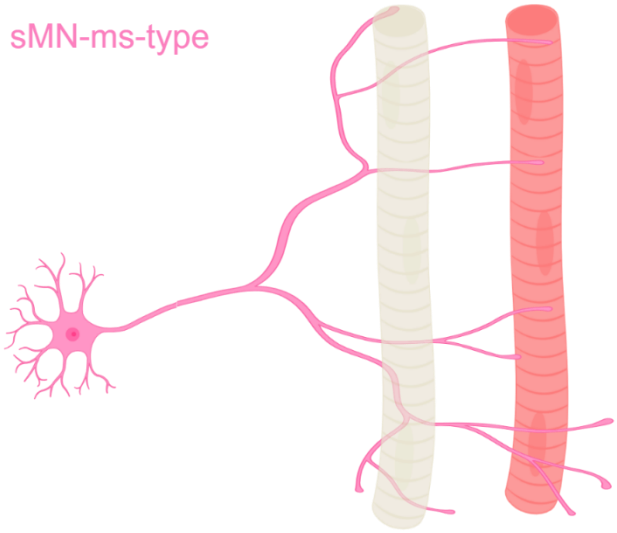

sMN-m-type

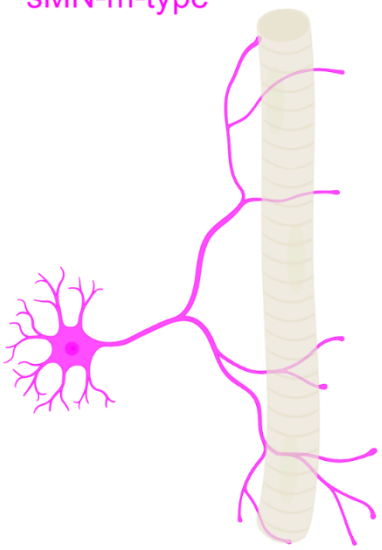

sMN-s-type

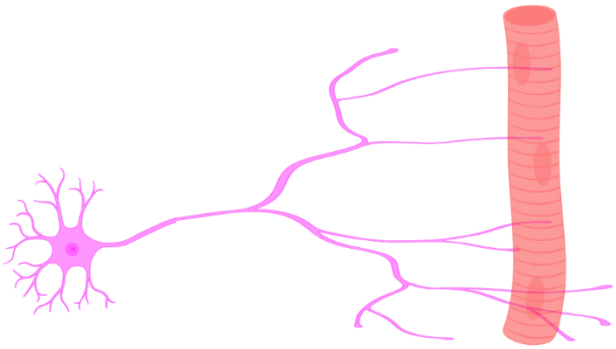

pMN

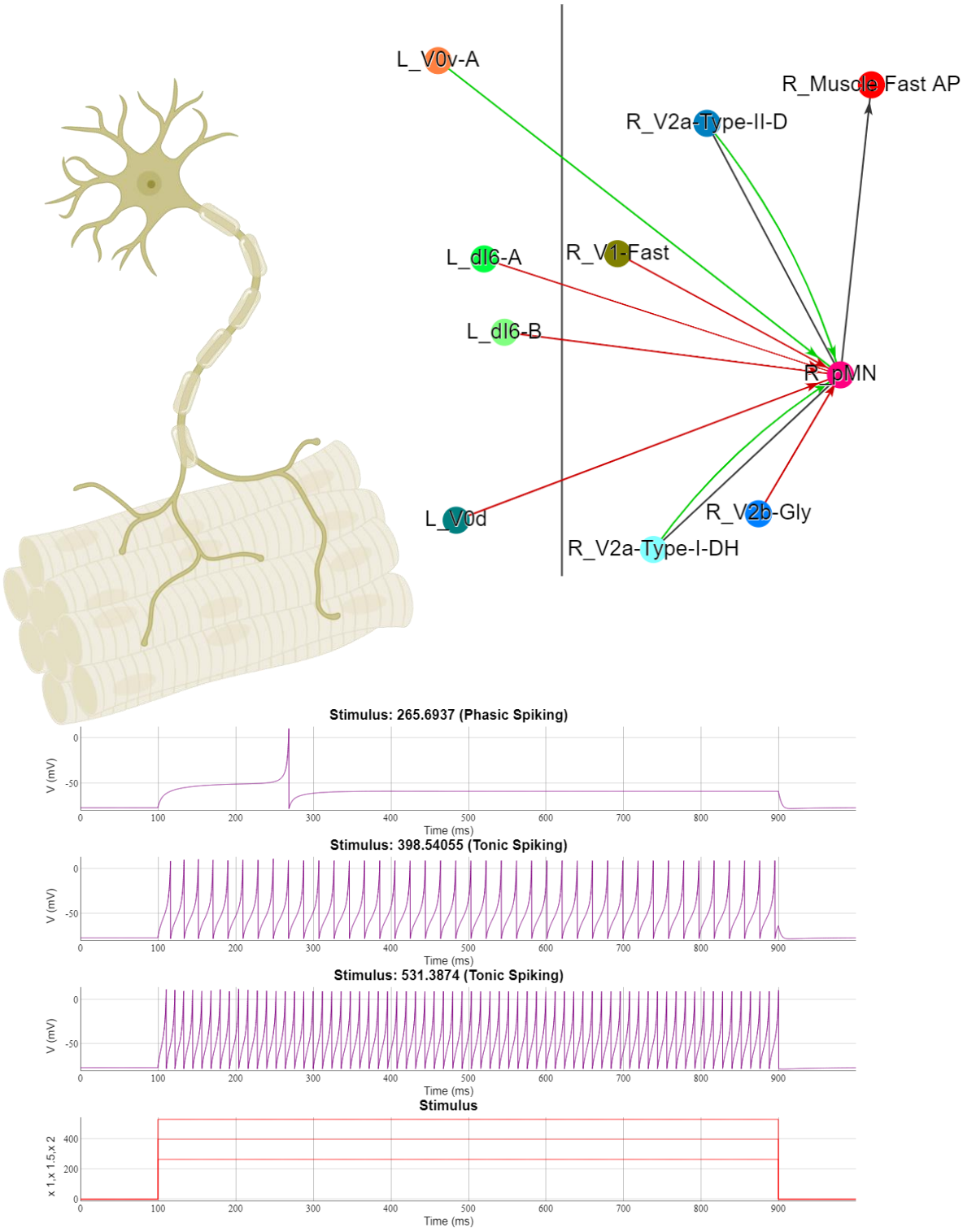
L_V0v-A
R_Muscle Fast AP
R_V2a-Type-II-D
L_dI6-A
R_V1-Fast
L_dI6-B
R_pMN
L_V0d
R_V2b-Gly
R_V2a-Type-I-DH
Stimulus: 265.6937 (Phasic Spiking)
Stimulus: 398.54055 (Tonic Spiking)
Stimulus: 531.3874 (Tonic Spiking)
Stimulus
V (mV)
Time (ms)
x 1, x 1.5, x 2

sMN-m-type

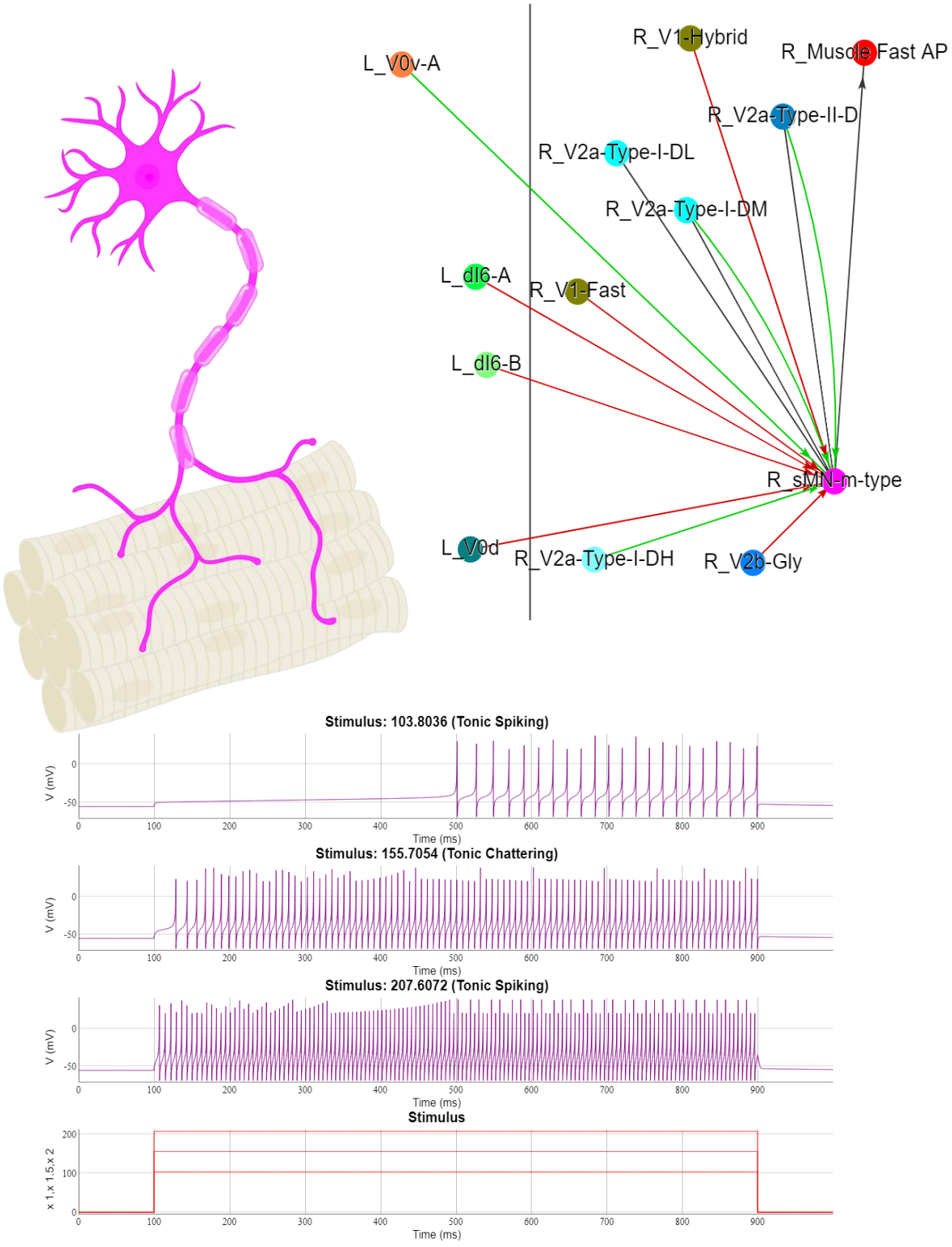
L_V0v-A
R_V1-Hybrid
R_Muscle Fast AP
R_V2a-Type-II-D
R_V2a-Type-I-DL
R_V2a-Type-I-DM
L_dI6-A
R_V1-Fast
L_dI6-B
R_sMN-m-type
L_V0d
R_V2a-Type-I-DH
R_V2b-Gly
Stimulus: 103.8036 (Tonic Spiking)
Stimulus: 155.7054 (Tonic Chattering)
Stimulus: 207.6072 (Tonic Spiking)
Stimulus
V (mV)
Time (ms)
x 1, x 1.5, x 2

sMN-ms-type

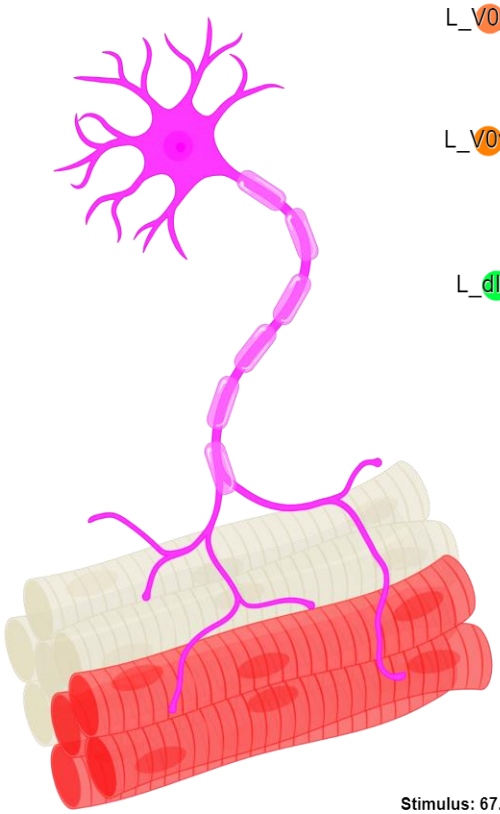

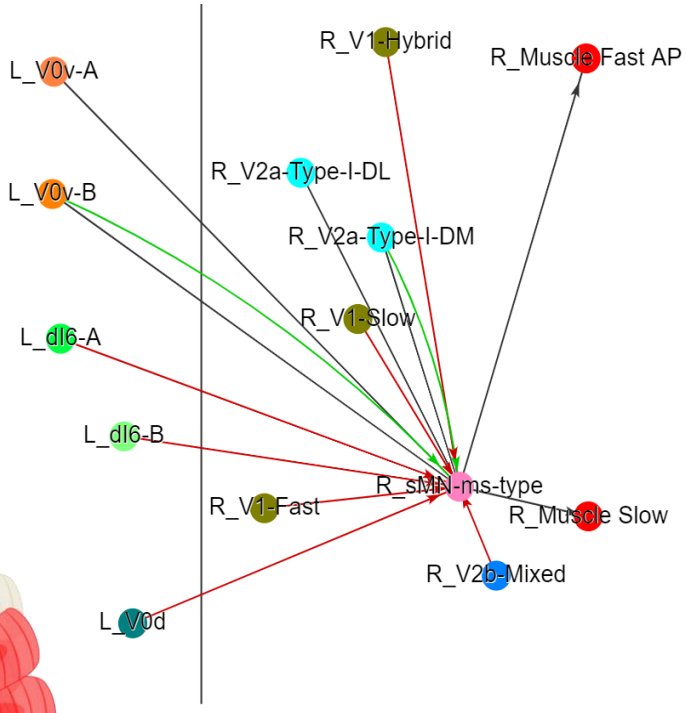
R_V1-Hybrid
R_Muscle Fast AP
L_V0v-A
R_V2a-Type-I-DL
L_V0v-B
R_V2a-Type-I-DM
R_V1-Slow
L_dI6-A
L_dI6-B
R_sMN-ms-type
R_V1-Fast
R_Muscle Slow
R_V2b-Mixed
L_V0d

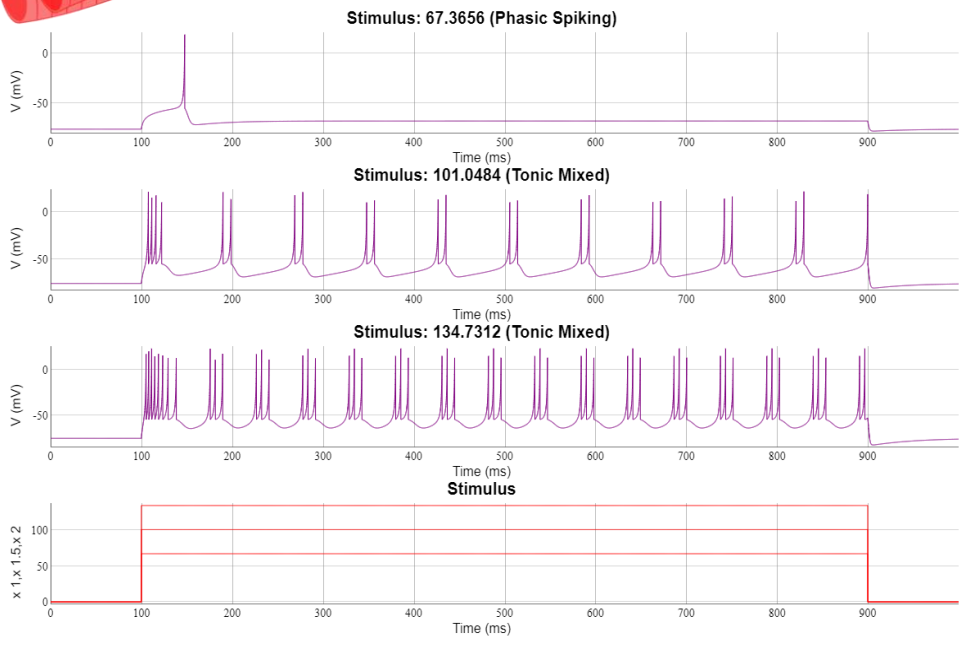
Stimulus: 67.3656 (Phasic Spiking)
V (mV)
Time (ms)
Stimulus: 101.0484 (Tonic Mixed)
V (mV)
Time (ms)
Stimulus: 134.7312 (Tonic Mixed)
V (mV)
Time (ms)
Stimulus
x 1,x 1.5,x 2
Time (ms)

sMN-s-type

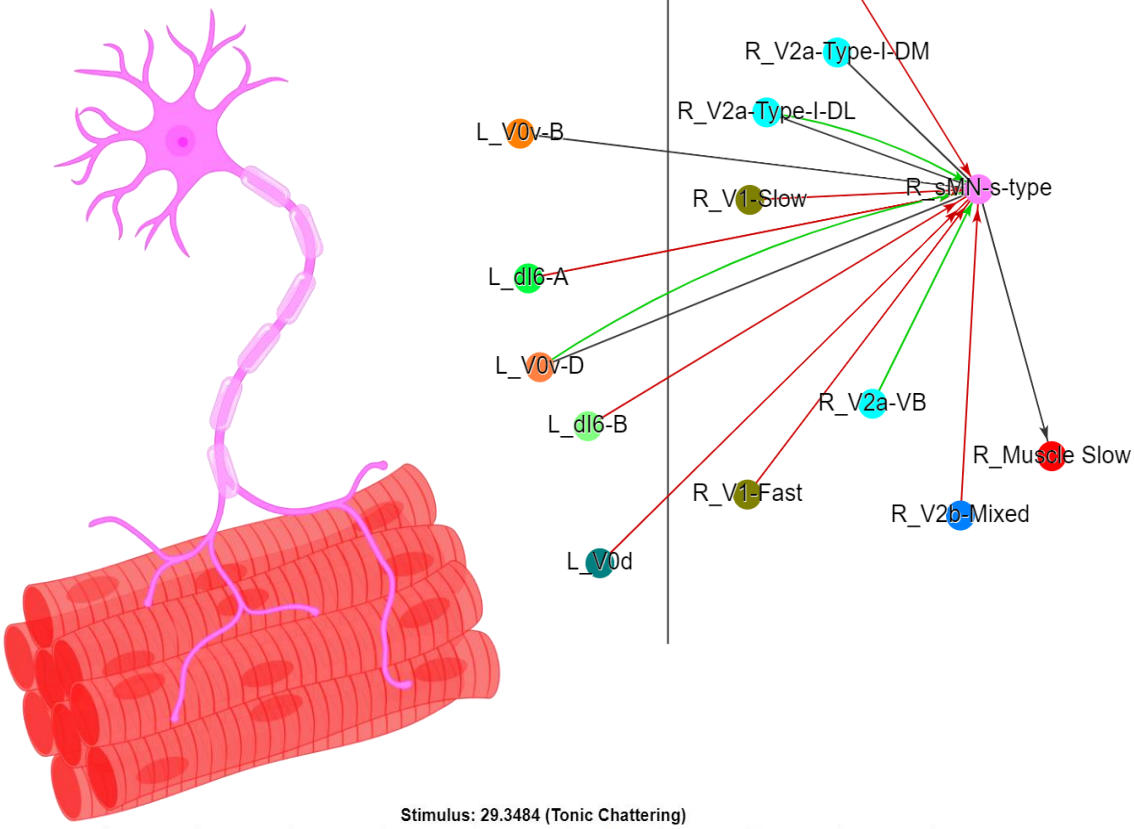
R_V1-Hybrid
R_V2a-Type-I-DM
R_V2a-Type-I-DL
L_V0v-B
R_sMN-s-type
R_V1-Slow
L_dI6-A
L_V0v-D
L_dI6-B
R_V2a-VB
R_Muscle Slow
R_V1-Fast
R_V2b-Mixed
L_V0d

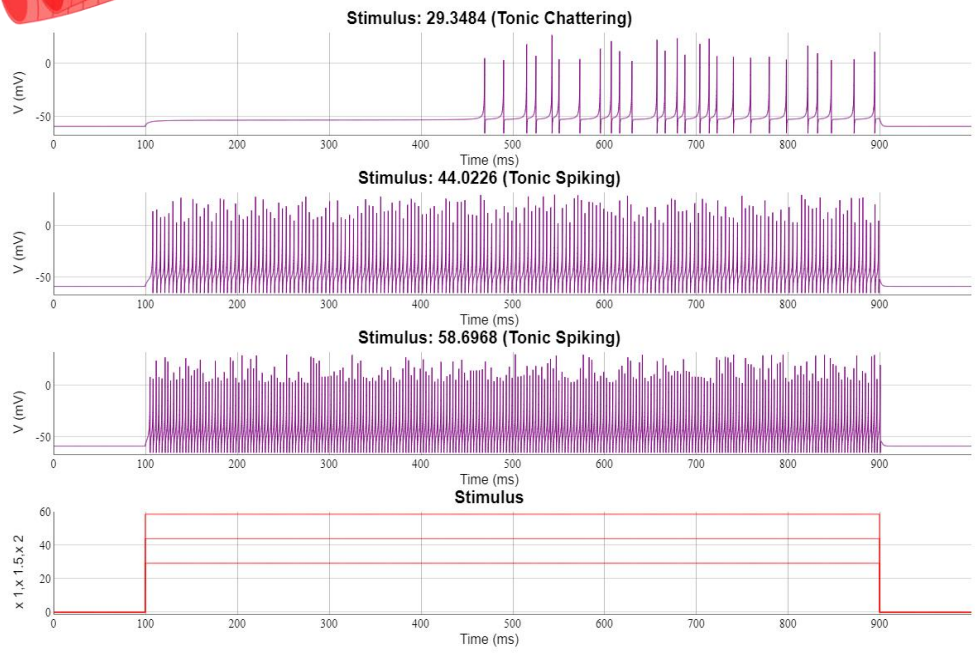
Stimulus: 29.3484 (Tonic Chattering)
V (mV)
Time (ms)
Stimulus: 44.0226 (Tonic Spiking)
V (mV)
Time (ms)
Stimulus: 58.6968 (Tonic Spiking)
V (mV)
Time (ms)
Stimulus
x 1, x 1.5, x 2
Time (ms)

dI6 Inhibitory

Projection: Bifurcating / Contralateral

Neurotransmitter: Glycine

dI6-A

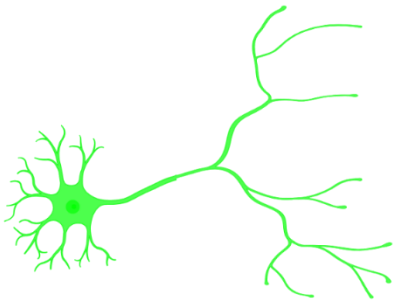

dI6-B

V0d Inhibitory

Projection: Bifurcating / Contralateral

Neurotransmitter: Glycine

V0d

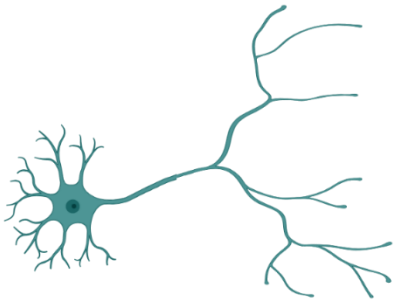

dI6-A

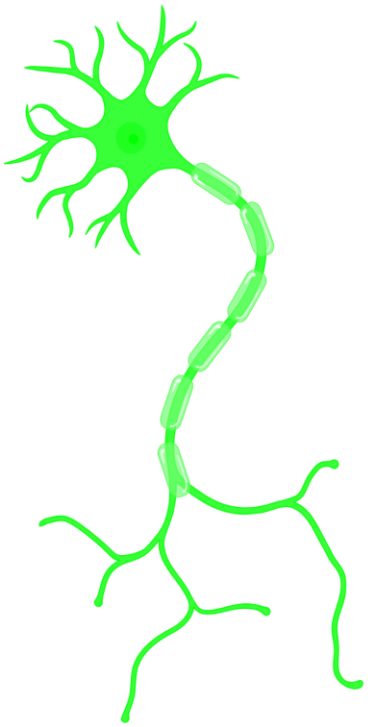

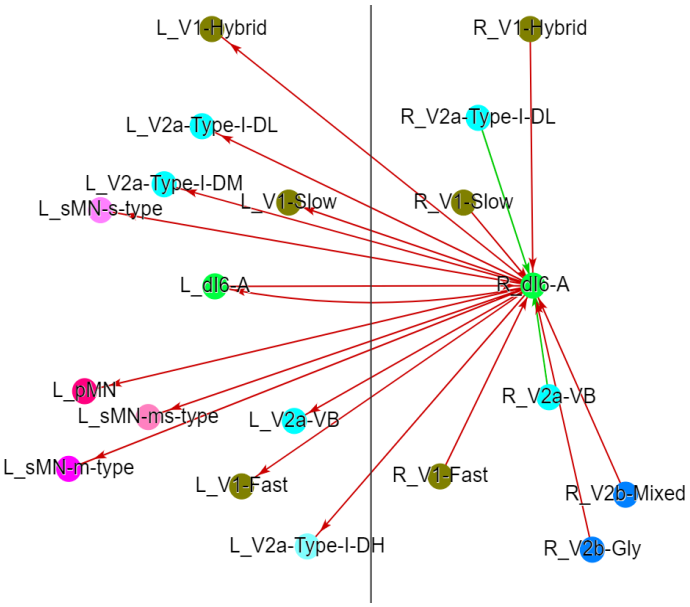
L_V1-Hybrid
R_V1-Hybrid
L_V2a-Type-I-DL
R_V2a-Type-I-DL
L_V2a-Type-I-DM
L_sMN-s-type
L_V1-Slow
R_V1-Slow
L_dI6-A
R_dI6-A
L_pMN
L_sMN-ms-type
L_V2a-VB
R_V2a-VB
L_sMN-m-type
L_V1-Fast
R_V1-Fast
R_V2b-Mixed
L_V2a-Type-I-DH
R_V2b-Gly

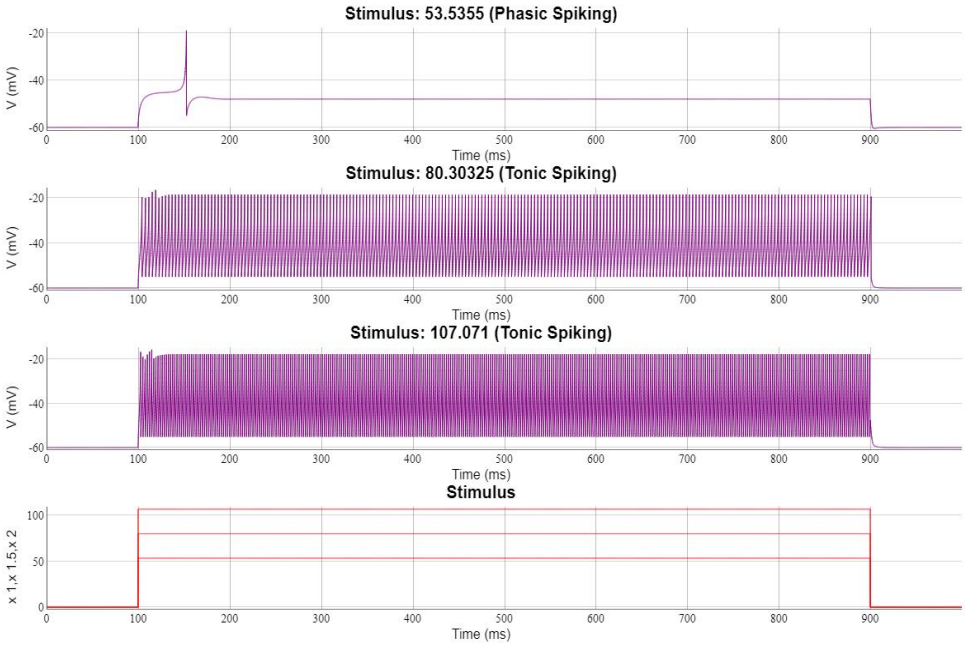
Stimulus: 53.5355 (Phasic Spiking)
Stimulus: 80.30325 (Tonic Spiking)
Stimulus: 107.071 (Tonic Spiking)
Stimulus
V (mV)
x 1,x 1.5,x 2
Time (ms)

dI6-B

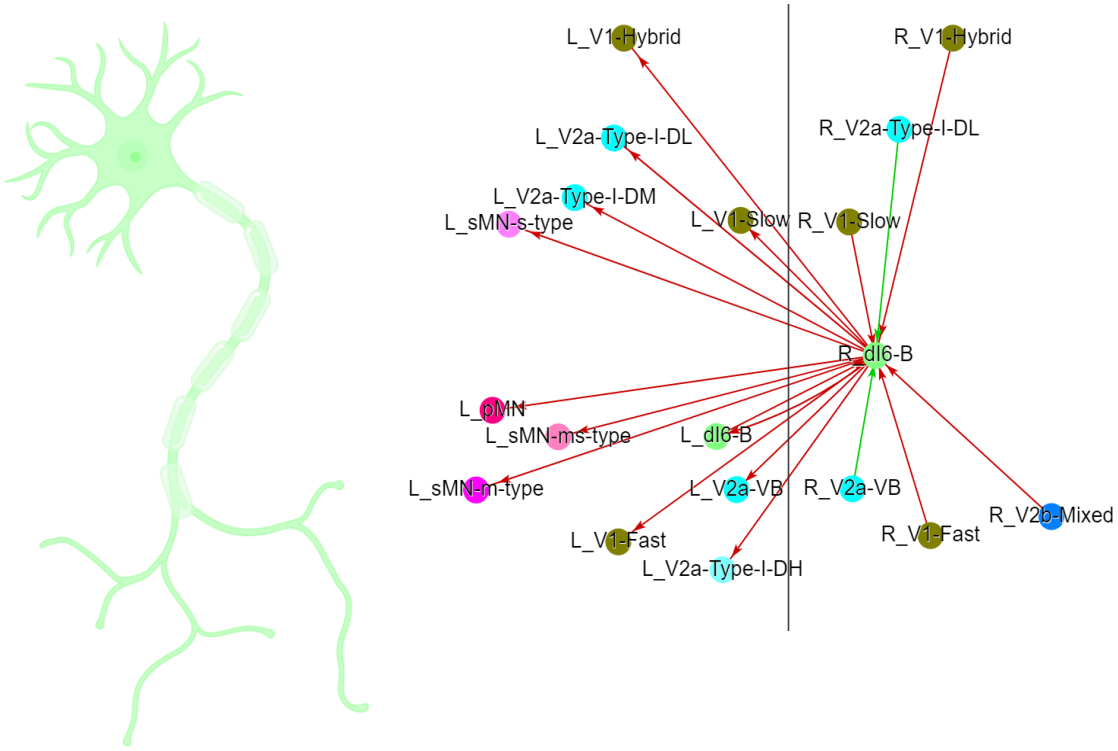
L_V1-Hybrid
R_V1-Hybrid
L_V2a-Type-I-DL
R_V2a-Type-I-DL
L_V2a-Type-I-DM
L_sMN-s-type
L_V1-Slow
R_V1-Slow
R_dI6-B
L_pMN
L_sMN-ms-type
L_dI6-B
L_sMN-m-type
L_V2a-VB
R_V2a-VB
R_V2b-Mixed
L_V1-Fast
R_V1-Fast
L_V2a-Type-I-DH

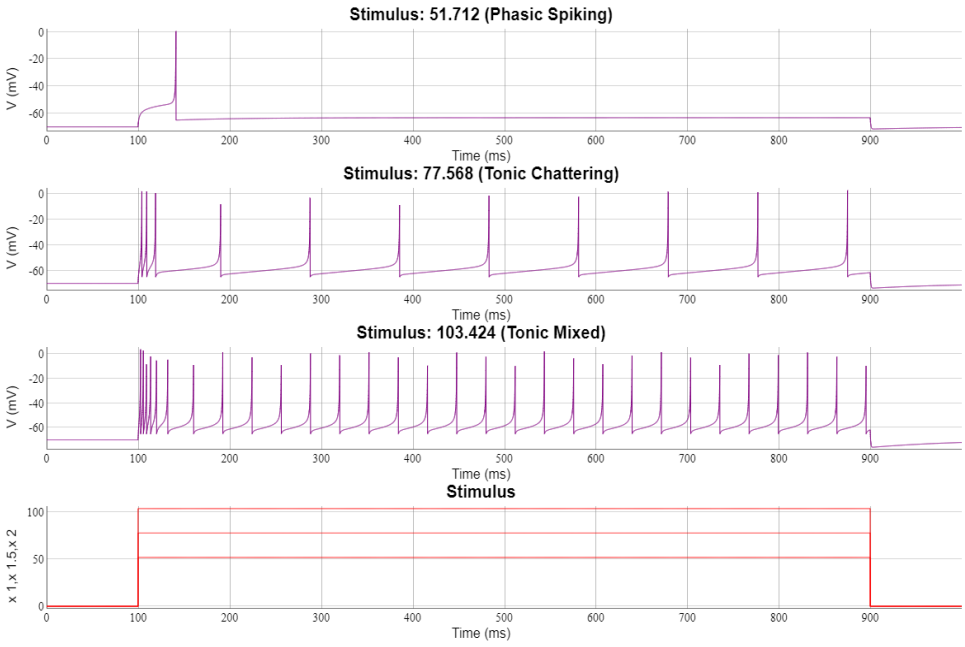
Stimulus: 51.712 (Phasic Spiking)
Stimulus: 77.568 (Tonic Chattering)
Stimulus: 103.424 (Tonic Mixed)
Stimulus
V (mV)
Time (ms)
x 1,x 1.5,x 2

V0d

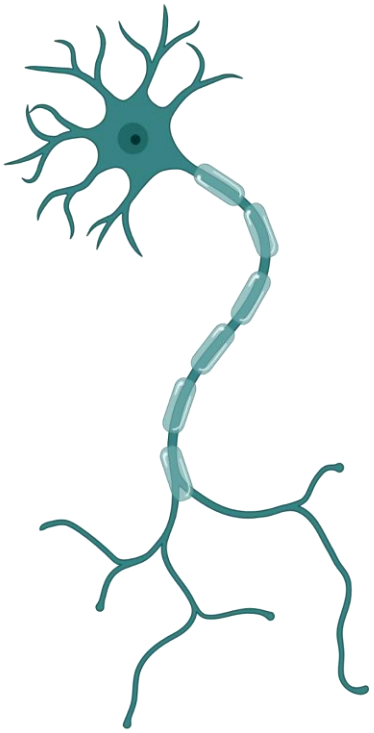

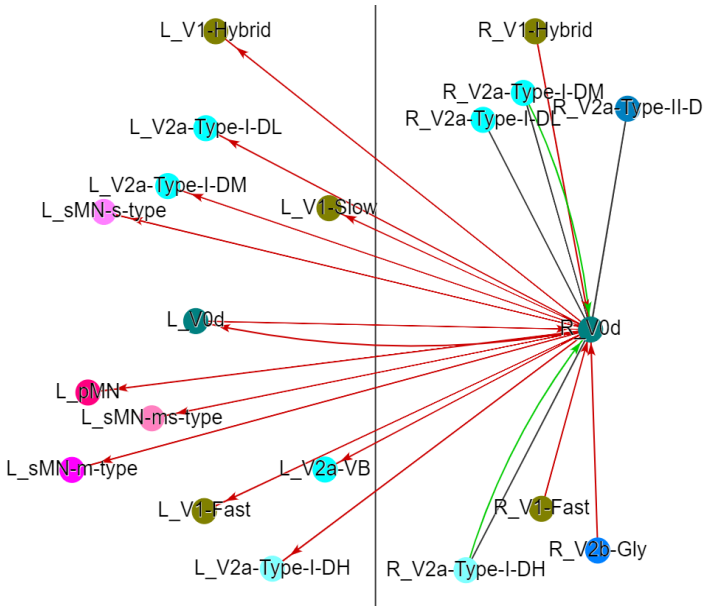
L_V1-Hybrid
R_V1-Hybrid
R_V2a-Type-I-DM
R_V2a-Type-II-D
R_V2a-Type-I-DL
L_V2a-Type-I-DL
L_V2a-Type-I-DM
L_sMN-s-type
L_V1-Slow
L_V0d
R_V0d
L_pMN
L_sMN-ms-type
L_sMN-m-type
L_V2a-VB
L_V1-Fast
R_V1-Fast
R_V2b-Gly
L_V2a-Type-I-DH
R_V2a-Type-I-DH


Stimulus: 23.6549 (Phasic Spiking)
Stimulus: 35.48235 (Tonic Spiking)
Stimulus: 47.3098 (Tonic Spiking)
Stimulus
V (mV)
x 1,x 1.5,x 2
Time (ms)

V0v

Projection: Contralateral

Neurotransmitter: Glutamate

V0v-A

Projection: Ascending

V0v-B

Projection: Bifurcating

V0v-D

Projection: Descending

V0v-A

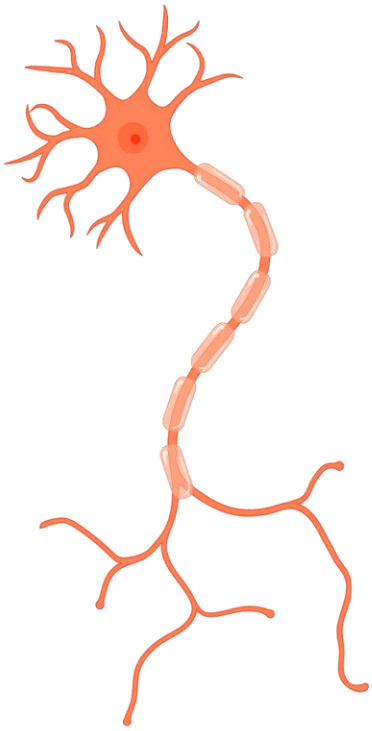

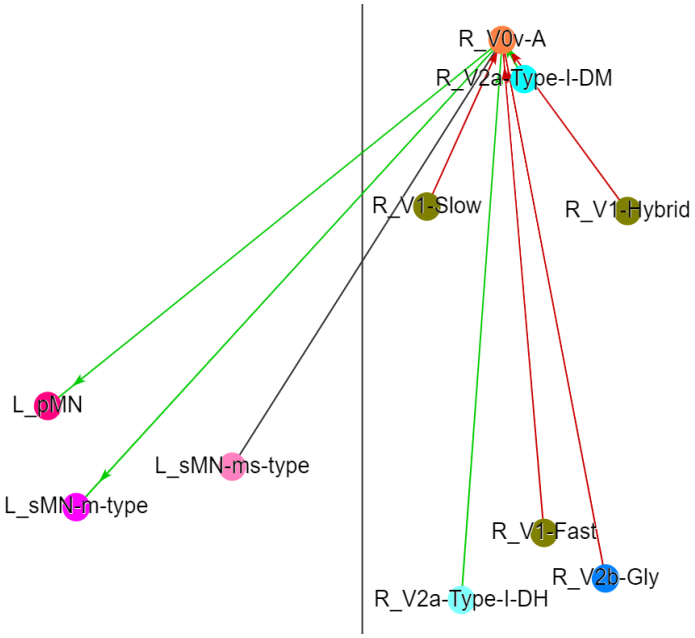
R_V0v-A
R_V2a-Type-I-DM
R_V1-Slow
R_V1-Hybrid
L_pMN
L_sMN-ms-type
L_sMN-m-type
R_V1-Fast
R_V2b-Gly
R_V2a-Type-I-DH

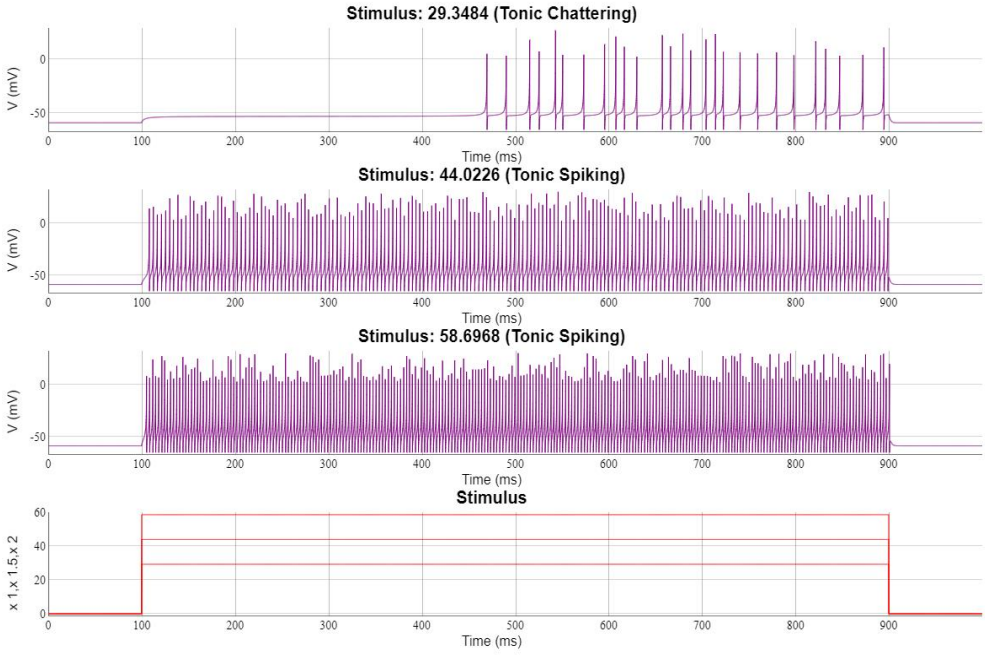
Stimulus: 29.3484 (Tonic Chattering)
Stimulus: 44.0226 (Tonic Spiking)
Stimulus: 58.6968 (Tonic Spiking)
Stimulus
V (mV)
x 1, x 1.5, x 2
Time (ms)

V0v-B

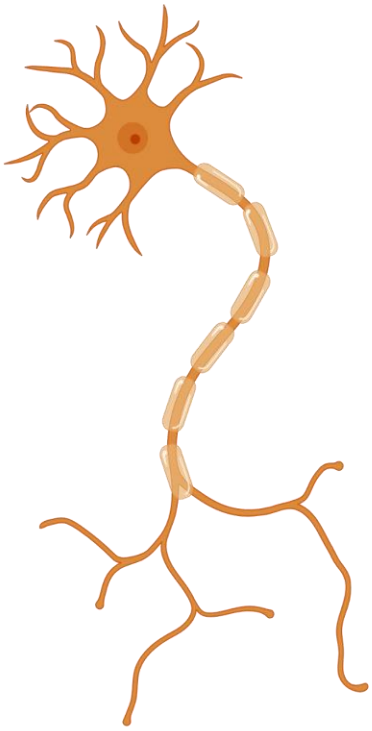

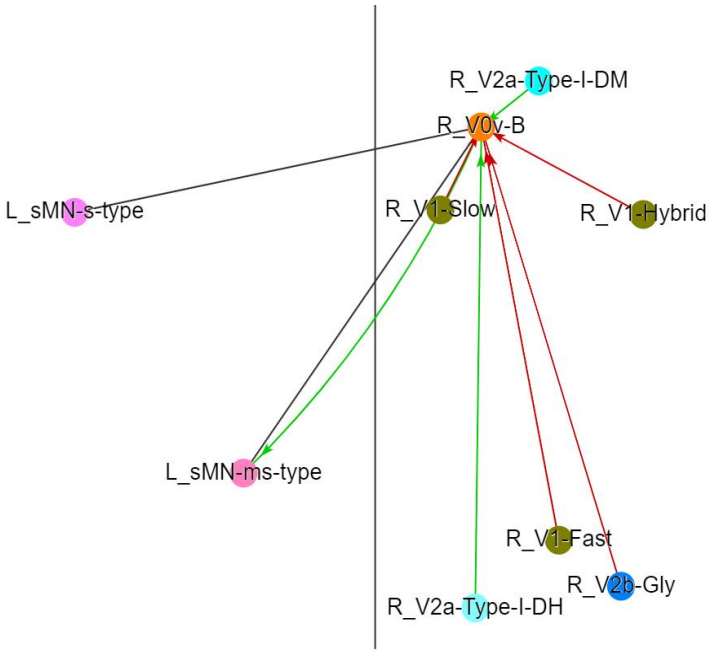
R_V2a-Type-I-DM
R_V0v-B
L_sMN-s-type
R_V1-Slow
R_V1-Hybrid
L_sMN-ms-type
R_V1-Fast
R_V2b-Gly
R_V2a-Type-I-DH


Stimulus: 14.8525 (Tonic Chattering)
Stimulus: 22.27875 (Tonic Spiking)
Stimulus: 29.705 (Tonic Spiking)
Stimulus
V (mV)
x 1, x 1.5, x 2
Time (ms)

V0v-D

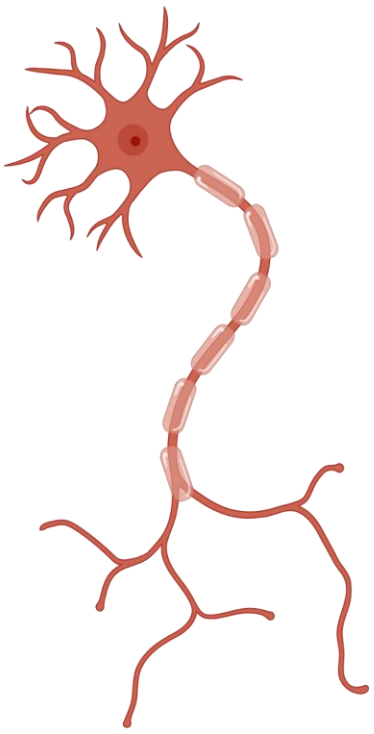

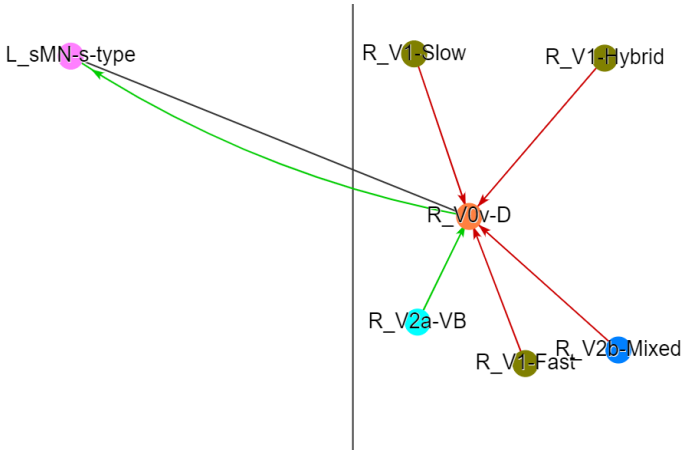
L_sMN-s-type
R_V1-Slow
R_V1-Hybrid
R_V0v-D
R_V2a-VB
R_V2b-Mixed
R_V1-Fast


Stimulus: 11.0683 (Phasic Spiking)
Stimulus: 16.60245 (Tonic Spiking)
Stimulus: 22.1366 (Tonic Spiking)
Stimulus
V (mV)
x 1,x 1.5,x 2
Time (ms)

V1 Inhibitory

Projection: Bifurcating / Ipsilateral

Neurotransmitter: Glycine & GABA

V1-Fast

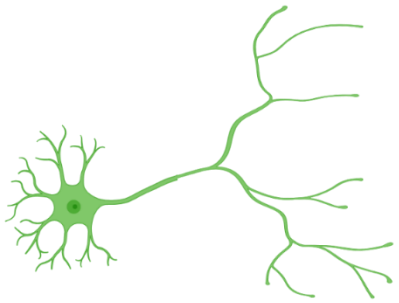

V1-Hybrid

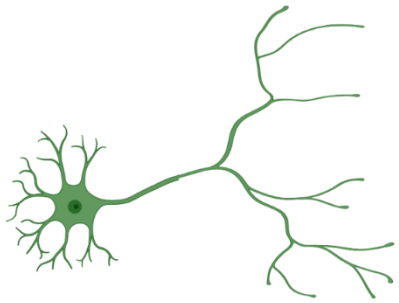

V1-Slow

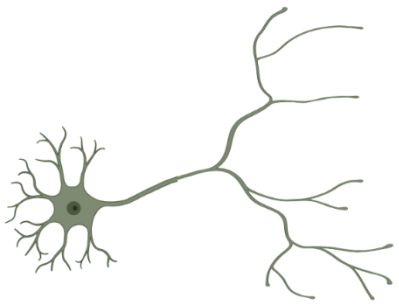

V1-Fast

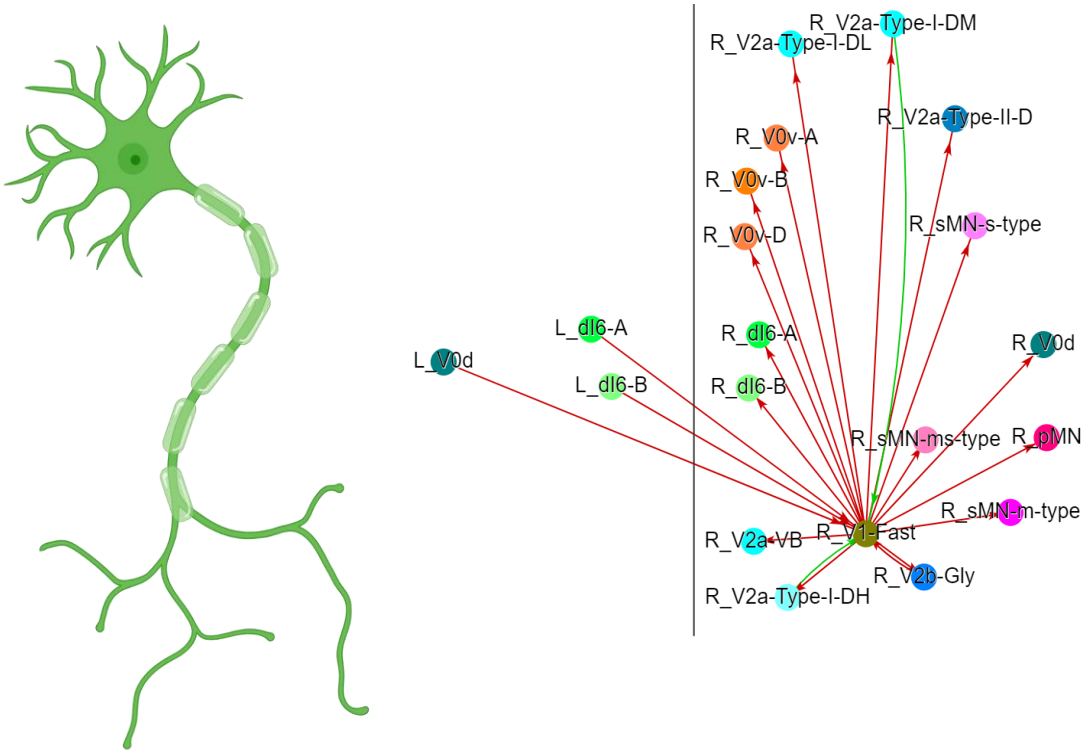
R_V2a-Type-I-DM
R_V2a-Type-I-DL
R_V2a-Type-II-D
R_V0v-A
R_V0v-B
R_V0v-D
R_sMN-s-type
L_dI6-A
L_V0d
R_dI6-A
R_V0d
L_dI6-B
R_dI6-B
R_sMN-ms-type
R_pMN
R_sMN-m-type
R_V2a-VB
R_V1-Fast
R_V2b-Gly
R_V2a-Type-I-DH

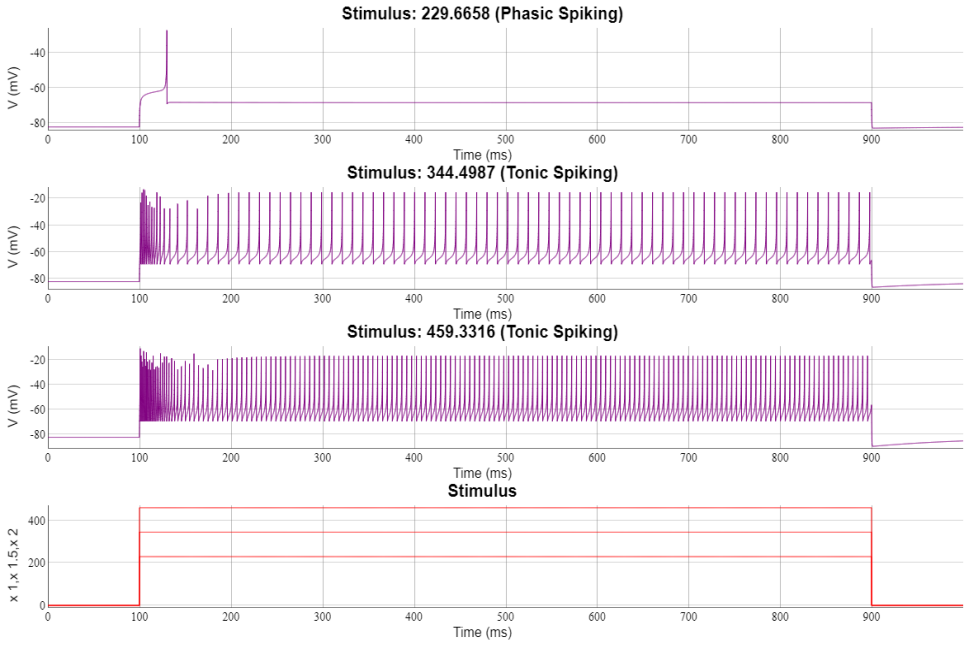
Stimulus: 229.6658 (Phasic Spiking)
V (mV)
Time (ms)
Stimulus: 344.4987 (Tonic Spiking)
V (mV)
Time (ms)
Stimulus: 459.3316 (Tonic Spiking)
V (mV)
Time (ms)
Stimulus
x 1, x 1.5, x 2
Time (ms)

V1-Hybrid

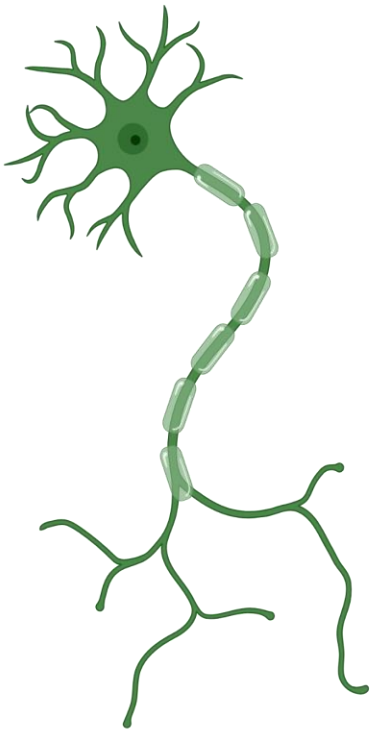

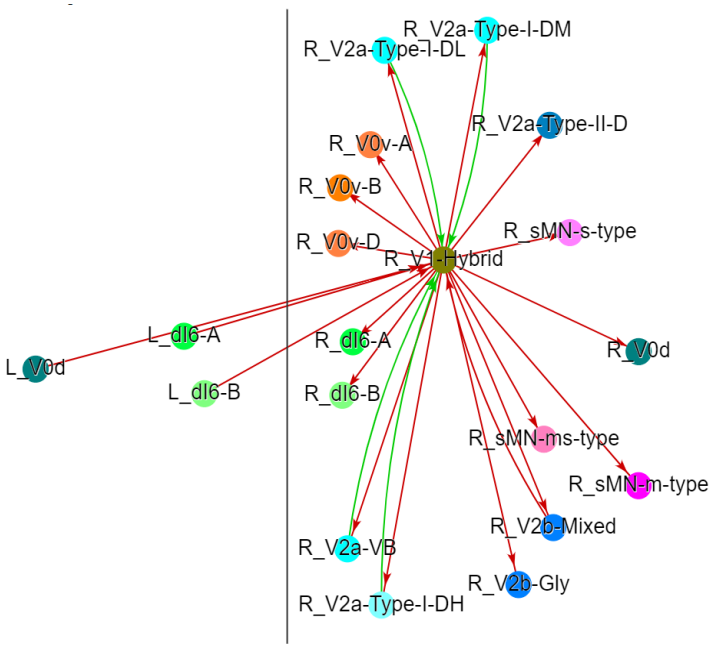
R_V2a-Type-I-DM
R_V2a-Type-I-DL
R_V2a-Type-II-D
R_V0v-A
R_V0v-B
R_V0v-D
R_sMN-s-type
R_V1-Hybrid
L_dI6-A
L_V0d
L_dI6-B
R_dI6-A
R_dI6-B
R_V0d
R_sMN-ms-type
R_sMN-m-type
R_V2b-Mixed
R_V2a-VB
R_V2b-Gly
R_V2a-Type-I-DH

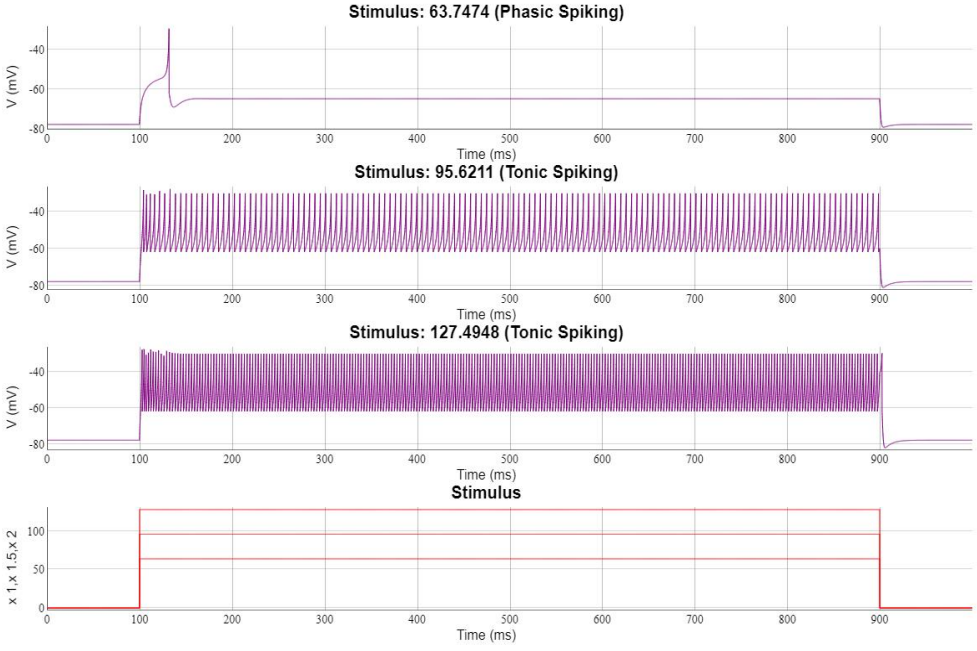
Stimulus: 63.7474 (Phasic Spiking)
Stimulus: 95.6211 (Tonic Spiking)
Stimulus: 127.4948 (Tonic Spiking)
Stimulus
V (mV)
x 1, x 1.5, x 2
Time (ms)

V1-Slow

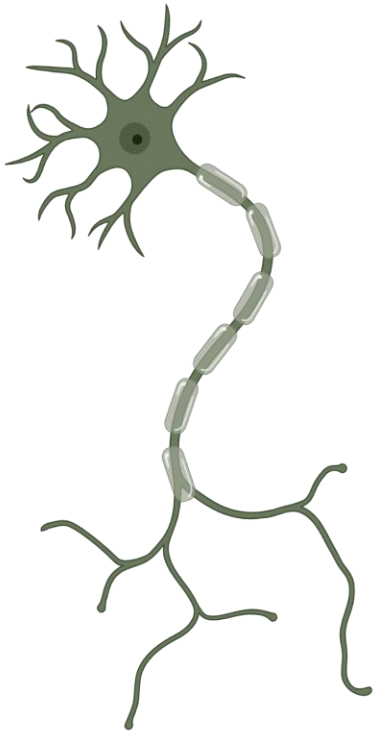

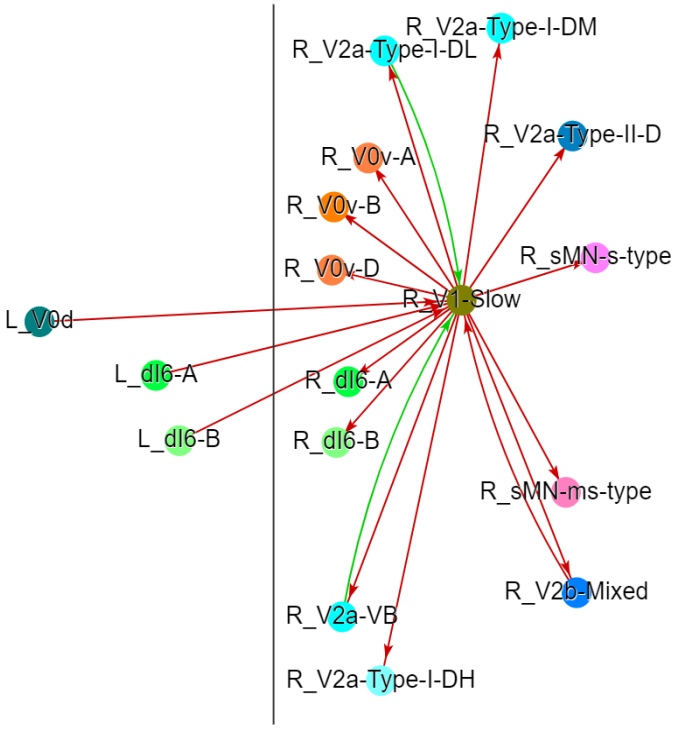
R_V2a-Type-I-DM
R_V2a-Type-I-DL
R_V2a-Type-II-D
R_V0v-A
R_V0v-B
R_sMN-s-type
R_V0v-D
R_V1-Slow
L_V0d
L_dI6-A
R_dI6-A
L_dI6-B
R_dI6-B
R_sMN-ms-type
R_V2b-Mixed
R_V2a-VB
R_V2a-Type-I-DH

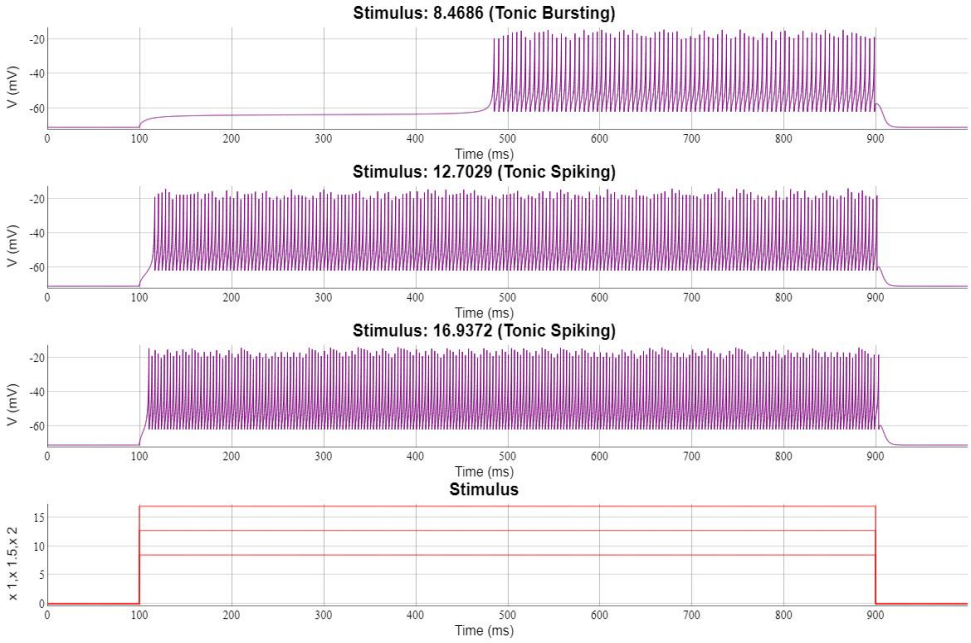
Stimulus: 8.4686 (Tonic Bursting)
Stimulus: 12.7029 (Tonic Spiking)
Stimulus: 16.9372 (Tonic Spiking)
Stimulus
V (mV)
x 1,x 1.5,x 2
Time (ms)

V2a Excitatory

Projection: Bifurcating / Ipsilateral

Neurotransmitter: Glutamate

V2a-Type-I-DH

V2a-Type-I-DM

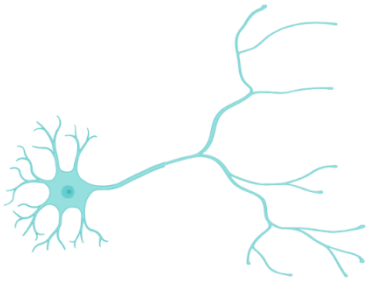

V2a-Type-I-DL

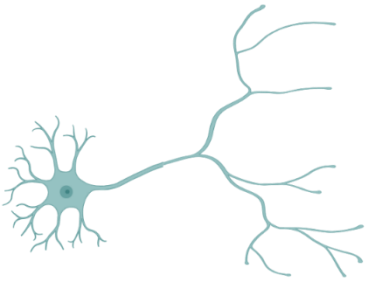

V2a-Type-II-D

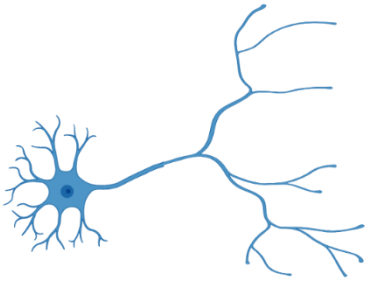

V2a-VB

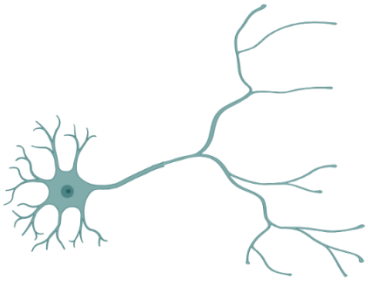

V2a-Type-I-DH

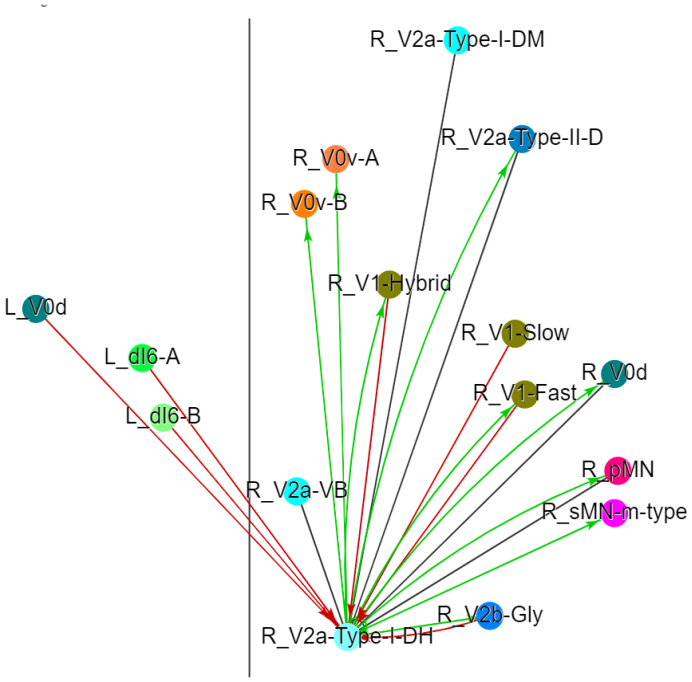
R_V2a-Type-I-DM
R_V2a-Type-II-D
R_V0v-A
R_V0v-B
R_V1-Hybrid
L_V0d
L_dI6-A
L_dI6-B
R_V1-Slow
R_V0d
R_V1-Fast
R_pMN
R_V2a-VB
R_sMN-m-type
R_V2b-Gly
R_V2a-Type-I-DH

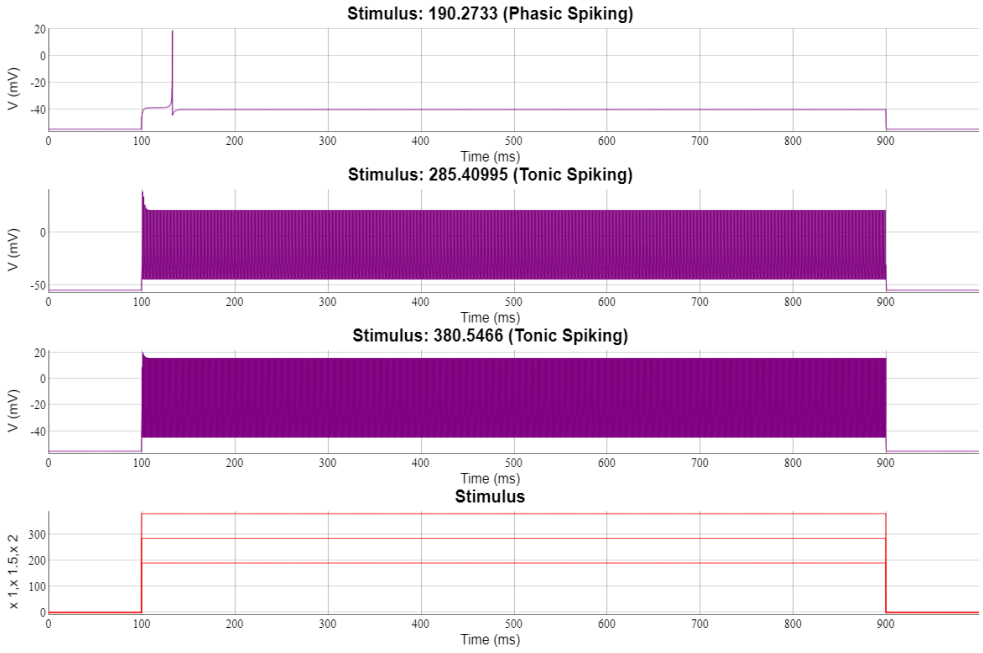
Stimulus: 190.2733 (Phasic Spiking)
V (mV)
Time (ms)
Stimulus: 285.40995 (Tonic Spiking)
V (mV)
Time (ms)
Stimulus: 380.5466 (Tonic Spiking)
V (mV)
Time (ms)
Stimulus
x 1, x 1.5, x 2
Time (ms)

V2a-Type-I-DL

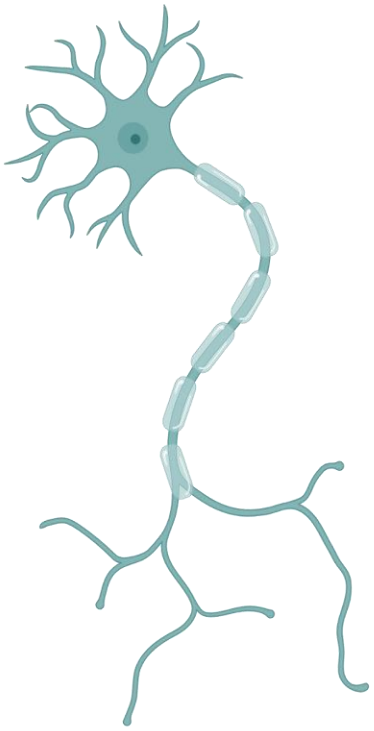

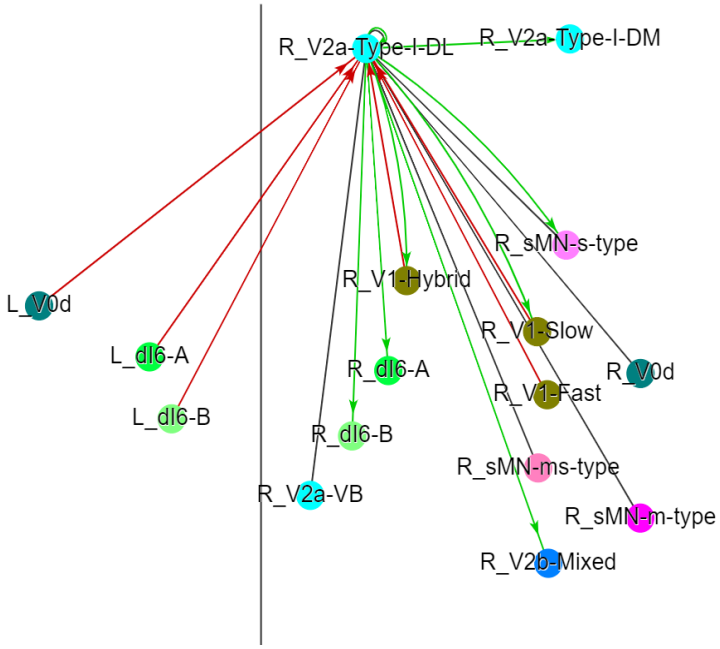
R_V2a-Type-I-DL
R_V2a-Type-I-DM
R_sMN-s-type
R_V1-Hybrid
L_V0d
R_V1-Slow
L_dI6-A
R_dI6-A
R_V0d
R_V1-Fast
L_dI6-B
R_dI6-B
R_sMN-ms-type
R_V2a-VB
R_sMN-m-type
R_V2b-Mixed

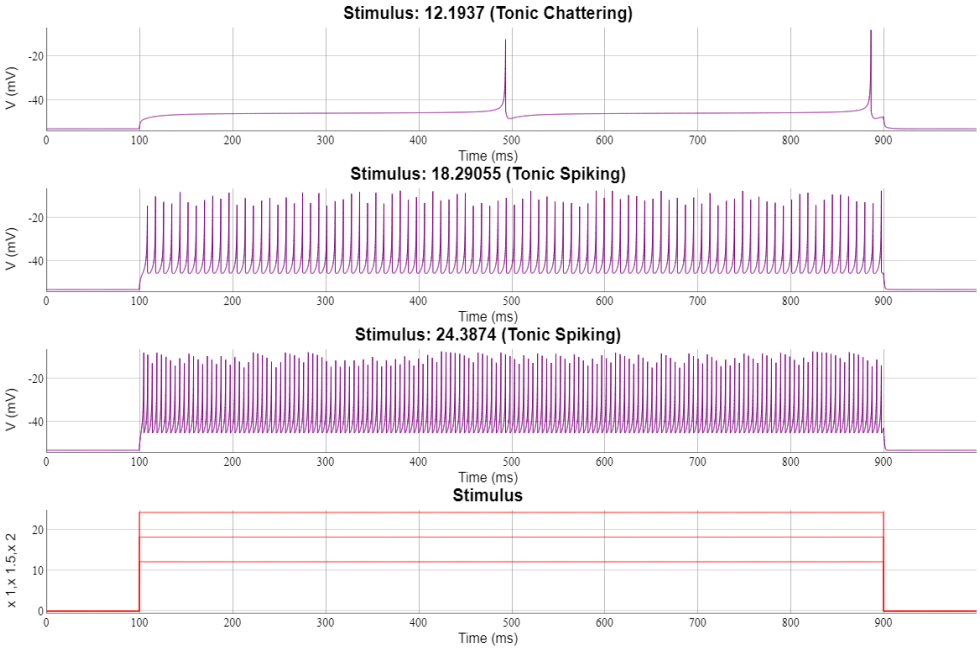
Stimulus: 12.1937 (Tonic Chattering)
Stimulus: 18.29055 (Tonic Spiking)
Stimulus: 24.3874 (Tonic Spiking)
Stimulus
V (mV)
x 1, x 1.5, x 2
Time (ms)

V2a-Type-I-DM

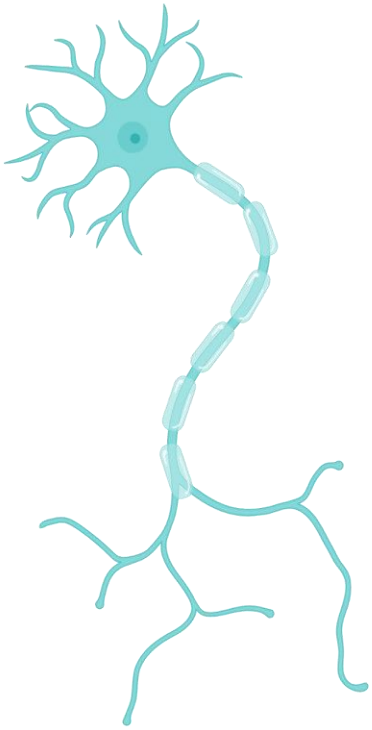

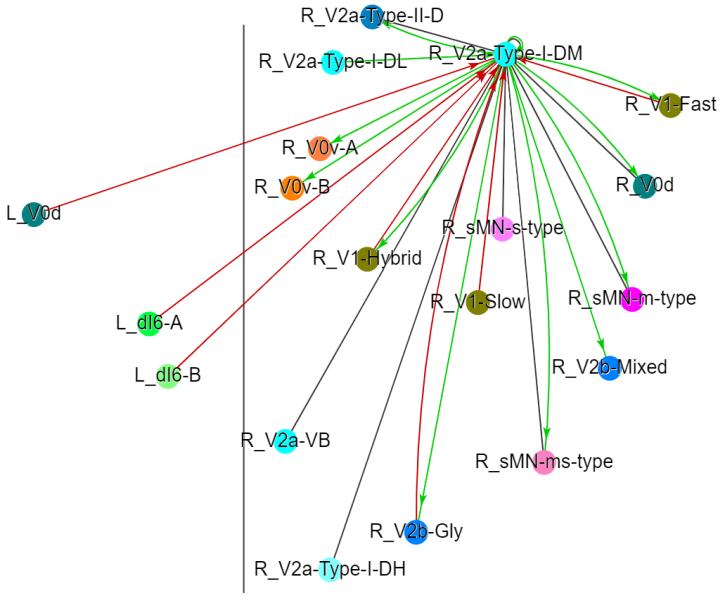
R_V2a-Type-II-D
R_V2a-Type-I-DL
R_V2a-Type-I-DM
R_V1-Fast
R_V0v-A
R_V0v-B
R_V0d
L_V0d
R_sMN-s-type
R_V1-Hybrid
R_V1-Slow
R_sMN-m-type
L_dI6-A
L_dI6-B
R_V2b-Mixed
R_V2a-VB
R_sMN-ms-type
R_V2b-Gly
R_V2a-Type-I-DH

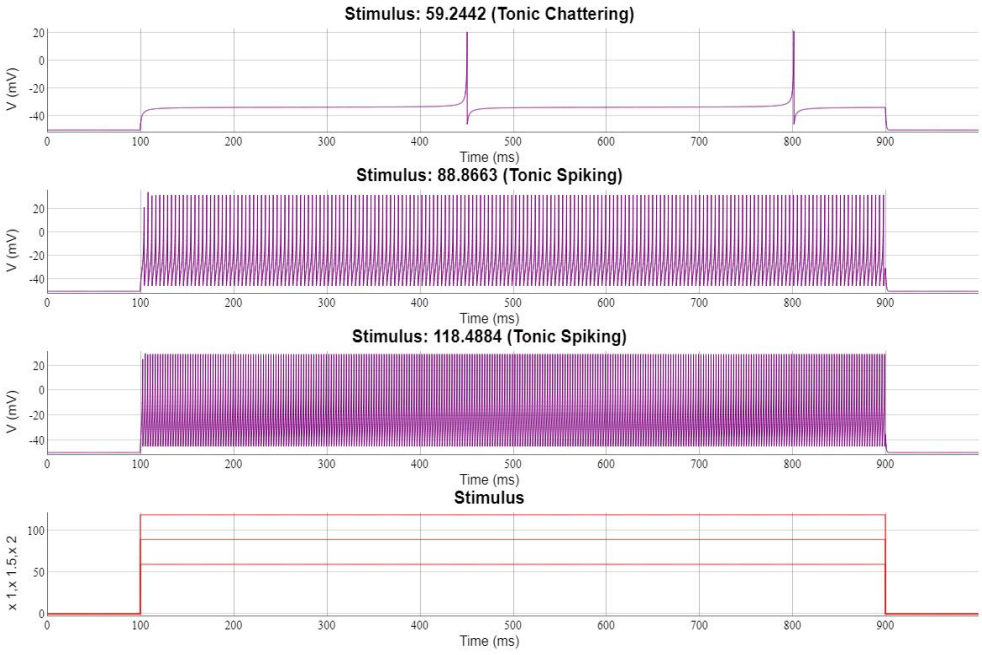
Stimulus: 59.2442 (Tonic Chattering)
V (mV)
Time (ms)
Stimulus: 88.8663 (Tonic Spiking)
V (mV)
Time (ms)
Stimulus: 118.4884 (Tonic Spiking)
V (mV)
Time (ms)
Stimulus
x 1, x 1.5, x 2
Time (ms)

V2a-Type-II-D

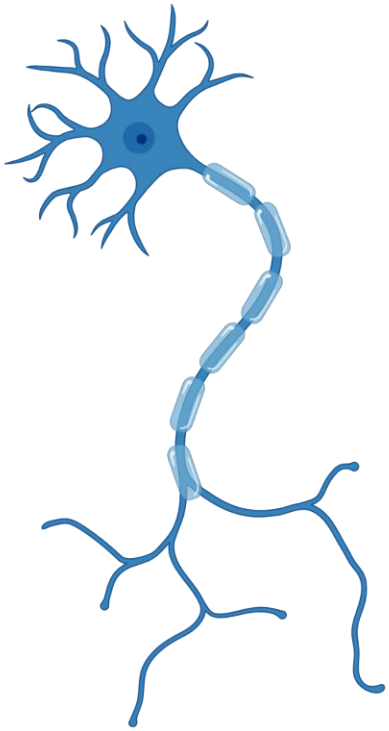

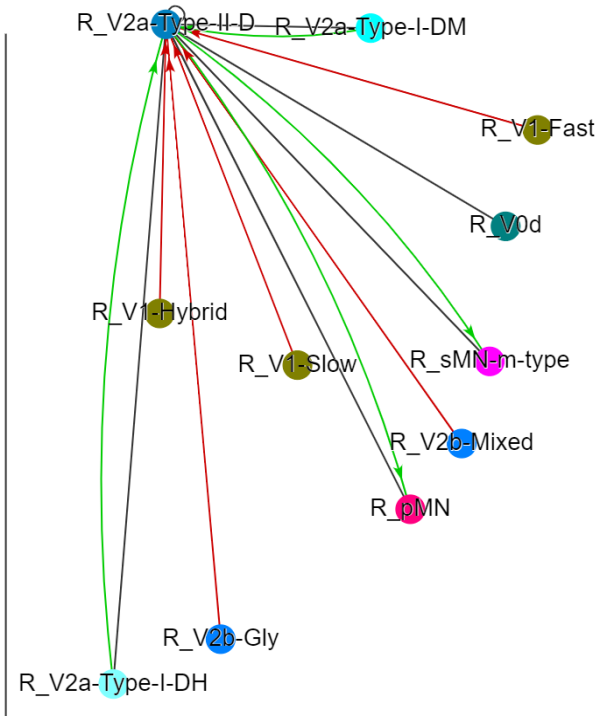
R_V2a-Type-II-D
R_V2a-Type-I-DM
R_V1-Fast
R_V0d
R_V1-Hybrid
R_V1-Slow
R_sMN-m-type
R_V2b-Mixed
R_pMN
R_V2b-Gly
R_V2a-Type-I-DH

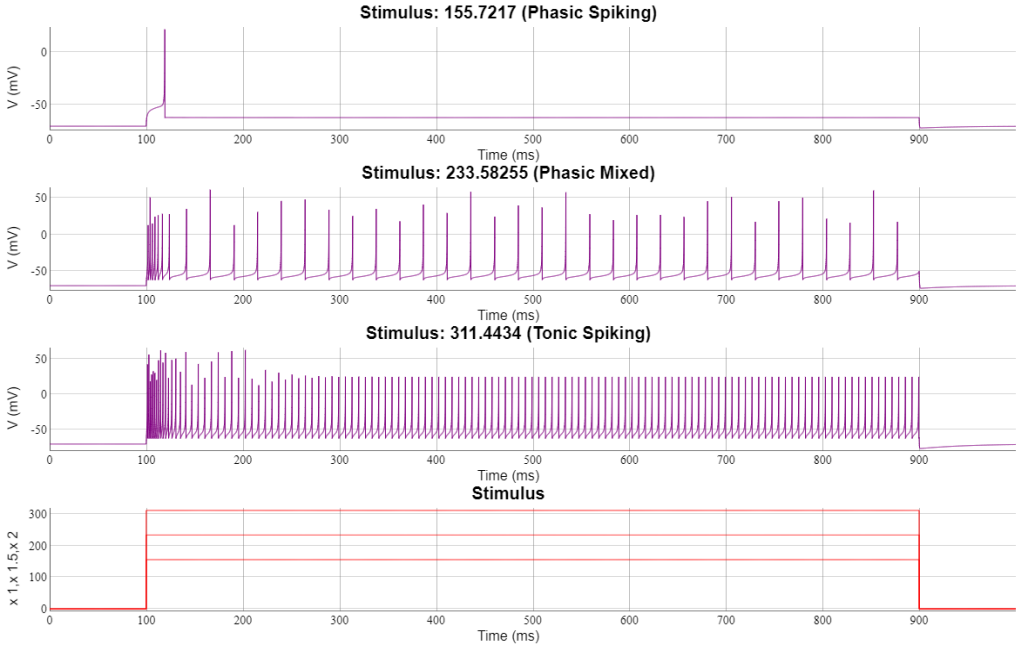
Stimulus: 155.7217 (Phasic Spiking)
V (mV)
Time (ms)
Stimulus: 233.58255 (Phasic Mixed)
V (mV)
Time (ms)
Stimulus: 311.4434 (Tonic Spiking)
V (mV)
Time (ms)
Stimulus
x 1,x 1.5,x 2
Time (ms)

V2a-VB

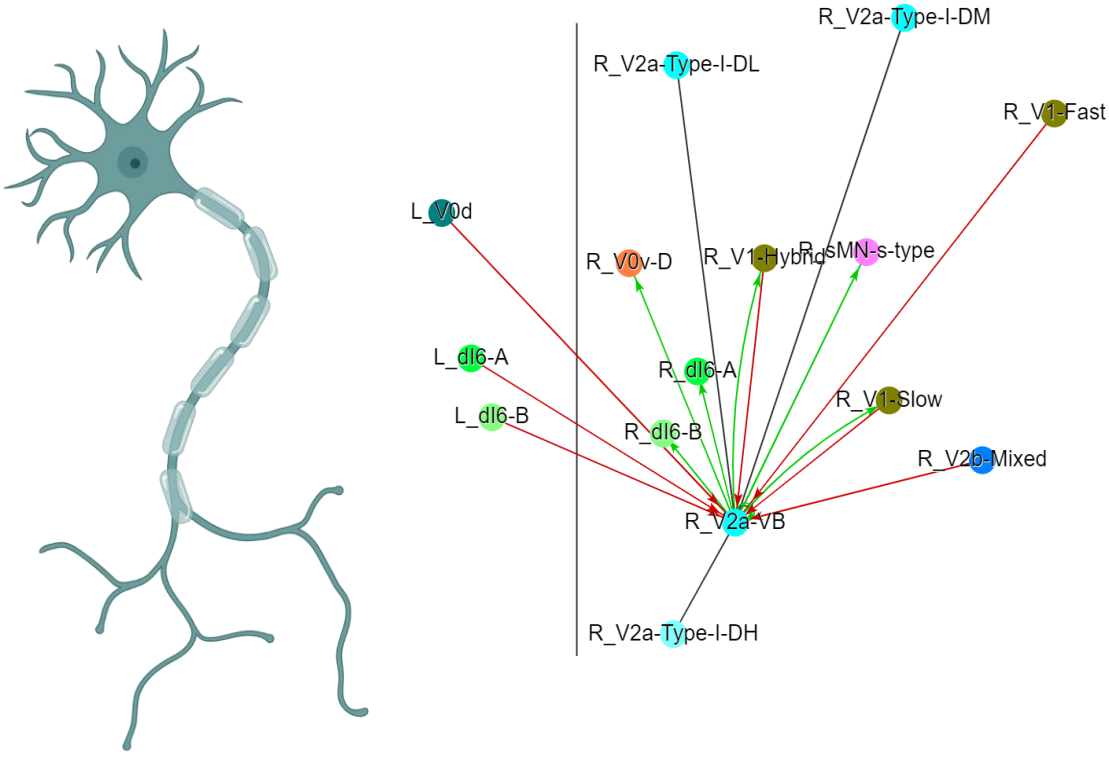
R_V2a-Type-I-DM
R_V2a-Type-I-DL
R_V1-Fast
L_V0d
R_V0v-D
R_V1-Hybrid
R_sMN-s-type
L_dI6-A
R_dI6-A
R_V1-Slow
L_dI6-B
R_dI6-B
R_V2b-Mixed
R_V2a-VB
R_V2a-Type-I-DH

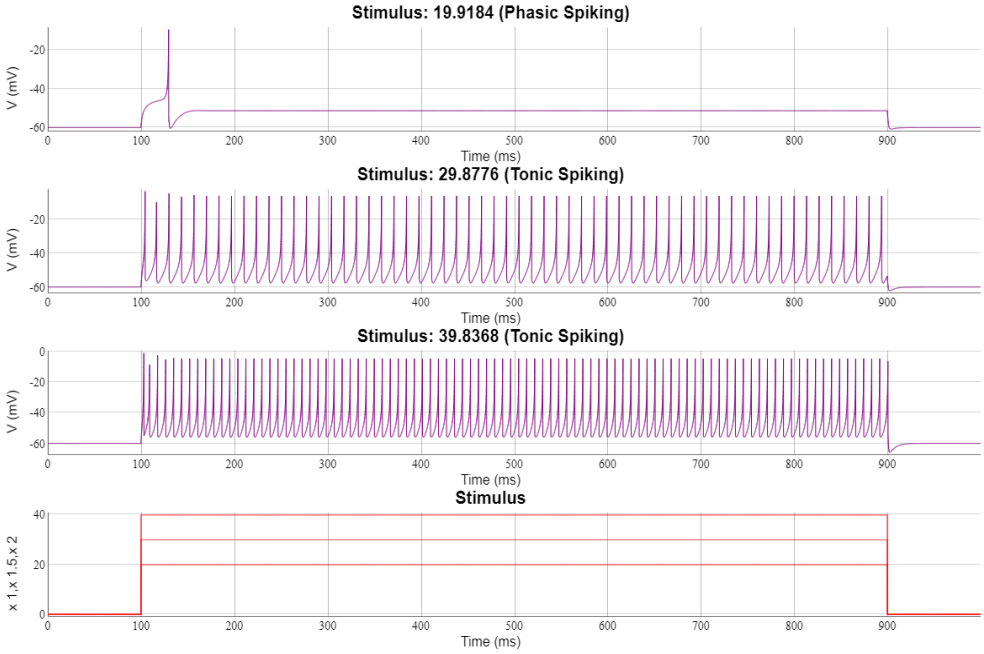
Stimulus: 19.9184 (Phasic Spiking)
Stimulus: 29.8776 (Tonic Spiking)
Stimulus: 39.8368 (Tonic Spiking)
Stimulus
V (mV)
x 1,x 1.5,x 2
Time (ms)

V2b Inhibitory

Projection: Descending / Ipsilateral

V2b-Gly

Neurotransmitter: Glycine

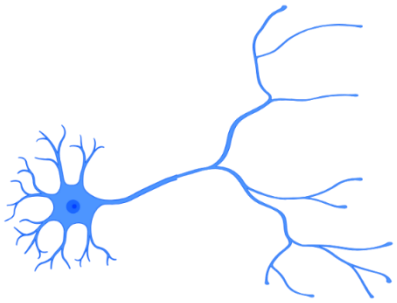

V2b-Mixed

Neurotransmitter: Glycine & GABA

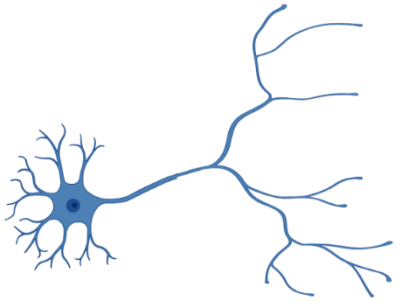

V2b-Gly

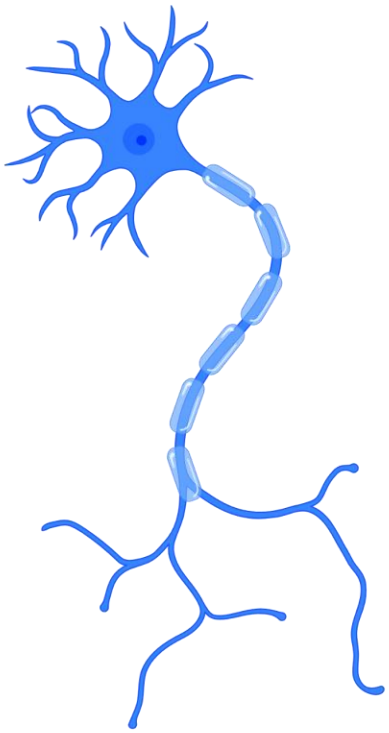

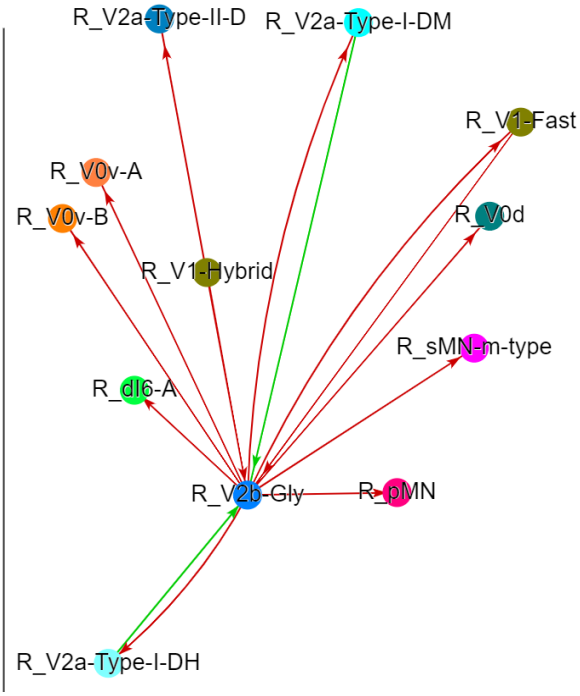
R_V2a-Type-II-D
R_V2a-Type-I-DM
R_V1-Fast
R_V0v-A
R_V0v-B
R_V0d
R_V1-Hybrid
R_sMN-m-type
R_dI6-A
R_V2b-Gly
R_pMN
R_V2a-Type-I-DH

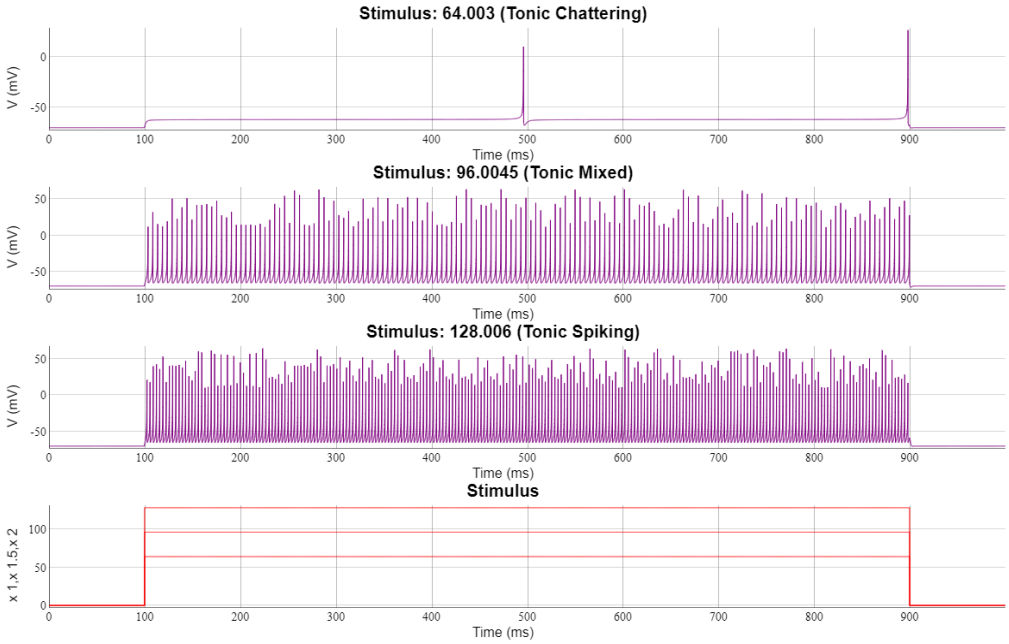
Stimulus: 64.003 (Tonic Chattering)
Stimulus: 96.0045 (Tonic Mixed)
Stimulus: 128.006 (Tonic Spiking)
Stimulus
V (mV)
x 1, x 1.5, x 2
Time (ms)

V2b-Mixed

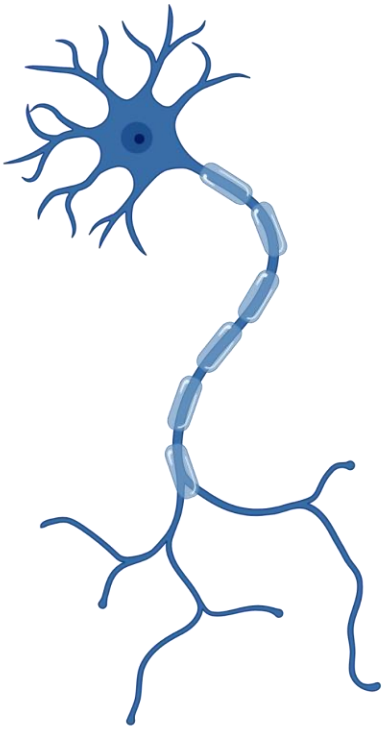

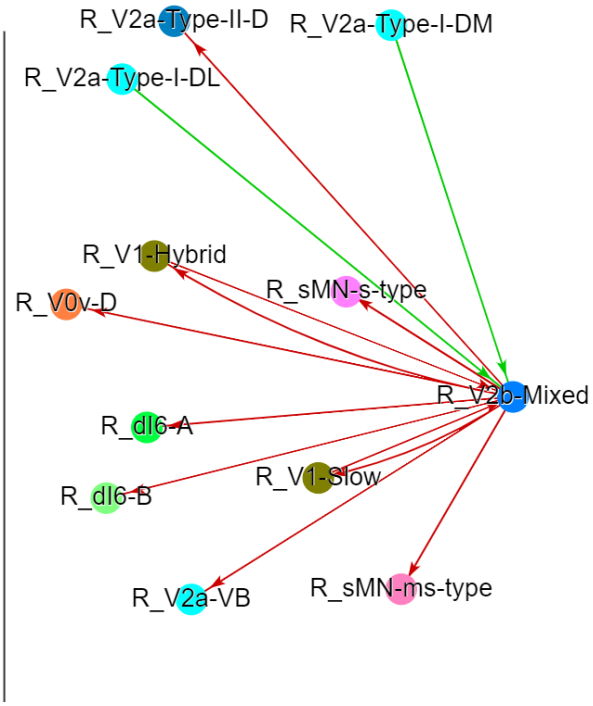
R_V2a-Type-II-D
R_V2a-Type-I-DM
R_V2a-Type-I-DL
R_V1-Hybrid
R_sMN-s-type
R_V0v-D
R_V2b-Mixed
R_dI6-A
R_V1-Slow
R_dI6-B
R_V2a-VB
R_sMN-ms-type

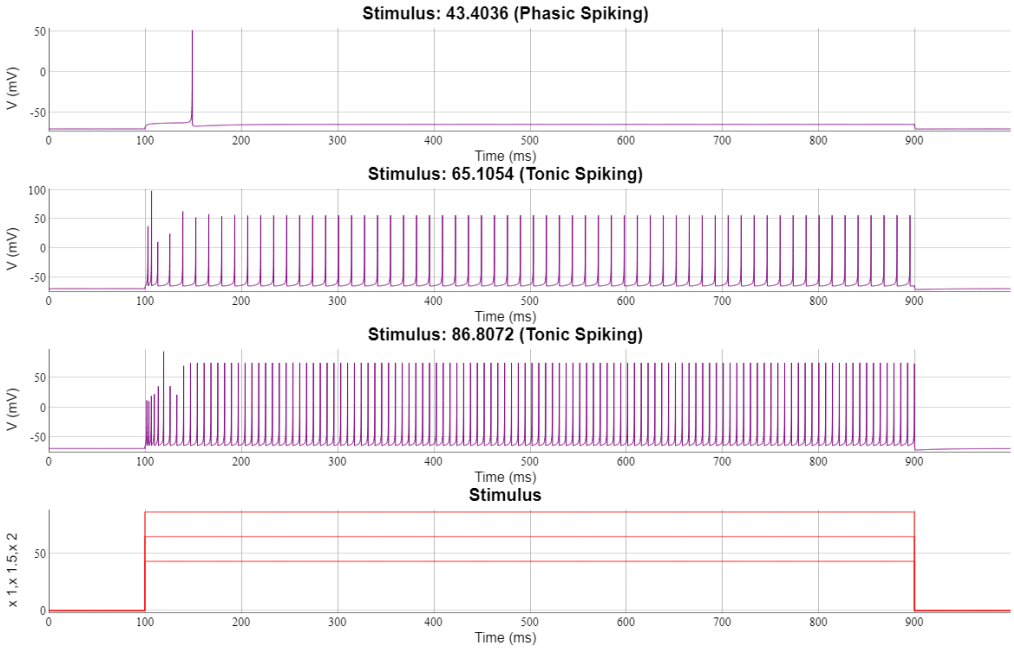
Stimulus: 43.4036 (Phasic Spiking)
Stimulus: 65.1054 (Tonic Spiking)
Stimulus: 86.8072 (Tonic Spiking)
Stimulus
V (mV)
x 1, x 1.5, x 2
Time (ms)

Muscle Fast AP

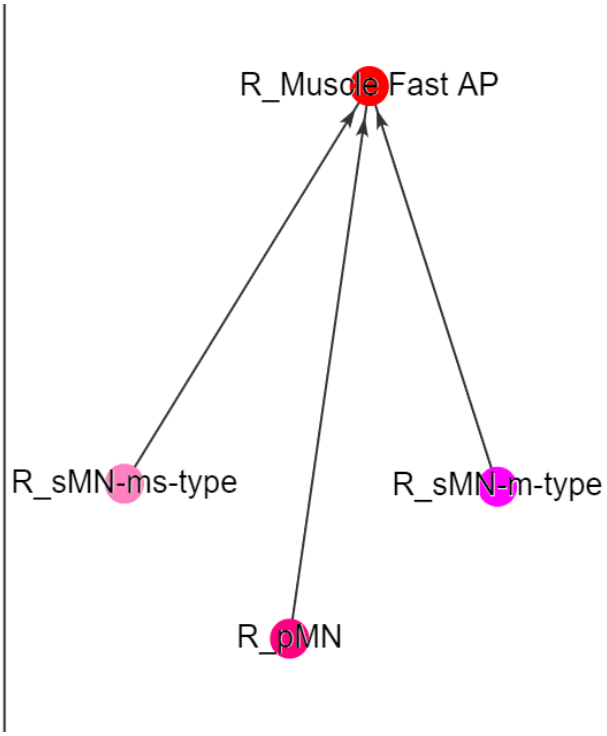

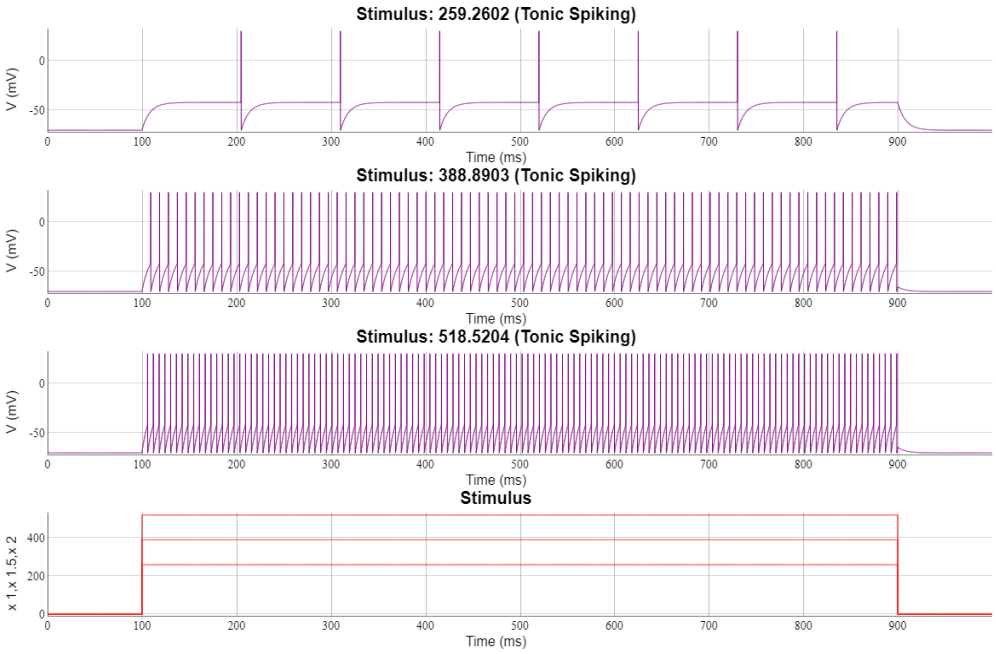

Muscle Slow

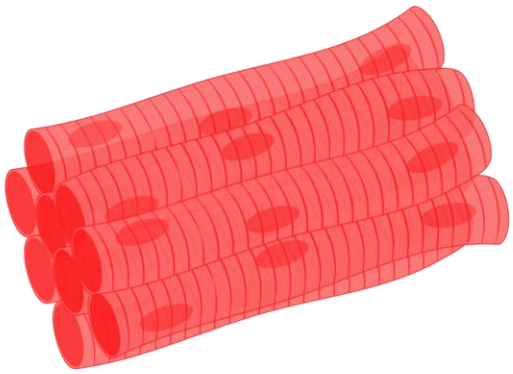

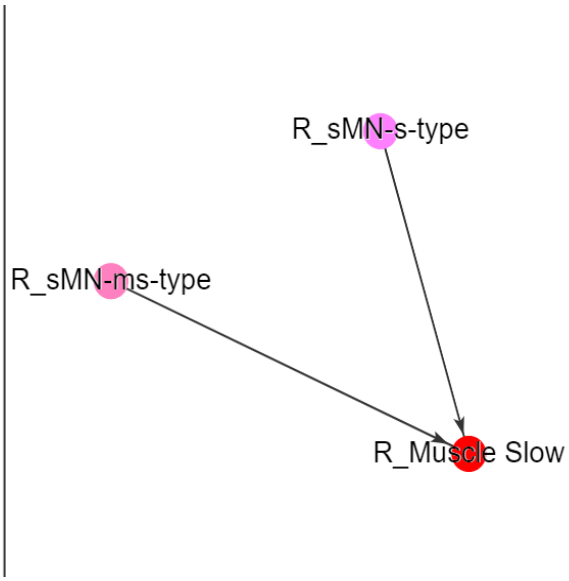
R_sMN-s-type
R_sMN-ms-type
R_Muscle Slow

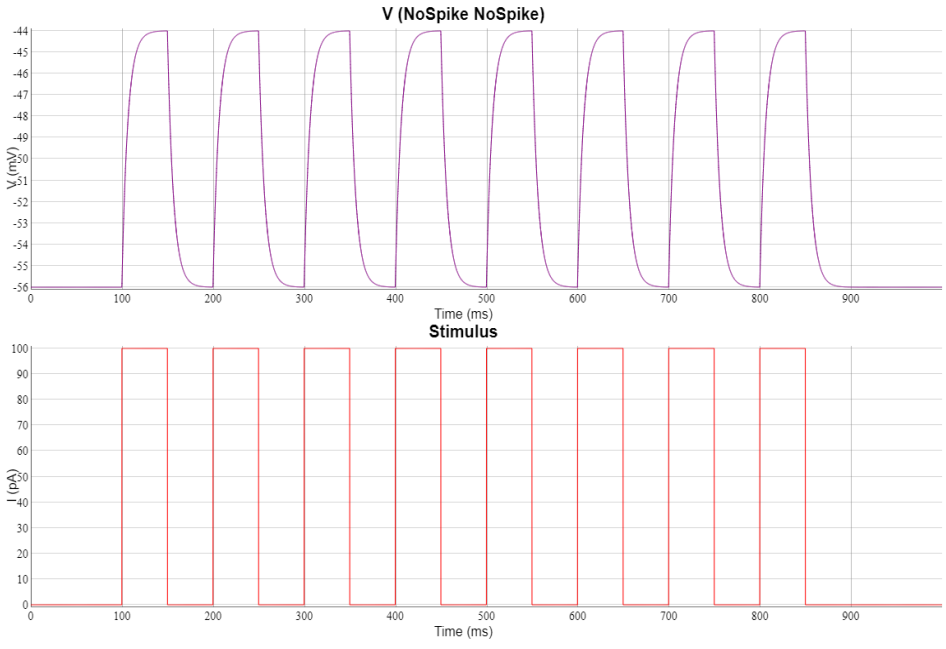
V (NoSpike NoSpike)
V (mV)
Time (ms)
Stimulus
I (pA)
Time (ms)